LIÈGE université
Sciences Appliquées

A damage to crack transition framework for ductile materials

A thesis submitted in partial fulfillment of the requirements
for the degree of Doctor of Philosophy (PhD) in Engineering Science

by

Julien LECLERC

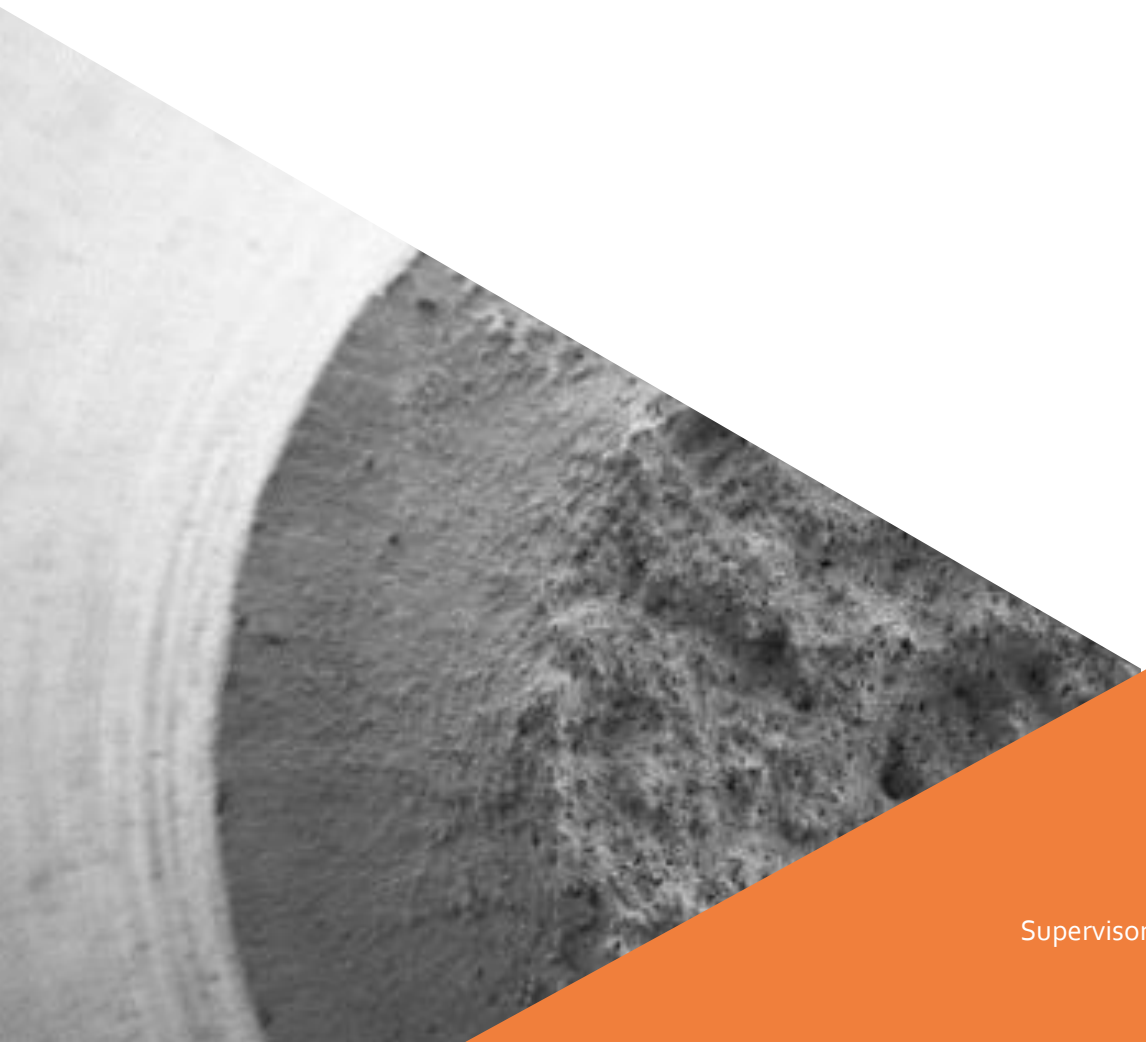

Supervisor: Ludovic NOELS

DOCTORAL COLLEGE IN AEROSPACE AND MECHANICS

MAY 2020

"*Sometimes, science is more art than science, Morty ! "*

Rick Sanchez — *Rick & Morty*

UNIVERSITY OF LIÈGE

Abstract

Faculty of Applied Sciences
Aerospace and Mechanical Engineering Department

Doctor in Engineering Sciences

A damage to crack transition framework for ductile materials

by Julien Leclerc

The simulation of the whole ductile fracture from the large-scale yielding to the localised crack initiation and propagation, is still challenging for scientists and engineers, especially under complex loading conditions. In this work, we develop a computationally efficient and energetically consistent damage to crack transition framework to address this issue. In addition, we provide an appropriate porous material model as well as the related calibration procedure.

Practically, an implicit non-local damage model represents the first diffuse damage stage, possibly beyond the softening onset. Once a crack insertion criterion is satisfied, a crack is introduced using a cohesive band model (CBM). This latter, contrarily to a cohesive zone model (CZM), accounts for 3D stress states during the crack opening which is mandatory in order to predict accurate results. The framework is implemented inside a Discontinuous Galerkin (DG) framework following the extrinsic CZM/DG formalism. Those choices ensure to the scheme interesting numerical properties demonstrated in this work: robustness upon failure, mesh-independence, energetic consistency and a reasonable trade-off between computational efficiency and simplicity.

The framework is first applied to a damage-enhanced elastic behaviour where the cohesive band thickness, the only introduced numerical parameter by the CBM, is determined from energetic considerations. It is then extended to the context of large strains and porous plasticity. Therewith, a micromechanics model including void nucleation, growth and coalescence, is presented. A suited crack insertion criterion is derived from a micro-mechanics coalescence model. In both cases, the numerical model is validated using experimental results from the literature.

Finally, the damage to crack transition model is validated with respect to an extensive experimental campaign studying a high-strength steel. The material and numerical models parameters are calibrated following micromechanics-based arguments. The framework, hence calibrated, is shown to be able to accurately predict the material behaviour until complete failure under different stress conditions and to include failure anisotropy. In particular, the complex experimental crack path on round bars and on grooved plates in plane strain is reproduced.

Acknowledgements

This doctoral thesis is the outcome of several years of research at the University of Liège and I would like to thank the numerous people who supported me and enabled this thesis to see the day light.

This research has been funded by the Walloon Region under the agreement no.7581-MRIPF in the context of the 16th MECATECH call.

I am grateful to all the members of the jury, Professors Jean-Philippe Ponthot, Anne-Marie Habraken, Stefanie Reese, Thomas Pardoen and Ling Wu for the time they spent reading and reviewing my work.

I am also very pleased to thank my advisor, Prof. Ludovic Noels who offered me to undertake this PhD. This thesis would never have been completed without his advices, his trust, his patience, his encouragement and all the time he spent helping during all these years.

This list would not be complete if I didn't acknowledge the help of my colleagues from UCLouvain, Marie-Stéphane Colla, Matthieu Marteleur and Prof. Thomas Pardoen with whom it is still a pleasure to collaborate. I am also thankful to my colleagues of my research group, Ling, Van-Dung for their help. Thanks to Nanda for granting us a pleasant office atmosphere.

A very special thanks to my friends, the old and the new ones, for everything. In particular, I would like to thank Jocelyn to whom I still own a fridge, Vince, thanks to whom the flute melody still rings in my head, Marco, Tilan, Ed, Thibault, Geoffrey and in particular, Romain for the nice never-ending discussions and for teaching me how to enjoy coffee. At this list, I would like to add many other friends and colleagues: some are still among us, some work on the floors below and some are left to other skies while still sometimes haunting the B52 corridors for a coffee break or an enjoyable lunchtime.

Je souhaite également exprimer ma gratitude envers ma famille pour leurs encouragements, et tout particulièrement à mes parents. Enfin, je ne pourrais oublier de remercier Mathilde pour avoir été une source intarrissable de motivation et de soutien.

Contents

List of Figures

List of Tables

List of Abbreviations

BC	**B**oundary **C**ondition
CBM	**C**ohesive **B**and **M**odel (**M**odel)
CDM	**C**ontinuous **D**amage **M**echanics (**M**odel)
CT(S)	**C**ompact **T**ension (**S**pecimen)
CZM	**C**ohesive **Z**one **M**odel
DENT	**D**ouble-**E**dge **N**otched **T**ensile specimen
DG	**D**iscontinuous **G**alerkin
DIC	**D**igital **I**mage **C**orrelation
EDX	**E**nergy **D**ispersive **X**-ray spectrometry
EFEM	**E**mbedded **L**ocalization **M**ethod
FE	**F**inite **E**lement
FEM	**F**inite **E**lement **M**ethod
GT	**G**urson **T**homason
GTN	**G**urson-**T**vergaard-**N**eedleman
PDE	**P**artial **D**ifferential **E**quations
SEM	**S**canning **E**lectron **M**icroscopy
short-GFRP	**short** **G**lass-**F**ibre **R**einforced **P**olymers (**P**olypropylene)
RVE	**R**epresentative **V**olume **E**lement
TSL	**T**raction-**S**eparation **L**aw
XFEM	e**X**tended **F**inite **E**lement **M**ethod

List of Symbols

Conventions

x	Scalar
$\boldsymbol{x}$	Vector
$\mathbf{x}$	Second-order tensor
$\mathfrak{x}$	Third-order tensor
$\boldsymbol{\mathcal{X}}$	Fourth-order tensor
$i, j, k...$	Tensorial index defined in the current configuration
$I, J, K...$	Tensorial index defined in the reference configuration
x_i	Vector components
x_{ij}	Second-order tensor component
$\mathfrak{x}_{ijk}$	Third-order tensor component
$\mathcal{X}_{ijkl}$	Fourth-order tensor component
[x]	Physical units
(i)	Iteration index
x_0	Variable related to the initial or reference configuration
x_I	Variable related to the interface surfaces
x^+	Variable related to the +-side of the interface surface
x^-	Variable related to the −-side of the interface surface
x_IC	Variable related to the cracked part of the interface surface
x_IU	Variable related to the uncracked part of the interface surface
x_b	Variable related to the cohesive band
x_ext	Variable related to the external surface
x_int	Variable related to the internal volume
x_vol	Variable related to a specific volume
x_surf	Variable related to a specific surface
x_c	Critical value of the variable x
x_f	Failure value of the variable x
x^e	Elastic part of the variable x
x^p	Plastic part of the variable x
x_pr	Predictor counterpart of the variable x
x^exact	Variable x related to the exact solution
$\tilde{x}$	Non-local counterpart of the variable x
$\hat{x}$	Effective counterpart of the variable x
$\bar{x}$	Prescribed value of the variable x

Mathematical operations and functions

$\cdot$	Tensorial product or scalar product
$\cdot^i$	Tens. product on the i$^{\mathrm{th}}$-index of the right hand side tensor
${}^i\cdot$	Tens. product on the i$^{\mathrm{th}}$-index of the left hand side tensor
$:$	Tensorial contraction
$\otimes$	Dyadic product
$[\![x]\!]$	Interface jump operator
$\langle x \rangle$	Mean operator

$\|\boldsymbol{x}\|$	Euclidean norm
$\|x\|$	Absolute value
$\frac{\partial f}{\partial x}$	Partial derivative of the function f with resp. to the var. x
$\dot{x}$	Partial time-derivative of the variable x
$\ddot{x}$	Second partial time-derivative of the variable x
$\boldsymbol{\nabla} x$	Gradient operator with respect to the current configuration
$\boldsymbol{\nabla}_0 x$	Gradient operator with respect to the initial configuration
$\nabla^2 x$	Laplace operator with respect to the current configuration
$\nabla_0^2 x$	Laplace operator with respect to the initial configuration
Δx	Increment of the variable x
δx	Variation of the variable x
$\mathtt{H}_{\mathrm{D}}(x)$	Heavyside function
$\mathtt{H}_{\mathrm{B}}(x)$	Linear-step function
$\mathbf{I}$	Second-order identity tensor
$\mathbf{x}^{\mathrm{dev}}$	Deviatoric counterpart of the tensor $\mathbf{x}$
$\mathbf{x}^{\mathrm{T}}$	Symmetric counterpart of the tensor $\mathbf{x}$
$\mathrm{tr}(\mathbf{x})$	Trace of the tensor $\mathbf{x}$
$\boldsymbol{\mathcal{I}}^{\mathrm{dev}}$	4-th order deviatoric symmetric identity tensor

Topology (with respect to the current configuration)

Ω	Material body in the current configuration
Γ	Material external boundary surface of Ω
Γ_{D}	Dirichelet part of the external surface Γ
Γ_{N}	Neumann part of the external surface Γ
$\boldsymbol{n}$	Unitary normal vector to Γ in the current configuration
Γ_{I}	Interface surfaces inside Ω
Γ_{IU}	Uncracked part of the interface surfaces Γ_{I}
Γ_{IC}	Cracked part of the interface surfaces inside Γ_{I}
Ω^+, Ω^-	Partition of Ω due to Γ_{I} in the current configuration
$\boldsymbol{n}_{\mathrm{I}}$	Unitary normal vector to interface surface Γ_{I}
$\boldsymbol{s}_{\mathrm{I}}, \boldsymbol{s}'_{\mathrm{I}}$	Unitary tangent vector to interface surface Γ_{I}

Topology (with respect to the initial or reference configuration)

Ω_0	Material body in the initial configuration
Γ_0	Material external boundary surface of Ω_0
Γ_{D0}	Dirichelet part of the external surface Γ_0
Γ_{N0}	Neumann part of the external surface Γ_0
$\boldsymbol{N}$	Unitary normal vector to Γ_0 in the initial configuration
Γ_{I0}	Interface surfaces inside Ω_0
Γ_{IU0}	Uncracked part of the interface surfaces Γ_{I0}
Γ_{IC0}	Cracked part of the interface surfaces inside Γ_{I0}
Ω_0^+, Ω_0^-	Partition of Ω_0 due to Γ_{I0} in the initial configuration
$\boldsymbol{N}_{\mathrm{I}}$	Unitary normal vector to interface surface Γ_{I0}
$\boldsymbol{S}_{\mathrm{I}}, \boldsymbol{S}'_{\mathrm{I}}$	Unitary tangent vector to interface surface Γ_{I0}
Ω_{b0}	Cohesive band volume in the reference configuration

Kinematic variables

x, y, z	Spatial cartesian coordinates	[m]
r	Radial cylindrical coordinates	[m]
θ	Azimuthal cylindrical coordinates	[rad]
z	Axial cylindrical coordinates	[m]

$\boldsymbol{x}$	Current material position vector	[m]
$\boldsymbol{X}$	Initial material position vector	[m]
$\boldsymbol{X}_{\mathrm{I}}$	Initial material position vector on the crack interface $\Gamma_{\mathrm{I}0}$	[m]
$\boldsymbol{u}$	Displacement vector	[m]
$\mathbf{F}$	Deformation gradient tensor	[−]
$\mathbf{R}^{\mathrm{e}}$	Rotation part of the elastic deformation gradient tensor	[−]
$\mathbf{U}^{\mathrm{e}}$	Symmetric part of the elastic deformation gradient tensor	[−]
$\boldsymbol{\epsilon}$	Cauchy strain tensor	[−]
J	Jacobian of the deformation gradient tensor	[−]
$\mathbf{C}$	Right Cauchy strain tensor	[−]
$\mathbf{E}$	Natural or logarithmic strain tensor	[−]

Stress variables

$\boldsymbol{\sigma}$	Cauchy stress tensor	[Pa]
$\boldsymbol{\kappa}$	Kirchhoff stress tensor	[Pa]
$\boldsymbol{\tau}$	Corotational Kirchhoff stress tensor	[Pa]
$\mathbf{P}$	First Piola-Kirchhoff stress tensor (PK1)	[Pa]
p_τ	Pressure in terms of the Kirchhoff stresses	[Pa]
p_σ	Pressure in terms of the Cauchy stresses	[Pa]
x^{eq}	Von Mises or J2-equivalent value of the stress x	[Pa]
T	Stress triaxiality	[−]
ζ	Lode variable	[−]
θ	Lode angle	[−]
ρ	Density per unit volume in the current configuration	$[\mathrm{kg/m^3}]$
ρ_0	Density per unit volume in the reference configuration	$[\mathrm{kg/m^3}]$
$\boldsymbol{b}$	Volumic external force in the cur. config. per unit of cur. volume	$[\mathrm{N/m^3}]$
$\boldsymbol{b}_0$	Volumic external force in the cur. config. per unit of init. volume	$[\mathrm{N/m^3}]$
$\bar{\boldsymbol{t}}_{\mathrm{N}}$	Surfacic external force in the cur. config. per unit of cur. surface	[Pa]
$\bar{\boldsymbol{t}}_{\mathrm{N}0}$	Surfacic external force in the cur. config. per unit of init. surface	[Pa]

Energetic variables

ψ	Helmholtz (reversible) free energy per volume	$[\mathrm{J/m^3}]$
φ	Dissipated energy per volume	$[\mathrm{J/m^3}]$
W_{int}	Work of the internal forces per volume	$[\mathrm{J/m^3}]$
Ψ	Total Helmholtz free energy	[J]
Φ	Total dissipated energy	[J]
$\mathscr{W}_{\mathrm{surf}}$	Total work of the surfacic forces	[J]
$\mathscr{W}_{\mathrm{ext}}$	Total work of the external forces	[J]
$\mathscr{W}_{\mathrm{int}}$	Total work of the internal forces	[J]

Elastic damage constitutive behaviour

Z	Internal variable	[−]
$\boldsymbol{\mathcal{H}}$	Hooke tensor	[Pa]
D	Damage	[−]
$\boldsymbol{\mathcal{H}}^D$	Stiffness tensor of the damaged material	[Pa]
Y	Damage energy release rate	$[\mathrm{J/m^3}]$
e	Equivalent elastic strain	[−]
l_{c}	Non-local length	[m]
$\mathbf{C}_{\mathrm{l}}$	Non-local symmetric tensor	$[\mathrm{m^2}]$
w	Non-local weight function	[−]
W_{G}	Non-local Green weight function	[−]

$W_{\mathrm{G-BC}}$	Boundary contribution to the non-local Green weight function	[−]

Plasticity

ϕ	Yield function	[−]
ϕ_{G}	Gurson yield function	[−]
ϕ_{GTN}	GTN-model yield function	[−]
ϕ_{T}	Thomason yield function	[−]
$\phi_{\mathrm{T}^+}(\phi_{\mathrm{T}^-})$	Tension (compression) part of the Thomason yield function	[−]
C_{T}^{ϕ}	Concentration factor of the Thomason model	[−]
τ_{Y}	Yield stress in terms of Kirchhoff stress	[Pa]
τ_{Y0}	Initial yield stress in terms of Kirchhoff stress	[Pa]
R	Hardening function in terms of Kirchhoff stress	[Pa]
h	Derivative of h in terms of the equivalent plastic strain	[Pa]
V	Overstress function in terms of the equivalent plastic strain rate	[Pa]
σ_{Y}	Yield stress in terms of Cauchy stress	[Pa]
σ_{Y0}	Initial yield stress in terms of Cauchy stress	[Pa]
d	Deviatoric equivalent plastic strain	[−]
q	Volumetric equivalent plastic strain	[−]
p	Matrix equivalent plastic strain	[−]
γ	Plastic multiplier	[Pa]
$\boldsymbol{v}$	Plastic increment vector	[−]
$\boldsymbol{r}_{\mathrm{p}}$	Plastic return residues in terms of $\boldsymbol{v}$	[−]
$\mathbf{N}^{\mathrm{p}}$	Plastic normal	[1/Pa]
N^{d}	Deviatoric part of the plastic normal	[1/Pa]
N^{q}	Volumetric plastic normal	[1/Pa]
$N_{\mathrm{G}}^{\mathrm{d}}$	Deviatoric part of the plastic normal of the Gurson model	[1/Pa]
$N_{\mathrm{G}}^{\mathrm{q}}$	Volumetric plastic normal of the Gurson model	[1/Pa]
$N_{\mathrm{T}}^{\mathrm{d}}$	Deviatoric part of the plastic normal of the Thomason model	[1/Pa]
$N_{\mathrm{T}}^{\mathrm{q}}$	Volumetric plastic normal of the Thomason model	[1/Pa]

Micromechanics

f_{V}	Local porosity fraction	[−]
f_{V_0}	Initial porosity fraction	[−]
$\tilde{f}_{\mathrm{V}}$	Non-local porosity fraction	[−]
$\hat{f}_{\mathrm{V}}$	Effective porosity fraction	[−]
$f_{\mathrm{V_C}}$	Critical porosity fraction (GTN model)	[−]
δ_{GTN}	Phenomenological acceleration rate of porosity growth (GTN model)	[−]
$f_{\mathrm{V}}^{\star}$	Phenomenological/corrected porosity value (GTN model)	[−]
$f_{\mathrm{V_f}}$	Porosity value at failure without correction (GTN model)	[−]
$f_{\mathrm{V_f}}^{\star}$	Phenomenological/corrected porosity value at failure (GTN model)	[−]
χ	Cell ligament ratio	[−]
λ	Cell aspect ratio	[−]
$f_{\mathrm{V_{nucl}}}$	Nucleated porosity fraction	[−]
A_{n}	Plastic strain-controlled nucleation rate	[−]
B_{n}	Shear-induced growth rate function	[−]
k_{ω}	Shear-induced growth coefficient	[−]
$\boldsymbol{\sigma}_{\mathrm{n_c}}$	Critical stress nucleation tensor	[Pa]
$\boldsymbol{\sigma}_{\mathrm{n}}$	Inclusions nucleation stress tensor	[Pa]
$\mathbf{k}$	Tensorial stress concentration factor	[−]

Cohesive band model

h_b	Cohesive band thickness	[m]
$\mathbf{F}_\mathrm{b}$	Enhanced cohesive band deformation gradient	[−]
$\boldsymbol{\epsilon}_\mathrm{b}$	Cohesive band Cauchy strain tensor	[−]
$\boldsymbol{\sigma}_\mathrm{b}$	Cohesive band Cauchy stress tensor	[Pa]
$\mathbf{P}_\mathrm{b}$	Cohesive band PK1 tensor	[Pa]
D_b	Cohesive band damage value	[−]
D_c	Damage value linked to the crack insertion	[−]
$\hat{\epsilon}_\mathrm{c}$	Equivalent elastic strain value linked to the crack insertion	[−]
$\hat{\sigma}_\mathrm{c}$	Critical effective stress value linked to the crack insertion	[Pa]
β_c	Opening mode I/II ratio	[−]
G_c	Energy release rate (by unit of crack surface created)	$[\mathrm{J/m^2}]$
$\boldsymbol{t}_\mathrm{I}$	Interface traction force per unit of current surface	[Pa]
$\boldsymbol{t}_\mathrm{I0}$	Interface traction force per unit of initial surface	[Pa]
δ_c	Critical crack opening value	[m]

Finite element discretisation

B	Finite volume element	
S	Finite surface element	
N_n	Number of node in an element	
$x^{e,s}$	Variable related to the element e or s	
$x^{a,b,...}$	Variable related to the node $a, b, ...$	
N^a	Shape function linked to the node a	[−]
$\boldsymbol{w_u}$	Test functions linked to the displacement field	[m]
$w_{\tilde{e}}$	Test functions linked to the non-local equivalent strain field	[−]
$w_{\tilde{Z}}$	Test functions linked to the non-local variable field	[−]
$\boldsymbol{q}$	Finite element unknowns vector	[m, −]
$\boldsymbol{f}^e$,$\boldsymbol{f}^s$	Elementary force vector linked to element e or s	$[\mathrm{N}, \mathrm{m^3}]$
$\mathbf{M}$	Finite element mass matrix	[kg]
$\boldsymbol{r}$	Finite element residual vector	$[\mathrm{N}, \mathrm{m^3}]$
$K, \boldsymbol{K}, \mathbf{K}$	Finite element stiffness variable	$[\mathrm{N/m}, \mathrm{N}, \mathrm{m^3}, \mathrm{m^2}]$
$C, \mathbf{C}, \mathfrak{C}, \boldsymbol{\mathcal{C}}$	Material tangent variable	$[\mathrm{Pa}, \mathrm{Pa/m}, -, \mathrm{m^{-1}}]$
β_s	Stability parameter	[−]
h_s	Mesh characteristic size parameter	[m]
l_mesh	Mesh size	[m]

Chapter 1

Introduction

1.1 General context

With the development of computational tools, the mechanical simulations of an industrial product gain more and more in importance. Accurate and reliable numerical predictions allow reducing the cost of expensive experimental campaigns while improving structural design. It is even more crucial in some sectors. For instance, in aeronautics, mechanical reliability improvements and weight savings are highly encouraged by strong economic and environmental incentives. Moreover, simulations of fragmentations or impacts afford precious insights in the physical process with a reduced cost compared to real experiments.

However, the modelling of ductile fracture under complex loading conditions involves many unsolved challenges for scientists and engineers. As illustrated for a metal sheet on Fig. 1.1, this process usually starts with a homogeneous or spread damage evolution (step (a) to (b)). In this example, this damage is materialised by small defects or cracks under the microscopic scale. Typically, small voids nucleate from inclusions that break or separate themselves from the steel matrix (Pineau, Benzerga, and Pardoen, 2016). These latter gradually grow. During the process, the damage evolution eventually localises due to material softening or mechanical instabilities (steps (b) and (c)). At some point, the cavities in the most damaged area start to fuse with their neighbours. This coalescence process provokes the onset of macroscopic cracks (step (d)). These discontinuities then propagate through the material, leading to its failure (step (e)). However, the origin, the behaviour and the sequence of the damage process strongly vary from a material to another (Noell, Carroll, and Boyce, 2018). In the following, we focus on the particular case consisting in two phases: a diffuse growth stage followed by a localised damage step.

When this kind of failure process is considered in its globality, i.e. including both the diffuse growth and localisation stages, regular numerical models, generally based on finite element methods (FEM), are of very limited reliability. At best, they need to be calibrated on a case by case basis while others do not conserve mass and energy or suffer from numerical issues. In short, no solution is nowadays totally predictive. The ideal sought framework should be able to predict the failure of ductile metals under various loading conditions while avoiding case-dependent calibration. Among others, mesh-dependency has to be prevented. It is also mandatory to be energetically consistent. In other words, general physical principles as mass and energy conservations have to be ensured. Moreover, the ideal framework should be a trade-off between implementation simplicity, 3D simulation capabilities, scalability and computational efficiency.

In this context, this thesis will investigate this gap while keeping in mind the ideal numerical properties. It will attempt to fill in this lack with a suitable numerical framework, along with an adapted material model and a calibration procedure. Indeed, in terms of numerical approaches, traditional frameworks developed in a finite element (FE) formulation may be separated in two categories. On the one hand, the first category gathers the models based on the Continuous Damage Mechanics (or CDM) (Chaboche, 1988; Lemaitre, 1986; Lemaitre

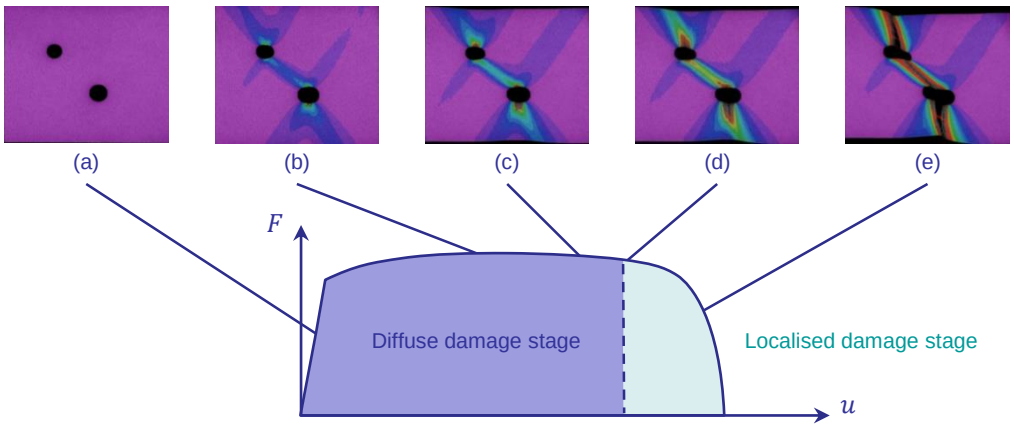

FIGURE 1.1: Example of typical failure process observed for a metal sheet with two holes under a traction test (the force is applied horizontally). Pictures (Source: radome.ec-nantes.fr) show the horizontal strain field using DIC (Digital Image Correlation) at different steps of the damage evolution: (a) elastic regime, (b) softening onset, (c) strain localisation, (d) crack initiation and propagation and (e) final failure. Each step can be classified either in the diffuse or the localised damage stage. .

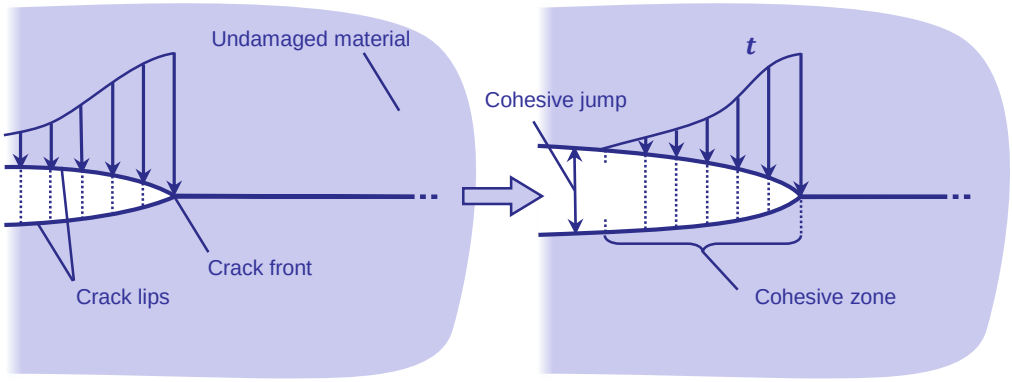

FIGURE 1.2: Schematic representation of a growing failure process using a Cohesive Zone Model (CZM). All the damage process is concentrated on the crack surface while the vicinity stays intact.

et al., 2009). On the other hand, the second family is rather inspired by the fracture mechanics (Anderson, 2017; Zehnder, 2012).

1.1.1 Discontinuous approaches

On the one side, this category of fracture modelling, the discontinuous approaches, idealises the material degradation by the propagation of a sharp discrete crack. One of the most popular adaptations of this approach to numerical methods is the cohesive zone model (CZM), schematised on Fig. 1.2. It was initiated by Barenblatt (1962) and Dugdale (1960) and firstly used in a FE context by Hillerborg, Modéer, and Petersson (1976). The damage process and energy dissipation emanate from crack surfaces creation in the process zone. Meanwhile, the uncracked parts stay intact. The model is defined through its traction-separation law (TSL). This law describes how the bonding forces between the crack lips irreversibly decrease while the crack opening (or the cohesive jump) increases.

However, the use of CZM implies extensive modifications of the FE discretisation to take into account the description of discontinuities. The most popular methods to address this issue are (i) the extended finite element method (XFEM (Moës, Dolbow, and Belytschko, 1999;

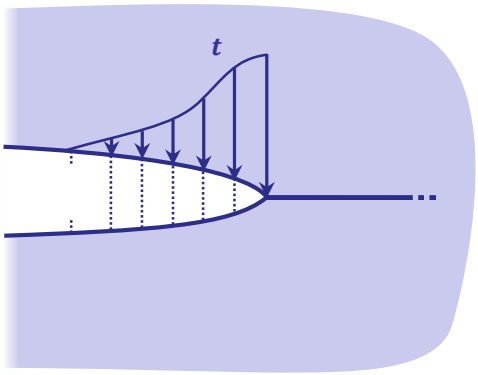

(a) an extrinsic cohesive zone,

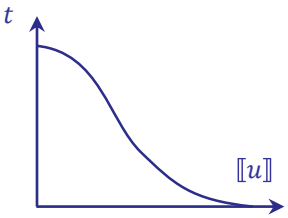

(b) an extrinsic TSL,

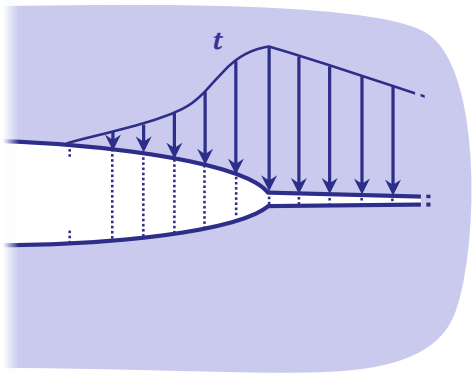

(c) an intrinsic cohesive zone,

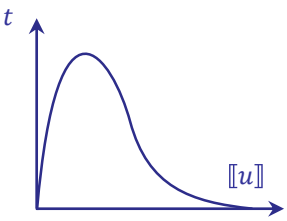

(d) an intrinsic TSL.

FIGURE 1.3: Comparison of the crack front modelling between (a) an extrinsic and (b) an intrinsic Cohesive Zone Model (CZM), and their respective (c) extrinsic and (d) intrinsic traction-separation law (TSL).

Vigueras et al., 2015)), (ii) the embedded localization method (EFEM (Linder and Armero, 2007)), (iii) the interface elements (Hillerborg, Modéer, and Petersson, 1976), and (iv) the Discontinuous Galerkin (DG) method (Mergheim, Kuhl, and Steinmann, 2004). The first two methods consist in respectively a global and a local enrichment of the displacement field: the crack can propagate through the bulk elements following an arbitrary path. The third method introduces a CZM using an interface element between two neighbouring volume elements. Two main insertion techniques exist. On the one hand, Camacho and Ortiz (1996) and Pandolfi et al. (2000) inserted cohesive interface elements on the fly between two volume elements once their crack initiation criterion is reached. In this case, the cohesive law is so-called extrinsic as it represents only the crack opening (see Figs. 1.3a and 1.3b). However, this dynamic insertion by node splitting decreases the scalability of the method as the mesh topology is modified; unless a graph-based internal structure is used (Mota, Knap, and Ortiz, 2008; Paulino et al., 2008). On the other hand, the insertion can also be performed before the simulation, at its beginning (see Fig. 1.3c). The CZM is therefore so-called intrinsic (Needleman, 1987; Tvergaard, 1990; Xu and Needleman, 1994). As shown on Fig. 1.3d, the intrinsic TSL has to represent the pre-crack material response (i.e. the loading part), by opposition to Fig. 1.3b. The crack criterion is implicitly incorporated within the TSL (which can be assimilated to the maximal stress value). Unfortunately, the presence of the initial loading phase induces non-consistent elastic responses and mesh-dependency as demonstrated by Falk, Needleman, and Rice (2001) and Tabiei and Zhang (2017) e.g. Therefore, the intrinsic method is restricted to simple and a priori known crack paths (Xu and Lu, 2013). The fourth method, analogous to the third one, overcomes the issues of intrinsic and extrinsic interface methods by involving a Discontinuous Galerkin (DG) finite element discretisation. The DG method is based on the concept of ensuring inter-element continuity in a weak sense. Therefore, discontinuities are dormant, and thus, inherently present between elements since the beginning in the DG

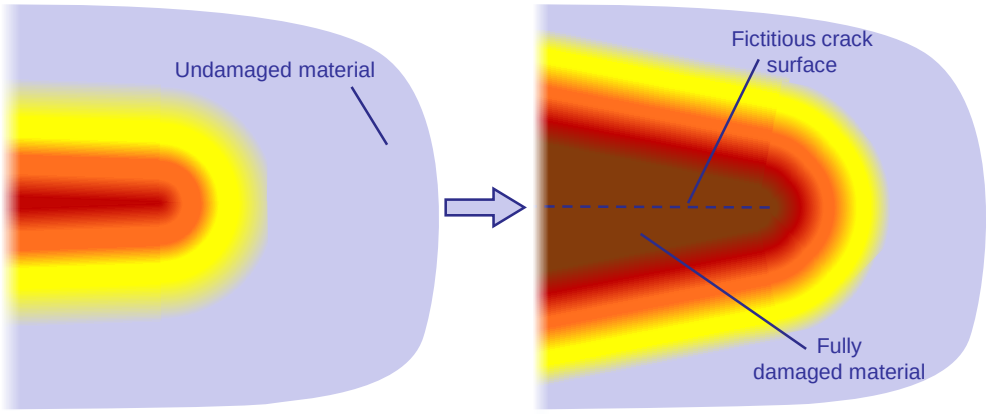

FIGURE 1.4: Schematic representation of a growing failure process modelled by a continuous damage mechanics (CDM).

formulation. Cracks can be easily inserted by releasing the DG-constraints at crack initiation and replacing them by the cohesive relation. By this way, the hybrid DG-CZM scheme easily allows a large number of crack insertion and propagation without scalability or consistency issues as demonstrated by Radovitzky et al. (2011).

The CZM approach succeeds well in the prediction of brittle or small-scale yielding materials, when the damage can be assumed to be concentrated at the crack surface. However, it logically fails to accurately represent the diffuse damage phase of any ductile failure. Indeed, it is unable to represent the complex interactions between the free crack surface creation and the homogeneous damage diffusion.

1.1.2 Continuous approaches

On the other side, the other category of fracture modelisation, the continuous damage mechanics (CDM), allows modelling a large range of different degradation processes using any classical finite element formulations. The main idea is to sum up the material history and the progressive mechanical degradation through the intermediary of internal or damage variables. Practically, as shown on Fig. 1.4, damage diffusively grows (from an initial state in blue on the schematic) with the deformation until a point where the material is considered as fully damaged or broken (in brown).

From the numerical point of view, continuous damage models can be distinguished from the way they consider and compute these variables: there are coupled and decoupled models. Decoupled ones simplify the problem by disregarding any coupling between the evolution of the damage and the mechanical properties. In this case, damage variables simply determine when the material fails by using a fracture locus. The complexity level of such failure surface is various (Johnson and Cook, 1985; Liu, Kang, and Ge, 2019, e.g.). Conversely, coupled damage models directly impact the material behaviour. The model formulation can be a mix between a purely phenomenological approach and a micromechanical-based description. For instance, the model pioneered by Chaboche (1988) and Lemaitre (1986) acts on the Young's modulus (see Lemaitre et al. (2009)), gradually reducing its effective value during the damage evolution. Another example is the Gurson model (Gurson, 1977), which belongs to a more general family, the porous models. In this case, the degradation of macroscopic mechanical properties derives from the evolution of microscopic porosities distributed inside the material.

However, the coupled CDM, under a local form, exhibit a mesh dependency during the softening regime, as it has been demonstrated many times in the literature (Bažant, Belytschko, and Chang, 1984; Peerlings et al., 2001; Pijaudier-Cabot and Bažant, 1987; Reusch, Svendsen, and Klingbeil, 2003a, e.g.). Indeed, at the material softening onset, the equations become

ill-posed as they loose their ellipticity. The damage growth therefore concentrates itself in a one-element-thick volume. Results will thus depend on the mesh size and orientation. However, this issue is overcome by introducing regularisation methods like phase field approaches (de Borst and Verhoosel, 2016; Miehe, Welschinger, and Hofacker, 2010; Miehe et al., 2016; Shen, Waisman, and Guo, 2019, e.g.) or non-local models (Nguyen, Korsunsky, and Belnoue, 2015; Peerlings et al., 1998; Pijaudier-Cabot and Bažant, 1987). The phase field replaces the cracks by a regularised or diffusive crack field. However, there is no real damage evolution definition, preventing the use of complex models such as porous models under a pure phase field. The non-local models drop the local action principle: some local internal variables are substituted by their non-local averaged counterpart. The non-local averaging can be done through an integral (Pijaudier-Cabot and Bažant, 1987) or a differential procedure. The latter option has the advantage to naturally treat boundaries and complex geometries. For instance, the implicit non-local method, pioneered by Peerlings et al. (1996), involves non-local variables separately interpolated from the displacement field. A characteristic length, resulting from the interaction distance between micro-defects, controls the process diffusion. The non-local models may be generalised under a micromorphic approach (Aldakheel, 2017; Forest, 2009) using non-local thermodynamic potentials.

These non-local CDM succeed well in the description of diffuse damage mechanisms. However, numerical issues arise at the end of the damage process since highly damaged elements induce spurious damage diffusion. In response, Geers et al. (1998) and others (Poh and Sun, 2017; Vandoren and Simone, 2018) have developed transient-gradient models. In the latter, the non-local length fades at a high level of damage to lower this spurious spread. Besides, Aldakheel, Wriggers, and Miehe (2018) have used a phase-field approach near failure to restrain the spread of the micromorphic (i.e. non-local) approach developed in a previous work (Aldakheel, 2017).

Nevertheless, those failure simulations still entail highly distorted elements in highly damaged zones around the real crack surface, affecting numerical convergence. Element erosion and remeshing can be set up as in the work of Mediavilla, Peerlings, and Geers (2006). However, in addition to be potentially computationally inefficient, this procedure leads to mass and energy losses. The first inconsistency may be limited by reporting the deleted element mass on neighbouring nodes/elements. The second one may be decreased by postponing as much as possible the deletion. Nonetheless, at the end of the day, crack initiation and propagation do not necessarily involve a negligible amount of fracture energy and do not definitely occur at the very end of the fracture process. Moreover, a proper crack modelling is mandatory in the context of fracture or fragmentation simulations, or to multi-physics problems (e.g. heat or electrical conduction, fluid leakage).

1.1.3 Damage to crack transition framework

In brief, both the fracture mechanics and the continuous damage mechanics are used to simulate ductile fracture in the literature. However, although they perform well in their respective scope, neither continuous nor discontinuous approaches are able to describe alone the whole ductile process. This reason led to develop damage models with a crack transition in order to take advantage of the complementary of both approaches, as schematised on Fig. 1.5. In such a framework, a CDM simulates the initial homogeneous damage stage (left side). Then, a crack is introduced using a CZM until complete failure (right side). This last one can be inserted with any crack insertion technique, i.e. using either remeshing (Cuvilliez et al., 2012), XFEM (Wang and Waisman, 2018), EFEM or DG (Aduloju and Truster, 2019; Wu, Becker, and Noels, 2014).

This transition between non-local damage models and cohesive zone methods is meaningful since numerous papers (Cazes et al., 2009, 2010; Dufour et al., 2008; Leclerc et al., 2018;

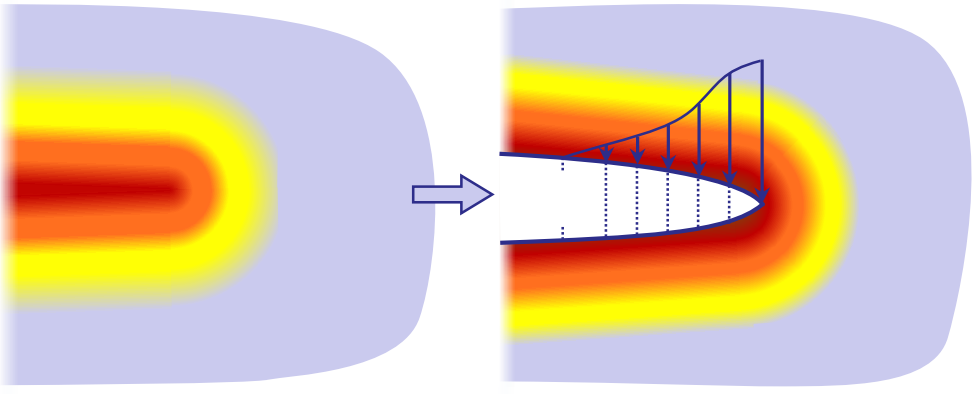

FIGURE 1.5: Schematic representation of a growing failure process using a continuous damage model followed by a cohesive zone model inside a damage to crack transition framework.

Mazars and Pijaudier-Cabot, 1996; Wang and Waisman, 2016; Wu et al., 2016; Wu, Becker, and Noels, 2014, e.g.) have drawn energetic equivalences between both approaches. Indeed, for instance, Cazes et al. (2009, 2010) and Mazars and Pijaudier-Cabot (1996) have demonstrated that either the non-local CDM alone or the CDM-CZM transition framework is consistent as long as the total dissipated energy during the whole fracture process corresponds to the physically-based one. Therefore, at its insertion, the CZM has to dissipate the amount of energy not yet dissipated by the non-local model. This energetic quantity can be determined by comparison for a mode I crack in a one-dimensional setting in terms of a reached value of damage or effective stress (Comi, Mariani, and Perego, 2007; Cuvilliez et al., 2012; Wu, Becker, and Noels, 2014, e.g.). Besides, Cazes et al. (2009) constructed their TSL by conserving the equivalence of dissipated energy increments with the pure non-local model.

However, as pointed out by Wu, Becker, and Noels (2014), the classical CZM does not include the influence of in-plane stress components, and thus does not correctly represent pressure and triaxiality, or Lode variable effects. Usually, the CZM shape is fixed. The dissipated energy is stated in advance. No coupling with in-plane stress components, or Poisson effect, is including. However, Brünig, Gerke, and Schmidt (2018), Faleskog and Barsoum (2013), Nahshon and Hutchinson (2008), and Xue, Faleskog, and Hutchinson (2013) have shown that those latter effects are essential for accurate predictions of ductile failure. According to some authors (Remmers et al., 2013; Tvergaard and Hutchinson, 1992), those aspects can be ignored if the CZM is inserted at a very high level of damage. In which case, the surface contribution would be smaller and negligible compared to the volumic dissipation. However, as previously explained, crack initiation and propagation do not necessarily involve a negligible amount of fracture energy. Those effects have to be logically taken into account in the traction-separation law.

Therefore, to include those necessary effects, a simple method is to define CZM key parameters explicitly dependent on stress triaxiality (Siegmund and Brocks, 2000). But this relation rises the complex question of its proper calibration in terms of the material history. Scheyvaerts, Pardoen, and Onck (2010) have approached this issue by using a micromechanical model or simulations on representative volume elements (RVE) to predict the unloading slope in terms of the stress triaxiality. A more general and natural way is to redefine a 3D stress state at the interface and deduce from it the cohesive behaviour (Bosco, Kouznetsova, and Geers, 2015; Esmaeili, Steinmann, and Javili, 2017; Huespe et al., 2009; Remmers et al., 2013; Tvergaard, 2004, e.g.). This implicitly incorporates a triaxiality-dependent behaviour during the crack propagation stage. These approaches distinguish themselves by the procedure to

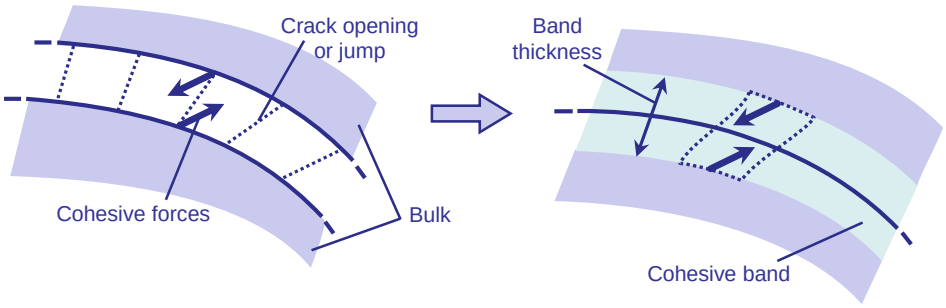

FIGURE 1.6: Schematic representation of the cohesive band model.

obtain the cohesive 3D state. Esmaeili, Javili, and Steinmann (2016a,b) and Esmaeili, Steinmann, and Javili (2017) have computed it through the coupling with an energetic interface. Huespe et al. (2009, 2012) have introduced a damaging band of finite thickness as an embedded weak discontinuity through the elements. A 3D state has been recovered through multi-scale analyses: Bosco, Kouznetsova, and Geers (2015) have extracted the cohesive behaviour from a RVE. Tvergaard (2004) have used the jump discontinuity to compute a 3D-strain state at an intrinsic cohesive interface. Remmers et al. (2013) have enhanced the strain state by adding surrounding in-plane bulk deformation to model the behaviour of a delaminating interface.

1.2 Objectives

The objective of this thesis is to develop an energetically consistent damage to crack transition framework suitable for ductile failure. In particular, the framework should be able to predict the failure under various loading conditions while minimising case-dependent calibration. The method is requested to be consistent, mesh-independent, scalable and computationally efficient, and applicable in a large deformation 3D setting. Besides, the developed methodology should be versatile enough to account for different material behaviours.

The model developed in this thesis is initiated from the last solution suggested by Remmers et al. (2013), the so-called the Cohesive Band Model (CBM). When the crack criterion is reached in the last failure steps, we assume that all the subsequent material degradation occurs in a thin band surrounding the crack surface. As represented on Fig. 1.6, the cohesive model is taken as representative of this thin band behaviour. The strain state inside this band corresponds to the neighbouring bulk strains enriched with the cohesive jump. By redefining the underlying constitutive material model in a local form, a stress tensor, and then the surface tension between the crack lips, are evaluated. The presented method has the advantages of (i) requiring relatively few modifications of the cohesive model compared to the multi-scale or the finite band method; (ii) offering the possibility of reusing the underlying damage material model and the interface Gauss points of the DG-scheme and (iii) following on-the-fly the local stress state and material history. These advantages ensure that the developed method can achieved the stated objectives since it allows modelling the crack formation whilst accounting for the damaging process physics. Nonetheless, an adapted calibration procedure needs to be provided.

In particular, the developed framework includes an implicit non-local damage model (Peerlings et al., 1996; Reusch, Svendsen, and Klingbeil, 2003a,b) and a cohesive band model (Remmers et al., 2013) inside a DG-formulation (Radovitzky et al., 2011). In other words, the initial diffuse damage state is simulated using an implicit non-local damage model without mesh-dependency beyond the onset of softening. This is of particular importance when considering a physically-based crack initiation criterion which can physically be met in the strain

softening stage, as it will be shown by several examples in this thesis. Once this crack insertion criterion is satisfied, an extrinsic cohesive band is inserted between volume elements using the Discontinuous Galerkin framework. The cohesive band model allows the determination on-the-fly of the cohesive behaviour while taking into account the current local 3D stress state and the material history. Apart from the crack insertion criterion, the CBM only introduces one extra parameter: the cohesive band thickness which controls the total dissipated energy. Guidelines to calibrate the band thickness is extracted from the study of its effects.

Moreover, the framework is implemented with damage models of increasing complexity to demonstrate its versatility. In particular, the numerical scheme is initiated in the context of linear elasticity in small strains (Geers, 1997). Afterwards, we develop a suited porous elasto-plastic model in the context of ductile failure. Derived from a Gurson-like approach (Pineau, Benzerga, and Pardoen, 2016), they include void growth and coalescence models. Furthermore, we also compare various crack transition criteria and post-crack insertion behaviours, which can differ from the pre-crack behaviour. On the other hand, the underlying material model can be reused with relatively minor changes. Besides, for both CDM contexts, we also provide the calibration procedure for the constitutive behaviour as well the transition framework.

Furthermore, we show that the numerical scheme meets the expected numerical properties. Although the use of EFEM, XFEM (Vigueras et al., 2015, e.g.) or any other crack insertion techniques is conceivable, the DG-CZM (or DG-CBM) combination has still several advantages in terms of the desired numerical properties against its competitors. Indeed, even if the crack path is limited to element boundaries, the crack insertion is naturally managed by the DG-CBM scheme. Conversely, although enrichment methods (i.e. the XFEM or EFEM) enable propagation along arbitrary paths, a crack direction criterion needs to be provided. This task is not trivial in 3D, in particular with the aim of considering fragmentation. Moreover, their implementation require radical changes in the numerical scheme (particularly in 3D, see Agathos et al. (2018) for instance). Comparatively, the DG-method requires only the implementation of interface elements. Its parallelisation is simply done using a face-based ghost implementation (Wu et al., 2013). Unfortunately, the hybrid DG-CZM (or DG-CBM) method implies an increase of the system size and a fine mesh to accurately describe the crack patterns with interface elements as demonstrated by Molinari et al. (2007). However, this drawback is mitigated by the high scalability of the method. Ultimately, all the crack insertion techniques require anyway a fine mesh to correctly describe the patterns.

1.3 Outline

This thesis is organised as follows. After this introduction, in Chapter 2, the framework will be first established in the context of small displacements in the elastic regime. Energetic equivalence will be discussed with a 1D case in a semi-analytical way. In particular, the cohesive band and the effects of its thickness will be studied. A relation between the non-local length and the cohesive thickness will be drawn such that the energy dissipated by the hybrid CDM/CBM framework corresponds to the energy that would be dissipated by a pure non-local damage simulation. Afterwards, the announced capabilities of the framework will be demonstrated in 2D as well as in 3D. In particular, proof of mesh insensitivity will be brought. Evidences of the inclusion of triaxiality effects will be shown. Moreover, the method will be compared to the phase field approach. Finally, experimental results obtained by Geers (1997) on short glass-fiber reinforced polymers (short-GFRP) will be reproduced. In addition to available experimental results, this material is chosen because of its mechanical properties. Indeed, it deforms elastically with a relatively important ductility thanks to the reinforcement with glass fibers (Geers, 1997).

Chapter 3 will be devoted to the extension of the framework to the ductile case. According to the micromechanical process described earlier, a porous plastic model will be first developed. It will incorporate a coupling between several plasticity models. Namely, a Gurson model (Gurson, 1977) represents the diffuse damage process linked to the void growth phase. Meanwhile, a Thomason model (Thomason, 1985a,b) simulates the coalescence stage. The transition framework will be adapted to this case and different crack insertion criteria and behaviours will be compared. Moreover, using data available in literature, the benefits of such a framework will be demonstrated. In particular, we will show that the non-local model is essential to obtain reliable and meaningful results. Moreover, the value of the framework will be demonstrated by reproducing typical failure modes in different triaxiality states. Indeed, after a short calibration procedure, we will show that the model is rich enough to qualitatively reproduce the slant and the cup-cone fracture modes respectively in plane strain and in axisymmetric states.

Once the capabilities of the framework will have been demonstrated in the first chapters, the developed transition framework will be calibrated to reproduce the behaviour of a high-strength steel alloy in Chapter 4. To achieve this goal, guidelines for the experimental campaign will be first emitted. These experiments have been performed by Marie-Stéphane Colla and Matthieu Marteleur (UCLouvain) in the context of the collaborative project MRIPF. A methodology will be developed to limit sensitivity analysis and trial-and-error procedure as a large number of material parameters is involved. In addition to classical mechanical tests, this procedure will involve cell simulations, as suggested by Van Dung Nguyen (ULiege) in the context of the MRIPF project, and microstructure analyses realised pre- and post-mortem to reduce the fitting parameters. Moreover, an anisotropic nucleation model will be developed and calibrated to reproduce failure anisotropy in accordance to microstructural measurements. Finally, it will be shown that a complex failure mode such as the cup-cone of a round bar or the slant one of a plate can be reproduced both qualitatively in terms of the failure surface shape and quantitatively in terms of the failure strength.

1.4 Contributions

In this thesis we have introduced the following original contributions:

1. The development of a continuum-damage-mechanics to crack transition framework based on a cohesive band model accounting for the triaxiality state during the crack opening;

2. The application of the framework in the case of damage-enhanced elasticity with the determination of the cohesive band thickness from energetic considerations;

3. The extension of the framework to a porous plasticity model, with the determination of the crack insertion from a localisation criterion and the definition of the cohesive band evolution law from a localisation micro-mechanics model;

4. The identification of the porous model parameters, and in particular of an anisotropic porosity nucleation model, from experimental tests.

We published the following papers related to this thesis:

- Julien Leclerc, Ling Wu, Van-Dung Nguyen, Ludovic Noels (2018). *A damage to crack transition model accounting for stress triaxiality formulated in a hybrid nonlocal implicit discontinuous Galerkin-cohesive band model framework.* International Journal for Numerical Methods in Engineering, 113(3), 374–410.
https://doi.org/10.1002/nme.5618

- Julien Leclerc, Van-Dung Nguyen, Thomas Pardoen, Ludovic Noels (2020). *A micro-mechanics-based non-local damage to crack transition framework for porous elastoplastic solids.* International Journal of Plasticity, 127, 102631. https://doi.org/10.1016/j.ijplas.2019.11.010

- Matthieu Marteleur, Julien Leclerc, Marie-Stéphane Colla, Van-Dung Nguyen, Ludovic Noels, Thomas Pardoen (In preparation). *Micro-mechanics-based modelling of high-strength forged steel - Part I. Micromechanics and experimental campaigns.*

- Julien Leclerc, Matthieu Marteleur, Marie-Stéphane Colla, Van-Dung Nguyen, Thomas Pardoen, Ludovic Noels (In preparation). *Micro-mechanics-based modelling of high-strength forged steel - Part II. Porous-plastic damage to crack transition.*

Chapter 2

Transition in small strain elastic regime[1]

In this chapter, emphasis is on the development of the framework methodology in small strain elasticity. The question of energy consistency will be also assessed and numerical properties will be studied, in order to pave the way to more complex behaviours.

Practically, Section 2.1 is dedicated to the constitutive model descriptions. At first, the continuous damage model (CDM) and the cohesive band model (CBM) are separately developed following a thermodynamic approach in the context of small displacements in the elastic regime. Isotropic and isothermal behaviours are also assumed. Then, the framework is particularised to the non-local elastic damage model developed by Geers et al. (1998), Peerlings et al. (1998), and Peerlings et al. (1996). Despite the model simplicity, this choice is motivated by the large number of studies available in the literature. Moreover, this model was calibrated for short glass-fiber reinforced polymers (short-GFRP) (Geers, 1997) which allows us to validate the applications in regard to experimental results. This material has the advantage to deform elastically with a relatively important ductility thanks to the reinforcement with glass fibers.

During this first step, emphasis is to energy consistency under different stress triaxiality states. Section 2.2 will be devoted to energetic consistency. In particular, the failure of a bar under tension is studied in a semi-analytical way in order to derive a relation between the numerical thickness of the CBM and the characteristic length of the non-local damage model. This relation is such that the energy dissipated by the hybrid CDM/CBM framework corresponds to the energy that would be dissipated by a pure non-local damage simulation, *i.e.* without crack insertion. Therefore no new numerical parameter is introduced in the modelisation.

Using these results, Section 2.3 is devoted to the numerical implementation of the hybrid CDM/CBM framework in a parallel setting.

The developed method is finally illustrated through numerical examples in Section 2.4. In particular, it is shown that the effects of the triaxiality state can be captured by the cohesive band model. The mesh insensitivity of the CDM/CBM framework is first studied on a 2D holed plate. Then, by modifying the boundary conditions, different stress triaxiality states are investigated and the improvements brought by the new framework when compared to a pure continuum damage model and to a cohesive zone model, are demonstrated. The methodology is then compared with a phase field approach as both numerical schemes share common characteristics. We refer to the recent comparisons between the two approaches provided by de Borst and Verhoosel (2016) and Steinke, Zreid, and Kaliske (2017). The numerical predictions of the hybrid CDM/CBM on single edge notched specimens are therefore compared to the phase field results available in the literature (Miehe, Welschinger, and Hofacker, 2010). Finally, the model is validated with experimental measurements from the literature (Geers, 1997) on the standard Compact Tension Specimen (CTS) made of short-GFRP.

[1] This chapter is an adapted version of the paper Leclerc et al. (2018)

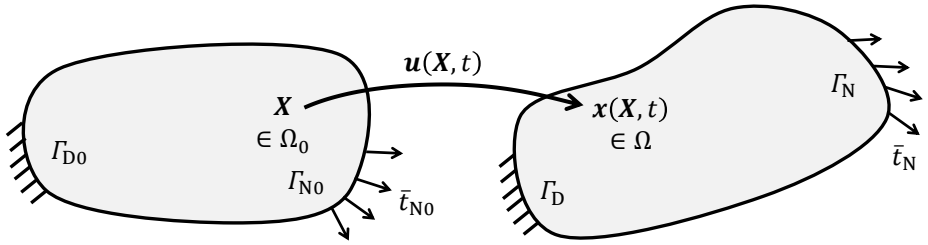

FIGURE 2.1: The body deformation mapping $\boldsymbol{u}(\boldsymbol{X},t)$ defining the transformation of the material body in the reference configuration Ω_0 (left) to the current configuration Ω (right).

2.1 Constitutive models for the damage to crack transition

In this section, the damage to crack transition framework is presented. At first, the non-local continuum damage mechanics model used for the early damage stage is detailed following a thermodynamical approach. Then, the formulation of the cohesive band model is developed. Finally, the relations are particularised for a linear isotropic elastic law involving a non-local damage model.

2.1.1 Non-local continuum damage mechanics

Let $\Omega_0 \subset \mathcal{R}^3$ be a structural body in the reference configuration at the initial time $t = 0$ as shown on Fig. 2.1. Its counterpart in the current configuration at a given time $t > 0$ during the mechanical deformation is $\Omega \subset \mathcal{R}^3$. Its external boundary surface Γ_0 at initial time becomes Γ at the current configuration. It is divided into a Neumann part Γ_{N} where a surface traction is prescribed and a Dirichlet part Γ_{D} where a displacement is prescribed. These two distinct parts satisfy $\Gamma_{\mathrm{N}} \cap \Gamma_{\mathrm{D}} = \emptyset$ and $\Gamma_{\mathrm{N}} \cup \Gamma_{\mathrm{D}} = \Gamma \quad \forall t$.

2.1.1.1 Kinematic relationships

During the time evolution of the body Ω, the motion of a material particle initially at the position $\boldsymbol{X} \in \Omega_0$ and currently at the position $\boldsymbol{x}(\boldsymbol{X},t) \in \Omega$, is defined by the displacement field $\boldsymbol{u}(\boldsymbol{X},t) = \boldsymbol{x}(\boldsymbol{X},t) - \boldsymbol{X}$. The derivative of the current spatial position in terms of the material configuration, or in other words, the deformation gradient, reads

$$\mathbf{F} = \boldsymbol{\nabla}_0 \boldsymbol{x} = \frac{\partial \boldsymbol{x}}{\partial \boldsymbol{X}} = \mathbf{I} + \frac{\partial \boldsymbol{u}}{\partial \boldsymbol{X}}, \tag{2.1}$$

with $\mathbf{I}$ the second-order identity tensor, and $\boldsymbol{\nabla}_0$ the gradient operator with respect to the initial configuration. One can also define the Jacobian $J = \det \mathbf{F} > 0$.

In a small deformation context, one can derive the Cauchy strain tensor $\boldsymbol{\epsilon}$ from the symmetric part of the deformation gradient

$$\boldsymbol{\epsilon} = \frac{1}{2}\left[\mathbf{F} + \mathbf{F}^{\mathrm{T}}\right] - \mathbf{I}. \tag{2.2}$$

2.1.1.2 Governing relationships

The mechanical behaviour of the material body obeys to classical conservation laws presented here. The mass conservation links the initial density ρ_0 and the current one ρ through the Jacobian by

$$\rho_0 = J\rho \qquad \text{in } \Omega. \tag{2.3}$$

In the current configuration, the linear momentum conservation in terms of the Cauchy stress tensor $\boldsymbol{\sigma}$ reads

$$\rho\ddot{\boldsymbol{u}} = \boldsymbol{\nabla}\cdot\boldsymbol{\sigma} + \boldsymbol{b} \qquad \text{on } \Omega, \tag{2.4}$$

where ρ is the density, $\boldsymbol{b}$ are body-forces per unit of volume and $\boldsymbol{\nabla}$ is the gradient operator with respect to the current configuration. Angular momentum is ensured by the symmetry of the Cauchy stress tensor $\boldsymbol{\sigma}$. Boundary conditions are applied on the current external surface. Prescribed displacement $\bar{\boldsymbol{u}}(t)$ and traction surface $\bar{\boldsymbol{t}}_{\mathrm{N}}(t)$ are respectively stipulated on the Dirichlet boundary Γ_{D} and on the Neumann one Γ_{N}:

$$\begin{array}{rcll} \boldsymbol{\sigma}\cdot\boldsymbol{n} & = & \bar{\boldsymbol{t}}_{\mathrm{N}} & \text{in } \Gamma_{\mathrm{N}}, \\ \boldsymbol{u} & = & \bar{\boldsymbol{u}} & \text{on } \Gamma_{\mathrm{D}}, \end{array} \tag{2.5}$$

where $\boldsymbol{n}$ is the outward unit normal to Γ.

2.1.1.3 Energetic relationships

The boundary value problem stated by Eqs. (2.4)-(2.5) is completed by a material constitutive law. This law can be expressed as

$$\boldsymbol{\sigma}(t) = \boldsymbol{\sigma}\left(\mathbf{F}(t); \boldsymbol{Z}(t'), t' \in [0,t]\right), \tag{2.6}$$

where $\boldsymbol{Z}(t')$ is the vector of internal variables representing all the material history.

A thermodynamic potential function (so-called state function) can be associated to each equilibrium state of the system in terms of a strain tensor and of the state variables $\boldsymbol{Z}(t')$. For simplicity, an elastic isothermal case in a small deformation setting with isotropic damage model is considered in this chapter. Accordingly, the law (2.6) can be expressed as

$$\boldsymbol{\sigma}(t) = \boldsymbol{\sigma}\left(\boldsymbol{\epsilon}(t); \boldsymbol{Z}(t'), t' \in [0,t]\right). \tag{2.7}$$

The (irreversible) material degradation is assumed to be described through a scalar damage variable D which varies monotonically from 0 (undamaged material) to 1 (at complete fracture). At this point, the stiffness vanishes and the material is unable to sustain any subsequent load.

If the free (reversible) Helmholtz energy per unit volume inside the damaged material, ψ, is chosen as this thermodynamic potential, one has in terms of a damage variable and of a quadratic form of elastic strains:

$$\psi(\boldsymbol{\epsilon}, D) = \frac{1}{2}\boldsymbol{\epsilon} : \boldsymbol{\mathcal{H}}^{D}(D) : \boldsymbol{\epsilon}, \tag{2.8}$$

where $\boldsymbol{\mathcal{H}}^{D}$ is the positive-definite fourth-order stiffness tensor in terms of the isotropic scalar damage value D. The evolution of this free energy with respect to time reads

$$\dot{\psi}(\boldsymbol{\epsilon}, D) = \frac{\partial\psi}{\partial\boldsymbol{\epsilon}} : \dot{\boldsymbol{\epsilon}} + \frac{\partial\psi}{\partial D}\dot{D} = \boldsymbol{\sigma} : \dot{\boldsymbol{\epsilon}} - Y\dot{D} \quad \text{with} \quad \left\{ \begin{array}{l} \boldsymbol{\sigma} = \frac{\partial\psi}{\partial\boldsymbol{\epsilon}} = \boldsymbol{\mathcal{H}}^{D} : \boldsymbol{\epsilon}; \\ Y = -\frac{\partial\psi}{\partial D} = -\frac{1}{2}\boldsymbol{\epsilon} : \frac{\partial\boldsymbol{\mathcal{H}}^{D}}{\partial D} : \boldsymbol{\epsilon}, \end{array} \right. \tag{2.9}$$

where Y is defined as the damage energy release rate.

The variation of dissipated energy $\dot{\varphi}$ is constrained by the second thermodynamic principle formulated by the Clausius-Duhem inequality

$$\dot{\varphi} = \dot{W}_{\mathrm{int}} - \dot{\psi} = \boldsymbol{\sigma} : \dot{\boldsymbol{\epsilon}} - \dot{\psi} \geq 0, \tag{2.10}$$

in which the first term involves the specific internal work W_{int}. By using the previous Eq. (2.9), one has

$$\dot{\varphi} = Y\dot{D} \geq 0, \tag{2.11}$$

which implies $\dot{D}$, $Y \geq 0$ and $\frac{\partial \boldsymbol{\mathcal{H}}^D}{\partial D}$ to be a semi-negative definite tensor matrix. The total dissipated power inside the structural volume Ω is determined by

$$\dot{\Phi}_{\text{vol}} = \int_\Omega \dot{\varphi}\, dV = \int_\Omega Y\dot{D}\, dV \geq 0. \tag{2.12}$$

The evolution of the damage D is governed by the strain history of the material through a loading function $\phi \leq 0$ that governs the damage growth. In its local form, the loading function depends only on the local strain components and history by a function g through:

$$\dot{D} = \begin{cases} g\left(Y,\, \boldsymbol{Z}\right) & \text{if } \phi\left(D(t),\, \boldsymbol{\epsilon}(t); \boldsymbol{Z}(t'), t' \in [0,t]\right) = 0 \text{ and } \dot{\phi} = 0\,; \\ 0 & \text{if } \phi < 0, \text{ or } \phi = 0 \text{ and } \dot{\phi} < 0. \end{cases} \tag{2.13}$$

However, this local form loses its solution uniqueness when softening appears, resulting in spurious localisation and mesh dependency issues. A well-posed problem can be recovered by using the non-local implicit method (Peerlings et al., 1998). The main idea is to replace one internal variable $Z_i \in \boldsymbol{Z}$ (as damage, accumulated plastic strains...) by its non-local counterpart $\tilde{Z}_i \in \tilde{\boldsymbol{Z}}$, which corresponds to a weighted average on neighbouring material points. In other words, $\tilde{Z}$ can be computed by

$$\tilde{Z}\left(\boldsymbol{X}\right) = \frac{1}{V}\int_V Z\left(\boldsymbol{Y}\right) w\left(\|\boldsymbol{Y} - \boldsymbol{X}\|\right) d\boldsymbol{Y}, \tag{2.14}$$

where V is a characteristic volume around point $\boldsymbol{X}$, and $w\left(\|\boldsymbol{Y} - \boldsymbol{X}\|\right)$ is the normalised weight function that depends on the distance between both points $\boldsymbol{X}$ and $\boldsymbol{Y}$ only. This function w defines the influence of the neighbouring material points and satisfies

$$\frac{1}{V}\int_V w\left(\|\boldsymbol{Y} - \boldsymbol{X}\|\right) d\boldsymbol{Y} = 1. \tag{2.15}$$

As the integral form of Eq. (2.14) would be difficult to evaluate for non-regular geometries, it is therefore replaced by a more convenient diffusion-like partial differential equations. Indeed, as detailed by Peerlings et al. (2001), for specific weight functions, Eq. (2.14) can be transformed into a differential form associated with a natural boundary condition:

$$\tilde{Z} - l_{\text{c}}^2 \nabla^2 \tilde{Z} = Z \qquad \text{in } \Omega\,, \tag{2.16}$$

$$\boldsymbol{\nabla}\tilde{Z} \cdot \boldsymbol{n} = 0 \qquad \text{on } \Gamma. \tag{2.17}$$

The local value acts as a source term and l_{c}, the characteristic length of the material, governs the spreading or the averaging volume V of the non-local value.

Adding this boundary value problem to Eq. (2.4) allows thus restoring the solution uniqueness. Therefore, the damage evolution is rewritten in its non-local form in terms of the averaged variable:

$$\dot{D} = \begin{cases} g\left(Y,\, \tilde{\boldsymbol{Z}},\, \boldsymbol{Z}\right) & \text{if } \phi\left(D(t),\, \boldsymbol{\epsilon}(t); \tilde{\boldsymbol{Z}}(t'),\, \boldsymbol{Z}(t'), t' \in [0,t]\right) = 0 \\ & \quad \text{and } \dot{\phi} = 0; \\ 0 & \text{if } \phi < 0, \text{ or } \phi = 0 \text{ and } \dot{\phi} < 0. \end{cases} \tag{2.18}$$

Equations (2.8) to (2.18) remain valid for any isothermal isotropic elastic behaviour. In this work, we consider a linear isotropic elastic law enhanced with an implicit non-local isotropic

damage evolution to complete the boundary value problem stated by Eqs. (2.4)-(2.5) and (2.16)-(2.17). The constitutive relations are detailed in Section 2.1.3.

2.1.2 Cohesive band model

Let Γ_{I} (and resp. Γ_{I0}) be a discontinuity surface dividing the structural volume Ω (Ω_0) into two parts: Ω^+ and Ω^- (Ω_0^+ and Ω_0^-). The unit normal $\boldsymbol{n}_{\mathrm{I}}$ to Γ_{I} is defined oriented towards Ω^+ as illustrated in Fig. 2.2, the unit tangential vectors $\boldsymbol{s}_{\mathrm{I}}$ and $\boldsymbol{s}'_{\mathrm{I}}$ define with $\boldsymbol{n}_{\mathrm{I}}$ an orthonormal local basis at the interface. The vectors $\boldsymbol{N}_{\mathrm{I}}$, $\boldsymbol{S}_{\mathrm{I}}$ and $\boldsymbol{S}'_{\mathrm{I}}$ are their counterparts in the reference configuration. At a given time t, the discontinuity path Γ_{I} (resp. Γ_{I0}) is divided into an already cracked part Γ_{IC} (Γ_{IC0}) and an uncracked one Γ_{IU} (Γ_{IU0}), satisfying $\Gamma_{\mathrm{IU}} \cap \Gamma_{\mathrm{IC}} = 0$ and $\Gamma_{\mathrm{IU}} \cup \Gamma_{\mathrm{IC}} = \Gamma_{\mathrm{I}}$.

In the following equations, we introduce two operators to link variable values $\bullet^+$ and $\bullet^-$ from both sides of Γ_{I}:

$$\begin{array}{lrcl} \text{the jump operator:} & [\![\bullet]\!] & = & [\bullet^+ - \bullet^-]\,, \quad \text{and} \\ \text{the mean operator:} & \langle\bullet\rangle & = & \dfrac{1}{2}[\bullet^+ + \bullet^-]\,. \end{array} \tag{2.19}$$

Pioneered by Barenblatt (1962) and Dugdale (1960), the cohesive zone model describes the irreversible evolution of attraction forces $\boldsymbol{t}_{\mathrm{I}}$ between both separation planes in terms of the crack opening $[\![\boldsymbol{u}]\!]$. In this case, the dissipated energy during the crack opening process corresponds to the fracture energy per unit crack surface G_{c}:

$$G_{\mathrm{c}} = \int_0^{\delta_{\mathrm{c}}} \boldsymbol{t}_{\mathrm{I}} \cdot d\,[\![\boldsymbol{u}]\!]\,, \tag{2.20}$$

where δ_{c} is a critical opening value at which the complete fracture state is reached (i.e. when the attraction forces vanished). The dissipated power is related to the rate of crack surface creation $\dot{A}$ by

$$\dot{\Phi}_{\mathrm{surf}} = G_{\mathrm{c}}\dot{A}. \tag{2.21}$$

Hence, this model is intrinsically surfacic, by opposition to the bulk law which is volumic and depends on a 3D-state. In this work, the idea exploited is to replace the classical cohesive zone model by a cohesive band one (Remmers et al., 2013), representative of a thin band surrounding the crack surface. In this way, the underlying model is close to the reality of the failure process. Indeed, after a preliminary diffuse damage stage, all the degradation for ductile materials tends to localise in a thin band, before the appearance of macroscopic cracks and the complete loss of mechanical integrity. Moreover, this method reconstructs a pseudo

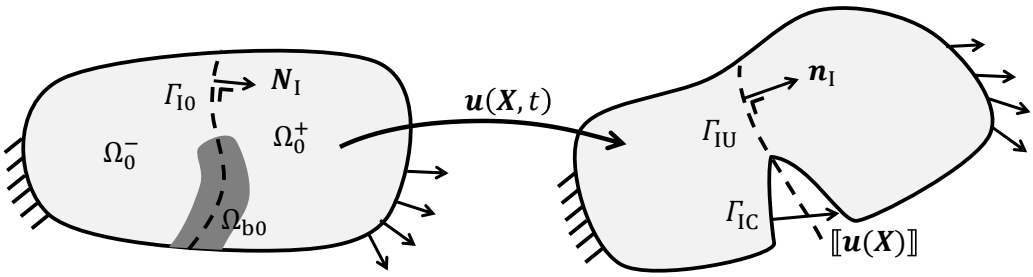

FIGURE 2.2: A discontinuity surface Γ_{I0} in the reference configuration Ω_0 (left) and the current configuration Ω (right).

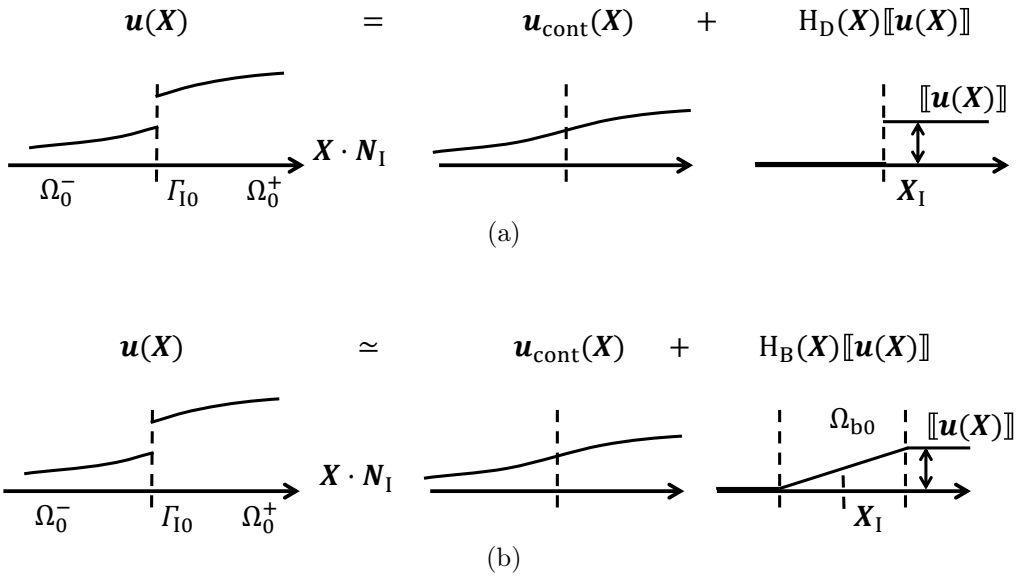

FIGURE 2.3: (a) Discontinuous displacement field decomposition around the crack surface Γ_{IC0} into a smoothed (continuous) part $\boldsymbol{u}_{\mathrm{cont.}}(\boldsymbol{X})$ and a jump or discontinuous one $[\![\boldsymbol{u}(\boldsymbol{X})]\!]$. (b) With the cohesive band approximation, the discontinuous part is smeared through a numerical thin band Ω_{b0}. The displacement values at both crack sides, $\boldsymbol{u}^-$ and $\boldsymbol{u}^+$, are obtained by respectively $\boldsymbol{u}^- = \boldsymbol{u}^-_{\mathrm{cont.}} + \boldsymbol{u}^-_{\mathrm{b}}$ and $\boldsymbol{u}^+ = u^+_{\mathrm{cont.}} + \boldsymbol{u}^+_{\mathrm{b}}$.

3D-state at the interface and harmonises itself with the volumic nature of the bulk law, thus including naturally triaxiality effects.

Similarly to the work of Remmers et al. (2013), the displacement field $\boldsymbol{u}(\boldsymbol{X})$ inside the volume can be conveniently separated as illustrated in Fig. 2.3a into a smoothed (continuous) part $\boldsymbol{u}_{\mathrm{cont.}}(\boldsymbol{X})$ and a jump or discontinuous one $[\![\boldsymbol{u}(\boldsymbol{X})]\!]$ according to:

$$\boldsymbol{u}(\boldsymbol{X}) = \boldsymbol{u}_{\mathrm{cont.}}(\boldsymbol{X}) + \mathtt{H}_{\mathrm{D}}(\boldsymbol{X})\,[\![\boldsymbol{u}(\boldsymbol{X})]\!]\,, \tag{2.22}$$

with the Heaviside's function $\mathtt{H}_{\mathrm{D}}(\boldsymbol{X})$

$$\mathtt{H}_{\mathrm{D}}(\boldsymbol{X}) = \begin{cases} 0 & \text{if } \boldsymbol{X} \in \Omega_0^-; \\ 1 & \text{if } \boldsymbol{X} \in \Omega_0^+. \end{cases} \tag{2.23}$$

By using the cohesive band model, the discontinuity surface is assumed to be smoothed and smeared through a numerical thin band Ω_{b0} of thickness h_{b} (Huespe et al., 2012) as shown in Fig. 2.3b. Without losing any generality, Γ_{IC} is assumed to be locally planar and it corresponds to the mid-plan of the encompassing band Ω_{b0}. The displacement field $\boldsymbol{u}(\mathbf{X})$ is thus rewritten as

$$\boldsymbol{u}(\boldsymbol{X}) = \boldsymbol{u}_{\mathrm{cont.}}(\boldsymbol{X}) + \mathtt{H}_{\mathrm{B}}(\boldsymbol{X})\,[\![\boldsymbol{u}(\boldsymbol{X})]\!]\,, \tag{2.24}$$

with the function $\mathtt{H}_{\mathrm{B}}(\boldsymbol{X})$ corresponding to a piecewise linear-step:

$$\mathtt{H}_{\mathrm{B}}(\boldsymbol{X}) = \begin{cases} 0 & \text{if } \boldsymbol{X} \in \Omega_0^- \setminus \Omega_{\mathrm{b0}}; \\ \dfrac{(\boldsymbol{X} - \boldsymbol{X}_{\mathrm{I}}) \cdot \boldsymbol{N}_{\mathrm{I}}}{h_{\mathrm{b}}} + \dfrac{1}{2} & \text{if } \boldsymbol{X} \in \Omega_{\mathrm{b0}}; \\ 1 & \text{if } \boldsymbol{X} \in \Omega_0^+ \setminus \Omega_{\mathrm{b0}}, \end{cases} \tag{2.25}$$

where $\boldsymbol{X}_{\mathrm{I}}$ is a point on the mid plan of the band, on the crack surface. By smearing the jump

across the thickness, the displacement field remains continuous inside the band and allows us to define a strain tensor.

The band deformation gradient $\mathbf{F}_\mathrm{b}$ is computed by derivating the band displacement field of Eq. (2.24), leading to

$$\mathbf{F}_\mathrm{b} = \mathbf{I} + \frac{\partial \boldsymbol{u}_{\text{cont.}}(\boldsymbol{X})}{\partial \boldsymbol{X}} + \frac{1}{h_\mathrm{b}} [\![\boldsymbol{u}(\boldsymbol{X})]\!] \otimes \boldsymbol{N}_\mathrm{I} + \left(\frac{(\boldsymbol{X} - \boldsymbol{X}_\mathrm{I}) \cdot \boldsymbol{N}_\mathrm{I}}{h_\mathrm{b}} + \frac{1}{2} \right) \frac{\partial [\![\boldsymbol{u}(\boldsymbol{X})]\!]}{\partial \boldsymbol{X}}. \tag{2.26}$$

The band, resulting from strain localisation, is assumed to be very thin regarding to its longitudinal dimensions: the band thickness h_b is finite but negligible compared to others structural dimensions. The determination of h_b will be discussed in Section 2.2.4. The band deformation gradient $\mathbf{F}_\mathrm{b}$ deduced from Eq. (2.26) is thus approximated on both sides $\boldsymbol{X}_\mathrm{I}^\pm$ accordingly with the chosen DG-discretisation (see Section 2.3) by

$$\mathbf{F}_\mathrm{b}^\pm = \mathbf{F}^\pm + \frac{1}{h_\mathrm{b}} [\![\boldsymbol{u}]\!] \otimes \boldsymbol{N}_\mathrm{I} + \frac{1}{2} \frac{\partial [\![\boldsymbol{u}]\!]}{\partial \boldsymbol{X}}, \tag{2.27}$$

where $\mathbf{F}^\pm = \mathbf{F}\left(\boldsymbol{X}_\mathrm{I}^\pm\right)$. In this last equation, the displacement discontinuity $[\![\boldsymbol{u}(\boldsymbol{X})]\!]$ is assumed constant along the thickness, i.e

$$\frac{\partial [\![\boldsymbol{u}(\boldsymbol{X})]\!]}{\partial \boldsymbol{X}} \cdot \boldsymbol{N}_\mathrm{I} = \mathbf{0}, \tag{2.28}$$

since the normal jump is of limited size with respect to the crack length.

For numerical stability reasons, when considering damage-enhanced elasticity[2], the current jump-enhanced bulk components $\mathbf{F}_\mathrm{N}$, defined as

$$\mathbf{F}_\mathrm{N} = \mathbf{F} \cdot \boldsymbol{N}_\mathrm{I} \otimes \boldsymbol{N}_\mathrm{I}, \tag{2.29}$$

are replaced by their counterparts at the crack insertion $\mathbf{F}_\mathrm{Nc}$, which are related to the deformation gradient at the crack insertion $\mathbf{F}_\mathrm{c}$ in the same way as Eq. (2.29). Indeed, using jump-enhanced current components implies a permanent stress equilibrium between the interface and the bulk which is not always the case during dynamic integration. If this balance is not satisfied, the delay in the decrease of the bulk contributions could induce spurious damage growth. In this chapter, $\mathbf{F}_\mathrm{b}^\pm$ is thus approximated by

$$F_{\mathrm{b}iJ}^\pm = F_{iJ}^\pm + F_{\mathrm{Nc}iJ}^\pm - F_{\mathrm{N}iJ}^\pm + \frac{[\![u_i]\!] N_{\mathrm{I}J}}{h_\mathrm{b}} + \frac{1}{2} \frac{\partial [\![u_i]\!]}{\partial X_J}, \tag{2.30}$$

or by using the local basis decomposition,

$$\begin{aligned} F_{\mathrm{b}iJ}^\pm \;=\; & F_{iJ}^\pm \\ & + n_{\mathrm{I}i} n_{\mathrm{I}k} \left[\left(F_{\mathrm{c}kL}^\pm - I_{kL}\right) \frac{\delta_\mathrm{n}}{\delta_\mathrm{n}^{\max}} - \left(F_{kL}^\pm - I_{kL}\right) \right] N_{\mathrm{I}L} N_{\mathrm{I}J} \\ & + s_{\mathrm{I}i} s_{\mathrm{I}k} \left[\left(F_{\mathrm{c}kL}^\pm - I_{kL}\right) \frac{\delta_\mathrm{t}}{\delta_\mathrm{t}^{\max}} - \left(F_{kL}^\pm - I_{kL}\right) \right] N_{\mathrm{I}L} N_{\mathrm{I}J} \\ & + s'_{\mathrm{I}i} s'_{\mathrm{I}k} \left[\left(F_{\mathrm{c}kL}^\pm - I_{kL}\right) \frac{\delta_\mathrm{s}}{\delta_\mathrm{s}^{\max}} - \left(F_{kL}^\pm - I_{kL}\right) \right] N_{\mathrm{I}L} N_{\mathrm{I}J} \\ & + \frac{[\![u_i]\!] N_{\mathrm{I}J}}{h_\mathrm{b}} + \frac{1}{2} \frac{\partial [\![u_i]\!]}{\partial X_J}. \end{aligned} \tag{2.31}$$

In this last equation, δ_n, δ_t, and δ_s correspond to effective opening components along the directions of the local basis $(\boldsymbol{n}_\mathrm{I}, \boldsymbol{s}_\mathrm{I}, \boldsymbol{s}'_\mathrm{I})$, and $\delta_\mathrm{n}^{\max}$, $\delta_\mathrm{t}^{\max}$ and $\delta_\mathrm{s}^{\max}$ are their maximal values

[2] In the context of the porous plasticity presented in the next chapter, we do not need to introduce this correction since plasticity stabilises the process.

reached during crack opening, following

$$\begin{aligned}\delta_{\mathrm{n}}^{\max} &= \max\left(\delta_{\mathrm{n}}(t'), t' \in [0,t]\right);\\ \delta_{\mathrm{t}}^{\max} &= \max\left(\delta_{\mathrm{t}}(t'), t' \in [0,t]\right);\\ \delta_{\mathrm{s}}^{\max} &= \max\left(\delta_{\mathrm{s}}(t'), t' \in [0,t]\right).\end{aligned} \tag{2.32}$$

The introduction of the ratio coefficients $\delta_{\mathrm{n}}/\delta_{\mathrm{n}}^{\max}$, $\delta_{\mathrm{t}}/\delta_{\mathrm{t}}^{\max}$, and $\delta_{\mathrm{s}}/\delta_{\mathrm{s}}^{\max}$ allows recovering a deformation gradient equal to the identity in case of unloading up to crack closing in each direction of the local basis $(\boldsymbol{n}_{\mathrm{I}}, \boldsymbol{s}_{\mathrm{I}}, \boldsymbol{s}'_{\mathrm{I}})$. To avoid an indetermination in case of unloading just after crack insertion, an offset δ_0 is added to the effective openings δ_{n}, δ_{t}, and δ_{s} at crack insertion. Practically, the effective opening in the different directions read

$$\delta_{\mathrm{n}} = [\![\boldsymbol{u}]\!] \cdot \boldsymbol{n}_{\mathrm{I}} + \delta_0,\ \delta_{\mathrm{t}} = [\![\boldsymbol{u}]\!] \cdot \boldsymbol{s}_{\mathrm{I}} + \delta_0,\ \text{ and }\ \delta_{\mathrm{s}} = [\![\boldsymbol{u}]\!] \cdot \boldsymbol{s}'_{\mathrm{I}} + \delta_0. \tag{2.33}$$

The value of δ_0 is fixed around $10^{-3} h_{\mathrm{b}}$, to be small enough in order to avoid spurious jump offset without hurting numerical convergence or stability.

In a similar way as to derive the bulk Cauchy strain tensor $\boldsymbol{\epsilon}$ in Eq. (2.2), its band counterpart $\boldsymbol{\epsilon}_{\mathrm{b}}$ is derived from the band deformation gradient $\mathbf{F}_{\mathrm{b}}$ following

$$\boldsymbol{\epsilon}_{\mathrm{b}} = \frac{1}{2}\left[\mathbf{F}_{\mathrm{b}} + \mathbf{F}_{\mathrm{b}}{}^{\mathrm{T}}\right] - \mathbf{I}. \tag{2.34}$$

Afterwards, the stress state $\boldsymbol{\sigma}_{\mathrm{b}}$ inside the band is computed from the constitutive bulk law in its local version since the material in the band has a uniform internal variable state across its thickness. So, by similarity to Eq. (2.7), one has:

$$\boldsymbol{\sigma}_{\mathrm{b}}(t) = \boldsymbol{\sigma}_{\mathrm{b}}\left(\boldsymbol{\epsilon}_{\mathrm{b}}(t); \boldsymbol{Z}(t'), t' \in [0,t]\right), \tag{2.35}$$

where the damage evolution is described by a local damage model similar to Eq. (2.13):

$$\dot{D} = \begin{cases} g\left(Y,\, \boldsymbol{Z}\right) & \text{if } \phi\left(D(t),\, \boldsymbol{\epsilon}_{\mathrm{b}}(t); \boldsymbol{Z}(t'), t' \in [0,t]\right) = 0 \text{ and } \dot{\phi} = 0\,; \\ 0 & \text{if } \phi < 0, \text{ or } \phi = 0 \text{ and } \dot{\phi} < 0. \end{cases} \tag{2.36}$$

At the crack initiation occurring at time t_{c}, for a deformation gradient $\mathbf{F}_{\mathrm{c}}$ and a Cauchy strain tensor $\boldsymbol{\epsilon}_{\mathrm{c}}$, the damage and internal variables are initialised from the material state at cracking onset in order to avoid stress discontinuity and to conserve history continuity. The cohesive traction force is now recovered by:

$$\boldsymbol{t}_{\mathrm{I}} = \boldsymbol{\sigma}_{\mathrm{b}} \cdot \boldsymbol{n}_{\mathrm{I}}. \tag{2.37}$$

By this way, the values of the cohesive forces are dependent on the in-plane stretch components and using the behaviour of that band as a cohesive law allows the triaxiality effects to be introduced during the last stage of failure within a formalism similar to a cohesive zone model.

2.1.3 Implicit non-local damage model for isotropic elasticity

All previous relations are applicable to elastic isothermal material laws with isotropic damage models in a small deformation setting and can be particularised for a specific material behaviour. We assume here linear isotropic elasticity modified to take into account the isotropic damaging process. By considering an isotropic damage model and a constant elastic tensor for linear elasticity, the free energy introduced in Eq. (2.8) becomes

$$\psi\left(\boldsymbol{\epsilon}, D\right) = \frac{1}{2}\left(1 - D\right) \boldsymbol{\epsilon} : \boldsymbol{\mathcal{H}} : \boldsymbol{\epsilon}, \tag{2.38}$$

where $\boldsymbol{\mathcal{H}}^D$ is replaced by $(1-D)\,\boldsymbol{\mathcal{H}}$, introducing $\boldsymbol{\mathcal{H}}$ as the Hooke's tensor of the virgin material. The partial derivatives of the free energy yield the equations for the Cauchy stress tensor and the energy release rate

$$\begin{array}{rcrl} \boldsymbol{\sigma} & = & \frac{\partial \psi}{\partial \boldsymbol{\epsilon}} & = (1-D)\,\boldsymbol{\mathcal{H}} : \boldsymbol{\epsilon} = (1-D)\,\hat{\boldsymbol{\sigma}}; \\ Y & = & -\frac{\partial \psi}{\partial D} & = \dfrac{1}{2}\boldsymbol{\epsilon} : \boldsymbol{\mathcal{H}} : \boldsymbol{\epsilon}, \end{array} \tag{2.39}$$

by using the concept of effective Cauchy stress tensor $\hat{\boldsymbol{\sigma}}$ introduced by Lemaitre et al. (2009). These definitions are compatible with constraints resulting from Eq. (2.11) as long as D is semi-monotonically increasing, considering the positive definite nature of the Hooke's tensor.

The evolution of the damage D, described by Eq. (2.18), is governed by the strain history of the material through an historical parameter κ. It corresponds to the maximum equivalent strain reached during the material history. The loading function in Eq. (2.18) reduces to

$$\phi(\tilde{e}, D, \kappa_\mathrm{i}) = \tilde{e} - \kappa(\kappa_\mathrm{i}, D) \leq 0. \tag{2.40}$$

In this formula, $\tilde{e}$ is a non-local equivalent strain and κ_i is the initial threshold, limiting the domain of linear elasticity. The local equivalent strain e is defined as the norm of the positive principal strain components ϵ_i^+

$$e = \sqrt{\sum_{i=1,2,3} \left(\epsilon_i^+\right)^2}. \tag{2.41}$$

This way, only the tensile contributions are included while keeping the effects of multi-axial tension. The non-local equivalent strain field is then obtained by solving the diffusion equation (2.16), which is rewritten as

$$\tilde{e} - l_\mathrm{c}^2 \nabla^2 \tilde{e} = e\,, \tag{2.42}$$

where l_c plays the role of the characteristic length of damage diffusion extension. Its link with h_b will be discussed in Section 2.2.4. The diffusion equation is completed with the natural boundary condition (2.17) which is rewritten as

$$\boldsymbol{\nabla}\tilde{e} \cdot \boldsymbol{n} = 0\,. \tag{2.43}$$

In this work, the damage law is a power-law, defined by two exponents: α and β. The damage evolution is triggered at κ_i and failure occurs when the strain reaches the critical value κ_c:

$$\dot{D}\left(\kappa\right) = \begin{cases} 0 & \text{if } \kappa < \kappa_\mathrm{i}; \\ (1-D)\left(\dfrac{\beta}{\kappa} + \dfrac{\alpha}{(\kappa_\mathrm{c} - \kappa)}\right)\dot{\kappa} & \text{if } \kappa_\mathrm{i} < \kappa < \kappa_\mathrm{c}; \\ 0 & \text{if } \kappa_\mathrm{c} < \kappa. \end{cases} \tag{2.44}$$

By integration, an explicit function of D in terms of κ is available:

$$D\left(\kappa\right) = \begin{cases} 0 & \text{if } \kappa < \kappa_\mathrm{i}\,; \\ 1 - \left(\dfrac{\kappa_\mathrm{i}}{\kappa}\right)^\beta \left(\dfrac{\kappa_\mathrm{c} - \kappa}{\kappa_\mathrm{c} - \kappa_\mathrm{i}}\right)^\alpha & \text{if } \kappa_\mathrm{i} < \kappa < \kappa_\mathrm{c}\,; \\ 1 & \text{if } \kappa_\mathrm{c} < \kappa. \end{cases} \tag{2.45}$$

After crack insertion, the damage evolution inside the band, described by the local form (2.36), is now depending on the local equivalent band strain. The damage growth criterion (2.40) thus becomes

$$\phi\left(e_\mathrm{b}, D, \kappa_\mathrm{i}\right) = e_\mathrm{b} - \kappa(\kappa_\mathrm{i}, D) \leq 0, \tag{2.46}$$

where e_b follows the variation of the local equivalent band strain $\dot{e}_\mathrm{b} = \dot{e}$, and is initiated at the

crack insertion $e_{\mathrm{b}}(t_{\mathrm{c}}) = \tilde{e}(t_{\mathrm{c}})$. Further details on the $\boldsymbol{\sigma}_{\mathrm{b}}$ computation are given in Appendix A.2.

2.2 Energetic equivalence during transition

In the damage to crack transition framework presented in the previous section, a new quantity was introduced: the cohesive band thickness. In this case, this variable is not an additional material parameter but this new numerical parameter can be determined from the underlying non-local model to ensure the energetic consistency. To this end, we study in this section a one-dimensional case in order to demonstrate the properties of the cohesive band model. In particular, the relation between the non-local length and the cohesive band thickness is derived to ensure energy consistency during the transition. The results can then be applied to general 3D simulations. Indeed, as the variations in the crack plane are negligible compared to those normal to the crack plane, the problem can be locally reduced to a one-dimensional problem at the crack front as suggested by Cazes et al. (2009).

2.2.1 Energy consideration

Several works have studied the equivalences between diffuse damage models and cohesive zone ones. For instance, Cazes et al. (2009) have shown that a cohesive zone can substitute for a non-local damage model as long as the total dissipated energy is conserved.

Indeed, in a hybrid or coupled scheme, energy can be dissipated, on the one hand through damage or others internal variables evolution inside the volume elements ($d\Phi_{\mathrm{vol}}$) following Eq. (2.12) or, on the other hand, through the crack opening of a cohesive zone ($d\Phi_{\mathrm{surf}}$) following Eq. (2.21). At the end of the process, the total dissipated energy $\Phi_{\mathrm{tot,h}}$ in a hybrid scheme is the sum of both contributions:

$$\Phi_{\mathrm{tot,h}} = \Phi_{\mathrm{vol}} + \Phi_{\mathrm{surf}}. \tag{2.47}$$

By comparison with a pure non-local model where all energy dissipation $\Phi_{\mathrm{tot,nl}}$ results from the volume elements (i.e. $d\Phi_{\mathrm{vol}} \neq 0$, $d\Phi_{\mathrm{surf}} = 0$), both frameworks (hybrid and pure non-local) are equivalent in an energetic point of view if the dissipated energy in both cases is conserved and corresponds to the physical fracture energy $\Phi_{\mathrm{tot,phys}}$. One has thus:

$$\Phi_{\mathrm{tot,phys}} = \Phi_{\mathrm{tot,nl}} = \Phi_{\mathrm{tot,h}} = \Phi_{\mathrm{vol}} + \Phi_{\mathrm{surf}}. \tag{2.48}$$

This last equation can be rewritten as

$$\Phi_{\mathrm{surf}} = \Phi_{\mathrm{tot,nl}} - \Phi_{\mathrm{vol}}, \tag{2.49}$$

which gives an equation for Φ_{surf} and expresses the fact that the cohesive zone has to dissipate the remaining energy not yet dissipated by the non-local model to ensure an energetic equivalence between both frameworks.

2.2.2 One dimensional problem setting

Let us assume that the body Ω reduces to a uniform bar of length L and constant section A as represented on Fig. 2.4. Displacements are prescribed at the extremities ($u(0,t) = \bar{u}_0(t) = 0$ and $u(L,t) = \bar{u}_{\mathrm{L}}(t)$ with $\bar{u}_{\mathrm{L}}(0) = 0$). During the traction test assumed to occur under quasi-static conditions and without body forces, a strain localisation and finally a crack appear at $x_{\mathrm{I}} = L/2$, where x is the axial coordinate varying in $[0, L]$.

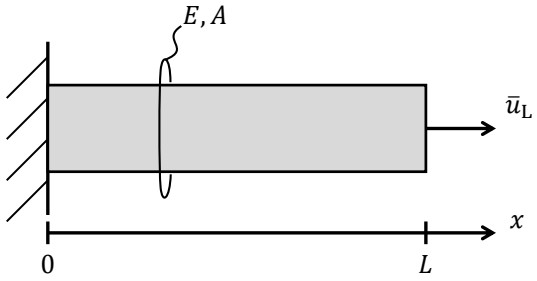

FIGURE 2.4: Geometry of the uniform 1D bar.

2.2.2.1 Non-local problem

Due to the geometry, the Cauchy stress tensor reduces to $\sigma_{xx} = \sigma$ with all the others components vanishing. The equilibrium equations (2.4) enforce a constant stress value σ along the bar and the Hooke's law becomes

$$\sigma = \left[1 - D\left(\tilde{e}(x)\right)\right] E\epsilon(x), \tag{2.50}$$

where E is the Young's modulus, and Eq. (2.2) is rewritten as

$$\epsilon(x) = \frac{\partial u(x)}{\partial x}. \tag{2.51}$$

This strain is linked to the boundary conditions by a compatibility equation:

$$\int_0^L \epsilon(x)dx = u|_{x=L} = \bar{u}_L(t). \tag{2.52}$$

The non-local problem presented by Eqs. (2.42) and (2.43) reduces to

$$\tilde{e}(x) - l_c^2 \frac{\partial^2 \tilde{e}(x)}{\partial x^2} = e(x) \quad \text{with} \quad \left.\frac{\partial \tilde{e}(x)}{\partial x}\right|_{x=0,L} = 0. \tag{2.53}$$

For a uni-axial traction, the equivalent strain $e(x)$ corresponds to $\boldsymbol{\epsilon}(x)$. This differential problem is equivalent to Eq. (2.14) with the Green functions $W_G(x, y)$ used as weigth functions, leading to

$$\tilde{e}(x) = \int_0^L W_G(y, x)e(y)dy. \tag{2.54}$$

For the one-dimensional bar problem, the corresponding Green functions (Peerlings et al., 2001) read

$$W_G(x, y) = \frac{1}{2l_c} \exp\left[-\frac{|x - y|}{l_c}\right] + W_{G-BC}(x, y), \tag{2.55}$$

with $W_{G-BC}(x, y)$ depending on the boundary conditions

$$W_{G-BC}(x, y) = \frac{C_1(y)}{2l_c} \exp\left[\frac{x}{l_c}\right] + \frac{C_2(y)}{2l_c} \exp\left[\frac{L - x}{l_c}\right], \tag{2.56}$$

where

$$C_1(y) = \frac{2\cosh\left[\frac{y}{l_c}\right]}{\exp\left[\frac{2L}{l_c}\right] - 1} \quad \text{and} \quad C_2(y) = \frac{2\cosh\left[\frac{L-y}{l_c}\right]}{\exp\left[\frac{2L}{l_c}\right] - 1}. \tag{2.57}$$

Finally, the damage evolution is computed from Eq. (2.45) with the damage growth criterion (2.40) and with $\kappa(t) = \max(e(t'), t' \in [0,t])$.

Using Eqs. (2.38), (2.50) and considering a uniform value of σ along the bar, the increment of the internal work $d\mathscr{W}_{\text{int}}$ and the free energy Ψ_{vol} stored in the system are written as

$$\begin{aligned} d\mathscr{W}_{\text{int}} &= A\int_0^L dW_{\text{int}}dx = A\int_0^L (\sigma d\epsilon)\,dx = \sigma A d\bar{u}_{\text{L}}, \\ \Psi_{\text{vol}} &= A\int_0^L \psi dx = A\int_0^L \frac{1}{2}\sigma\epsilon(x)dx = \frac{A}{2}\sigma\bar{u}_{\text{L}}, \end{aligned} \tag{2.58}$$

and the dissipated energy inside the bar can be obtained as follows

$$d\Phi_{\text{vol}} = dW_{\text{int}} - d\Psi_{\text{vol}} = A\sigma d\bar{u}_{\text{L}} - \frac{A}{2}d(\sigma\bar{u}_{\text{L}}) = \frac{A}{2}(\sigma d\bar{u}_{\text{L}} - \bar{u}_{\text{L}}d\sigma). \tag{2.59}$$

2.2.2.2 Cohesive band model

When a crack is inserted, a discontinuity $[\![u]\!]$ in the displacement field is introduced at the centre of the localisation zone. The damaging process concentrates inside the cohesive zone while the remaining part of the bar is elastically unloaded. Thus the compatibility condition becomes:

$$\bar{u}_{\text{L}} = \int_0^L \epsilon(x)dx + [\![u]\!]. \tag{2.60}$$

During this process, the damage is only increasing at the crack surface in a local way as expressed by Eq. (2.13) and depends on the band strain. The band strain is obtained by applying Eq. (2.31) in the case of a monotonically increasing jump:

$$\epsilon_{\text{b}} = \epsilon_{\text{c}}(\frac{L}{2}) + \frac{[\![u]\!]}{h_{\text{b}}}, \tag{2.61}$$

where ϵ_{c} is the strain value at crack initiation. The bulk material is then elastically unloaded whilst the damage distribution in the volume remains constant and equal to the damage distribution $D_{\text{c}}(x)$ reached at the insertion of the cohesive band. The equilibrium equation thus reads

$$\sigma = (1 - D_{\text{c}}(x))\,E\epsilon(x) = \sigma_{\text{b}} = (1 - D_{\text{b}}(\epsilon_{\text{b}}))\,E\epsilon_{\text{b}}. \tag{2.62}$$

Following the work of Wu, Becker, and Noels (2014), the free energy associated with the crack surface in a one-dimensional setting is assumed to be stated under the form $\Psi_{\text{surf}} = \Psi_{\text{surf}}([\![u]\!]; \boldsymbol{Z})$, or in other words, to be dependent on the jump and some internal variables $\boldsymbol{Z}$. If the material unloading is linear elastic, the closing of the cohesive band follows the same non-dissipative behaviour. The free energy reduces thus to

$$\Psi_{\text{surf}} = \frac{A}{2}\sigma[\![u]\!], \tag{2.63}$$

and, using the work done by the cohesive force $d\mathscr{W}_{\text{surf}} = A\sigma d[\![u]\!]$, the energy dissipation is equal to

$$d\Phi_{\text{surf}} = d\mathscr{W}_{\text{surf}} - d\Psi_{\text{surf}} = A\sigma d[\![u]\!] - \frac{A}{2}d([\![u]\!]\sigma) = \frac{A}{2}(\sigma d[\![u]\!] - [\![u]\!]d\sigma). \tag{2.64}$$

2.2.3 Semi-analytical resolution of the localisation problem

The equations for both cases (non-local and hybrid frameworks) have been simplified in the previous paragraphs to a one-dimensional case. Such a system of equations has been solved by

Wu, Becker, and Noels (2014) using a cohesive zone model (instead of a cohesive band model) by assuming that the transition occurs at a damage value close to one. In this work, a more general solving strategy is developed in order to extract the cohesive band behaviour and to deduce an appropriate band thickness value.

2.2.3.1 Non-local problem

The problem considers as unknowns the strain field, which is discretized and represented by its n discrete values. From the discrete strain field ϵ^i, $i = 1, ..., n$, the non-local strain is computed by using the convolution of Eq. (2.54) and therefore the damage field and the stress field σ^i are obtained from Eq. (2.45) and Eq. (2.50), respectively. As unstable branches can appear, the equations are formulated to involve an arc-length method (de Borst et al., 2012; Riks, 1979) to be able to capture snap-back behaviours. Concretely, an additional unknown, a loading parameter λ, is added, bringing the total number of unknowns to $n+1$. The system of $n+1$ equations can be rewritten under a residual form $\boldsymbol{r}\left(\epsilon^i, \lambda\right)$ as

$$\boldsymbol{r}\left(\epsilon^i, \lambda\right) = \begin{cases} \sigma^{i+1} - \sigma^i & \text{for } i = 1, ..., n-1, \\ \displaystyle\int_0^L \epsilon(x)dx - \lambda\bar{v}, & \\ \sum_j \left(\Delta\epsilon^j\right)^2 + \vartheta^2\Delta\lambda^2\bar{v}^2 - \Delta l^2, & \end{cases} \tag{2.65}$$

where the first $n-1$ equations correspond to the static equilibrium, the next one to the compatibly equation, and the last one is introduced by the arc-length method to control the loading variation. In this last equation, ϑ is a numerical scaling parameter, $\bar{v}$ is a characteristic displacement $\bar{v} = \bar{u}_{\mathrm{L}}/\lambda$ which is associated with the loading parameter λ, and Δl is the arc-length. In the last equation, $\Delta\epsilon^j$ and $\Delta\lambda$ correspond to the increments respectively of the j^{th} discrete strain value and of the loading parameter between two consecutive steps. The integral in Eq. (2.65) is computed using the trapezoidal rule.

A predictor-corrector scheme with an iterative Newton-Raphson procedure is applied to solve the system, with the tangent matrix $\mathbf{K}_{\mathrm{al}}$ of the problem reading

$$\mathbf{K}_{\mathrm{al}} = \begin{bmatrix} \dfrac{\partial\sigma^{i+1}}{\partial\epsilon^j} - \dfrac{\partial\sigma^i}{\partial\epsilon^j} & 0 \\ \dfrac{\partial}{\partial\epsilon^j}\displaystyle\int_0^L \epsilon(x)dx & -\bar{v} \\ 2\Delta\epsilon^j & 2\vartheta^2\Delta\lambda\bar{v}^2 \end{bmatrix}, \tag{2.66}$$

wherein the partial derivatives are computed by perturbation. As two possible solutions, namely elastic unloading or damage increase, always exist, the last one is promoted by the predictor that gives the guess state of the first iteration. Once the system has converged, the arc-length value Δl is adapted in terms of the number of iterations needed to converge.

2.2.3.2 Crack insertion

After crack insertion, the system is modified to take into account the discontinuity and the linear elastic unloading of the structure. As the bulk behaviour is now linear (linear elastic unloading), the problem reduces to only two unknowns: the total bulk displacement $\int_0^L \epsilon(x)dx$ and the crack opening $[\![u]\!]$. After transition, the jump, initially zero, is increased at each step and the corresponding cohesive band strain, damage, and stress are computed using Eqs. (2.61), (2.45) and (2.62), respectively. Knowing the axial stress, the bulk state can be deduced from its stiffness as it behaves linearly with respect to the stress.

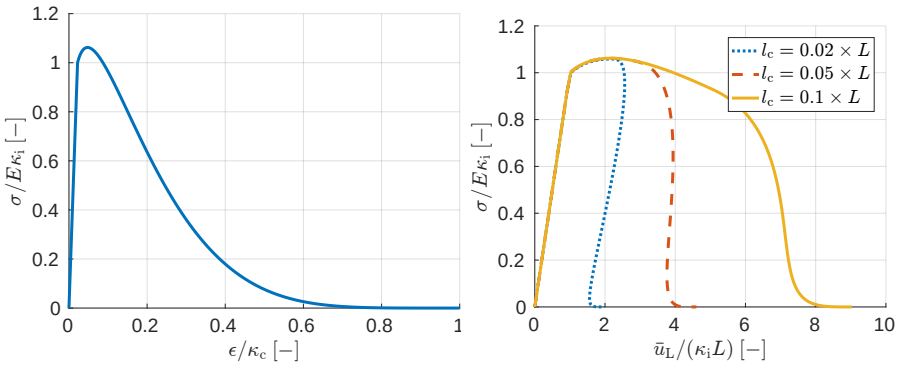

FIGURE 2.5: Stress response (a) for a uniform strain state, and (b) with localisation for different values of l_c.

2.2.4 Band thickness computation and relation with the damage process zone

As both cases (non-local and hybrid framework) can now be solved, we are able to compare both model dissipations, to characterise the behaviour of the cohesive band model, and to compute the energetically-consistent value of the band thickness. As a numerical example, the material properties are assimilated to short glass-fiber-reinforced polypropylene (short-GFRP) (Geers, 1997). In this case, the Young's modulus E has a value of 3.2 [GPa]. The damage law (2.44) parameters are $\kappa_i = 0.011$, $\kappa_c = 0.5$, $\alpha = 5.0$, and $\beta = 0.75$. Figure 2.5a shows the stress response in the absence of strain localisation effect, or in other words, with a uniform strain value. By derivating Eq. (2.50), the damage value D_{soft} at which strain softening regime begins is given by

$$D_{soft} = D\left(\kappa_{soft}\right) = 0.51 \quad \text{with} \quad \kappa_{soft} = \max\left(\frac{\left(1-\beta\right)\kappa_c}{1-\beta+\alpha}\,;\,\kappa_i\right). \tag{2.67}$$

In order to trigger the localisation, a defect at the middle of the bar has been introduced in a similar way as by Dufour et al. (2008) by weakening by 1% the Young's modulus E on 1% of the bar length (at the bar centre). Figure 2.5b shows that the results are dependent on the ratio l_c/L: a lower value of this ratio induces a more brittle behaviour. The fracture process can be divided into two parts. Before localisation, a homogeneous damage evolution takes place inside the bar, according to the curve on Fig. 2.5a. Then, during the softening, a localisation zone develops around the defect, in which the damage grows, while other parts of the bar are elastically unloaded.

In the following analyses, the bar is taken of unitary length, $L = 1$ [m], and the non-local length is taken equal to $0.05L$.

2.2.4.1 Influence of the band thickness h_b

Now, we introduce a discontinuity once a critical damage value D_c is reached. To have meaningful results, this value has to be high enough above D_{soft} in order to be in the strain softening regime. Here, D_c is taken equal to 0.8. At this point, 40% of the total fracture energy in the reference non-local case, $\Phi_{tot,nl}$, has already been dissipated (this value corresponds to Φ_{vol} in Eq. (2.47)) and a cohesive band is introduced. Figure 2.6a illustrates the effect of the band thickness on the stress response. By analogy to a classical cohesive zone, equivalent

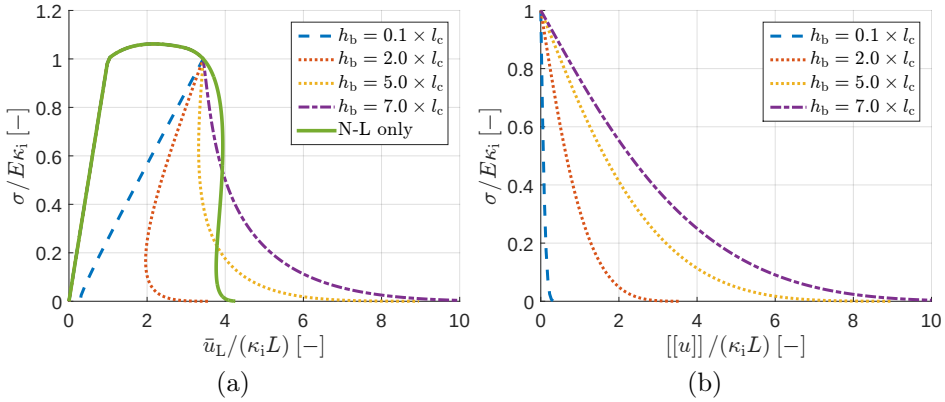

FIGURE 2.6: (a) Stress response for the hybrid framework with a cohesive band introduced at $D_c = 0.8$ and different values of h_b. (b) The corresponding traction-separation laws.

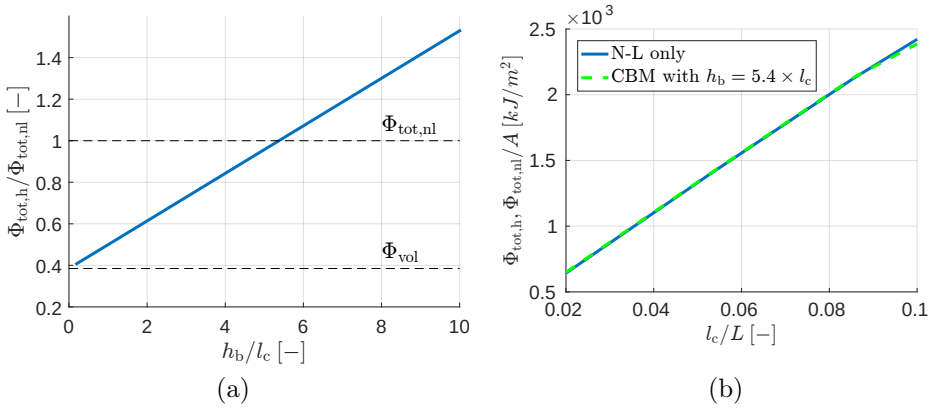

FIGURE 2.7: Ratio of the dissipated energy by the transition scheme $\Phi_{tot,h}$ compared to the reference value $\Phi_{tot,nl}$ (i.e. the pure non-local case) (a) in terms of the band thickness for $D_c = 0.8$ and $l_c = 0.05L$ and (b) in terms of the non-local length.

traction-separation laws can be extracted for comparison as shown in Fig. 2.6b. One can see that a decreasing value of h_b leads to a more brittle behaviour of the bar. When h_b tends to 0, the cohesive band is almost perfectly brittle. The corresponding dissipated energy $\Phi_{tot,h}$ is plotted in Fig. 2.7a and shows a linear dependency to h_b. In particular, the contribution of the cohesive band to the dissipation vanishes for a vanishing band thickness. For this given critical damage value ($D_c = 0.8$), the conservation of the total dissipated energy ($\Phi_{tot,h}(h_b) = \Phi_{tot,nl}$) is obtained for $h_b = 5.4 l_c$.

2.2.4.2 Influence of the non-local length on the band thickness

As the non-local length is directly related to the spreading of damage, the dissipated energy increases linearly with l_c as long as there is no boundary effects, or in other words, as long as the damage process zone is much smaller than the bar length. The dissipated energy shown in Fig. 2.7b is conserved if the ratio h_b/l_c is kept constant for small values of l_c/L.

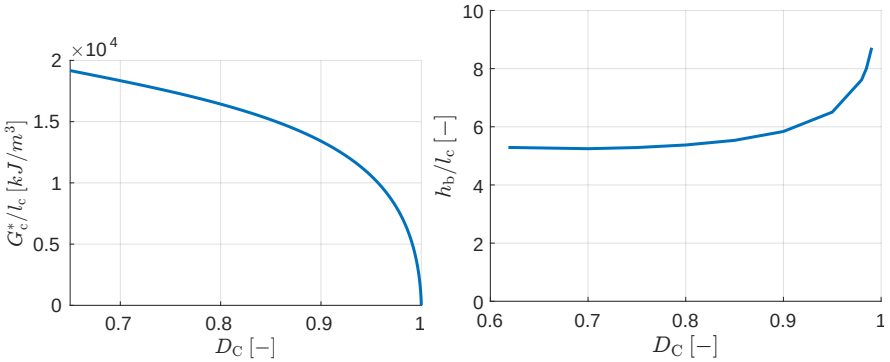

(a) (b)

FIGURE 2.8: (a) The fracture energy which remains to be dissipated by the cohesive model G_c^* in terms of damage value of crack insertion. (b) The corresponding band thickness in terms of damage value of crack insertion.

2.2.4.3 Influence of the critical damage on the band thickness

The fracture energy which remains to be dissipated by a cohesive model G_c^*, divided by the non-local characteristic length l_c to remove its influence, is represented in Fig. 2.8a in terms of the damage at crack insertion. The influence of the damage value at crack insertion on h_b is shown in Fig. 2.8b. The lowest meaningful value of D_c here is governed by the localisation onset, occurring practically at the uniform damage value observed far from the crack tip (here at $D = 0.62$), which is slightly higher than the theoretical (and minimal) value $D_{soft} = 0.51$. This offset is due to the localisation latency and can be reduced if the ratio l_c/L is lowered. For moderate values of critical damage transition point, h_b is constant. Then, as D_c tends to one, the corresponding value of h_b starts growing rapidly. This unphysical behaviour can be explained by the involved non-local model: high strains values at the centre produces spurious damage diffusion and energy dissipation. This issue can be addressed by using a variable characteristic length as by Geers et al. (1998).

2.2.4.4 Influence of the damage model on the band thickness

In Figs. 2.9a and 2.9b, the dissipated energy is represented in terms of respectively the damage exponent α and of the initial damage threshold κ_i for the pure non-local model and for the CBM with $D_c = 0.8$. For the damage exponent α, the error in the energy due to the insertion of the CBM is within 2% for $\alpha \in [3.5; 8]$. This range of α ensures that localisation has occured at the crack insertion. For lower values of α crack insertion occurs before localisation regime, leading to a higher error on the dissipated energy. For the second parameter, the relative error on the dissipated energy is under 3% for $\kappa_i \in [0.005; 0.018]$. As D_{soft} increases with smaller κ_i, a higher error is expected for such values (9.6% for $\kappa_i = 0.001$ for which the corresponding D_{soft} is equal to 0.927). Therefore, as long as the CBM is inserted during the localisation regime, the band thickness is independent of the damage model parameters as those effects are already included in the computation of the cohesive response by reusing the same constitutive relations.

2.2.4.5 Determination of the cohesive band thickness summary

In this subsection we have studied the effect of the cohesive band thickness of the hybrid CDM/CBM framework on the failure of a one-dimensional bar under tension. It has been

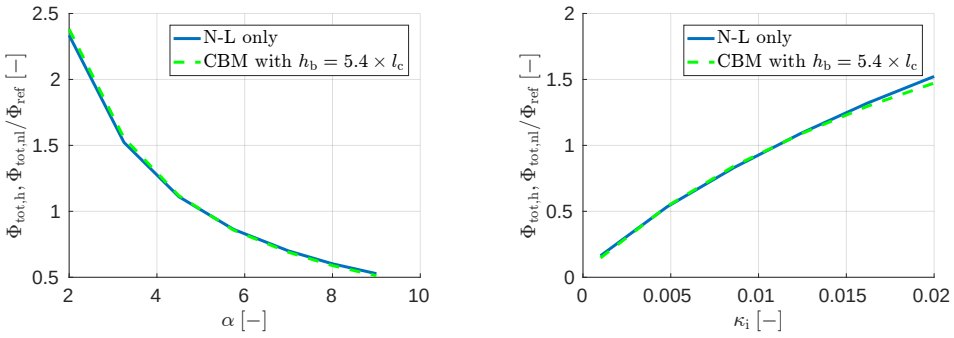

(a) (b)

FIGURE 2.9: The dissipated energy for non-local model (a) in terms of the damage exponent α and (b) in terms of the initial damage threshold κ_i.

shown in Fig. 2.6 that increasing the numerical band thickness h_b results in increasing the ductility of the material since the energy dissipated by the model increases, see Fig. 2.7a. However in order to avoid, on the one hand, the introduction of a new parameter, and, on the other hand, a method that would be sensitive to the point at which the damage to crack transition occurs, we have ensured energy consistency of the hybrid CDM/CBM with a pure non-local model, *i.e.* without crack insertion. Indeed, it has been shown that for the damage law (2.44), by selecting $h_b = 5.4l_c$, the hybrid CDM/CBM framework dissipates the same amount of energy than the pure non-local model for different values of the non-local length l_c, for different points of the crack insertion, and for different possible parameters of the damage law. The numerical band thickness h_b is thus directly related to the non-local length l_c and is no longer a model parameter. However, the non-local length l_c remains a model parameter that affects the softening response. Moreover, if another damage model is used, the numerical band thickness h_b should be evaluated again in order to ensure energy consistency.

2.3 Discontinuous Garlerkin framework and finite element discretisation

In this section, the implementation of the hybrid energetically-consistent CDM/CBM scheme inside a Discontinuous Galerkin (DG) framework is detailed. In particular, the weak form is developed from the strong form, leading to interface terms related to the DG formalism. Then, based on a finite element discretisation, a differential set of equations is obtained and integrated either following (i) a quasi-static implicit scheme, (ii) the $\alpha-$*generalised* method or (iii) a coupled implicit-explicit scheme. The numerical properties of these schemes are also summarised.

2.3.1 Discontinuous Galerkin framework

The discontinuous Galerkin method is designed to solve various kinds of partial differential equations. Similarly to classical continuous Galerkin finite element methods, the geometry is also approached by polyhedral elements. Inside them, the interpolated field is approximated by nodal shape polynomial functions associated to each node. However, the support of a node is limited to the element to which it belongs. While the intra-element continuity is warranted

by the shape functions, the inter-element continuity is therefore, not strongly but, weakly ensured by compatibility and penalty terms introduced by the DG formalism. The inherent presence of interface discontinuities allows then naturally initiating and propagating a large number of cracks simultaneously without numerical problems by just switching the DG terms by the cohesive law. Despite the increase of the system size due to the formalism, the high scalability of the method mitigates this drawback. Indeed, the decoupling between elements eases parallel implementation. The following lines explain how the non-local DG formalism developed by Wu, Becker, and Noels (2014) is extended to the hybrid CDM/CBM scheme.

2.3.1.1 Strong form of equations

The evolution of the body Ω through time, determined by the field $(\boldsymbol{u}, \tilde{e})$, is assessed by the set of partial differential equations (2.4) and (2.42) associated with boundary conditions (2.5) and (2.43).

Cracked Γ_{IC} and uncracked Γ_{IU} interface surfaces are present inside the structural volume. As the exact solution $\left(\boldsymbol{u}^{\mathrm{exact}}, \tilde{e}^{\mathrm{exact}}, \boldsymbol{\sigma}^{\mathrm{exact}}, \boldsymbol{\nabla}\tilde{e}^{\mathrm{exact}}\right)$ is continuous on the uncracked surfaces, one has

$$\begin{aligned} \left[\!\left[\boldsymbol{u}^{\mathrm{exact}}\right]\!\right] &= \boldsymbol{0}, \quad \left[\!\left[\boldsymbol{\sigma}^{\mathrm{exact}}\right]\!\right] = \boldsymbol{0}, \\ \left[\!\left[\tilde{e}^{\mathrm{exact}}\right]\!\right] &= 0, \quad \left[\!\left[l_{\mathrm{c}}^2 \boldsymbol{\nabla}\tilde{e}^{\mathrm{exact}}\right]\!\right] = \boldsymbol{0} \quad \text{on } \Gamma_{\mathrm{IU}}. \end{aligned} \tag{2.68}$$

For the cracked parts, the interface traction $\boldsymbol{t}_{\mathrm{I}}$ between both crack lips is determined by

$$[\![\boldsymbol{t}_{\mathrm{I}}]\!] = \boldsymbol{0}; \;\; \boldsymbol{t}_{\mathrm{I}} = \langle \boldsymbol{\sigma}_{\mathrm{b}} \rangle \cdot \boldsymbol{n}_{\mathrm{I}}; \;\; \left(l_{\mathrm{c}}^2 \boldsymbol{\nabla}\tilde{e}^{\mathrm{exact}}\right) \cdot \boldsymbol{n}_{\mathrm{I}} = 0 \text{ on } \Gamma_{\mathrm{IC}}, \tag{2.69}$$

which express the equilibrium of the traction forces over the interface, and their evaluation from the cohesive band model (2.37). The last equation of Eq. (2.69) considers a cracked surface as a free boundary in terms of the non-local variable, see a discussion in the work of Wu, Becker, and Noels (2014).

2.3.1.2 Weak form of equations

The body Ω of external surface Γ is divided in finite elements B^e of boundary S^e. The internal boundary of the elements $\Gamma_{\mathrm{I}} = \cup_e S^e \setminus \Gamma$ is divided between cracked interface surfaces Γ_{IC} and uncracked ones Γ_{IU}, satisfying $\Gamma_{\mathrm{IC}} \cup \Gamma_{\mathrm{IU}} = \Gamma_{\mathrm{I}}$ and $\Gamma_{\mathrm{IC}} \cap \Gamma_{\mathrm{IU}} = \emptyset$. Between each pair of neighbouring elements (arbitrary called B^{e+} and B^{e-}), an interface element S^s is inserted on their common boundary surface $S^s = S^{e+} \cap S^{e-}$.

In a discontinuous Galerkin approach, an element-wise continuous polynomial approximation of $(\boldsymbol{u}, \tilde{e})$ is sought. Consequently, the test functions $(\boldsymbol{w}_{\boldsymbol{u}}, w_{\tilde{e}})$ are also continuous inside the elements and discontinuous across them, i.e. $(\boldsymbol{w}_{\boldsymbol{u}}, w_{\tilde{e}}) \in \mathcal{H}^1(B^e)$ and $(\boldsymbol{w}_{\boldsymbol{u}}, w_{\tilde{e}}) \in \mathcal{L}^2(\Omega)$.[3] The weak form is obtained by multiplying the differential equations by the test functions and by performing an integration by parts over each element. Indeed, as discontinuities are present inside the body, the integration has to be performed element-wise, resulting in the emergence of supplementary terms, so-called consistency terms, on the interfaces in comparison with classical continuous Galerkin methods. Similarly to the work of Wu, Becker, and Noels (2014),

[3] In the former, $\mathcal{H}^1$ corresponds to the Hilbert space and $\mathcal{L}^2$ to the square-integrable function space

one thus has

$$\begin{aligned}\int_\Omega \left(\rho \boldsymbol{w_u}\cdot\ddot{\boldsymbol{u}} + \boldsymbol{\nabla w_u} : \boldsymbol{\sigma}\right) dV + \int_{\Gamma_{\mathrm{IC}}} [\![\boldsymbol{w_u}]\!]\cdot\langle\boldsymbol{\sigma}_{\mathrm{b}}\rangle\cdot\boldsymbol{n}_{\mathrm{I}} dS + \int_{\Gamma_{\mathrm{IU}}} [\![\boldsymbol{w_u}]\!]\cdot\langle\boldsymbol{\sigma}_{\mathrm{b}}\rangle\cdot\boldsymbol{n}_{\mathrm{I}} dS \\ = \int_\Omega \boldsymbol{w_u}\cdot\boldsymbol{b} dV + \int_{\Gamma_{\mathrm{N}}} \boldsymbol{w_u}\cdot\bar{\boldsymbol{t}}_{\mathrm{N}} dS, \\ \int_\Omega \left(w_{\tilde{e}}\tilde{e} + l_{\mathrm{c}}^2 \boldsymbol{\nabla} w_{\tilde{e}}\cdot\boldsymbol{\nabla}\tilde{e}\right) dV + \int_{\Gamma_{\mathrm{IU}}} [\![w_{\tilde{e}}]\!]\left\langle l_{\mathrm{c}}^2\boldsymbol{\nabla}\tilde{e}\right\rangle\cdot\boldsymbol{n_{\mathrm{I}}} dS = \int_\Omega w_{\tilde{e}} e dV.\end{aligned} \tag{2.70}$$

Compatibility equations $\boldsymbol{u}^+ - \boldsymbol{u}^- = \boldsymbol{0}$ and $\tilde{e}^+ - \tilde{e}^- = 0$ are weakly added to the formulation (2.70) in order to enforce weakly the inter-element continuity on Γ_{IU} and the stability of the system: the so-called symmetrisation and stability terms are added at the element interfaces. The first one ensures an optimal convergence rate with respect to the mesh size in the case of uncracked bodies while the second one ensures the stability throught a sufficiently high quadratic penalty term. Introducing h_{s} as the mesh characteristic size (this is not the mesh size l_{mesh} since h_{s} depends on the polynomial approximation) and β_{s} the penalty parameter, the weak form (2.70) is reformulated as finding the field $(\boldsymbol{u}, \tilde{e})$ such that

$$\begin{aligned}\int_\Omega \left(\rho \boldsymbol{w_u}\cdot\ddot{\boldsymbol{u}} + \boldsymbol{\nabla w_u} : \boldsymbol{\sigma}\right) dV + \int_{\Gamma_{\mathrm{IC}}} [\![\boldsymbol{w_u}]\!]\cdot\langle\boldsymbol{\sigma}_{\mathrm{b}}\rangle\cdot\boldsymbol{n}_{\mathrm{I}} dS + \int_{\Gamma_{\mathrm{IU}}} [\![\boldsymbol{w_u}]\!]\cdot\langle\boldsymbol{\sigma}\rangle\cdot\boldsymbol{n}_{\mathrm{I}} dS \\ + \int_{\Gamma_{\mathrm{IU}}} [\![\boldsymbol{u}]\!]\cdot\langle\boldsymbol{\mathcal{H}} : \boldsymbol{\nabla w_u}\rangle\cdot\boldsymbol{n}_{\mathrm{I}} dS + \int_{\Gamma_{\mathrm{IU}}} [\![\boldsymbol{w_u}]\!]\otimes\boldsymbol{n}_{\mathrm{I}} : \left\langle\frac{\beta_{\mathrm{s}}}{h_{\mathrm{s}}}\boldsymbol{\mathcal{H}}\right\rangle : [\![\boldsymbol{u}]\!]\otimes\boldsymbol{n}_{\mathrm{I}} dS \\ = \int_\Omega \boldsymbol{w_u}\cdot\boldsymbol{b} dV + \int_{\Gamma_{\mathrm{N}}} \boldsymbol{w_u}\cdot\bar{\boldsymbol{t}}_{\mathrm{N}} dS, \\ \int_\Omega \left(w_{\tilde{e}}\tilde{e} + l_{\mathrm{c}}^2 \boldsymbol{\nabla} w_{\tilde{e}}\cdot\boldsymbol{\nabla}\tilde{e}\right) dV + \int_{\Gamma_{\mathrm{IU}}} [\![w_{\tilde{e}}]\!]\left\langle l_{\mathrm{c}}^2\boldsymbol{\nabla}\tilde{e}\right\rangle\cdot\boldsymbol{n}_{\mathrm{I}} dS + \int_{\Gamma_{\mathrm{IU}}} [\![\tilde{e}]\!]\left\langle l_{\mathrm{c}}^2\boldsymbol{\nabla} w_{\tilde{e}}\right\rangle\cdot\boldsymbol{n}_{\mathrm{I}} dS \\ + \int_{\Gamma_{\mathrm{IU}}} [\![w_{\tilde{e}}]\!]\,\boldsymbol{n}_{\mathrm{I}}\left\langle\frac{\beta_{\mathrm{s}}}{h_{\mathrm{s}}} l_{\mathrm{c}}^2\right\rangle\cdot\boldsymbol{n}_{\mathrm{I}}\,[\![\tilde{e}]\!]\, dS = \int_\Omega w_{\tilde{e}} e dV,\end{aligned} \tag{2.71}$$

is satisfied for $\forall\,(\boldsymbol{w_u}, w_{\tilde{e}})$ kinematically admissible.

2.3.1.3 Finite element discretisation

Now, the finite element discretisation is derived from the weak form (2.71). The displacement field $\boldsymbol{u}(\boldsymbol{X})$ and the non-local effective strain $\tilde{e}(\boldsymbol{X})$ are interpolated by the same nodal shape functions, as well as their respective test functions in the volume element B^e:

$$\begin{aligned}\boldsymbol{u}(\boldsymbol{X}) &= \sum_{a=1}^{N_{\mathrm{n}}} N^a(\boldsymbol{X})\,\boldsymbol{u}^a, \qquad \tilde{e}(\boldsymbol{X}) = \sum_{a=1}^{N_{\mathrm{n}}} N^a(\boldsymbol{X})\,\tilde{e}^a, \qquad \text{and} \\ \boldsymbol{w_u}(\boldsymbol{X}) &= \sum_{a=1}^{N_{\mathrm{n}}} N^a(\boldsymbol{X})\,\delta\boldsymbol{u}^a, \quad w_{\tilde{e}}(\boldsymbol{X}) = \sum_{a=1}^{N_{\mathrm{n}}} N^a(\boldsymbol{X})\,\delta\tilde{e}^a,\end{aligned} \tag{2.72}$$

where $N^a(\boldsymbol{X})$ are the shape functions evaluated at node a, and N_{n} the number of nodes per volume elements. The unknowns are gathered inside the nodal vectors $\boldsymbol{q}^a = \left[(\boldsymbol{u}^a)^{\mathrm{T}}\ \tilde{e}^a\right]^{\mathrm{T}}$ associated with each node a, and inside a global vector $\boldsymbol{q} = \left[\boldsymbol{u}^{\mathrm{T}}\ \tilde{\boldsymbol{e}}^{\mathrm{T}}\right]^{\mathrm{T}}$ for all the unknowns of the mesh. Applying the discrete fields (2.72) to the weak form (2.71), and taking into account the inter-element discontinuities, we obtain this following set of differential equations

$$\left\{\begin{array}{lcll}\mathbf{M}\ddot{\boldsymbol{u}} + \boldsymbol{f}_{\boldsymbol{u}\,\mathrm{int}}(\boldsymbol{q}) + \boldsymbol{f}_{\boldsymbol{u}\,\mathrm{I}}(\boldsymbol{q}) & = & \boldsymbol{f}_{\mathrm{ext}} & \forall t > 0, \\ \boldsymbol{f}_{\tilde{e}\,\mathrm{int}}(\boldsymbol{q}) - \boldsymbol{f}_{e\,\mathrm{int}}(\boldsymbol{q}) + \boldsymbol{f}_{\tilde{e}\,\mathrm{I}}(\boldsymbol{q}) & = & \boldsymbol{0} & \end{array}\right. \tag{2.73}$$

with the following initial conditions

$$\boldsymbol{u}^a\left(t=0\right)=\boldsymbol{0},\ \ \dot{\boldsymbol{u}}^a\left(t=0\right)=\dot{\boldsymbol{u}}_0^a, \tag{2.74}$$

where $\dot{\boldsymbol{u}}_0^a$ is the nodal vector of initial velocities. In the system (2.73), $\mathbf{M}$ corresponds to the discretised mass matrix; the vectors $\boldsymbol{f}_{\boldsymbol{u}\,\mathrm{int}}$, $\boldsymbol{f}_{\boldsymbol{u}\,\mathrm{I}}$, and $\boldsymbol{f}_{\mathrm{ext}}$ state respectively for the internal, interface, and external forces related to the displacement field, and the vectors $\boldsymbol{f}_{\tilde{e}\,\mathrm{int}}$, $\boldsymbol{f}_{e\,\mathrm{int}}$, and $\boldsymbol{f}_{\tilde{e}\,\mathrm{I}}$ state respectively for the non-local internal, local internal, and interface forces related to the non-local field. The expressions, development, and computation of these vectors can be found in Appendix A.3.

The numerical properties connected to spatial discretisation of the presented framework inherit from those of the interior penalty formulation for elliptic problems (Noels and Radovitzky, 2006), as discussed by Wu, Becker, and Noels (2014). During crack propagation, the dissipated energy and the crack path converge for unstructured meshes as the cohesive band model can be assimilated to an extrinsic cohesive zone, for which such a property has been shown by Molinari et al. (2007). As large systems need to be solved, the presented framework is implemented in parallel inside Gmsh (Geuzaine and Remacle, 2009) using the scalable face-based ghost element implementation, detailed by Wu et al. (2013).

In all the simulations of this work, parabolic Lagrangian 6-node triangular or 10-node tetrahedron bulk elements are used respectively for 2D and 3D computations. Those elements are under-integrated following the Gauss quadrature rule with respectively 3 and 4 Gauss points. Regarding the interface elements, 3-node segment and 6-node triangular elements are involved with a full integration (i.e. involving respectively 3 and 6 Gauss points) to avoid spurious penetration modes, as explained by Noels and Radovitzky (2008).

2.3.1.4 Damage to crack transition

Inside this DG framework, both cracked and uncracked interface terms are integrated through the interface elements S^s, present from the beginning and inserted between each volume element. Once the criterion of crack initiation is reached at a Gauss point on Γ_{IU}, this one is thereafter associated to Γ_{IC} and the DG terms are replaced by the cohesive one. Since only the computation of the elementary force term is modified at crack insertion, topology or mesh modifications are avoided, which makes the implementation computationally efficient.

The damage is not directly used as a crack insertion criterion: it is based on the norm of the effective traction forces at the interface (Wu et al., 2013). This criterion avoids simultaneous crack insertion around an element of quasi-constant damage value and adds a directional component. Practically, switch occurs if

$$\frac{1}{1-D}\sqrt{\left\|\boldsymbol{t}_{\mathrm{I}}\cdot\boldsymbol{n}_{\mathrm{I}}\right\|^2+\frac{1}{\beta_{\mathrm{c}}^2}\left\|\boldsymbol{t}_{\mathrm{I}}-\left\|\boldsymbol{t}_{\mathrm{I}}\cdot\boldsymbol{n}_{\mathrm{I}}\right\|\boldsymbol{n}_{\mathrm{I}}\right\|^2}>\hat{\sigma}_{\mathrm{c}}\quad\text{and if}\quad\boldsymbol{t}_{\mathrm{I}}\cdot\boldsymbol{n}_{\mathrm{I}}>0, \tag{2.75}$$

where $\|\bullet\|$ states for the norm, $\boldsymbol{t}_{\mathrm{I}}=\boldsymbol{\sigma}\cdot\boldsymbol{n}_{\mathrm{I}}$ for the surface traction, $\hat{\sigma}_{\mathrm{c}}$ for the critical effective stress value, and β_{c} for the ratio between opening mode I and mode II. Practically, this parameter is set as the ratio between fracture toughness of mode I and mode II. A distribution is applied on $\hat{\sigma}_{\mathrm{c}}$ (a scatter of 1% around the mean value $\hat{\sigma}_{\mathrm{c}}$) for explicit simulations in order to capture crack propagation as proposed by Zhou and Molinari (2004).

During crack propagation, once the majority of the Gauss points of an interface element have switched to the cohesive band model, the CBM is also introduced on the remaining Gauss points of that interface element although Eq. (2.75) is not satisfied yet. By this way, spurious rotation of elements around one point/line is avoided. Once an interface element is completely opened, damage evolution is blocked inside the neighbouring bulk elements as they should be elastically unloaded. Moreover, the bulk local equivalent strain evolution, e of Eq. (2.42), is

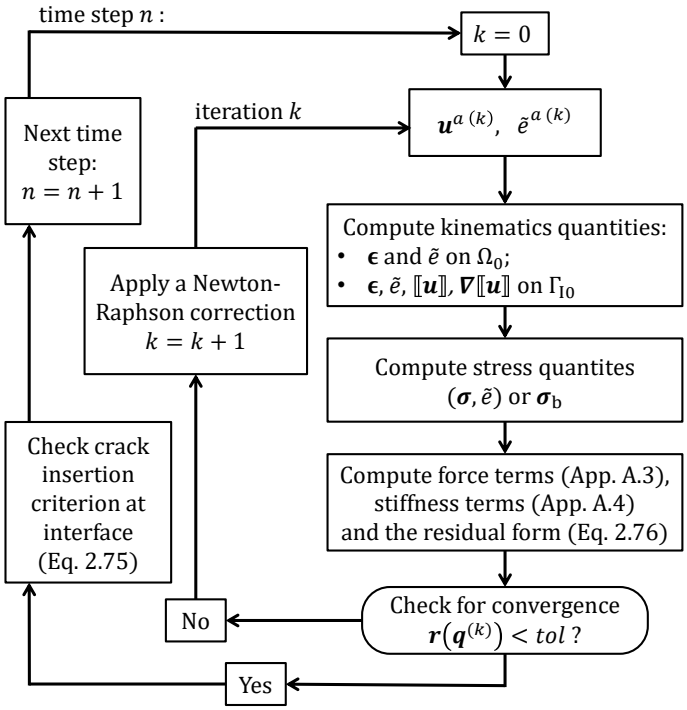

FIGURE 2.10: The implicit monolithic scheme structure.

limited to the maximal value it ever reached in order to avoid spurious damage spread and crack insertion around the element, but also to force elastic unloading. In case of crack closing and penetration, a normal quadratic penalty force is added. This form is preferred to a linear one in order to avoid tangent discontinuities and improve convergence.

2.3.2 Numerical time integration

The set of differential equations (2.73) has to be integrated. Different schemes are considered in this work. On the one hand, the system can be integrated in a fully coupled iterative procedure either under quasi-static loading assumption as detailed in Section 2.3.2.1, or considering the dynamic effects using the α-generalised method (Chung and Hulbert, 1993) as detailed in Section 2.3.2.2. On the other hand, a weakly coupled explicit-implicit scheme can be used as explained in Section 2.3.2.3.

2.3.2.1 Quasi-static implicit integration scheme

The whole procedure is schematised on Fig. 2.10. Under the assumption of quasi-static loading, the inertia or acceleration force term $\mathbf{M}\ddot{\boldsymbol{u}}$ in the set of differential equations (2.73) can be neglected. In absence of strain rate effects, the time has therefore here only a role of chronological ordering and the system is integrated in an incremental way. An iterative Newton-Raphson procedure is used to compute the equilibrium state at each discrete time step t^{n+1}, given the system state at t^n and the time step $\Delta t = t^{n+1} - t^n$. The system (2.73) is rewritten in the residual form $\boldsymbol{r}\left(\boldsymbol{q}^{(k)}(t^{n+1}),\, t^{n+1}\right)$

$$\boldsymbol{r}\left(\boldsymbol{q}^{(k)}(t^{n+1}), t^{n+1}\right) = \boldsymbol{f}_{\boldsymbol{q}}\left(\boldsymbol{q}^{(k)}(t^{n+1}),\, t^{n+1}\right), \tag{2.76}$$

which corresponds to the force unbalance at time t^{n+1}. In this last equation, $\boldsymbol{q}^{(k)}\left(t^{n+1}\right)$ corresponds to the fields values at iteration (k) and at time step t^{n+1}. $\boldsymbol{f}_{\boldsymbol{q}}\left(\boldsymbol{q}\left(t\right)\right)$ states for the

sum of the internal, external and interface force terms as

$$\boldsymbol{f}_{\boldsymbol{q}}\left(\boldsymbol{q}(t)\right) = \begin{bmatrix} \boldsymbol{f}_{\boldsymbol{u}\,\mathrm{int}}\left(\boldsymbol{q}(t)\right) + \boldsymbol{f}_{\boldsymbol{u}\,\mathrm{I}}\left(\boldsymbol{q}(t)\right) - \boldsymbol{f}_{\boldsymbol{u}\,\mathrm{ext}}(t) \\ \boldsymbol{f}_{\tilde{e}\,\mathrm{int}}\left(\boldsymbol{q}(t)\right) - \boldsymbol{f}_{e\,\mathrm{int}}\left(\boldsymbol{q}(t)\right) + \boldsymbol{f}_{\tilde{e}\,\mathrm{I}}\left(\boldsymbol{q}(t)\right) \end{bmatrix} . \tag{2.77}$$

The Newton-Raphson linearisation reads

$$\boldsymbol{r}\left(\boldsymbol{q}^{(k+1)}, t^{n+1}\right) = \boldsymbol{r}\left(\boldsymbol{q}^{(k)}, t^{n+1}\right) + \left.\frac{\partial \boldsymbol{r}\left(\boldsymbol{q}^{(k)}, t^{n+1}\right)}{\partial \boldsymbol{q}}\right|_{\boldsymbol{q}^{(k)}} \Delta\boldsymbol{q}^{(k)}\left(t^{n+1}\right) = \boldsymbol{0}\,, \tag{2.78}$$

or, again using the residual form (2.76),

$$\underbrace{\frac{\partial \boldsymbol{f}_{\boldsymbol{u}\,\mathrm{int}}}{\partial \boldsymbol{u}}}_{\mathbf{K}_{\boldsymbol{u}\boldsymbol{u}\,\mathrm{int}}} \Delta\boldsymbol{u} + \underbrace{\frac{\partial \boldsymbol{f}_{\boldsymbol{u}\,\mathrm{int}}}{\partial \tilde{\boldsymbol{e}}}}_{\mathbf{K}_{\boldsymbol{u}\tilde{e}\,\mathrm{int}}} \Delta\tilde{\boldsymbol{e}} + \underbrace{\frac{\partial \boldsymbol{f}_{\boldsymbol{u}\,\mathrm{I}}}{\partial \boldsymbol{u}}}_{\mathbf{K}_{\boldsymbol{u}\boldsymbol{u}\,\mathrm{I}}} \Delta\boldsymbol{u} + \underbrace{\frac{\partial \boldsymbol{f}_{\boldsymbol{u}\,\mathrm{I}}}{\partial \tilde{\boldsymbol{e}}}}_{\mathbf{K}_{\boldsymbol{u}\tilde{e}\,\mathrm{I}}} \Delta\tilde{\boldsymbol{e}} = \boldsymbol{f}_{\mathrm{ext}}\left(t^{n+1}\right) - \boldsymbol{f}_{\boldsymbol{u}\,\mathrm{int}}\left(\boldsymbol{q}^{(k)}\right) - \boldsymbol{f}_{\boldsymbol{u}\,\mathrm{I}}\left(\boldsymbol{q}^{(k)}\right), \tag{2.79}$$

and,

$$\begin{aligned} &\underbrace{\frac{\partial \boldsymbol{f}_{\tilde{e}\,\mathrm{int}}}{\partial \boldsymbol{u}}}_{\mathbf{K}_{\tilde{e}\boldsymbol{u}\,\mathrm{int}}} \Delta\boldsymbol{u} + \underbrace{\frac{\partial \boldsymbol{f}_{\tilde{e}\,\mathrm{int}}}{\partial \tilde{\boldsymbol{e}}}}_{\mathbf{K}_{\tilde{e}\tilde{e}\,\mathrm{int}}} \Delta\tilde{\boldsymbol{e}} - \underbrace{\frac{\partial \boldsymbol{f}_{e\,\mathrm{int}}}{\partial \boldsymbol{u}}}_{\mathbf{K}_{e\boldsymbol{u}\,\mathrm{int}}} \Delta\boldsymbol{u} - \underbrace{\frac{\partial \boldsymbol{f}_{e\,\mathrm{int}}}{\partial \tilde{\boldsymbol{e}}}}_{\mathbf{K}_{e\tilde{e}\,\mathrm{int}}} \Delta\tilde{\boldsymbol{e}} + \underbrace{\frac{\partial \boldsymbol{f}_{\tilde{e}\,\mathrm{I}}}{\partial \boldsymbol{u}}}_{\mathbf{K}_{\tilde{e}\boldsymbol{u}\,\mathrm{I}}} \Delta\boldsymbol{u} + \underbrace{\frac{\partial \boldsymbol{f}_{\tilde{e}\,\mathrm{I}}}{\partial \tilde{\boldsymbol{e}}}}_{\mathbf{K}_{\tilde{e}\tilde{e}\,\mathrm{I}}} \Delta\tilde{\boldsymbol{e}} \\ &\qquad = \boldsymbol{f}_{e\,\mathrm{int}}\left(\boldsymbol{q}^{(k)}\right) - \boldsymbol{f}_{\tilde{e}\,\mathrm{int}}\left(\boldsymbol{q}^{(k)}\right) - \boldsymbol{f}_{\tilde{e}\,\mathrm{I}}\left(\boldsymbol{q}^{(k)}\right), \end{aligned} \tag{2.80}$$

in which the matrices $\mathbf{K}_{\ldots}$ are the contributions to the stiffness matrix. Their expressions are reported in Appendix A.4. The correction $\Delta\boldsymbol{q}^{(k)}\left(t^{n+1}\right)$ is computed by solving the system (2.79)-(2.80)

$$\mathbf{K}\left(\boldsymbol{q}^{(k)}(t^{n+1}), t^{n+1}\right)\Delta\boldsymbol{q}^{(k)}\left(t^{n+1}\right) = -\boldsymbol{r}\left(\boldsymbol{q}^{(k)}(t^{n+1}), t^{n+1}\right), \tag{2.81}$$

with $\mathbf{K}$, the stiffness matrix. If explicitly written, (2.81) corresponds to

$$\begin{aligned} &\underbrace{\begin{bmatrix} \mathbf{K}_{\boldsymbol{u}\boldsymbol{u}\,\mathrm{int}} + \mathbf{K}_{\boldsymbol{u}\boldsymbol{u}\,\mathrm{I}} & \mathbf{K}_{\boldsymbol{u}\tilde{e}\,\mathrm{int}} + \mathbf{K}_{\boldsymbol{u}\tilde{e}\,\mathrm{I}} \\ \mathbf{K}_{\tilde{e}\boldsymbol{u}\,\mathrm{int}} - \mathbf{K}_{e\boldsymbol{u}\,\mathrm{int}} + \mathbf{K}_{\tilde{e}\boldsymbol{u}\,\mathrm{I}} & \mathbf{K}_{\tilde{e}\tilde{e}\,\mathrm{int}} - \mathbf{K}_{e\tilde{e}\,\mathrm{int}} + \mathbf{K}_{\tilde{e}\tilde{e}\,\mathrm{I}} \end{bmatrix}}_{\mathbf{K}\left(\boldsymbol{q}^{(k)}\right)} \underbrace{\begin{bmatrix} \Delta\boldsymbol{u} \\ \Delta\tilde{\boldsymbol{e}} \end{bmatrix}}_{\Delta\boldsymbol{q}^{(k)}} \\ &\qquad = \underbrace{\begin{bmatrix} \boldsymbol{f}_{\mathrm{ext}}\left(t^{n+1}\right) - \boldsymbol{f}_{\boldsymbol{u}\,\mathrm{int}}\left(\boldsymbol{q}^{(k)}\right) - \boldsymbol{f}_{\boldsymbol{u}\,\mathrm{I}}\left(\boldsymbol{q}^{(k)}\right) \\ \boldsymbol{f}_{e\,\mathrm{int}}\left(\boldsymbol{q}^{(k)}\right) - \boldsymbol{f}_{\tilde{e}\,\mathrm{int}}\left(\boldsymbol{q}^{(k)}\right) - \boldsymbol{f}_{\tilde{e}\,\mathrm{I}}\left(\boldsymbol{q}^{(k)}\right) \end{bmatrix}}_{\boldsymbol{r}\left(\boldsymbol{q}^{(k)}\right)}, \end{aligned} \tag{2.82}$$

and its resolution for $\Delta\boldsymbol{q}$ gives the new guess $\boldsymbol{q}^{(k+1)} = \boldsymbol{q}^{(k)} + \Delta\boldsymbol{q}^{(k)}$ at the end of the iteration k. This Newton-Raphson procedure has to be repeated until the convergence is reached. To ensure a well-conditioned system, a ratio is applied between the force equilibrium and the non-local system. Finally, snap-back can be captured by considering a path following scheme as introduced in Section 2.2.3.1.

The main advantage of the fully coupled implicit solving is that it is unconditionally stable. However, implicit iterations are time-consuming. Convergence needs small time steps and cannot always be reached, especially in case of local snap-backs, unstable crack propagations, or in the case of the arising of new rigid body modes because of the full separation of the

structure.

2.3.2.2 α-generalised implicit integration scheme

In this section, the set of equations (2.73) obtained previously is integrated through time using the α-generalised method developed by Chung and Hulbert (1993). The unknowns at time t^{n+1} and their time derivatives are approximated following

$$\begin{aligned} \boldsymbol{q}\left(t^{n+1}\right) &= \boldsymbol{q}\left(t^{n}\right) + \Delta t \dot{\boldsymbol{q}}\left(t^{n}\right) + \left[\tfrac{1}{2} - \beta\right] \Delta t^2 \ddot{\boldsymbol{q}}\left(t^{n}\right) + \beta \Delta t^2 \ddot{\boldsymbol{q}}\left(t^{n+1}\right) \,, \\ \dot{\boldsymbol{q}}\left(t^{n+1}\right) &= \dot{\boldsymbol{q}}\left(t^{n}\right) + \left[1 - \gamma\right] \Delta t \ddot{\boldsymbol{q}}\left(t^{n}\right) + \gamma \Delta t \ddot{\boldsymbol{q}}\left(t^{n+1}\right) \,, \end{aligned} \tag{2.83}$$

introducing β and γ as the Newmark integration parameters. From the force balance system (2.73) weighted at time t^n and t^{n+1}, a residual form $\boldsymbol{r}\left(\boldsymbol{q}^{(k)}(t^{n+1}), t^{n+1}\right)$ is obtained as

$$\begin{aligned} \boldsymbol{r}\left(\boldsymbol{q}^{(k)}(t^{n+1}), t^{n+1}\right) &= \left[1 - \alpha_{\mathrm{M}}\right] \begin{bmatrix} \mathbf{M} & \mathbf{0} \\ \mathbf{0} & \mathbf{0} \end{bmatrix} \ddot{\boldsymbol{q}}^{(k)}\left(t^{n+1}\right) + \alpha_{\mathrm{M}} \begin{bmatrix} \mathbf{M} & \mathbf{0} \\ \mathbf{0} & \mathbf{0} \end{bmatrix} \ddot{\boldsymbol{q}}\left(t^{n}\right) \\ &+ \left[1 - \alpha_{\mathrm{F}}\right] \boldsymbol{f}_{\boldsymbol{q}}\left(\boldsymbol{q}^{(k)}\left(t^{n+1}\right)\right) + \alpha_{\mathrm{F}} \boldsymbol{f}_{\boldsymbol{q}}\left(\boldsymbol{q}\left(t^{n}\right)\right) \end{aligned} \,, \tag{2.84}$$

where $\boldsymbol{q}^{(k)}(t^n)$ is the nodal values vector of the field at iteration k and at time step t^n. The parameter α_{M} weights the inertia forces expressed at time t^{n+1} and t^n while α_{F} scales the sum of the internal, external and interface force terms $\boldsymbol{f}_{\boldsymbol{q}}\left(\boldsymbol{q}(t)\right)$ defined by Eq. (2.77).

The iterative Newton-Raphson scheme is initialised by considering the initial acceleration at t^{n+1} as null in Eq. (2.83). The new state at the iteration $k+1$ is then obtained from the correction $\Delta\boldsymbol{q}^{(k)}\left(t^{n+1}\right)$ by

$$\begin{aligned} \boldsymbol{q}^{(k+1)}\left(t^{n+1}\right) &= \boldsymbol{q}^{(k)}\left(t^{n+1}\right) + \Delta\boldsymbol{q}^{(k)}\left(t^{n+1}\right) \,, \\ \dot{\boldsymbol{q}}^{(k+1)}\left(t^{n+1}\right) &= \dot{\boldsymbol{q}}^{(k)}\left(t^{n+1}\right) + \tfrac{\gamma}{\beta\Delta t} \Delta\boldsymbol{q}^{(k)}\left(t^{n+1}\right) \,, \\ \ddot{\boldsymbol{q}}^{(k+1)}\left(t^{n+1}\right) &= \ddot{\boldsymbol{q}}^{(k)}\left(t^{n+1}\right) + \tfrac{1}{\beta\Delta t^2} \Delta\boldsymbol{q}^{(k)}\left(t^{n+1}\right) \,. \end{aligned} \tag{2.85}$$

This correction is computed by solving the system (2.81), using, instead of $\mathbf{K}$, the following tangent matrix $\mathbf{S}$

$$\mathbf{S} = \frac{\partial \boldsymbol{r}}{\partial \boldsymbol{q}} = \left[1 - \alpha_{\mathrm{M}}\right] \frac{1}{\beta \Delta t^2} \begin{bmatrix} \mathbf{M} & \mathbf{0} \\ \mathbf{0} & \mathbf{0} \end{bmatrix} + \left[1 - \alpha_{\mathrm{F}}\right] \mathbf{K} \tag{2.86}$$

where the stiffness matrix $\mathbf{K}$ is defined in Eq. (2.82). The values of the four integration parameters are determined in terms of the (infinite) spectral radius ρ_∞ in the work of Chung and Hulbert (1993).

This numerical integration scheme is unconditionally stable, allowing large time steps and mitigating the large CPU cost of the material law integration. Despite we do not focus on dynamic effects in this work, the introduction of inertial effects has a stabilising effect on the solution. They ease, for instance, to overcome local or global snap backs, unstable crack propagations, or the arising of new rigid body modes due to dust elements.

2.3.2.3 Coupled explicit-implicit integration scheme

The first set of equations in the system (2.73) can be integrated with an explicit integration scheme. The numerical method developed by Hulbert and Chung (1996) is considered here because of its second-order accuracy and its controlled numerical damping. From the solution

at time t^n, the solution at the next time step $t^{n+1} = t^n + \Delta t$ is obtained by

$$\begin{aligned}
\ddot{\boldsymbol{u}}^a\left(t^{n+1}\right) &= \tfrac{1}{1-\alpha_{\mathrm{M}}} \sum_{b=1}^{N_{\mathrm{n}}} \left(\mathbf{M}^{-1}\right)^{ba} \left(\boldsymbol{f}^b_{\mathrm{ext}}\left(t^n\right) - \boldsymbol{f}^b_{\boldsymbol{u}\,\mathrm{int}}\left(t^n\right) - \boldsymbol{f}^b_{\boldsymbol{u}\,\mathrm{I}}\left(t^n\right)\right) - \tfrac{\alpha_{\mathrm{M}}}{1-\alpha_{\mathrm{M}}} \ddot{\boldsymbol{u}}^a\left(t^n\right), \\
\dot{\boldsymbol{u}}^a\left(t^{n+1}\right) &= \dot{\boldsymbol{u}}^a\left(t^n\right) + \left(1-\gamma_{\mathrm{M}}\right)\Delta t \ddot{\boldsymbol{u}}^a\left(t^n\right) + \gamma_{\mathrm{M}} \Delta t \ddot{\boldsymbol{u}}^a\left(t^{n+1}\right), \text{ and} \\
\boldsymbol{u}^a\left(t^{n+1}\right) &= \boldsymbol{u}^a\left(t^n\right) + \Delta t \dot{\boldsymbol{u}}^a\left(t^n\right) + \left(\tfrac{1}{2} - \beta_{\mathrm{M}}\right)\Delta t^2 \ddot{\boldsymbol{u}}^a\left(t^n\right) + \beta_{\mathrm{M}} \Delta t^2 \ddot{\boldsymbol{u}}^a\left(t^{n+1}\right),
\end{aligned} \tag{2.87}$$

with the parameters α_{M}, β_{M} and γ_{M} depending on the sought numerical dissipation (Hulbert and Chung, 1996).

Since there is no mass matrix associated to the non-local equation, the remaining system has to be solved implicitly. By linearising the non-local equation (2.73) around the state $\boldsymbol{q}^{(k)}$ obtained at a given iteration k, one has in terms of the non-local increment $\Delta\tilde{\boldsymbol{e}}$:

$$\mathbf{K}_{\tilde{e}\tilde{e}} \Delta\tilde{\boldsymbol{e}} = \boldsymbol{f}_{e\,\mathrm{int}}\left(\boldsymbol{q}^{(k)}\right) - \boldsymbol{f}_{\tilde{e}\,\mathrm{int}}\left(\boldsymbol{q}^{(k)}\right) - \boldsymbol{f}_{\tilde{e}\,\mathrm{I}}\left(\boldsymbol{q}^{(k)}\right), \tag{2.88}$$

where

$$\mathbf{K}_{\tilde{e}\tilde{e}} = \underbrace{\frac{\partial \boldsymbol{f}_{\tilde{e}\,\mathrm{int}}}{\partial \tilde{\boldsymbol{e}}}}_{\mathbf{K}_{\tilde{e}\tilde{e}\,\mathrm{int}}} - \underbrace{\frac{\partial \boldsymbol{f}_{e\,\mathrm{int}}}{\partial \tilde{\boldsymbol{e}}}}_{\mathbf{K}_{e\tilde{e}\,\mathrm{int}}} + \underbrace{\frac{\partial \boldsymbol{f}_{\tilde{e}\,\mathrm{I}}}{\partial \tilde{\boldsymbol{e}}}}_{\mathbf{K}_{\tilde{e}\tilde{e}\,\mathrm{I}}}. \tag{2.89}$$

The expressions for these stiffness matrices can be found in Appendix A.4. Taking advantage of the unconditional stability of the implicit resolution of the non-local equations, these equations are solved every 100 to 1000 time steps to avoid computational over-costs.

The main advantages of this weakly coupled scheme are its low-cost of step computation and the lower restrictions due to convergence problem. However, a stability criterion on the time step has to be respected to ensure method stability. Indeed, the explicit time integration of the first set of equations in Eq. (2.73) using the Hulbert-Chung algorithm is conditionally stable. The time step Δt is bounded to satisfy a Courant-Friedrichs-Lewy (CFL) condition. The stability criterion depends on the spatial DG-discretisation mesh size h_{s}, the sound speed c_{s}, the stability parameter β_{s}, and the stability non-dimensional frequency of the time integration method $\Omega_{\mathrm{s}} \leq 2$ (Hulbert and Chung, 1996). The CFL-condition reads $\Delta t < \frac{h_{\mathrm{s}}\Omega_{\mathrm{s}}}{2c_{\mathrm{s}}\sqrt{\beta_{\mathrm{s}}}}$ (Noels and Radovitzky, 2008).

2.4 Numerical applications and triaxiality effects

In this section, the numerical properties of the developed non-local damage/cohesive band model (CDM/CBM) transition are investigated through numerical examples. In particular, the impact of the triaxiality effect is studied. During this section, the numerical predictions of the hybrid CDM/CBM are compared with the results of the non-local scheme without crack insertion (N-L), and with the results obtained with an hybrid scheme involving a (classical) cohesive zone model (CDM/CZM) as developed by Wu, Becker, and Noels (2014). When available, the numerical predictions are compared with phase field results or validated with experimental results from the literature.

2.4.1 Slit plate

At first, the CDM/CBM is applied on a simple 2D slit specimen. After having verified the mesh insensitivity, the specimen is subjected to various loading ratio coefficients in order to show its sensibility of the method to triaxiality effects in contrast with the CDM/CZM model.

The 2D specimen consists in a square plate of length $W = 40$ [mm]. A thin elliptical hole of major radius $a/2 = 6$ [mm] and minor one $a/20$ is introduced at its centre. The plate is under plane strain condition along its thickness t. The geometry is illustrated in Fig. 2.11a.

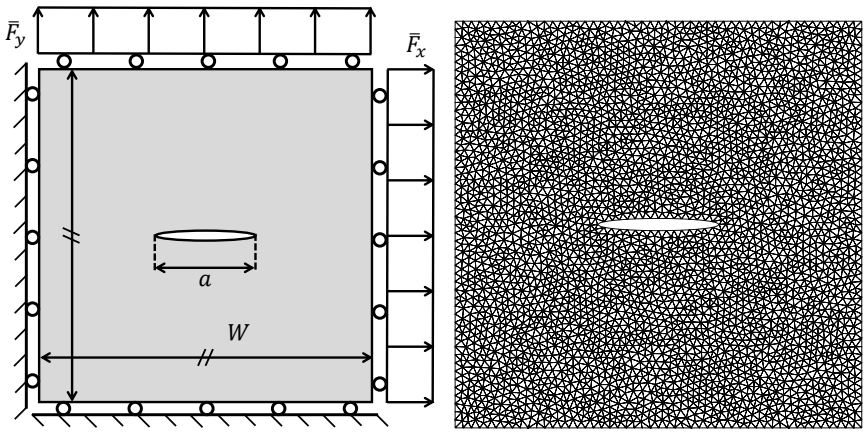

(a) (b)

FIGURE 2.11: (a) The slit plate geometry with $W = 40$ [mm] and $a = 12$ [mm]; and (b) its mesh.

TABLE 2.1: Material properties for short glass-fiber-reinforced polypropylene.

Elastic model properties, Eq. (2.38)		
Young's Modulus	E	3.2 [GPa]
Poisson ratio	ν	0.28
Damage model properties, Eq.(2.44):		
Initial damage threshold	κ_{i}	0.011
Failure equivalent strain	κ_{c}	0.50
Damage exponents	α	5.0
	β	0.75
Non-local model properties, Eq.(2.42):		
Non-local length	l_{c}^2	2.0 [mm^2]

The plate is loaded by applying a force $\bar{F}_{\mathrm{y}}$ on the top boundary and a force $\bar{F}_{\mathrm{x}} = k\bar{F}_{\mathrm{y}}$ on the right boundary. The plate edges are constrained to stay straight while the ratio k between the vertical and horizontal force is kept constant during each test. By varying the proportion between the vertical and horizontal loading conditions, the stress triaxiality T (ratio $p_\sigma/\sigma^{\mathrm{eq}}$ between the pressure $p_\sigma = \mathrm{tr}\,(\boldsymbol{\sigma})/3$ and equivalent von Mises stress σ^{eq}) inside the system evolves. The plate is uniformly meshed with 7058 6-node triangles of 0.8 [mm] mean size (unless stated otherwise) as shown in Fig. 2.11b. These elements involve quadratic shape functions for the displacement and the non-local field discretisations. The system is solved using the implicit scheme detailed in Section 2.3.2.1 completed by a path following method in order to capture a possible snap-back.

The material behaviour is assimilated to an isotropic non-local damage linear elastic model, combined with a cohesive band model as described in Section 2.1.3 or with a cohesive zone as done by Wu, Becker, and Noels (2014) for the sake of comparison. The material parameters are reported in Table 2.1 (Geers, 1997; Wu, Becker, and Noels, 2014). The damage to crack transition parameters for the hybrid CDM/CBM and CDM/CZM are listed in Table 2.2. The damage to crack transition is triggered by an effective critical stress $\hat{\sigma}_{\mathrm{c}}$, which is identical

TABLE 2.2: Damage to crack transition parameters for the slit plate.

Crack insertion criterion, Eq. (2.75):		
Effective critical stress	$\hat{\sigma}_c$	280 [MPa]
Critical damage	D_c	0.85
Mixed-mode ratio	β_c	0.87
Cohesive band model:		
Band thickness	h_b	7.6 [mm]
Cohesive zone model (Wu, Becker, and Noels, 2014):		
Remaining energy	G_c^*	21.4 $[\mathrm{kJ/m^2}]$

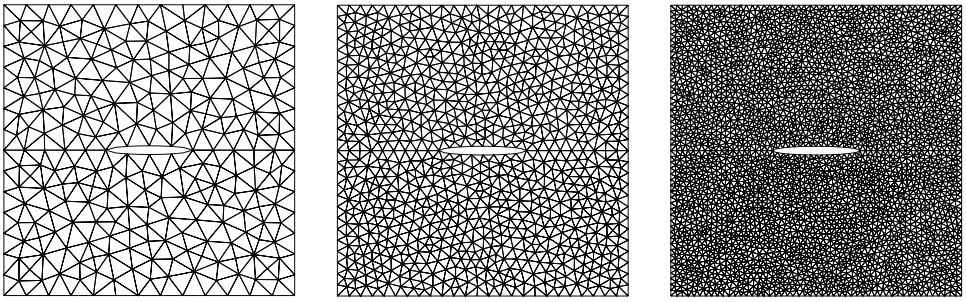

(a) l_{mesh} = 3.20 [mm], 536 elements

(b) l_{mesh} = 1.60 [mm], 1820 elements

(c) l_{mesh} = 0.8 [mm], 6944 elements

FIGURE 2.12: The mesh of the slit plate with different uniform mesh sizes l_{mesh}.

for both hybrid frameworks. An approximate corresponding value[4] of damage D_c at which transition occurs can be obtained by comparison with the one-dimensional case. The effective critical stress $\hat{\sigma}_c$ is here chosen to insert crack at a damage value around 0.75 for a uniaxial loading, in order to highlight the differences between the three models. The fracture energy G_c^* of the cohesive zone model, corresponding to the remaining energy needed to be dissipated after crack transition, is extracted from the one-dimensional simulation as shown in Fig. 2.8a. The values used here are slightly higher than the corresponding ones used by Wu, Becker, and Noels (2014) because Wu, Becker, and Noels (2014) used a variable non-local length instead of a constant one in this work. For the cohesive band model, only the band thickness is required and has been computed in Section 2.2.

2.4.1.1 Mesh insensitivity

The mesh insensitivity of the CDM/CBM framework is here investigated. The force evolution in terms of the displacement and the total dissipated energy are compared for different mesh sizes. The involved simulations have constrained crack paths along the symmetry planes in order to focus on the cohesive band effect only since the other framework features are mesh-independent. Indeed, because a non-local model is used, no mesh-dependency is expected during the softening before crack insertion (Peerlings et al., 1998), providing that the mesh size is sufficiently small in regard to the characteristic length. Moreover, the crack path should converge for the extrinsic cohesive zone (Molinari et al., 2007) during the crack propagation.

[4] This is an approximate value since it is obtained for the stress triaxiality which corresponds to a uniaxial loading

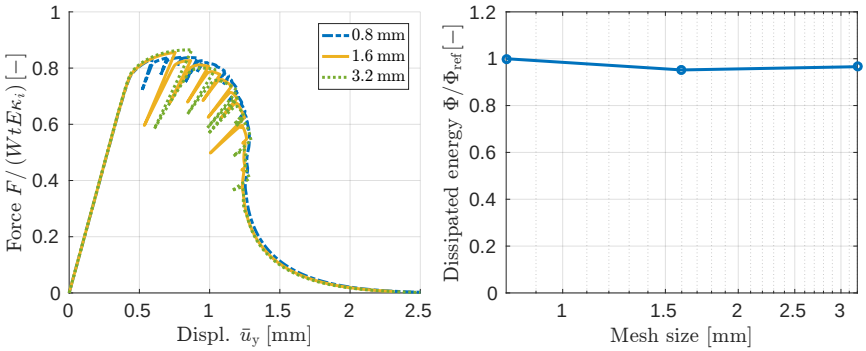

(a) (b)

FIGURE 2.13: (a) Vertical loading force in terms of the vertical displacement $\bar{u}_y$ for the different mesh sizes and (b) the corresponding total dissipated energy. The reference dissipated energy Φ_{ref} is here the value associated with the finest mesh.

The problem is simulated with the 3 different meshes shown in Fig. 2.12. The vertical loading force evolutions in terms of the vertical displacement $\bar{u}_y$ and for a loading ratio $k = 0$ are shown in Fig. 2.13a for the different mesh sizes. The three curves are similar, although unloading-loading cycles are observed at crack insertion due to the combination of damage freezing around cracked interfaces and the use of the path-following method. The depth of those cycles is more pronounced with an increasing mesh size. Moreover, a larger mesh size delays the crack insertion since the stress at the crack tip is lower at the first Gauss point. The total dissipated energy in terms of the mesh size is represented in Fig. 2.13b and no signifiant variation is observed with respect to the mesh size. The difference results from the numerical approximations (loading increments).

2.4.1.2 Study of the triaxiality effects

The plate is now loaded with different ratio coefficients $k = [-1/2; 0; 1/2]$ and the simulation results obtained by using the non-local model (N-L), the hybrid CDM/CBM model, and the hybrid CDM/CZM model are compared. The three models are identical before crack insertion. The damage fields are represented just before first crack insertion in Figs. 2.14a to 2.14c for the different values of k. The three distributions have a similar pattern but are more developed for the lower value of k since the transition occurs later in those less constrained states. The corresponding triaxiality distributions are shown in Figs. 2.14d to 2.14f and, as expected, are different for each case and increases with k.

After initiation, the cracks propagate near the median line of the plate for both hybrid frameworks while strains and damage continue to grow for simulations involving the non-local model only. The final damage distributions at material failure (when the vertical force drops to 0) are presented in the deformed configurations in Fig. 2.16. Globally, for a given numerical model, the damage fields at failure tend to be more spread for smaller values of k. For the non-local model, high damage values spread around the fictitious crack surface due to the highly stretched elements while damage evolution is stopped behind the crack tip with the hybrid frameworks. For a given value of k, the final crack opening is higher with the cohesive band model than with the cohesive zone, which expresses a less brittle behaviour for the band model.

The evolutions of the vertical loading forces F_y in terms of the vertical displacements $\bar{u}_y$ are reported in Figs. 2.16a, 2.16c, and 2.16e for the three frameworks. Increasing k tends

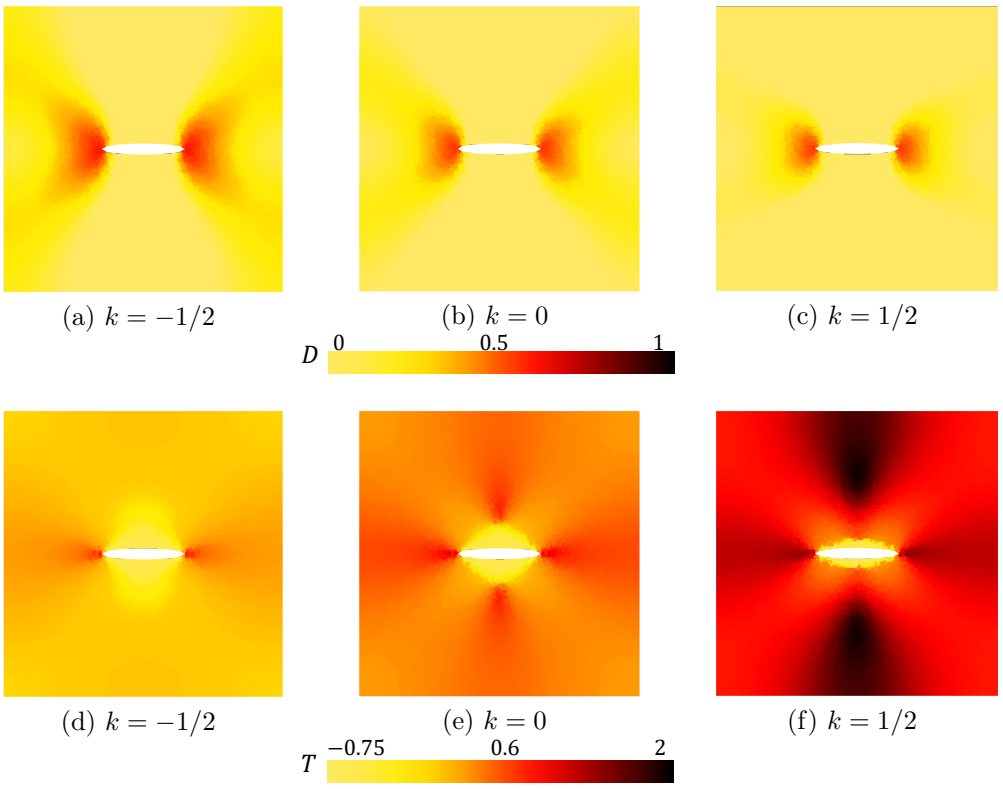

(a) $k = -1/2$ (b) $k = 0$ (c) $k = 1/2$

(d) $k = -1/2$ (e) $k = 0$ (f) $k = 1/2$

FIGURE 2.14: (a-c) Damage D field and (d-f) triaxiality T state at first crack insertion for different values of k.

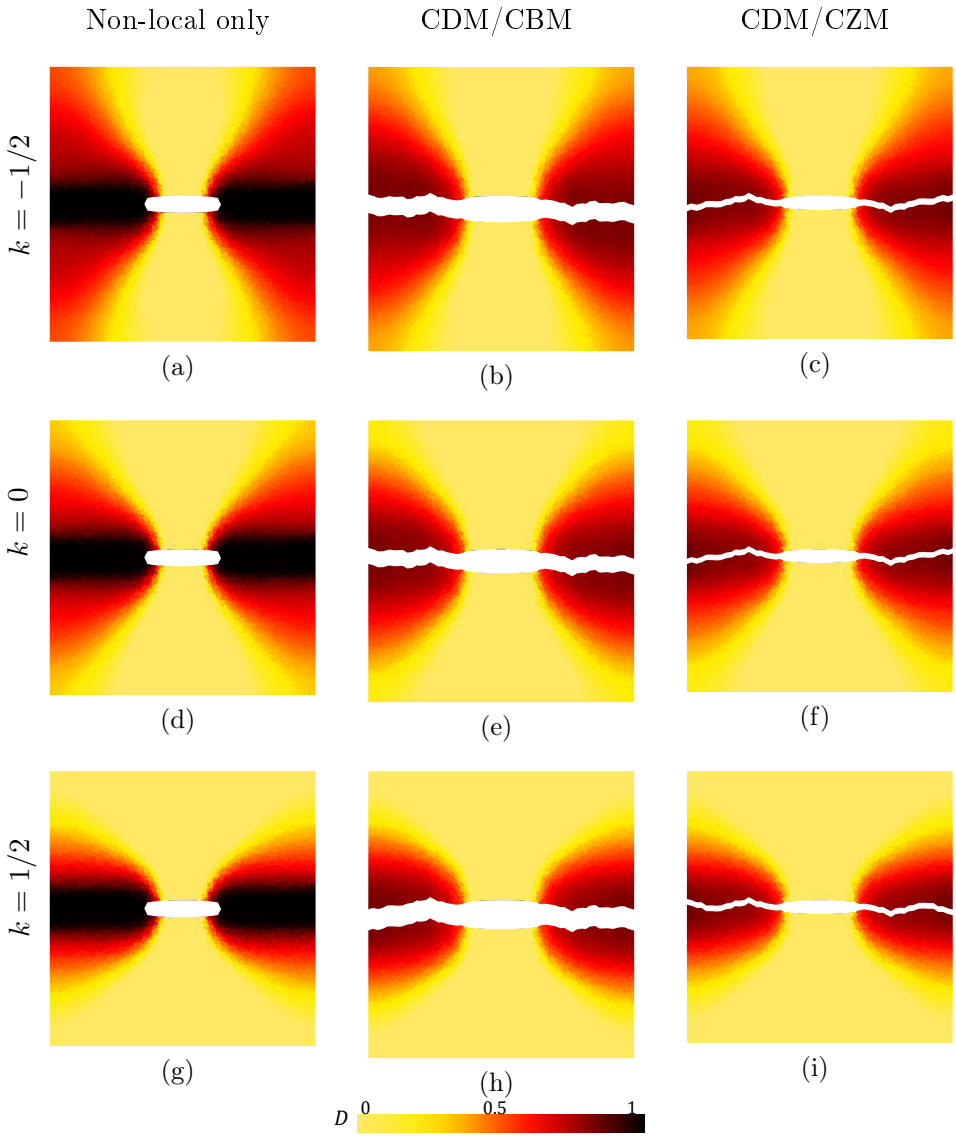

FIGURE 2.15: Damage field at material failure for the pure non-local, CDM/CBM, and CDM/CZM frameworks, and for different values of the loading ratio k.

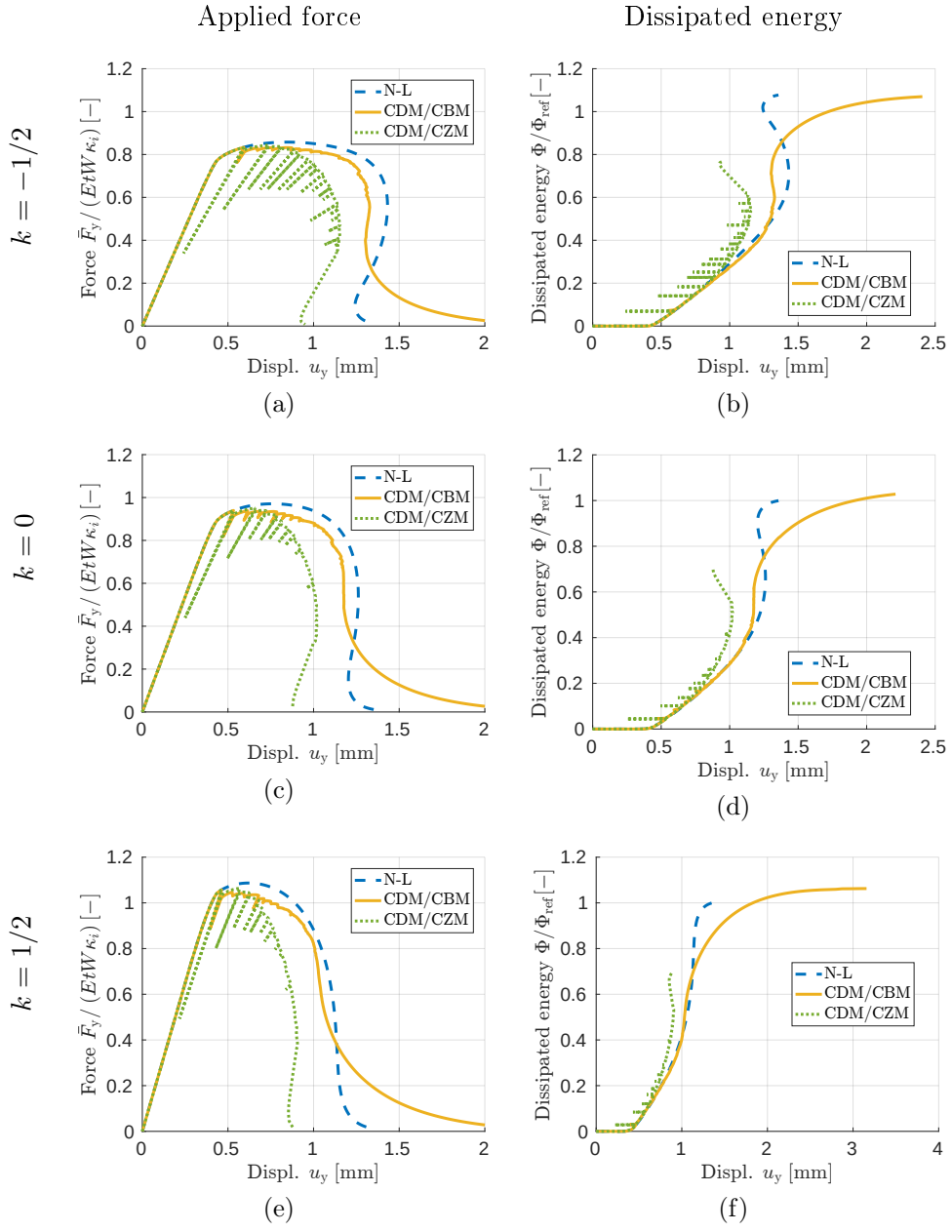

FIGURE 2.16: Vertical loading force F_y (left) and dissipated energy Φ (right) *vs.* vertical displacement $\bar{u}_y$ evolutions for the pure non-local, CDM/CBM, and CDM/CZM frameworks, and for different values of the loading ratio k. The reference dissipated energy Φ_{ref} is here the value associated with the pure non-local model and $k = 0$.

globally to rise the peak stress value but to decrease the displacement value at which this peak is reached. When comparing the models, no difference is observable before crack insertion as expected. During crack propagation, the CDM/CZM exhibits a more brittle behaviour than the hybrid CDM/CBM and than the non-local model. This is explained by the fact that CDM/CZM does not account for the triaxiality induces by the out-of-plane plane strain state and by the loading ratio k. The maximum stress value reached is higher for the non-local model than for the CDM/CBM but this is balanced by a longer response tail with the CBM. This longer tail results in a larger crack opening at failure than with the the fictitious crack opening of the pure non-local model. This could be avoided by considering a different damage evolution law in the CBM after shift has occurred. In order to address this issue, we will consider a coalescence model as governing law of the CBM in the next chapter.

The corresponding dissipated energy evolutions are shown in Figs. 2.16b, 2.16d, and 2.16f where Φ_{ref} is defined as being the energy dissipated by the pure non-local model with $k = 0$. During the crack propagation, the results of the hybrid CDM/CBM predictions remain closer from those of the non-local model than the prediction of the CDM/CZM until the sample is totally cracked. Despite the two dissipation rates differ, the final total amounts of dissipated energy are coherent between the non-local model and the CDM/CBM for the different triaxiality states. The CDM/CBM differs from the non-local model by maximum 5%; this difference can be partially explained by the non-straight crack pattern which increases the crack surface and thus the dissipation.

Besides, the more brittle behaviour of CDM/CZM previously mentioned reflects that the CDM/CZM is unable to dissipate the correct amount of energy, resulting in one order of magnitude higher in the error for all tests (i.e. around 30%). This is explained by the inability of the CZM to incorporate stress triaxiality effects since the fracture energy of the cohesive zone is fixed in advance (here, calibrated on a one-dimensional uniaxial tension). Moreover, the crack criterion is based on an effective stress. Therefore, the damage value at crack insertion is not guaranteed. To overcome these problems, the CZM could be calibrated for each specific case, which is avoided by the CDM/CBM since the cohesive band thickness does not depend on the damage insertion value. Nevertheless, this approach would not account for the variation of stress triaxiality state during the sample loading, whistle the CDM/CBM framework includes those triaxiality effects and therefore is able to follow the variation of dissipated energy.

2.4.2 Single edge notched specimens

The hybrid CDM/CBM framework is now compared to the phase field framework applied to brittle fracture (Miehe, Welschinger, and Hofacker, 2010, *e.g.*). To this end, the single edge notched specimens considered by de Borst and Verhoosel (2016) and Miehe, Hofacker, and Welschinger (2010) are simulated under tensile and shear loading conditions.

2.4.2.1 Material parameters

The elastic material properties reported by de Borst and Verhoosel (2016) and Miehe, Hofacker, and Welschinger (2010) are a Young's modulus $E = 210.0$ [GPa] and a Poisson ratio $\nu = 0.3$. The critical energy release rate is $G_{\text{c}} = 2700$ $\left[\text{J/m}^2\right]$ and the length scale associated to the phase field results is $l^{\text{pf}} = 15 \times 10^{-3}$ [mm]. The plane strain state is assumed.

First, the material parameters of the underlying non-local damage model of the hybrid CDM/CBM framework have to be calibrated with respect to the brittle behaviour studied by de Borst and Verhoosel (2016) and Miehe, Hofacker, and Welschinger (2010). In particular, the non-local length, the damage model, and the crack insertion properties have to be determined. The elastic properties are taken as such, see Table 2.3. The damage model is parametrised in order to fit the one-dimensional homogeneous response related to the phase field approach,

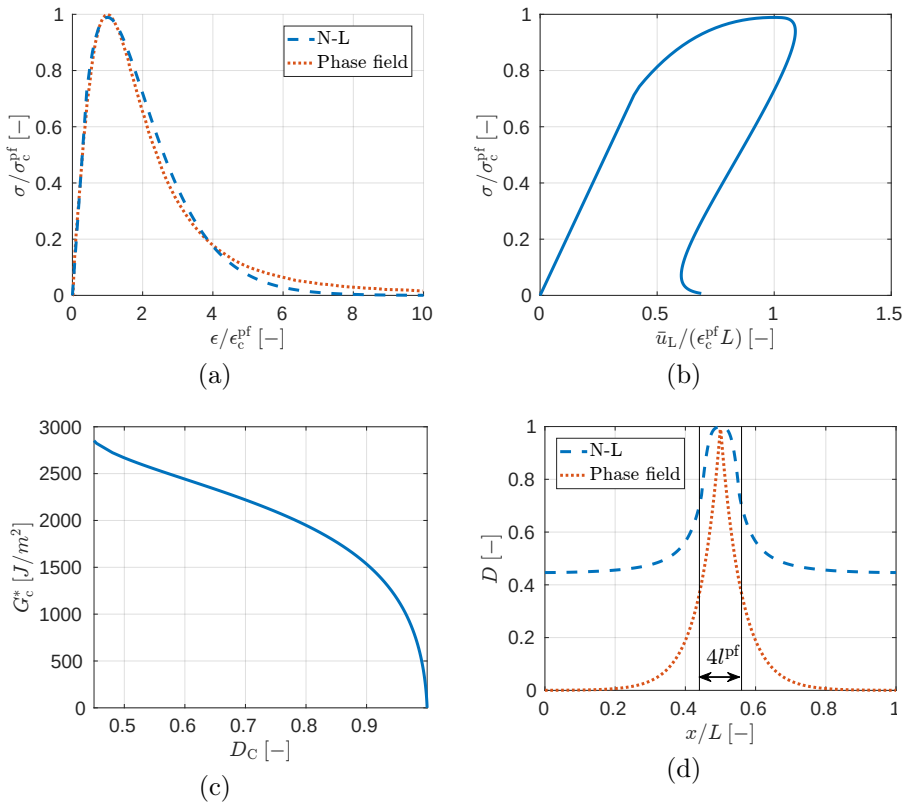

FIGURE 2.17: Stress response (a) for a one-dimensional uniform strain state, and (b) with localisation in a bar of length $L = 0.5$ [mm]. (c) Corresponding fracture energy which remains to be dissipated in terms of crack damage insertion. (d) Comparison between non-local damage profile and the idealised phase field one; the vertical dashed lines represent the phase field smeared crack of width $4l^{pf}$.

TABLE 2.3: Material properties for the single edge notched specimen tests.

Elastic model properties, Eq. (2.38):		
Young's Modulus	E	210.0 [GPa]
Poisson ratio	ν	0.3
Damage model properties, Eq.(2.44):		
Initial damage threshold	κ_i	0.0049
Failure equivalent strain	κ_c	0.49
Damage exponents	α	40.0
	β	0.0
Non-local model properties, Eq.(2.42):		
Non-local length	l_c	16.5×10^{-3} [mm]

TABLE 2.4: Damage to crack transition parameters for the single edge notched specimen tests.

Crack insertion criterion, Eq. (2.75):		
Effective critical stress	$\hat{\sigma}_{\mathrm{c}}$	5.9 [GPa]
Critical damage	D_{c}	0.85
Mixed-mode ratio	β_{c}	0.87
Cohesive band model:		
Band thickness	h_{b}	89.1×10^{-3} [mm]

see the discussion of de Borst and Verhoosel (2016), and in particular the peak stress $\hat{\sigma}_{\mathrm{c}}^{\mathrm{pf}}$ and strain $\hat{\epsilon}_{\mathrm{c}}^{\mathrm{pf}}$, with

$$\hat{\sigma}_{\mathrm{c}}^{\mathrm{pf}} = \frac{9}{16}\sqrt{\frac{G_{\mathrm{c}}E}{6l^{\mathrm{pf}}}} = 1.42 \ \ [\mathrm{GPa}] \quad \text{and} \quad \hat{\epsilon}_{\mathrm{c}}^{\mathrm{pf}} = \sqrt{\frac{G_{\mathrm{c}}}{6l^{\mathrm{pf}}E}} = 0.012. \tag{2.90}$$

To this end, the power damage law (2.45) is still used and the value of the exponent β is fixed to a small value while a high value of α is chosen in order to ensure a fast stress decrease followed by a long tail, which characterises the one-dimensional homogeneous phase field response. The two remaining parameters κ_{i} and κ_{c} are then computed in order to ensure that the stress peak corresponds to the values given by (2.90). The chosen material damage parameters are summarised in Table 2.3 and the corresponding stress-strain response is compared to the one-dimensional homogeneous phase field response in Fig. 2.17a.

The non-local length is now calibrated using the previously described one-dimensional simulations with localisation, see Section 2.2, with the aim of recovering the same fracture energy G_{c} after localisation than the phase field model input. The resulting non-local length is evaluated to be $l_{\mathrm{c}} = 16.5 \times 10^{-3}$ [mm]. The corresponding one-dimensional stress response –with localisation– of the non-local damage model is represented on Fig. 2.17b. The fracture energy after localisation onset –which corresponds to a damage value $D_{\mathrm{soft}} = 0.44$ as obtained from (2.67)– in terms of the crack damage insertion is shown on Fig. 2.17c. Clearly the critical energy release rate evaluated at softening onset is close to $G_{\mathrm{c}} = 2700 \ \ [\mathrm{J/m^2}]$. Moreover, it can be seen in Fig. 2.17d that a comparable damage diffusion between the non-local damage model and the phase field solution is recovered. In this figure, the damage profile obtained at failure is compared with the idealised damage distribution of the phase field method, which reads (de Borst and Verhoosel, 2016)

$$D^{\mathrm{pf}}(x) = \exp\left(-|x|/2l^{\mathrm{pf}}\right). \tag{2.91}$$

Apart from the non-zero homogeneous damage value of the non-local model, both distributions exhibit a similar damage spread.

For the damage to crack transition parameters, the insertion effective stress is chosen so that the crack initiation appears around a damage value $D_{\mathrm{c}} = 0.85$. The cohesive band thickness h_{b} is still computed as determined in Section 2.2 and is equal to $h_{\mathrm{b}} = 5.4l_{\mathrm{c}}$.

2.4.2.2 Tensile tests

The tensile boundary conditions applied on the plate of width $W = 1$ [mm] are represented on Fig. 2.18a. A prescribed vertical displacement is applied on the top edge while lateral edges remain traction-free. Both bottom and top edges are constrained along the horizontal direction. The specimen is meshed with 2779 quadratic triangular elements as shown on Fig. 2.18b. Small elements, with a characteristic size of 0.01 [mm] are used along the expected

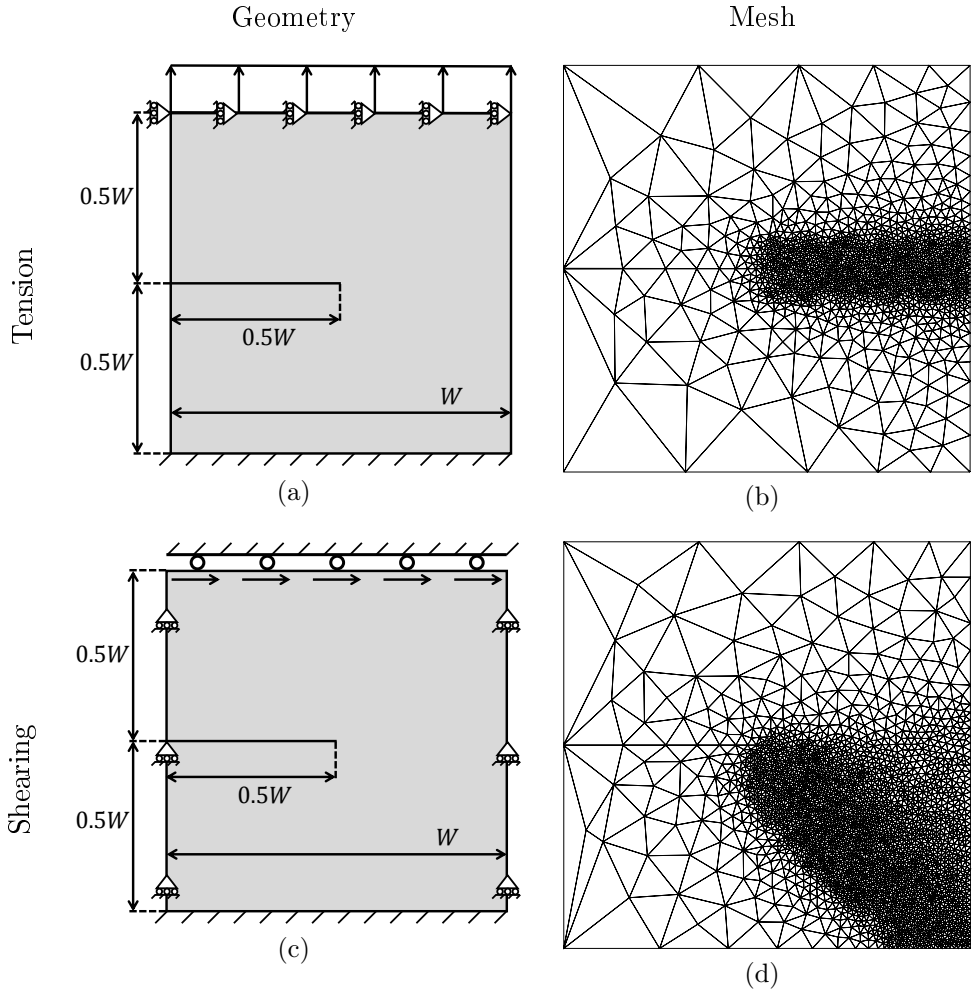

FIGURE 2.18: The single edge notched specimen geometries (left) of width $W = 1$ [mm] with their boundary conditions and the corresponding meshes (right) for the tensile (a-b) and shear cases (c-d).

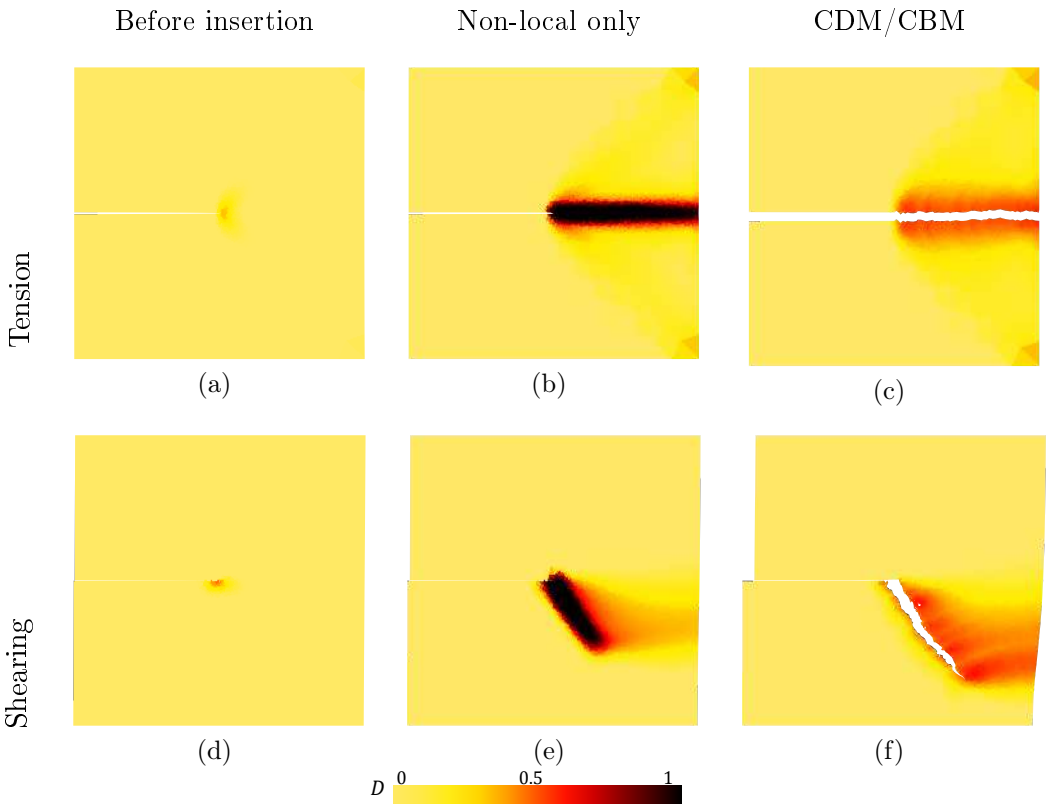

FIGURE 2.19: Damage field (a and d) before crack insertion and at material failure for (b and e) the pure non-local case and (c and f) the CDM/CBM frameworks. Displacements have been magnified for the hybrid CDM/CBM in order to visualise the crack path. The damage distributions are reported for the tensile (first row) and shear (second row) tests.

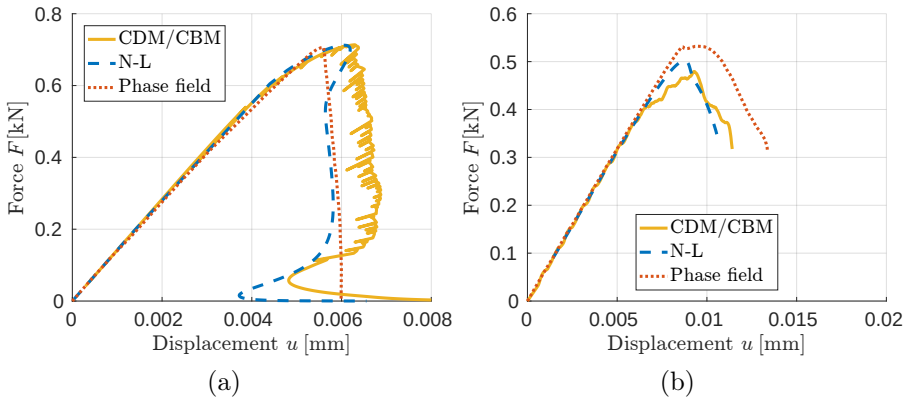

FIGURE 2.20: Loading force (for a 1 [mm]-thick plate) *vs.* displacement evolution for the pure non-local, the hybrid CDM/CBM framework, and the phase field framework for (a) the tensile test and (b) the shear test.

crack path while coarser ones are used away from it. The system is solved using the implicit scheme detailed in Section 2.3.2.1 completed with a path-following method due to possible snap-back.

The damage field before first crack insertion is developing at the crack tip, as shown on Figs. 2.19a and is then growing along the symmetry plane. The distributions obtained at material failure for the pure non-local model and the hybrid CDM/CBM framework are shown respectively on Fig. 2.19b and 2.19c. The close-to-one damage band obtained with the non-local model is replaced by a crack for the hybrid CDM/CBM framework which is surrounded by lower damage values. The force evolution for both models is now compared on Fig. 2.20a with the results reported for the phase field method by Miehe, Hofacker, and Welschinger (2010). Comparable results are obtained with the three methods: failure appears for the same peak load although it is slightly delayed for the non-local model and the hybrid CDM/CBM framework. For this application the pure non-local simulation exhibits a stronger snap-back than the hybrid CDM/CBM framework because of the spreading of the highly damage zone arising with the former method.

2.4.2.3 Shear tests

Shear boundary conditions are now applied on the previous specimen as illustrated in Fig. 2.18a: vertical displacements are constrained along all edges while a horizontal one is applied on the top one. The mesh, represented on Fig. 2.18b, consists of 5362 quadratic triangles. Small elements (around 0.01 [mm] characteristic size) are located along a 45°-line along which the crack is assumed to propagate. The zone of refinement is wide enough in order to correctly describe the damage diffusion and to avoid any artificial guidance of the crack. The hybrid CDM/CBM system is solved using the coupled explicit-implicit integration scheme detailed in Section 2.3.2.3.

Figure 2.19d illustrates the damage distribution developing below the crack tip before first crack insertion. The distributions obtained for the same remaining force as the reported phase field results (Miehe, Hofacker, and Welschinger, 2010) are shown on Figs. 2.19e and 2.19f for respectively the pure non-local model and the hybrid CDM/CBM framework. The close-to-one damage band obtained with the non-local model is replaced by a crack kinking for the hybrid CDM/CBM framework. Note that because the hybrid CDM/CBM simulations have been conducted with a dynamic explicit integration, some single dust elements arise during the crack opening and have been removed for visualisation purpose. The force *vs.* displacement histories of both models are compared on Fig. 2.20b with the phase field predictions reported in Miehe, Hofacker, and Welschinger (2010). Note that because the hybrid CDM/CBM simulations have been conducted with a dynamic explicit integration, the resulting numerical oscillations have been filtered for visualisation purpose. The reached peak load is about 10 % lower when using non-local CDM although the softening strain is the same than with the phase-field model. However the peak stress of the phase field simulations is sensitive to the associated length scale l^{pf}.

2.4.3 Compact tension specimen test

This test was studied experimentally (Geers, 1997) using the non-local CDM developed by Geers et al. (1998). The Compact Tension Specimen (CTS) tests were carried out on short glass-fiber-reinforced polypropylene. The geometry is shown in Fig. 2.21a with the dimensions $W = 50$ [mm], $a_{\mathrm{n}} = 10$ [mm] and the thickness $t = 3.8$ [mm].

The specimen is meshed with 5099 10-node 3D tetrahedral elements and partitioned between 16 processors as shown in Fig. 2.21b. Quadratic shape functions are used to approximate both the displacement and the non-local fields. Due to the symmetry of the system, only one

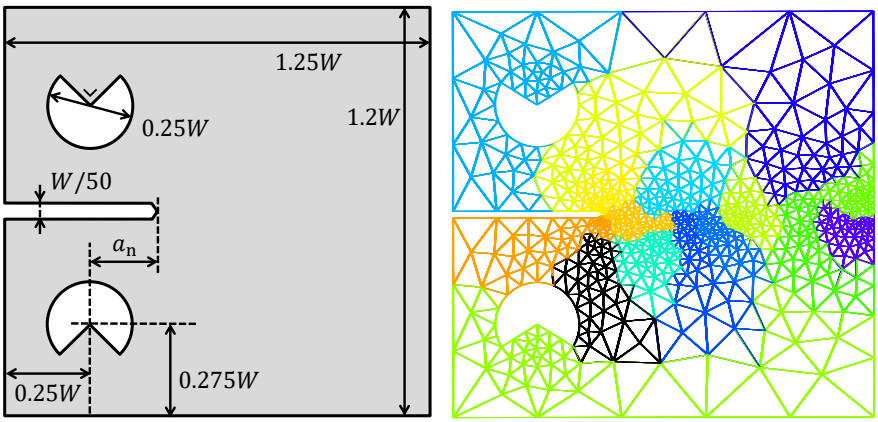

(a) (b)

FIGURE 2.21: (a) The Compact-Tension Specimen geometry with $W = 50$ [mm], $a_n = 10$ [mm] and $t = 3.8$ [mm]; and (b) its partitioned mesh.

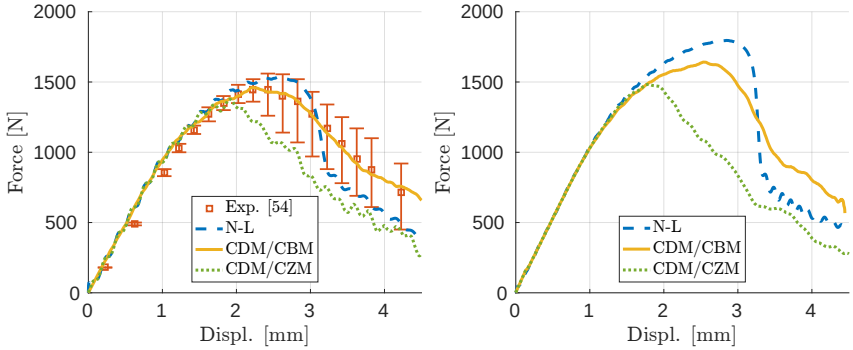

(a) (b)

FIGURE 2.22: Loading force *vs.* pin displacement evolutions with the hybrid CDM/CBM framework, the CDM/CZM, the pure non-local, and the experimental measurements in (a) plane stress state and (b) in plane strain state.

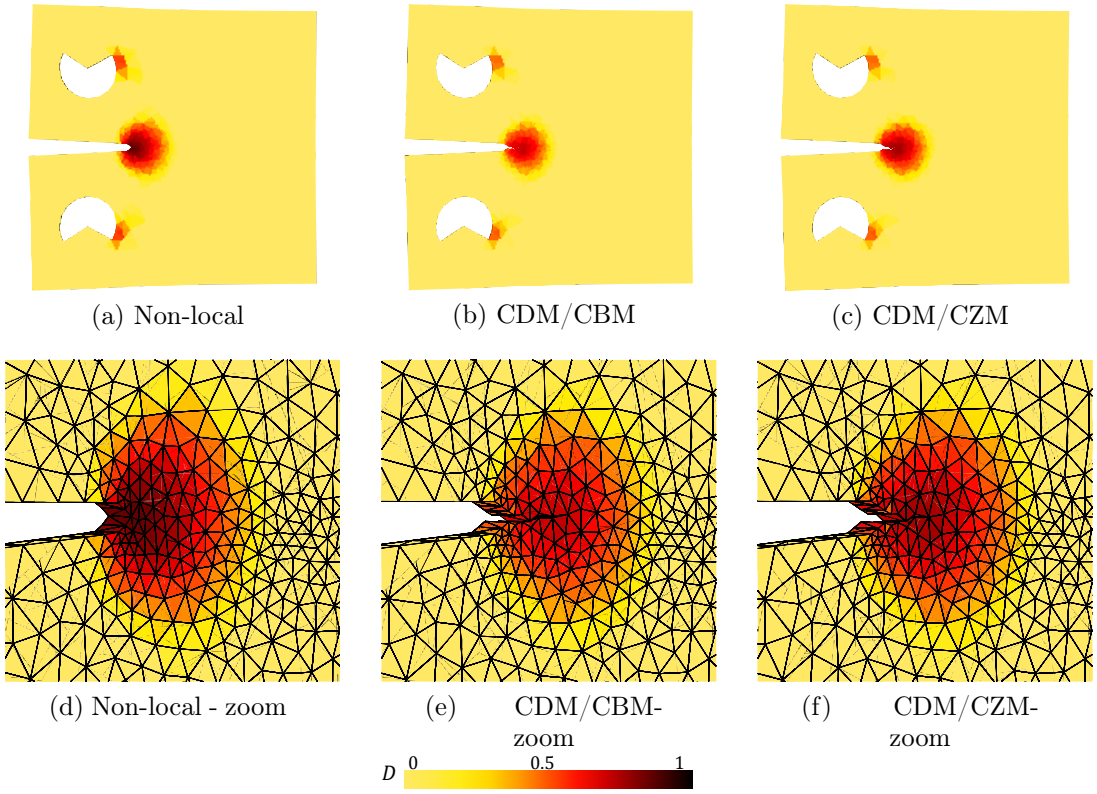

(a) Non-local (b) CDM/CBM (c) CDM/CZM

(d) Non-local - zoom (e) CDM/CBM-zoom (f) CDM/CZM-zoom

FIGURE 2.23: Damage field at pin displacement $d = 2$ [mm] in the whole sample (top) and zoomed on the process zone (bottom) for the non-local model (left), the hybrid CDM/CBM (centre) and the hybrid CDM/CZM (right).

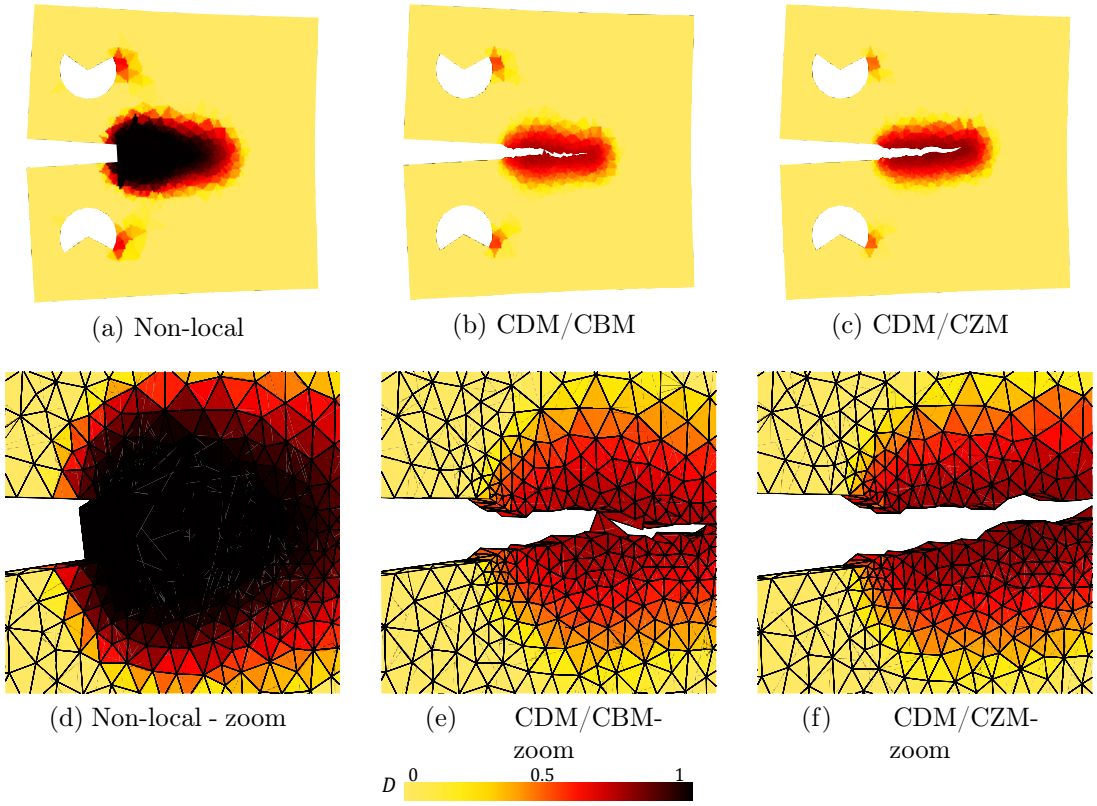

(a) Non-local (b) CDM/CBM (c) CDM/CZM

(d) Non-local - zoom (e) CDM/CBM-zoom (f) CDM/CZM-zoom

FIGURE 2.24: Damage field at pin displacement $d = 4$ [mm] in the whole sample (top) and zoomed on the process zone (bottom) for the non-local model (left), the hybrid CDM/CBM (centre) and the hybrid CDM/CZM (right).

half of the thickness is effectively modelled. A finer mesh is used near the expected crack path while a coarser one is used in other mesh regions. To apply the loading, loading pins are modelled with quarters of cylinder of higher stiffness ($E = 30$ [GPa]). The displacements of the pin axes are controlled in the vertical direction and constrained in the other ones, while axes rotation is left free. The material properties are reported in Table 2.1. The system is solved using the coupled explicit-implicit integration scheme detailed in Section 2.3.2.3.

The hybrid CDM/CBM framework is applied on the CTS in plane stress and compared with the experimental results (Geers, 1997), the CDM/CZM, and with the pure non-local model. The sample is also simulated in plane strain state using the three frameworks. The set of damage to crack transition parameters is given in Table 2.2.

The loading force with respect to the displacements between both pins (evaluated for the full thickness), is represented in Fig. 2.22a in the plane stress state for the three different frameworks and for the experiment results (Geers, 1997) [5]. Note that because the simulations have been conducted with a dynamic explicit integration, the resulting numerical oscillations have been filtered for visualisation purpose. If numerical and experimental results are globally consistent, the CBM shows a better agreement with the experimental results than the other frameworks. A small discrepancy is observed from the beginning between the numerical results and the experimental ones, which is not due to the numerical framework, but to the finite element model itself since it is present even in the elastic part of the simulation. Indeed, the loading pins introduce a spurious compliance as there are not perfectly rigid; They should be replaced by rigid springs in compression without tension stiffness. Before crack insertion, no difference is observed between the frameworks as expected. After the crack is inserted for both the CDM/CBM framework and the CDM/CZM framework, the curve predicted by the non-local model keeps increasing, resulting in an higher peak value. Then, the force quickly drops, due to the high damage spreading within the specimen. For the hybrid frameworks, both models allow a transition without unacceptable loss of energy. However, a much better agreement is obtained with the CDM/CBM than the CDM/CZM. Indeed, taking advantage of the constant value of the band thickness, the CBM does not suffer from the variation of damage value at which crack insertions occur. A similar analysis can be carried out in the plane strain state shown in Fig. 2.22b.

The corresponding damage fields in the plate stress configuration are presented in the deformed configuration in Figs. 2.23a to 2.23f for a pin displacement $d = 2$ [mm]. At this point, all models predict similar results. A crack has just started to propagate in the hybrid frameworks while damage is slightly more developed for the non-local model. For $d = 4$ [mm] in Figs. 2.24a to 2.24f, the simulation involving only the non-local model suffers from high element distortions and spurious damage spreads from either side of the physical crack surface as no limiting mechanism was introduced. This non-physical spread reaches the free border of the initial notch. This problem is avoided with the hybrid frameworks where damage development is replaced by a crack propagation. In this case, the damage zone thickness remains constant along the crack path.

2.5 Conclusions

In this chapter, we have established a numerical framework based on a non-local CDM/CBM transition in the context of small displacements and in the elastic regime. The diffuse damage stage is modelled by a non-local implicit damage model. Its purpose is to simulate the diffuse degradation process without suffering from a mesh dependency. However, large distortions appear inside the most damaged elements, which induce spurious damage spreading and numerical problems. To overcome this issue, a discontinuity is inserted through a cohesive band

[5] The experimental results from Geers (1997) have been translated in order to pass by the origin.

to simulate the last failure stage. It consists in a cohesive model with a finite thickness along which the stress is assumed to be uniform. The strains in this band are reconstructed by enhancing the neighbouring bulk strain by the cohesive jump. From this strain tensor, the bulk material damage constitutive law is used in its local way to compute the corresponding traction forces.

In order to assess the framework behaviour, energetic equivalence and consistency have been discussed with a 1D case in a semi-analytical way. It appears that, once the softening onset is reached, the dissipated energy depends directly on the characteristic lengths, i.e the non-local length and/or the cohesive band thickness. A relation between the non-local length and the cohesive thickness can be drawn such that the energy dissipated by the hybrid CDM/CBM framework corresponds to the energy that would be dissipated by a pure non-local damage simulation, independently of the damage parameters or the insertion point.

Moreover, several numerical examples, in 2D and 3D, demonstrated the expected numerical properties of the proposed scheme. In particular, we have demonstrated the interest of the CBM over the classical CZM and pure non-local model. Indeed, CBM includes triaxiality effects during the final stage and avoids spurious damage diffusion. Moreover, the method actually inherits from the scalability of the DG-scheme. Finally, we have shown that the CDM/CBM method is able to produce comparable results to the phase field approach.

Furthermore, we have also validated the method by comparison with experimental results published by Geers (1997). Meanwhile, we have again confirmed the benefits of the CDM/CBM framework compared to the cohesive zone or the pure non-local model. Indeed, only the CDM/CBM framework is able to dissipate the correct amount of energy in regards to the experimental results obtained on a CTS specimen.

However, the involved material behaviour is here limited to the elastic regime in small strains. In the next chapter, we will extend the framework to more elaborated models in the context of large deformations. In particular, elasto-plastic porous models will be addressed. Despite the higher complexity of the constitutive relations, we will show that the numerical properties demonstrated here are conserved. Moreover, we will explore the possibility to use different crack criteria and a coalescence behaviour after the crack insertion.

Chapter 3

Transition framework applied to ductile materials[1]

In order to illustrate the transition framework on a simplified case, an elastic damage model was used in the previous chapter inside the hybrid framework. Henceforth, the hybrid framework will be adapted in this chapter to a family of more complex constitutive models which represent in a realistic way the ductile failure process in metals (and in some polymers exhibiting cavitations): the porous plasticity models.

As schematised on Fig. 3.1, the ductile damage process usually starts with the nucleation of voids or microcracks which add up to the pre-existing porosity resulting from the metal processing inside the metal matrix (step 1). The porosity then grows by plastic flow spread inside the matrix (step 2). This process ends with strain and damage localisation due to shear bands or to microscopic voids coalescing together (Tekoglu, Hutchinson, and Pardoen, 2015). This leads to the coalescence stage where the plastic flow is localised between voids (step 3). This mechanisms then leads to the initiation and propagation of a macroscopic crack, and ultimately to material failure.

Several CDM have been developed to model this failure process. The simplest approaches consist in using the progressive accumulation of damage to determine when failure occurs (Brünig, Gerke, and Schmidt, 2018; Johnson and Cook, 1985, e.g.). On the one hand, in the phenomenological CDM approaches as the Lemaitre et al. (2009) damage model, the damage growth induces the material properties degradation until failure. On the other hand, some models rely on the evolution of micromechanical-based behaviour. Among them, the Gurson model family has been developed since the seventies to take into account the effects of microscopic porosity evolution in metals. Only the main relevant stages in its fifty years of existence are recalled here: Benzerga et al. (2016), Besson (2010), and Pineau, Benzerga, and Pardoen (2016) have provided complete reviews of the extensions and applications. Inspired from Rice and Tracey (1969) solutions for an isolated void, the initial model of Gurson (1977) addressed the problem of the plastic yield locus of spherical voids in a rigid perfectly-plastic matrix. The model derivation implies an associated plastic flow. It also gives an evolution law derived from mass conservation for the porosity or void volume fraction parameter f_{V}.

The model was modified over the years to improve the accuracy of the void growth prediction and to represent fracture and coalescence using phenomenological arguments. This first led to a widely used and studied version, the so-called Gurson-Tvergaard-Needleman (GTN) model (Tvergaard and Needleman, 1984). In this version, void nucleation has been added to the damage growth rate (Chu and Needleman, 1980), accounting for the strain and/or stress-controlled contribution of newly created voids. The source of these new voids mostly comes from the debonding or the cracking of inclusions inside the material. Heuristic parameters were also added to the yield surface to better fit finite element (FE) void cell simulations (Tvergaard, 1981). Finally, a corrected effective porosity was introduced in the yield surface

[1] This chapter is an adapted version of the paper Leclerc et al. (2020)

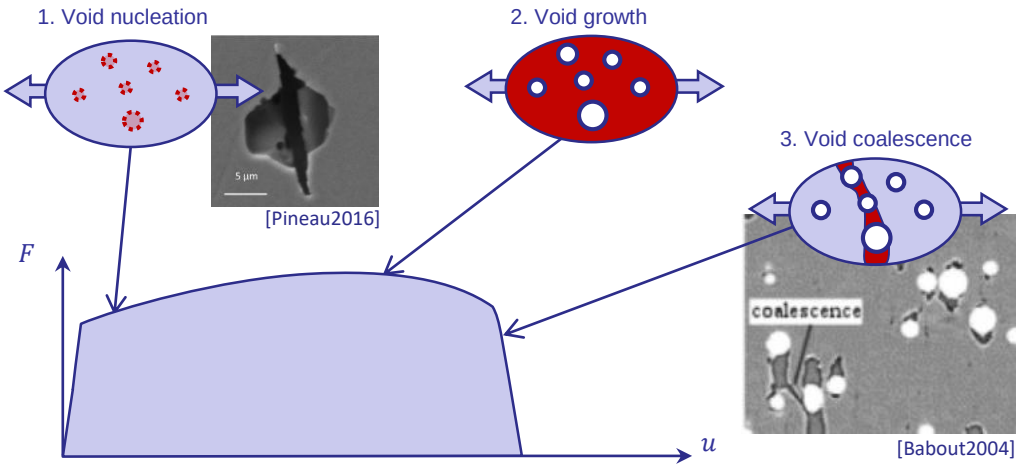

FIGURE 3.1: Schematic representation of a typical ductile failure process by (1) nucleation, (2) growth and (3) coalescence of voids, accompanied of SEM (scanning electron microscope) pictures.

near fracture to obtain realistic ductilities (Tvergaard and Needleman, 1984). This substitution aims at phenomenologically mimicking the damage growth acceleration due to void coalescence.

However, as shown by physical observations (see Fig. 3.1) and FE cell simulations by Koplik and Needleman (1988), the coalescence is more than just an abrupt void growth acceleration: the latter is rather a consequence of the former. Indeed, after a relatively diffuse plasticity and damage development stage, material behaviour suddenly changes into a localised deformation state. Plastic flow also shifts direction. All these changes indicate the onset of a new deformation mechanism. Therefore, even if a proper calibration of the GTN model can crudely reproduce the coalescence, a different model is more suitable to describe and to predict this physical process (Benzerga and Leblond, 2010; Besson, 2010; Brocks, Sun, and Hönig, 1995). In this context, different coalescence modes compete depending on the loading conditions and the micromechanical structure as recently studied by Brünig, Gerke, and Schmidt (2018), Cortese, Nalli, and Rossi (2016), Liu, Wong, and Guo (2016), Pineau, Benzerga, and Pardoen (2016), and Roth et al. (2018). The most investigated mode is by internal necking: the onset of coalescence is reached when plastic flow localises inside the intervoid ligament oriented normal to the main loading direction. The model of Thomason (1985a,b) provides a criterion based on the plastic limit-load of the intervoid ligament under tensile-dominated stress. This approach was then completed with evolution laws for the geometrical parameters of voids by Pardoen and Hutchinson (2000) and Benzerga (2002), and a fully analytical expression of the criterion was derived by Benzerga and Leblond (2014). Furthermore, by rewriting the criterion for arbitrary orientation, Pardoen and Hutchinson (2000) and Benzerga, Besson, and Pineau (2004) derived a yield surface for the coalescence stage to be used in combination to a void growth surface. However, shear stress effects are not accounted for by the Thomason model. To address this issue, Tekoglu, Leblond, and Pardoen (2012) and Torki et al. (2017) have extended the Thomason approach combining shear and tensile loading. Reddi, Areej, and Keralavarma (2019) have obtained similar results by using the multi-surface yield criterion developed by Keralavarma and Chockalingam (2016) and Keralavarma (2017). Furthermore, Nguyen, Pardoen, and Noels (2020) have proposed a non-local multi-surface model introducing a shear-dominated coalescence surface in addition to the growth and internal necking coalescence modes. In addition, Torki (2019) unified both void growth and coalescence criteria under tensile and shear conditions in a unique but complex yield function. Besides, Leblond and Mottet (2008) have provided an approximate solution of the problem

by substituting the central voided region of the RVE by a sandwich made of von Mises and porous layers.

Despite numerous studies and extensions, namely for coalescence representation as those previously described, the Gurson model stays inaccurate for low or vanishing stress triaxiality. In particular, the GTN model predicts the absence of void growth (i.e. or damage) in pure shear. Ignoring the void shape is only acceptable for initial spherical voids and inclusions at high triaxiality as they tend to more or less maintain their initial shape in these conditions. However, under shear-dominated stress, it is no more the case. To overcome this issue, Nahshon and Hutchinson (2008) added a shear-induced porosity growth term, henceforth enabling void growth without hydrostatic pressure in the Gurson model. Besides, Rousselier (1987) and Tanguy and Besson (2002) extracted the so-called Rousselier model, in which the yield surface is close to Gurson one but derived from a thermodynamic approach, which also generates damage growth under pure shear. The inclusion of void shape and evolution requires more complex constitutive models including void shape effect and evolution. For instance, the Gologanu model (Gologanu, Leblond, and Devaux, 1993, 1994) adapts the Gurson analysis for spheroidal voids. High porosity effects can also be accurately captured by combining the Gurson model with the mean-field homogenisation as recently done by El Ghezal and Doghri (2018).

As the framework developed in chapter 2 is intended to be applied to ductile elastoplastic solids, a porous plastic model as described by Besson (2009) is chosen as constitutive material model. It includes the description of the void growth and coalescence steps, but also the nucleation model developed by Chu and Needleman (1980) and the shear-induced growth term proposed by Nahshon and Hutchinson (2008). The model is set in a finite-strain setting. Moreover, it is developed under a non-local form as initiated by Reusch, Svendsen, and Klingbeil (2003b). Once again, this is of particular importance when considering a physically-based crack initiation criterion which can be met in the strain softening stage, as it will be shown in this chapter. Furthermore, the monolithic resolution of the combined non-local damage-cohesive band model requires the evaluation in a closed form of the weak formulation and material models tangent operators.

Two coalescence models are then successively considered. On the one hand, with a view to the model verification with the analyses by Huespe et al. (2012), a numerical crack insertion criterion is used to detect crack initiation at loss of ellipticity, whilst the crack opening is governed by an adequate calibration of the Gurson model parameters. On the other hand, following the work by Pardoen and Hutchinson (2000), a physically-based Thomason (1985a,b) criterion is used as crack insertion criterion, and the coalescence model is used as governing law of the cohesive band model (CBM) to model the crack opening.

The outline of this chapter is as follows. The continuous non-local damage model is first presented in Section 3.1. Afterwards, the damage to crack transition is introduced with the cohesive band model in Section 3.2. In particular, the questions of the crack insertion criterion and the cohesive band thickness are addressed. The practical implementation of the current framework is detailed in Section 3.3. The weak form is deduced from the strong form of equations and is then discretised following the DG-formulation. The numerical time integration is also discussed. Finally, Section 3.4 is devoted to illustrating the framework capability to correctly represent the ductile fracture process. In particular, the results obtained by a local form of the porous elastoplastic model and by introducing a crack at loss of ellipticity are shown to be in good agreement with the results by Huespe et al. (2012). Then, we show that when considering the Thomason criterion and the Thomason coalescence model to govern respectively the crack initiation and propagation, the model is able to reproduce slant and cup-cone failure modes in plane-strain specimens and axisymmetric bars, smooth and notched ones, respectively. These complex failure patterns driven by shearing are herein captured, and by Huespe et al. (2012) as well, because of the shear stress state obtained by the free surface

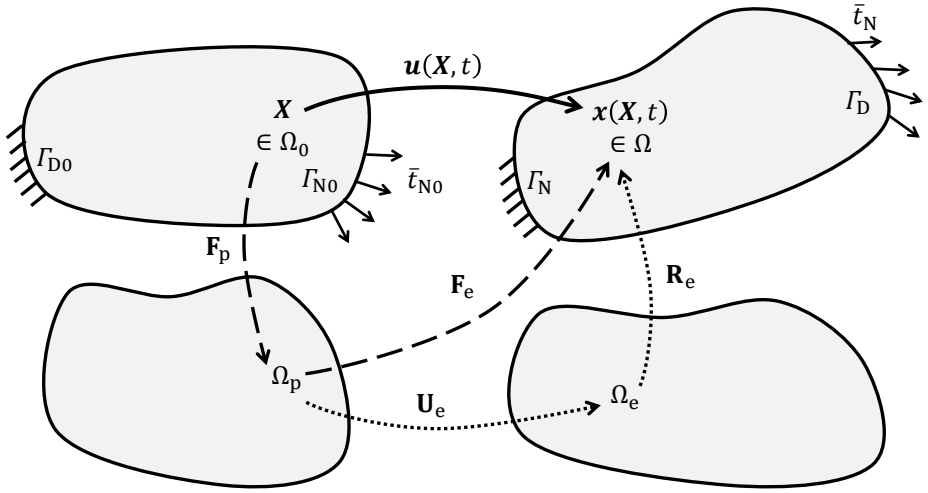

FIGURE 3.2: A material body in the reference configuration Ω_0 (left) and in the current configuration Ω (right). The body displacement field is defined by $\boldsymbol{u}(\boldsymbol{X},t)$ and the corresponding deformation gradient $\mathbf{F}$ between both configurations is decomposed into a plastic part $\mathbf{F}^{\mathrm{p}}$ followed by an elastic part $\mathbf{F}^{\mathrm{e}}$. The elastic part is also split in a symmetric stretch part $\mathbf{U}^{\mathrm{e}}$ and a rotational part $\mathbf{R}^{\mathrm{e}}$.

creation during crack propagation. Without the introduction of the crack, these patterns do not appear with a purely CDM model unless shear necking is considered in the yield surface as suggested by Nguyen, Pardoen, and Noels (2020) and Reddi, Areej, and Keralavarma (2019).

3.1 Non-local continuum damage mechanics for porous plasticity

In this section, the non-local continuum damage mechanics framework applied to porous plasticity is developed, combining the formulations of Reusch, Svendsen, and Klingbeil (2003a,b) and Besson (2009). Cracks are ignored in this description and the body is assumed to be continuous as it is during the early damage stage. At first, the governing equations of the mechanical problem is provided. Then, a hyperelastic non-local porous plastic model is presented before being particularised to the considered deformation mechanisms.

Consider a material body $\Omega_0 \subset \mathcal{R}^3$ in the reference configuration at time $t = 0$ and its boundary surface Γ_0 as shown on Fig. 3.2. The external surface Γ_0 is divided into a Dirichlet part Γ_{D0} where displacements are prescribed, and a Neumann part Γ_{N0} where the traction force is prescribed. This surface partition satisfies $\Gamma_{\mathrm{D0}} \cap \Gamma_{\mathrm{N0}} = \Gamma_0$ and $\Gamma_{\mathrm{D0}} \cup \Gamma_{\mathrm{N0}} = \emptyset$. Ω and Γ denote respectively the counterparts of Ω_0 and Γ_0 in the current configuration at a given time $t > 0$. During this time evolution, the displacement of a material particle initially at the position $\boldsymbol{X} \in \Omega_0$ to the current spatial position $\boldsymbol{x}(\boldsymbol{X},t) \in \Omega$ is defined by $\boldsymbol{u}(\boldsymbol{X},t) = \boldsymbol{x}(\boldsymbol{X},t) - \boldsymbol{X}$. The derivative of the current spatial position in terms of the material configuration, or in other words, the deformation gradient, is

$$\mathbf{F} = \frac{\partial \boldsymbol{x}}{\partial \boldsymbol{X}} = \mathbf{I} + \frac{\partial \boldsymbol{u}}{\partial \boldsymbol{X}}\,, \tag{3.1}$$

with its Jacobian $J = \det \mathbf{F} > 0$, and $\mathbf{I}$ the second-order identity tensor.

The linear momentum conservation, under large deformation setting over the body Ω with respect to the reference configuration, is given by

$$\rho_0 \ddot{\boldsymbol{u}} = \boldsymbol{\nabla}_0 \cdot \mathbf{P}^{\mathrm{T}} + \boldsymbol{b}_0 \text{ on } \Omega_0, \tag{3.2}$$

where ρ_0 is the initial mass density, $\boldsymbol{\nabla}_0$ is the gradient operator with respect to the reference configuration, $\mathbf{P}$ the first Piola-Kirchhoff (PK1) stress tensor and $\boldsymbol{b}_0$ is the volumetric external force vector (per unit of volume).

Boundary conditions are applied on the reference surface: prescribed displacement $\bar{\boldsymbol{u}}$ and traction surface $\bar{\boldsymbol{t}}_{\mathrm{N0}}$ are respectively applied on the Dirichlet boundary Γ_{D0} and on the Neumann boundary Γ_{N0}:

$$\begin{array}{ll} \boldsymbol{u} = \bar{\boldsymbol{u}} & \text{on } \Gamma_{\mathrm{D0}}, \text{ and} \\ \mathbf{P} \cdot \boldsymbol{N} = \bar{\boldsymbol{t}}_{\mathrm{N0}} & \text{on } \Gamma_{\mathrm{N0}}, \end{array} \tag{3.3}$$

with $\boldsymbol{N}$ the unit surface normal in the reference configuration and $\bar{\boldsymbol{t}}_{\mathrm{N0}}$ defined in the current configuration per unit surface in the reference configuration.

The boundary value problem defined by Eqs. (3.2) and (3.3) is completed by a material constitutive law which defines the evolution of the stress tensor $\mathbf{P}$ at time t as

$$\mathbf{P}\left(t\right) = \mathbf{P}\left(\mathbf{F}\left(t\right), \tilde{\boldsymbol{Z}}\left(t\right); \boldsymbol{Z}\left(t'\right), t' \in [0, t]\right), \tag{3.4}$$

in terms of the actual deformation gradient $\mathbf{F}$ and in terms of a set of local internal variables $\boldsymbol{Z}$ and, potentially, a set of non-local $\tilde{\boldsymbol{Z}}$ internal variables representative of all the material history and path-dependence.

Non-local variables are introduced to avoid mesh-dependency. An implicit non-local gradient approach (Peerlings et al., 1996), equivalent to a micromorphic approach (Aldakheel, 2017; Forest, 2009), is preferred as it is truly non-local in contrast to an explicit form, as demonstrated by Peerlings et al. (2001). Moreover, the treatment of complex geometries and boundaries is here more simple and convenient than with an equivalent integral approach (Leclerc et al., 2018; Peerlings et al., 2001; Wu, Becker, and Noels, 2014, see Sections 2.1 and 2.2). Practically, some local variables $Z_i \in \boldsymbol{Z}$ are replaced by their non-local counterpart $\tilde{Z}_i \in \tilde{\boldsymbol{Z}}$, following

$$\tilde{\dot{Z}}_i - \boldsymbol{\nabla}_0 \cdot \left(\mathbf{C}_{\mathrm{l}i} \cdot \boldsymbol{\nabla}_0 \tilde{\dot{Z}}_i\right) = \dot{Z}_i \text{ on } \Omega_0, \tag{3.5}$$

where $\mathbf{C}_{\mathrm{l}i}$ is a semi-positive definite symmetric tensor associated to the non-local variable $\tilde{Z}_i$. In an isotropic case, it reduces to $l_{\mathrm{c}}^2\mathbf{I}$; l_{c} being the associated characteristic diffusion length. Using $\tilde{Z}_i$ as in Eq. (2.16) or its time derivative in Eq. (3.5) is analogous since the diffusion equation is linear. However, this latter formulation avoids numerical instabilities due to evolving boundary conditions during the crack propagation presented in Section 3.2. Furthermore, the local model is recovered when the characteristic length vanishes.

The differential equation (3.5) is completed by a natural boundary condition:

$$\left(\mathbf{C}_{\mathrm{l}i} \cdot \boldsymbol{\nabla}_0 \tilde{\dot{Z}}_i\right) \cdot \boldsymbol{N} = 0 \text{ on } \Gamma_0. \tag{3.6}$$

3.1.1 Hyperelastic-based elasto-plastic material model

No assumption has been made yet on the material behaviour (3.4). First, as shown on Fig. 3.2, a classical multiplicative decomposition of the deformation gradient (3.1) for elasto–plastic materials is assumed

$$\mathbf{F} = \mathbf{F}^{\mathrm{e}} \cdot \mathbf{F}^{\mathrm{p}}, \tag{3.7}$$

with $\mathbf{F}^{\mathrm{e}}$ the elastic part of $\mathbf{F}$ and $\mathbf{F}^{\mathrm{p}}$, the plastic one. The tensor $\mathbf{F}^{\mathrm{e}}$ can be separated into a rotational part $\mathbf{R}^{\mathrm{e}}$ and a symmetric part $\mathbf{U}^{\mathrm{e}}$ as $\mathbf{F}^{\mathrm{e}} = \mathbf{R}^{\mathrm{e}} \cdot \mathbf{U}^{\mathrm{e}}$. The corresponding Jacobian

terms are defined by

$$J = \det \mathbf{F}\,,\ J^{\mathrm{p}} = \det \mathbf{F}^{\mathrm{p}}\,,\ \text{and}\ J^{\mathrm{e}} = \det \mathbf{F}^{\mathrm{e}}\,, \tag{3.8}$$

and the corresponding right Cauchy strain tensors read

$$\mathbf{C} = \mathbf{F}^{\mathrm{T}} \cdot \mathbf{F}\,,\ \mathbf{C}^{\mathrm{p}} = \mathbf{F}^{\mathrm{pT}} \cdot \mathbf{F}^{\mathrm{p}}\,,\ \text{and}\ \mathbf{C}^{\mathrm{e}} = \mathbf{F}^{\mathrm{eT}} \cdot \mathbf{F}^{\mathrm{e}}\,. \tag{3.9}$$

The macro-mechanical response of the material, represented by the first Piola-Kirchhoff stress tensor $\mathbf{P}$, is determined by postulating the existence of a thermodynamic potential in terms of the conjugate strain tensor $\mathbf{F}$. Assuming an isothermal rate-independent hyperelastic behaviour, the related free energy ψ can be written under the form $\psi\left(\mathbf{C}^{\mathrm{e}}, \boldsymbol{Z}\right)$. We note that is it possible to derive a non-local version of the thermodynamic setting, see the work of Forest (2009), Nguyen, Pardoen, and Noels (2020), and Peerlings et al. (1996, e.g.).

From the Clausius-Duhem inequality, the evolution of the free energy is bounded by

$$\mathbf{P} : \dot{\mathbf{F}} - \dot{\psi}\left(\mathbf{C}^{\mathrm{e}}, \boldsymbol{Z}\right) \geq 0\,, \tag{3.10}$$

where the equality is obtained in case of reversible elastic increment. We now assume that the free energy is split by $\psi = \psi^{\mathrm{e}} + \psi^{\mathrm{p}}$ into two contributions : an elastic reversible part $\psi^{\mathrm{e}}\left(\mathbf{C}^{\mathrm{e}}\right)$ and a plastic irreversible part $\psi^{\mathrm{p}}\left(\boldsymbol{Z}\right)$. The equation (3.10) is developed by using Eq. (3.7) and the form of ψ as

$$\mathbf{P} : \dot{\mathbf{F}}^{\mathrm{e}} \cdot \mathbf{F}^{\mathrm{p}} - \frac{\partial \psi^{\mathrm{e}}}{\partial \mathbf{C}^{\mathrm{e}}} : \dot{\mathbf{C}}^{\mathrm{e}} + \mathbf{P} : \mathbf{F}^{\mathrm{e}} \cdot \dot{\mathbf{F}}^{\mathrm{p}} - \sum_k \frac{\partial \psi^{\mathrm{p}}}{\partial Z_k} \dot{Z}_k \geq 0\,, \tag{3.11}$$

or, after developing $\dot{\mathbf{C}}^{\mathrm{e}}$, as

$$\left(\mathbf{P} - 2\mathbf{F}^{\mathrm{e}} \cdot \frac{\partial \psi^{\mathrm{e}}}{\partial \mathbf{C}^{\mathrm{e}}} \cdot \mathbf{F}^{\mathrm{p-T}}\right) : \dot{\mathbf{F}}^{\mathrm{e}} \cdot \mathbf{F}^{\mathrm{p}} + \mathbf{P} : \mathbf{F}^{\mathrm{e}} \cdot \dot{\mathbf{F}}^{\mathrm{p}} - \sum_k \frac{\partial \psi^{\mathrm{p}}}{\partial Z_k} \dot{Z}_k \geq 0\,. \tag{3.12}$$

Assuming an arbitrary elastic reversible increment, the inequality becomes

$$\left(\mathbf{P} - 2\mathbf{F}^{\mathrm{e}} \cdot \frac{\partial \psi^{\mathrm{e}}}{\partial \mathbf{C}^{\mathrm{e}}} \cdot \mathbf{F}^{\mathrm{p-T}}\right) : \dot{\mathbf{F}}^{\mathrm{e}} \cdot \mathbf{F}^{\mathrm{p}} = 0\,,\ \forall\, \dot{\mathbf{F}}^{\mathrm{e}}\,. \tag{3.13}$$

The PK1 stress is therefore defined by

$$\mathbf{P} = 2\mathbf{F}^{\mathrm{e}} \cdot \frac{\partial \psi^{\mathrm{e}}}{\partial \mathbf{C}^{\mathrm{e}}} \cdot \mathbf{F}^{\mathrm{p-T}}\,, \tag{3.14}$$

and the Clausius-Duhem inequality (3.10) reduces to

$$\mathbf{P} : \mathbf{F}^{\mathrm{e}} \cdot \dot{\mathbf{F}}^{\mathrm{p}} - \sum_k \frac{\partial \psi^{\mathrm{p}}}{\partial Z_k} \dot{Z}_k \geq 0\,. \tag{3.15}$$

Using a logarithmic strain measure, i.e.,

$$\mathbf{E} = \frac{1}{2} \ln \mathbf{C}\,,\ \mathbf{E}^{\mathrm{e}} = \frac{1}{2} \ln \mathbf{C}^{\mathrm{e}}\,,\ \text{and}\ \mathbf{E}^{\mathrm{p}} = \frac{1}{2} \ln \mathbf{C}^{\mathrm{p}}\,, \tag{3.16}$$

the following isotropic quadratic potential is chosen

$$\psi^{\mathrm{e}}(\mathbf{C}^{\mathrm{e}}) = \frac{K}{2} \left[\mathrm{tr}\left(\mathbf{E}^{\mathrm{e}}\right)\right]^2 + G\left(\mathbf{E}^{\mathrm{e}}\right)^{\mathrm{dev}} : \left(\mathbf{E}^{\mathrm{e}}\right)^{\mathrm{dev}}\,, \tag{3.17}$$

where $K = \frac{E}{3(1-2\nu)}$ and $G = \frac{E}{2(1+\nu)}$ are the bulk and shear modulii of the material, in terms of

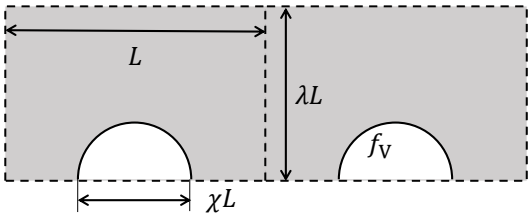

FIGURE 3.3: A representative volume cell and its geometrical description defined by the porosity f_V, the cell aspect ratio λ and the ligament ratio χ.

the Young's modulus E and the Poisson ratio ν. Finally, applying the definition of ψ (3.17) to Eq. (3.14) gives

$$\mathbf{P} = K\mathrm{tr}\left(\mathbf{E}^{\mathrm{e}}\right)\mathbf{F}^{-\mathrm{T}} + 2G\mathbf{F}^{\mathrm{e}}\cdot\mathbf{C}^{\mathrm{e}-1}\cdot\left(\mathbf{E}^{\mathrm{e}}\right)^{\mathrm{dev}}\cdot\mathbf{F}^{\mathrm{p}-\mathrm{T}}\,. \tag{3.18}$$

The Cauchy stress tensor $\boldsymbol{\sigma}$ is linked to the PK1 tensor by the classical relation

$$\mathbf{P} = J\boldsymbol{\sigma}\cdot\mathbf{F}^{-\mathrm{T}} = \boldsymbol{\kappa}\cdot\mathbf{F}^{-\mathrm{T}}\,, \tag{3.19}$$

introducing $\boldsymbol{\kappa}$ as the Kirchhoff stress tensor. This latter is obtained from the rewriting of Eq. (3.18):

$$\boldsymbol{\kappa} = K\mathrm{tr}\left(\mathbf{E}^{\mathrm{e}}\right)\mathbf{I} + 2G\mathbf{F}^{\mathrm{e}}\cdot\mathbf{C}^{\mathrm{e}-1}\cdot\left(\mathbf{E}^{\mathrm{e}}\right)^{\mathrm{dev}}\cdot\mathbf{F}^{\mathrm{eT}}\,. \tag{3.20}$$

Because $\mathbf{U}^{\mathrm{e}}$ and $\mathbf{E}^{\mathrm{e}}$ commute, one has

$$\boldsymbol{\kappa} = \mathbf{R}^{\mathrm{e}}\cdot\left(\underbrace{K\mathrm{tr}\left(\mathbf{E}^{\mathrm{e}}\right)}_{p_\tau}\mathbf{I} + \underbrace{2G\left(\mathbf{E}^{\mathrm{e}}\right)^{\mathrm{dev}}}_{\boldsymbol{\tau}^{\mathrm{dev}}}\right)\cdot\mathbf{R}^{\mathrm{eT}} = \mathbf{R}^{\mathrm{e}}\cdot\boldsymbol{\tau}\cdot\mathbf{R}^{\mathrm{eT}}\,, \tag{3.21}$$

introducing p_τ as the pressure, $\boldsymbol{\tau}^{\mathrm{dev}}$ as the deviatoric part of the corotational Kirchhoff stress tensor $\boldsymbol{\tau}$. The equivalent stress τ^{eq} is defined as $\tau^{\mathrm{eq}} = \sqrt{\frac{3}{2}\boldsymbol{\tau}^{\mathrm{dev}} : \boldsymbol{\tau}^{\mathrm{dev}}}$.

3.1.2 Porous elasto-plastic material model

The elastic domain in the stress space is limited by a yield function ϕ. As already announced at the beginning of this chapter, two modes of plastic deformation compete. Plastic flow can be diffuse in the matrix: it is described by the Gurson model. Conversely, it can be localised between voids during the coalescence phase, it is then described by the GTN model (i.e. GTN in the accelerated void growth phase) or by the Thomason model. By combining both modes of plastic flow, a full porous model is finally obtained.

3.1.2.1 Generalities

The description of the damage mechanism at the microscale is similar to Besson (2009): defects are assimilated as a periodic arrangement of spherical voids that stay spherical during the entire process and grow inside a J2-plastic matrix. A representative volume consists in a cuboid cell with a void at its centre as depicted on Fig. 3.3. Its geometrical state is fully described by 3 parameters: the porosity f_V, the relative ligament ratio χ and the cell aspect ratio λ. The porosity f_V corresponds to the void volume fraction while the ligament ratio χ is the ratio of the void diameter to the distance between neighbouring voids. Although more complex and accurate microscopic descriptions exist, this one is chosen because of its simplicity and isotropy.

Yield surface and plastic flow Whatever the selected plasticity model, the yield condition $\phi \leqslant 0$ is here expressed in terms of the corotational Kirchhoff stress $\boldsymbol{\tau}$ instead of the classical Kirchhoff stress $\boldsymbol{\kappa}$. As the rate of the plastic flow is assumed to be irrotational, this change does not modify the plasticity model while it simplifies its implementation thanks to the straightforward relation between the stress tensor $\boldsymbol{\tau}$ and the logarithmic strain tensor $\mathbf{E}^{\mathrm{e}}$. The yield criterion depends also on the matrix yield stress. At this level, a classical J2-plastic model is assumed with an isotropic hardening curve $\tau_{\mathrm{Y}}(p)$ in terms of the equivalent matrix plastic strain measure p. The yield surface is also dependent on the microscopic state, represented by some *effective* variables $\hat{\boldsymbol{Z}}$. The definition of the effective variables allows the transition from a non-local framework governed by $\tilde{\boldsymbol{Z}}$ to a local one governed by $\boldsymbol{Z}$ without discontinuity. In particular, this set sums up the cumulative damage evolution during the homogeneous non-local damage process and, in a second time, during the local crack propagation.

The macroscopic yield criterion, based on stress invariants, is therefore written under the mathematical form

$$\phi = \phi\left(\tau^{\mathrm{eq}}, p_\tau, \tau_{\mathrm{Y}}, \hat{\boldsymbol{Z}}\right) \leqslant 0\,. \tag{3.22}$$

If the yield criterion (3.22) is satisfied, plastic flow occurs, following an associated flow rule. As the plastic flow is irrotational,

$$\dot{\mathbf{F}}^{\mathrm{p}} \cdot \mathbf{F}^{\mathrm{p}-1} = \dot{\gamma}\mathbf{N}^{\mathrm{p}} = \dot{\gamma}\frac{\partial \phi}{\partial \boldsymbol{\tau}}\,, \tag{3.23}$$

where $\dot{\gamma} \geqslant 0$ is the macro-scale plastic multiplier associated with the plastic normal $\mathbf{N}^{\mathrm{p}}$. Since ϕ depends only on the first and second invariants of the stress tensor, the normal $\mathbf{N}^{\mathrm{p}}$ can be separated into a volumetric (or pressure) and a deviatoric part by stating $N^{\mathrm{d}} = \frac{\partial \phi}{\partial \tau^{\mathrm{eq}}}$ and $N^{\mathrm{q}} = \frac{\partial \phi}{\partial p_\tau}$ following

$$\dot{\gamma}\mathbf{N}^{\mathrm{p}} = \dot{\gamma}\frac{\partial \phi}{\partial \tau^{\mathrm{eq}}}\frac{\partial \tau^{\mathrm{eq}}}{\partial \boldsymbol{\tau}} + \dot{\gamma}\frac{\partial \phi}{\partial p_\tau}\frac{\partial p_\tau}{\partial \boldsymbol{\tau}} = \dot{\gamma}N^{\mathrm{d}}\frac{3\boldsymbol{\tau}^{\mathrm{dev}}}{2\tau^{\mathrm{eq}}} + \dot{\gamma}N^{\mathrm{q}}\frac{1}{3}\mathbf{I} = \dot{d}\frac{3\boldsymbol{\tau}^{\mathrm{dev}}}{2\tau^{\mathrm{eq}}} + \dot{q}\frac{1}{3}\mathbf{I}\,, \tag{3.24}$$

where $\dot{d}$ and $\dot{q}$ respectively stand for $\dot{\gamma}N^{\mathrm{d}}$ and for $\dot{\gamma}N^{\mathrm{q}}$.

Non-local variables Concerning the introduction of the non-locality, the model focuses on diffusing one variable: $\tilde{Z} = \tilde{f}_{\mathrm{V}}$, as previously proposed by Reusch, Svendsen, and Klingbeil (2003a,b). The related effective variable involved in the yield condition (3.22), $\hat{f}_{\mathrm{V}}$, is simply obtained through

$$\dot{\hat{f}}_{\mathrm{V}} = \dot{\tilde{f}}_{\mathrm{V}}\,, \tag{3.25}$$

as long as the non-local model is used. Otherwise, its evolution is linked to the local porosity growth (see Section 3.2.1 and in particular, Fig. 3.7 for more details). The porosity is foreseen because this key parameter plays a key role in the entire damage and failure process. Among all other possibilities, Nguyen, Pardoen, and Noels (2020) adopted three non-local variables corresponding to the three plastic variables (d, q, p) in order to capture void growth, coalescence by necking and shearing in a mesh-independent way. Another possible choice could be to diffuse the couple (f_{V}, χ). Thereby, each mechanism will have its non-local key parameter associated with a corresponding non-local length. However, in this work, mesh-dependency during the coalescence stage, linked to χ, is already avoided by introducing a cohesive band model.

Internal variables evolution The macroscopic deformation induces a microscopic structure modification and therefore, the evolution of the internal variables. The (local) porosity

evolution $\dot{f}_{\mathrm{V}}$ is governed by different contributions all linked to the plastic flow

$$\dot{f}_{\mathrm{V}} = \dot{f}_{\mathrm{V}_{\mathrm{nucl}}} + \dot{f}_{\mathrm{V}_{\mathrm{growth}}} + \dot{f}_{\mathrm{V}_{\mathrm{shear}}} \,. \tag{3.26}$$

Newly nucleated porosity $\Delta\dot{f}_{\mathrm{V}_{\mathrm{nucl}}}$ add to the already present porosity. This nucleation results from precipitate debonding or cracking during plastic flow. Among several existing models, a strain-controlled relation, presented by Chu and Needleman (1980), is used here: $\dot{f}_{\mathrm{V}_{\mathrm{nucl}}} = A_{\mathrm{n}}(p)\,\dot{p}$. Plastic flow also induces the growth of the voids $\dot{f}_{\mathrm{V}_{\mathrm{growth}}}$. As the macroscopic plastic flow is not purely deviatoric while the matrix volume is left unchanged by mass conservation, macroscopic plastic volume change induces a porosity growth rate $\dot{f}_{\mathrm{V}_{\mathrm{growth}}} = (1 - f_{\mathrm{V}})\,\mathrm{tr}\,(\dot{\gamma}\mathbf{N}^{\mathrm{p}})$. Furthermore, the term $\dot{f}_{\mathrm{V}_{\mathrm{shear}}}$ results from the extended Gurson model proposed by Nahshon and Hutchinson (2008). It corresponds to an apparent or effective void growth due to a shear-induced shape change with

$$\dot{f}_{\mathrm{V}_{\mathrm{shear}}} = B_{\mathrm{n}}(\zeta)\,\frac{\boldsymbol{\tau}^{\mathrm{dev}} : \dot{\gamma}\mathbf{N}^{\mathrm{p}}}{\tau^{\mathrm{eq}}} f_{\mathrm{V}} \,. \tag{3.27}$$

In this expression, $B_{\mathrm{n}}(\zeta) = k_\omega\left(1 - \zeta^2\right)$ is a growth coefficient, controlled by the shear damage coefficient k_ω, that vanishes under axisymmetric stress state and which is maximal under a combination of pure shear stress with an hydrostatic contribution. Nielsen and Tvergaard (2010) enhanced the coefficient by including a dependence on the triaxiality. Dunand and Mohr (2011) called $\zeta\left(\boldsymbol{\tau}^{\mathrm{dev}}\right)$ the normalised third invariant

$$\zeta = \frac{27\det\boldsymbol{\tau}^{\mathrm{dev}}}{2\tau^{\mathrm{eq}3}} \,. \tag{3.28}$$

The equivalent matrix plastic strain measure p is obtained by considering the energetic equivalence between both micro and macroscales:

$$(1 - f_{\mathrm{V}_0})\,\tau_{\mathrm{Y}}\dot{p} = \boldsymbol{\tau} : \dot{\gamma}\mathbf{N}^{\mathrm{p}} \,, \tag{3.29}$$

where f_{V_0}, the initial porosity, is used since Eq. (3.29) is stated here with respect to the reference volume[2].

The ligament size ratio χ is determined, following Besson (2009), from

$$\chi = \left[\frac{3}{2}\hat{f}_{\mathrm{V}}\lambda\right]^{\frac{1}{3}} \,, \tag{3.30}$$

where $\hat{f}_{\mathrm{V}}$ is the effective porosity and the evolution of λ is given by $\dot{\lambda} = \kappa\lambda\dot{p}$. By integration, one thus has

$$\chi = \left[\frac{3}{2}\hat{f}_{\mathrm{V}}\lambda_0\right]^{\frac{1}{3}} \exp\left(\frac{1}{3}\kappa p\right) \,, \tag{3.31}$$

where λ_0 is the initial value of λ, the ratio of the void spacing arrangement, and where κ is a fitting parameter (Besson, 2009).

The relationship (3.22) now needs to be particularised to the different considered porous plastic models while the features and equations common to each one have been presented.

[2] Rigorously speaking, this relation should also consider the nucleated porosity framed in the reference configuration, but this contribution is neglected herein.

3.1.2.2 The Gurson micro-mechanical growth porous plastic model

The void growth phase is described by the Gurson model for spherical voids (Tvergaard and Needleman, 1984). The corresponding yield surface ϕ_{G} is given by

$$\phi_{\mathrm{G}}\left(\tau^{\mathrm{eq}},\, p_{\tau},\, \tau_{\mathrm{Y}},\, \hat{f}_{\mathrm{V}}\right) = \left(\frac{\tau^{\mathrm{eq}}}{\tau_{\mathrm{Y}}}\right)^{2} + 2\hat{f}_{\mathrm{V}} q_1 \cosh\left(\frac{3q_2 p_{\tau}}{2\tau_{\mathrm{Y}}}\right) - q_3^2 \left(\hat{f}_{\mathrm{V}}\right)^{2} - 1 \leqslant 0\,, \tag{3.32}$$

where q_1, q_2 and q_3 are the Gurson parameters. Initially added by Tvergaard (1981), these parameters are determined to better fit cell experiments (Faleskog, Gao, and Fong Shih, 1998) and heuristically include several effects (e.g. strain hardening, void shape).

3.1.2.3 Phenomenological coalescence porous plastic model

After accumulation of plastic deformation and void growth, plastic flow localises between matrix voids, indicating the onset of void coalescence. It results in a significant change of the growth rate and overall deformation behaviour. This process can be described here by a phenomenological approach. In this case, the Gurson yield surface (3.32) is modified by a corrected porosity $f_{\mathrm{V}}^{\star}$ (Reusch, Svendsen, and Klingbeil, 2003b; Tvergaard and Needleman, 1984) once the coalescence criterion is met. The new coalescence yield surface is written

$$\phi_{\mathrm{GTN}} = \phi_{\mathrm{G}}\left(\tau^{\mathrm{eq}}, p_{\tau}, \tau_{\mathrm{Y}}, f_{\mathrm{V}}^{\star}\right) \leqslant 0\,, \tag{3.33}$$

where the corrected effective porosity $f_{\mathrm{V}}^{\star}$ is modified after the onset of coalescence by

$$f_{\mathrm{V}}^{\star}\left(\hat{f}_{\mathrm{V}}\right) = \begin{cases} \hat{f}_{\mathrm{V}} & \text{if } \hat{f}_{\mathrm{V}} \leqslant f_{\mathrm{V_C}}\,; \\ f_{\mathrm{V_C}} + \underbrace{\dfrac{f_{\mathrm{V_f}}^{\star} - f_{\mathrm{V_C}}}{f_{\mathrm{V_f}} - f_{\mathrm{V_C}}}}_{\delta_{\mathrm{GTN}}} \left(\hat{f}_{\mathrm{V}} - f_{\mathrm{V_C}}\right) & \text{if } f_{\mathrm{V_C}} < \hat{f}_{\mathrm{V}} \leqslant f_{\mathrm{V_f}}\,; \\ f_{\mathrm{V_f}}^{\star} & \text{if } \hat{f}_{\mathrm{V}} > f_{\mathrm{V_f}}\,. \end{cases} \tag{3.34}$$

In Eq. (3.34), $f_{\mathrm{V_C}}$ corresponds to the porosity value at the onset of coalescence. The value is fixed in advance and can either be considered as a material parameter (Tvergaard and Needleman, 1984) or corresponds to the value predicted by a more physically-based coalescence criterion as the Thomason model (Guzmán et al., 2018; Zhang, Thaulow, and Ødegård, 2000). After the onset of coalescence, the effective porosity growth rate $\dot{f}_{\mathrm{V}}^{\star}$ increases due to the acceleration rate δ_{GTN}. The porosity growth continues until the porosity $f_{\mathrm{V_f}}$ at final failure, and $f_{\mathrm{V_f}}^{\star}$ the corresponding corrected value, are reached. This coalescence model, besides the coalescence criterion, is defined either by δ_{GTN} or by $f_{\mathrm{V_f}}$. The last remaining parameter, $f_{\mathrm{V_f}}^{\star}$, corresponds to a vanishing yield surface, i.e. $f_{\mathrm{V}}^{\star}\left(f_{\mathrm{V_f}}\right) = f_{\mathrm{V_f}}^{\star} = \frac{q_1 - \sqrt{q_1^2 - q_3^2}}{q_3^2}$.

3.1.2.4 The Thomason micro-mechanical coalescence porous plastic model

Another possibility to describe the coalescence behaviour after its onset is to use a yield surface, representative of the plastic flow process during coalescence. According to the Thomason model (Benzerga and Leblond, 2014; Thomason, 1985a,b), plastic flow occurs inside voids ligaments when the coalescence stress $C_{\mathrm{T}}^{\phi}\tau_{\mathrm{Y}}$, linked to the stress concentration factor C_{T}^{ϕ} (due to void configuration) and the matrix flow stress τ_{Y} inside the localisation zone, is reached (Besson, 2009); i.e., assuming a traction along direction zz, the yield surface reads

$$\tau_{\mathrm{zz}} \leqslant C_{\mathrm{T}}^{\phi}\left(\chi\right)\tau_{\mathrm{Y}}\,. \tag{3.35}$$

Equation (3.35) can be rewritten for any arbitrary orientation (Pardoen and Hutchinson, 2000) in terms of the corotational Kirchhoff stress as

$$\phi_{\mathrm{T}^+} = \frac{2}{3}\tau^{\mathrm{eq}} + p_\tau - C_{\mathrm{T}}^{\phi}(\chi)\,\tau_{\mathrm{Y}} \leqslant 0\,. \tag{3.36}$$

Conversely, plastic flow can also occur in compression, resulting in a supplementary yield surface

$$\phi_{\mathrm{T}^-} = \frac{2}{3}\tau^{\mathrm{eq}} - p_\tau - C_{\mathrm{T}}^{\phi}(\chi)\,\tau_{\mathrm{Y}} \leqslant 0\,. \tag{3.37}$$

In order to ensure a smooth yield surface and remove vertices, Besson (2009) used an interpolation between both ϕ_{T^+} and ϕ_{T^-}, leading finally to

$$\phi_{\mathrm{T}}(\tau^{\mathrm{eq}}, p_\tau, \tau_{\mathrm{Y}}, \chi) = \left[\underbrace{\left(\frac{2}{3}\tau^{\mathrm{eq}} + p_\tau\right)^n}_{\tau_+} + \underbrace{\left(\frac{2}{3}\tau^{\mathrm{eq}} - p_\tau\right)^n}_{\tau_-}\right]^{1/n} - C_{\mathrm{T}}^{\phi}(\chi)\,\tau_{\mathrm{Y}} \leqslant 0\,, \tag{3.38}$$

with n a sufficiently high even integer interpolation exponent to stay close to the original surfaces.

The concentration factor C_{T}^{ϕ} is given in terms of the ligament size ratio χ,

$$C_{\mathrm{T}}^{\phi}(\chi) = \left(1-\chi^2\right)\left[\alpha(1/\chi - 1)^2 + \beta\sqrt{1/\chi}\right]\,, \tag{3.39}$$

where the parameters α and β depend on the strain-hardening exponent h_{exp} and are respectively equal to $0.1 + 0.217h_{\mathrm{exp}} + 4.83h_{\mathrm{exp}}^2$ and 1.24 for $0 \leqslant h_{\mathrm{exp}} \leqslant 0.3$ as calibrated by Pardoen and Hutchinson (2000).

3.1.2.5 A complete porous elastoplastic model: the Gurson-Thomason model

The full porous model is obtained when both diffuse and localised mechanisms are taken into account. First, the "growth" mode and its corresponding yield surface (3.32) is active. Afterwards, the coalescence mode (with the yield surface (3.38)) becomes dominant. During the transition, both modes can be active by considering a two-surface model: at this point, the effective elastic region results in their intersection as shown on Fig. 3.4. The yield condition can be summarised by

$$\phi_{\mathrm{GT}} = \max\left(\phi_{\mathrm{G}}, \phi_{\mathrm{T}}\right) \leqslant 0\,. \tag{3.40}$$

A particular treatment has to be applied to remove surface vertices and to ensure a unique and continuous $\mathbf{N}^{\mathrm{p}}$ between iterations for convergence purpose. Therefore, the management of the intersection of yield surfaces can be done by interpolation (as similarly done for ϕ_{T}) as suggested by Nguyen, Pardoen, and Noels (2020) or by using a cone of normals. A more simple choice is made here: the current active yield surface is selected at the end of the previous time step. This choice is justified because the coalescence surface shrinks faster than the void growth one. Once the coalescence is activated, oscillations between both strain modes are mainly limited to the onset stage.

3.1.3 Numerical integration of the constitutive law

The constitutive material law is integrated numerically following a backward Euler scheme. Before being adapted to the local model in Section 3.1.3.4, the methodology is first presented in the context of the non-local model, i.e. $\hat{\boldsymbol{Z}} = \tilde{\boldsymbol{Z}}$ or in this case $\hat{f}_{\mathrm{V}} = \tilde{f}_{\mathrm{V}}$. The objective

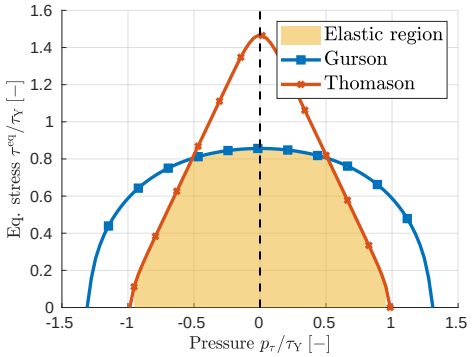

FIGURE 3.4: The two-yield surface model combining the Gurson yield surface ϕ_G and the Thomason yield model ϕ_T in the (p_τ, τ^{eq}) space.

is therefore to compute the stress state and the local internal variables at time t^{n+1} (i.e. $(\mathbf{P}^{n+1}, f_V^{n+1})$) from the known state at the previous discrete time step t^n and from the actual deformation gradient $\mathbf{F}^{n+1}$ and non-local variable $\tilde{f}_V^{n+1}$.

The procedure is summarised in Fig. 3.5. Using Eqs. (3.18) to (3.21), the problem is solved in terms of the $\boldsymbol{\tau}$ stress and the plastic deformation $\mathbf{F}^p$. The time integration on the interval $\left[t^n, t^{n+1}\right]$ is done using a predictor-corrector scheme similar to the one described by Cuitino and Ortiz (1992). At first, the strain increment is assumed to be purely elastic (Section 3.1.3.1). If this predictor stress is outside the yield surface, a plastic flow occurs: a plastic correction is therefore applied following the implicit radial return-like algorithm presented in Section 3.1.3.2. Section 3.1.3.3 provides in details the derivation of the material tangent operators. If a solution cannot be found, a classical linear sub-stepping scheme is used to solve the problem on smaller intervals $\left[t^{n'}, t^{n'+1}\right] \subset \left[t^n, t^{n+1}\right]$. In the following lines, the superscript $n+1$ used to refer to the variables evaluated at this time is omitted for readability purpose.

3.1.3.1 Elastic predictor

During the predictor step, the plastic deformation gradient is kept unchanged $\mathbf{F}_{pr}^{p\,n+1} = \mathbf{F}^{pn}$ as well as the others variables linked to plasticity. The stress state is computed following Eqs. (3.7) to (3.21), leading to the elastic predictor deformation gradient

$$\mathbf{F}_{pr}^{e} = \mathbf{F} \cdot \mathbf{F}_{pr}^{p\,-1}, \tag{3.41}$$

and the strain predictor tensors

$$\mathbf{C}_{pr}^{e} = \mathbf{F}_{pr}^{e\,T} \cdot \mathbf{F}_{pr}^{e} \quad \text{and} \quad \mathbf{E}_{pr}^{e} = \frac{1}{2} \ln\left(\mathbf{C}_{pr}^{e}\right). \tag{3.42}$$

The predictor stress components then read

$$\boldsymbol{\tau}_{pr}^{\,dev} = 2G\left(\mathbf{E}_{pr}^{e}\right)^{dev} \quad \text{and} \quad p_{\tau pr} = K\mathrm{tr}\left(\mathbf{E}_{pr}^{e}\right). \tag{3.43}$$

3.1.3.2 Plastic corrector

The yield condition (3.22) is assessed using the predictor state (3.43). If the criterion is satisfied, the elastic predictor state corresponds to the final one: $\mathbf{F}^p = \mathbf{F}_{pr}^p$ and $\boldsymbol{\tau} = \boldsymbol{\tau}_{pr}$. Otherwise, a plastic correction, which is defined in terms of the predictor state, is needed.

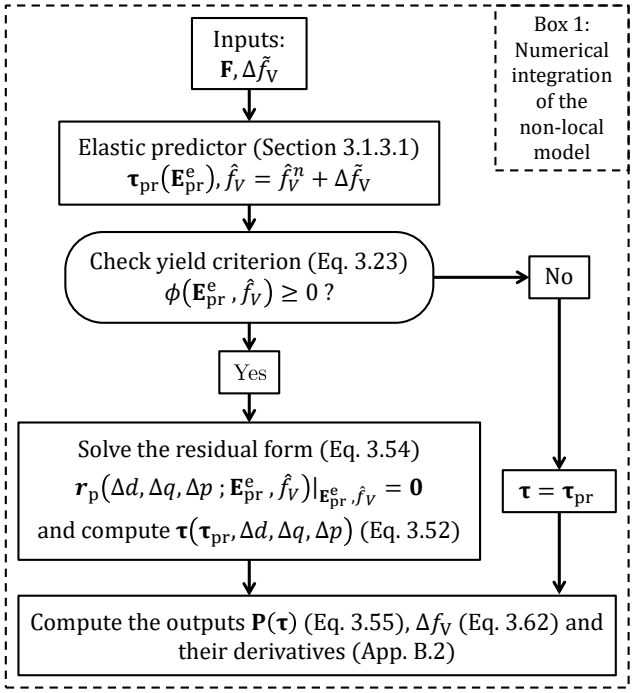

FIGURE 3.5: Numerical integration procedure of the non-local constitutive porous-plastic model (material model level).

Plastic flow and corrector stress The current plastic deformation gradient, re-expressed in terms of the plastic update $\Delta\gamma\mathbf{N}^p$ and of the predictor state, reads

$$\mathbf{F}^p = \exp\left(\Delta\gamma\mathbf{N}^p\right) \cdot \mathbf{F}^p_{pr}\,. \tag{3.44}$$

Using the flow decomposition (3.24), the plastic increment is given by

$$\Delta\gamma\mathbf{N}^p = \Delta d\frac{3\boldsymbol{\tau}^{dev}}{2\tau^{eq}} + \Delta q\frac{1}{3}\mathbf{I}\,, \tag{3.45}$$

where Δd is the increment of the deviatoric macroscopic plastic flow and Δq of the macroscopic volumetric part. The corresponding corrected elastic strain tensors are

$$\begin{array}{rcl} \mathbf{F}^e & = & \mathbf{F} \cdot {\mathbf{F}^p_{pr}}^{-1} \cdot \left[\exp\left(\Delta\gamma\mathbf{N}^p\right)\right]^{-1}, \text{ and} \\ \mathbf{E}^e & = & \mathbf{E}^e_{pr} - \Delta\gamma\mathbf{N}^p\,, \end{array} \tag{3.46}$$

From these equations, the corotational Kirchhoff stress components are computed thanks to Eqs. (3.21) and (3.43), using the flow decomposition (3.45),

$$\left\{\begin{array}{rcl} \boldsymbol{\tau}^{dev} & = & (\boldsymbol{\tau}_{pr})^{dev} - 3G\Delta d\frac{\boldsymbol{\tau}^{dev}}{\tau^{eq}}\,, \\ p_\tau & = & p_{\tau pr} - K\Delta q\,. \end{array}\right. \tag{3.47}$$

This relation directly gives the relationshi between the corrected pressure p_τ in terms of the predictor stress and the volumetric plastic increment Δq. The deviatoric counterpart is obtained by exploiting the chosen form of the decomposition (3.45). Indeed, the predictor and

corrected deviatoric stresses are coaxial as shown by rewriting Eq. (3.47) as

$$\left[\frac{\tau^{\mathrm{eq}}+3G\Delta d}{\tau^{\mathrm{eq}}}\right]\boldsymbol{\tau}^{\mathrm{dev}}=(\boldsymbol{\tau}_{\mathrm{pr}})^{\mathrm{dev}}\ . \tag{3.48}$$

One has also, from the definition of the equivalent stress for both tensors,

$$(\tau^{\mathrm{eq}})^2=\frac{3}{2}(\boldsymbol{\tau})^{\mathrm{dev}}:(\boldsymbol{\tau})^{\mathrm{dev}}=\frac{3}{2}\left[\frac{\tau^{\mathrm{eq}}}{\tau^{\mathrm{eq}}+3G\Delta d}\right]^2(\boldsymbol{\tau}_{\mathrm{pr}})^{\mathrm{dev}}:(\boldsymbol{\tau}_{\mathrm{pr}})^{\mathrm{dev}}=\left[\frac{\tau^{\mathrm{eq}}}{\tau^{\mathrm{eq}}+3G\Delta d}\right]^2\left(\tau_{\mathrm{pr}}^{\mathrm{eq}}\right)^2\ , \tag{3.49}$$

which finally gives, after some manipulations, the sought relation

$$\tau^{\mathrm{eq}}=\tau_{\mathrm{pr}}^{\mathrm{eq}}-3G\Delta d\ \ \text{and}\ \ \boldsymbol{\tau}^{\mathrm{dev}}=\frac{\tau_{\mathrm{pr}}^{\mathrm{eq}}-3G\Delta d}{\tau_{\mathrm{pr}}^{\mathrm{eq}}}(\boldsymbol{\tau}_{\mathrm{pr}})^{\mathrm{dev}}\ . \tag{3.50}$$

Therefore, the corrected stress state after plastic flow reads

$$\tau^{\mathrm{eq}}=\tau_{\mathrm{pr}}^{\mathrm{eq}}-3G\Delta d\,,\ \boldsymbol{\tau}^{\mathrm{dev}}=\frac{\tau_{\mathrm{pr}}^{\mathrm{eq}}-3G\Delta d}{\tau_{\mathrm{pr}}^{\mathrm{eq}}}(\boldsymbol{\tau}_{\mathrm{pr}})^{\mathrm{dev}}\ ,\ \text{and}\ p_\tau=p_{\tau_{\mathrm{pr}}}-K\Delta q\,. \tag{3.51}$$

Furthermore, the deviatoric plastic correction can be simplified by this last equation:

$$\Delta\gamma\mathbf{N}^{\mathrm{pdev}}=\Delta d\frac{3\boldsymbol{\tau}^{\mathrm{dev}}}{2\tau^{\mathrm{eq}}}=\Delta d\frac{3\,(\boldsymbol{\tau}_{\mathrm{pr}})^{\mathrm{dev}}}{2\tau_{\mathrm{pr}}^{\mathrm{eq}}}\,, \tag{3.52}$$

which shows the advantage of this formulation in which the deviatoric part of the normal is constant during the plastic correction.

Solution procedure Using Eqs. (3.44) to (3.52), the corrector step can be summarised as finding, for a given couple $(\mathbf{E}^{\mathrm{e}}_{\mathrm{pr}},\tilde{f}_{\mathrm{V}})$, the macroscopic plastic increments $(\Delta d,\Delta q)$ and the microscopic one Δp that simultaneously satisfy the yield condition (3.22), the normality rule (3.23), the equivalence of the plastic power between scales (3.29), and the evolution laws of the internal variables, or again, as finding the set of plastic increments $\boldsymbol{v}=[\Delta d\ \Delta q\ \Delta p]^{\mathrm{T}}$ that satisfies the residual form

$$\boldsymbol{r}_{\mathrm{p}}\left(\Delta d,\,\Delta q,\,\Delta p;\,\mathbf{E}^{\mathrm{e}}_{\mathrm{pr}},\,\tilde{f}_{\mathrm{V}}\right)\Big|_{\mathbf{E}^{\mathrm{e}}_{\mathrm{pr}},\tilde{f}_{\mathrm{V}}}=\mathbf{0}\,, \tag{3.53}$$

which can solved using an iterative Newton-Raphson procedure. Once the stress state $\boldsymbol{\tau}$ and the plastic strain $\mathbf{F}^{\mathrm{p}}$ are obtained, $\mathbf{P}$ is finally recovered from Eq. (3.18):

$$\mathbf{P}=\mathbf{F}^{\mathrm{e}}\cdot(\boldsymbol{\tau}:\boldsymbol{\mathcal{L}}^{\mathrm{e}})\cdot\mathbf{F}^{\mathrm{p}-\mathrm{T}}\,, \tag{3.54}$$

with $\boldsymbol{\mathcal{L}}^{\mathrm{e}}=\frac{\partial\ln\mathbf{C}^{\mathrm{e}}}{\partial\mathbf{C}^{\mathrm{e}}}$ dependent on the approximation involved when computing the function $\ln\mathbf{C}^{\mathrm{e}}$.

Residual form This residual form $\boldsymbol{r}_{\mathrm{p}}(\boldsymbol{v})$ from Eq. (3.53) is now developed. The first equation $r_{\mathrm{p}1}$ corresponds to the consistency condition associated with the yield surface after plastic correction:

$$r_{\mathrm{p}1}=\phi\left(\tau^{\mathrm{eq}},p_\tau,\tau_{\mathrm{Y}},\hat{\boldsymbol{Z}}\right)\ , \tag{3.55}$$

involving $\tau^{\mathrm{eq}}=\tau_{\mathrm{pr}}^{\mathrm{eq}}-3G\Delta d$ and $p_\tau=p_{\tau_{\mathrm{pr}}}-K\Delta q$. The second equation links the volumetric and the deviatoric plastic increments through the normality rule. From Eqs. (3.24) and (3.45),

one has

$$\Delta\gamma = \frac{\Delta d}{N^{\mathrm{d}}} = \frac{\Delta q}{N^{\mathrm{q}}}\,, \tag{3.56}$$

or again,

$$r_{\mathrm{p}2} = \Delta d N^{\mathrm{q}} - \Delta q N^{\mathrm{d}}\,. \tag{3.57}$$

The third equation results from the integration of Eq. (3.29)

$$(1 - f_{\mathrm{V}_0})\tau_{\mathrm{Y}}\Delta p = \boldsymbol{\tau} : \Delta\gamma \mathbf{N}^{\mathrm{p}}\,. \tag{3.58}$$

Using again Eq. (3.45), one has

$$r_{\mathrm{p}3} = (1 - f_{\mathrm{V}_0})\tau_{\mathrm{Y}}\Delta p - \left(\tau_{\mathrm{pr}}^{\mathrm{eq}} - 3G\Delta d\right)\Delta d - \left(p_{\tau_{\mathrm{pr}}} - K\Delta q\right)\Delta q\,. \tag{3.59}$$

To this set of equations is added the internal variables evolution laws as constraints. For given values of the set $\boldsymbol{v}$, the hardening law $\tau_{\mathrm{Y}} = \tau_{\mathrm{Y}}\left(p^n + \Delta p\right)$ gives the expression of the yield stress in terms of the matrix plastic increment. The porosity growth equation (3.26) is rewritten by including the different growth term expressions and the flow description (3.24)

$$\dot{f}_{\mathrm{V}} = A_{\mathrm{n}}\left(p\right)\dot{p} + \left(1 - f_{\mathrm{V}}\right)\dot{q} + B_{\mathrm{n}} f_{\mathrm{V}}\dot{d}\,. \tag{3.60}$$

After using backward Euler integration, the porosity increment is obtained by

$$\Delta f_{\mathrm{V}} = \frac{\left(1 - f_{\mathrm{V}}^n\right)\Delta q + A_{\mathrm{n}}\left(p\right)\Delta p + B_{\mathrm{n}}(\zeta_{\mathrm{pr}}) f_{\mathrm{V}}^n \Delta d}{1 + \Delta q - B_{\mathrm{n}}(\zeta_{\mathrm{pr}})\Delta d}\,. \tag{3.61}$$

In Eq. (3.61), the Lode variable at the predictor ζ_{pr} is used as the plastic flow leaves it unchanged. Then, the current ligament ratio (3.31) is computed using

$$\chi = \chi^n \left(\frac{\hat{f}_{\mathrm{V}}}{\hat{f}_{\mathrm{V}}^n}\right)^{\frac{1}{3}} \exp\left(\frac{1}{3}\kappa\Delta p\right), \tag{3.62}$$

and the current cell aspect ratio given by

$$\lambda = \lambda^n \exp\left(\kappa\Delta p\right). \tag{3.63}$$

Exponential regulation is applied to smoothly avoid out-of range values on the porosity and the ligament ratio. Equations are also all dimensionless.

The problem is solved using a Newton-Raphson scheme from an initial guess $\boldsymbol{v}^{(0)}$ and the subsequent solutions $\boldsymbol{v}^{(i+1)} = \boldsymbol{v}^{(i)} + \Delta\boldsymbol{v}$ obtained with

$$\mathbf{J}_{\boldsymbol{v}}\left(\boldsymbol{v}^{(i)}\right)\Delta\boldsymbol{v} = -\boldsymbol{r}_{\mathrm{p}}\left(\boldsymbol{v}^{(i)}\right) \tag{3.64}$$

introducing $\mathbf{J}_{\boldsymbol{v}} = \frac{\partial \boldsymbol{r}_{\mathrm{p}}}{\partial \boldsymbol{v}}$, the Jacobian matrix. Its components are

$$\begin{aligned} J_{v1,\Delta d} &= -3GN^{\mathrm{d}}\,, \\ J_{v1,\Delta q} &= -KN^{\mathrm{q}}\,, \\ J_{v1,\Delta p} &= \frac{\partial\phi}{\partial\tau_{\mathrm{Y}}}h + \frac{\partial\phi}{\partial\chi}\frac{\partial\chi}{\partial\Delta p}\,, \end{aligned} \tag{3.65}$$

$$\begin{aligned} J_{v2,\Delta d} &= N^{\mathrm{q}} - 3\Delta d\frac{\partial N^{\mathrm{q}}}{\partial\tau^{\mathrm{eq}}}G + 3\Delta q\frac{\partial N^{\mathrm{d}}}{\partial\tau^{\mathrm{eq}}}G\,, \\ J_{v2,\Delta q} &= -\Delta d\frac{\partial N^{\mathrm{q}}}{\partial p_\tau}K - N^{\mathrm{d}} + \Delta q\frac{\partial N^{\mathrm{d}}}{\partial p_\tau}K\,, \\ J_{v2,\Delta p} &= \Delta d\frac{\partial N^{\mathrm{q}}}{\partial\tau_{\mathrm{Y}}}h - \Delta q\frac{\partial N^{\mathrm{d}}}{\partial\tau_{\mathrm{Y}}}h\,, \end{aligned} \tag{3.66}$$

$$\begin{aligned} J_{v3,\Delta d} &= -\tau^{\mathrm{eq}} + 3G\Delta d\,, \\ J_{v3,\Delta q} &= -p_\tau + K\Delta q\,, \\ J_{v3,\Delta p} &= (1-f_{\mathrm{V}_0})\,(\tau_{\mathrm{Y}} + h\Delta p)\;, \end{aligned} \tag{3.67}$$

where h corresponds to $\frac{\partial \tau_{\mathrm{Y}}}{\partial p}$. ϕ, N^{d}, N^{q}, and their derivatives with respect to τ^{eq}, p_τ, τ_{Y} and other internal variables for the involved strain mechanisms are specified in Appendix B.1 in order to complete the procedure.

3.1.3.3 Material linearisation

The constitutive model needs to provide the material tangent operators. Practically, these are obtained by linearising the output of the material law $(\mathbf{P}, f_{\mathrm{V}})$, given by Eqs. (3.54) and (3.26) (see the integral form in Appendix B.1) in terms of the input $(\mathbf{F}, \tilde{f}_{\mathrm{V}})$. Using the chain rule and tensorial calculus, the problem can be re-expressed in terms of the derivatives of the plastic increments $\boldsymbol{v}$. In this purpose, the residual vector (3.53) is linearised in terms of the predictor strain $\mathbf{E}^{\mathrm{e}}_{\mathrm{pr}}$ and the porosity $\tilde{f}_{\mathrm{V}}$:

$$\dot{\boldsymbol{r}}_{\mathrm{p}}\left(\boldsymbol{v};\, \mathbf{E}^{\mathrm{e}}_{\mathrm{pr}},\, \tilde{f}_{\mathrm{V}}\right) = \mathbf{0} = \frac{\partial \boldsymbol{r}_{\mathrm{p}}}{\partial \boldsymbol{v}}\dot{\boldsymbol{v}} + \frac{\partial \boldsymbol{r}_{\mathrm{p}}}{\partial \mathbf{E}^{\mathrm{e}}_{\mathrm{pr}}}\dot{\mathbf{E}}^{\mathrm{e}}_{\mathrm{pr}} + \frac{\partial \boldsymbol{r}_{\mathrm{p}}}{\partial \tilde{f}_{\mathrm{V}}}\dot{\tilde{f}}_{\mathrm{V}} = \mathbf{0}\,, \tag{3.68}$$

from which the derivatives can be easily extracted following the definition of the Jacobian matrix $\mathbf{J}_{\boldsymbol{v}} = \frac{\partial \boldsymbol{r}_{\mathrm{p}}}{\partial \boldsymbol{v}}$ explicited in Section 3.1.3.2, with

$$\frac{\partial \boldsymbol{v}}{\partial \mathbf{E}^{\mathrm{e}}_{\mathrm{pr}}} = -{\mathbf{J}_{\boldsymbol{v}}}^{-1}\frac{\partial \boldsymbol{r}_{\mathrm{p}}}{\partial \mathbf{E}^{\mathrm{e}}_{\mathrm{pr}}} \quad \text{and} \quad \frac{\partial \boldsymbol{v}}{\partial \tilde{f}_{\mathrm{V}}} = -{\mathbf{J}_{\boldsymbol{v}}}^{-1}\frac{\partial \boldsymbol{r}_{\mathrm{p}}}{\partial \tilde{f}_{\mathrm{V}}}\,. \tag{3.69}$$

The derivatives in terms of the predictor strain can then be replaced in terms of the deformation gradient, see Appendix B.2 for more details.

3.1.3.4 Local form of the porous model

The results of Sections 3.1.3.2 and 3.1.3.3 are now adapted under a local form, i.e. $\hat{\boldsymbol{Z}} = \boldsymbol{Z}$ or in this case $\hat{f}_{\mathrm{V}} = f_{\mathrm{V}}$. Henceforth, the effective variables increments are no longer dependent on the variations of the non-local values, and the stress state $\mathbf{P}^{n+1}$ is computed from the deformation gradient only. The residual form, from which the set of plastic increments $\boldsymbol{v}$ are obtained, is slightly modified

$$\boldsymbol{r}_{\mathrm{p}}\left(\Delta d,\, \Delta q,\, \Delta p;\, \mathbf{E}^{\mathrm{e}}_{\mathrm{pr}}\right)\big|_{\mathbf{E}^{\mathrm{e}}_{\mathrm{pr}}} = \mathbf{0}\,, \tag{3.70}$$

as well as the corresponding Jacobian matrix, both being detailed in Appendix B.3. The material tangent operator, $\frac{\partial \mathbf{P}}{\partial \mathbf{F}}$, is consequently reformulated following the same procedure as in Section 3.1.3.3, see Appendix B.3.2 for more details.

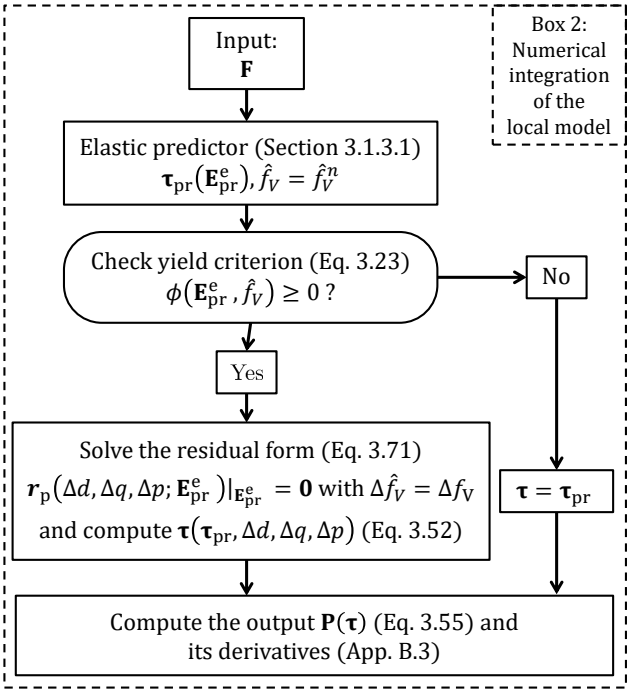

FIGURE 3.6: Numerical integration procedure of the local version of the constitutive porous-plastic model (material model level).

3.2 The damage to crack transition

Crack surfaces are introduced in the mechanical problem through a cohesive band model. For this purpose, the classical cohesive model is taken as a starting point and is extended into a cohesive band formulation following Leclerc et al. (2018) for the case of elastic damage (see Section 2.1.2). By contrast to the surfacic CZM, the damage model presented earlier in Section 3.1 is volumic and depends on the 3D stress state. Moreover, near failure, all the damage growth tends to concentrate within a band around the future crack surface. This band, where coalescence typically occurs, is of finite thickness although very thin (the calibration of this parameter will be discussed in the next chapter). These physical facts can be included by replacing the classical CZM by the cohesive band model (Huespe et al., 2012; Remmers et al., 2013). While respecting a traction-separation model formalism, this latter mimics the behaviour of a uniform thin band around the crack surface. A stress tensor is computed by using the underlying damage model with an enhanced strain tensor at the interface.

The crack insertion criterion and the calibration of the cohesive band thickness are explained next.

3.2.1 Cohesive band model

We refer to Section 2.1.2, see also Fig. 2.2, for the description of the CBM, and give herein the only difference related to the porous plasticity model.

The displacement field is not continuous across the cracked surfaces Γ_{IC0}: two initially neighbouring points at the same location $\boldsymbol{X}$ on Γ_{I0} are now separated by $[\![\boldsymbol{u}(\boldsymbol{X})]\!]$. To satisfy internal equilibrium, the surface traction forces in the current configuration per unit of surface in the reference configuration, $\boldsymbol{t}_{\mathrm{I0}}$, have to be continuous across the surface:

$$[\![\boldsymbol{t}_{\mathrm{I0}}]\!] = \mathbf{0} \text{ on } \Gamma_{\mathrm{IC0}}, \tag{3.71}$$

while this internal boundary surface is treated as a free boundary surface from a non-local point of view (similarly to Eq. (3.6)):

$$\left(\mathbf{C}_{\mathrm{l}} \cdot \boldsymbol{\nabla}_0 \dot{\tilde{Z}}_i\right) \cdot \boldsymbol{N}_{\mathrm{I}} = 0 \text{ on } \Gamma_{\mathrm{IC0}}. \tag{3.72}$$

The evolution of the traction force $\boldsymbol{t}_{\mathrm{I0}}$ is defined by the cohesive model. Pioneered by Dugdale (1960) and Barenblatt (1962), this representation of the material response locally dissipates energy by crack surface creation. As the crack gradually opens and the jump $[\![\boldsymbol{u}]\!]$ increases, the bounding traction forces $\boldsymbol{t}_{\mathrm{I0}}$ between crack lips irreversibly decrease and dissipate an amount of energy per unit of created surface in the reference configuration, G_{c} (so-called, critical energy release rate)

$$G_{\mathrm{c}} = \int_0^{\infty} \boldsymbol{t}_{\mathrm{I0}}\left([\![\boldsymbol{u}]\!]\right) \cdot d\,[\![\boldsymbol{u}]\!] \ . \tag{3.73}$$

Then, the dissipated power is related to the rate of crack surface creation $\dot{A}_0$ with respect to the reference configuration by

$$\dot{\Phi}_{\mathrm{surf}} = G_{\mathrm{c}} \dot{A}_0. \tag{3.74}$$

The cohesive law simply defines the relationship $\boldsymbol{t}_{\mathrm{I0}}([\![\boldsymbol{u}]\!])$ between the traction force and the crack opening.

As the displacement field $\boldsymbol{u}(\boldsymbol{X})$ is discontinuous at the interface, the deformation gradient cannot be directly defined at the discontinuous surface Γ_{IC}. Instead, we use the formulation (2.27) reported here below:

$$\mathbf{F}_{\mathrm{b}}^{\pm} = \mathbf{F}^{\pm} + \frac{1}{h_{\mathrm{b}}} [\![\boldsymbol{u}]\!] \otimes \boldsymbol{N}_{\mathrm{I}} + \frac{1}{2} \frac{\partial [\![\boldsymbol{u}]\!]}{\partial \boldsymbol{X}}, \tag{3.75}$$

with $\mathbf{F}^{\pm} = \mathbf{F}\left(\boldsymbol{X}_{\mathrm{I}}{}^{\pm}\right)$ evaluated on both sides of the band of thickness h_{b}. In this last equation, the displacement discontinuity $[\![\boldsymbol{u}\left(\boldsymbol{X}\right)]\!]$ is assumed constant across the thickness, i.e

$$\frac{\partial [\![\boldsymbol{u}\left(\boldsymbol{X}\right)]\!]}{\partial \boldsymbol{X}} \cdot \boldsymbol{N}_{\mathrm{I}} = \mathbf{0}. \tag{3.76}$$

Besides, an enhanced stabilisation procedure, different of the one used in Section 2.1.2, is involved herein. Due to the higher dissipation generated by the plastic flow, numerical instabilities are strongly reduced and the current bulk deformation gradient is kept (so Eq. (2.31) and the related ones are no longer needed). However, the normal part contribution of the jump to $\mathbf{F}_{\mathrm{b}}$ in Eq. (3.75) is limited in the case of negative values, i.e. in case of contact, in order to avoid negative Jacobian value.

The stress tensor $\mathbf{P}_{\mathrm{b}}^{\pm}$ on both sides of the interface is computed using the constitutive bulk law in its local form

$$\mathbf{P}_{\mathrm{b}}^{\pm}\left(t\right) = \mathbf{P}_{\mathrm{b}}^{\pm}\left(\mathbf{F}_{\mathrm{b}}^{\pm}(t); \hat{\boldsymbol{Z}}^{\pm}(t), \boldsymbol{Z}^{\pm}(t'), t' \in [0,t]\right), \tag{3.77}$$

where $\mathbf{F}_{\mathrm{b}}$ replaces the classical deformation gradient, and where the effective internal variables depend henceforth only on the local evolution after crack insertion, i.e. $\dot{\hat{\boldsymbol{Z}}} = \dot{\boldsymbol{Z}}$, see Section 3.1.3.4. This relation guarantees a continuous traction force at the interface during the transition. The cohesive traction forces are finally obtained by:

$$\boldsymbol{t}_{\mathrm{I0}} = \mathbf{P}_{\mathrm{b}} \cdot \boldsymbol{N}_{\mathrm{I}}. \tag{3.78}$$

Thereby, the cohesive forces are naturally defined in terms of the underlying material behaviour and the in-plane stretch components. Stress triaxiality effects are therefore included inside the cohesive law within a formalism similar to a classical cohesive zone model. The whole

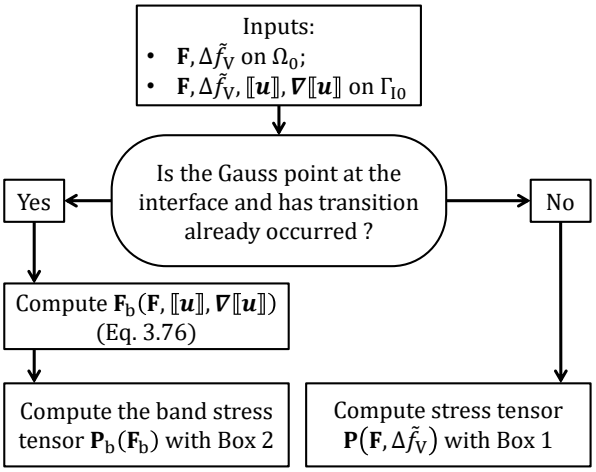

FIGURE 3.7: The non-local diffuse damage to crack transition algorithm, including the cohesive band model, in the context of the porous-plastic model.

procedure is summarised in Fig. 3.7. In the context of a hybrid DG/CZM framework, only a few changes are required to integrate this model, as the necessary Gauss points are already present at the interface and as a stress tensor is already computed at the interface before crack propagation, see Section 3.3.

3.2.2 Crack insertion criterion

A crack insertion criterion is now needed to decide how and when cracks should propagate on the uncracked surface $\mathit{\Gamma}_{\mathrm{IU}}$. A suitable condition has (i) to ensure a softening behaviour after insertion and an elastic unloading in the neighbouring elements, (ii) to predict the propagation direction. In this framework, two possibilities are selected.

3.2.2.1 Loss of ellipticity

In the context of a local model, a requirement to keep solution uniqueness is to introduce the CBM at the loss of strong ellipticity as detected using the acoustic tensor. This criterion will allow the comparison of the results with the simulation performed by Huespe et al. (2012) in the context of local models. Following Huespe et al. (2012), the strong ellipticity is lost at a given point once

$$\det\left[\boldsymbol{N} \cdot^2 \frac{\partial \mathbf{P}}{\partial \mathbf{F}} \cdot \boldsymbol{N}\right] \leqslant 0\,, \tag{3.79}$$

for any direction vector $\boldsymbol{N}$. The crack insertion is constrained along an interface perpendicular to the interface normal $\boldsymbol{N}_{\mathrm{I}}$, i.e.

$$\det\left[\boldsymbol{N}_{\mathrm{I}} \cdot^2 \frac{\partial \mathbf{P}}{\partial \mathbf{F}} \cdot \boldsymbol{N}_{\mathrm{I}}\right] \leqslant 0\,, \tag{3.80}$$

or, similarly

$$-\min\left(\mathrm{eig}\left[\boldsymbol{N}_{\mathrm{I}} \cdot^2 \frac{\partial \mathbf{P}}{\partial \mathbf{F}} \cdot \boldsymbol{N}_{\mathrm{I}}\right]\right) \geqslant \epsilon \geqslant 0\,, \tag{3.81}$$

where the operator "$\cdot^2$" stands for $\left[\mathbf{A} \cdot^2 \boldsymbol{\mathcal{B}}\right]_{ijkl} = A_{jm}\mathcal{B}_{imkl}$, the operator "eig" computes the eigenvalues of a tensor, and where a thresehold ϵ (equal to a fraction of the Young's modulus) has been introduced. Although numerical, this criterion will allow the comparison of the results with the simulation performed by Huespe et al. (2012).

3.2.2.2 Onset of coalescence

The second criterion is based on the onset of coalescence in order to adjust the physical damage localisation with the numerical one. Thereby, the fast damage growth related to the coalescence phase induces the localisation of damage process inside a band and initiates the cracking process. The use of a non-local model allows the insertion of the cohesive band after the onset of softening has been detected, as an approximation, by substituting the derivatives $\frac{\partial \mathbf{P}}{\partial \mathbf{F}}$ in the criterion (3.81) by $\frac{\partial \mathbf{P}}{\partial \mathbf{F}} + \frac{\partial \mathbf{P}}{\partial \hat{f}_\mathrm{V}} \frac{\partial f_\mathrm{V}}{\partial \mathbf{F}}$. The use of a non-local model allows the insertion of the cohesive band after the loss of ellipticity since there is no mesh-dependency. The condition needs also to carry a directional component. The coalescence condition (3.35) is thus rewritten in terms of the interface orientation $\boldsymbol{n}_\mathrm{I}$ and the Kirchhoff stress tensor (since both are defined in the current configuration, and since $\boldsymbol{\kappa}$ shares the same invariants as $\boldsymbol{\tau}$) as

$$\boldsymbol{n}_\mathrm{I} \cdot \boldsymbol{\kappa} \cdot \boldsymbol{n}_\mathrm{I} - C_\mathrm{T}^{\phi} \tau_\mathrm{Y} > 0\,. \tag{3.82}$$

3.2.3 Effects of the cohesive band thickness

The band thickness directly impacts the energy dissipated during crack propagation. Indeed, at this point, the damage accumulation concentrates inside the band while the surrounding bulk material is elastically unloading. As the main contribution results from the jump opening, the dissipated energy is proportional to h_b.

The thickness h_b can be calibrated by comparison of the dissipated energy or G_c with a reference case (Leclerc et al., 2018, see Section 2.2). This reference could be the underlying non-local model, based on another approach as a phase field model, a dedicated micromechanical model or RVE simulations (Scheyvaerts, Pardoen, and Onck, 2010) or again, experimental data. The band thickness can also be linked to a microstructure characteristic length: the coalescence process leads to the concentration of the damage process in a few voids thick layer. This effect will be studied in Section 3.4.

3.3 Numerical implementation

The implementation of the damage to crack transition inside a discontinuous Galerkin framework was explained in this Section 2.3 and is herein adapted for the finite deformation case. The weak form and its discretised version are derived from the differential partial equations and constitutive models defined in Sections 3.1 and 3.2. The implementation and the time integration algorithm for the finite element discretisation and the constitutive models are also described.

3.3.1 Strong form of the equations

The time evolution of the material volume Ω corresponds to the knowledge of the field variables $(\boldsymbol{u}(\boldsymbol{X},t), \tilde{Z}(\boldsymbol{X},t))$. In particular, this includes the location of discontinuity surfaces through time.

The exact solution of the problem ($\boldsymbol{u}^\mathrm{exact}$, $\tilde{Z}^\mathrm{exact}$; $\mathbf{P}^\mathrm{exact}$, $\boldsymbol{\nabla}_0 \tilde{Z}^\mathrm{exact}$) satisfies the system of partial differential equations (3.2) and (3.5) and their boundary conditions (3.3) and (3.6) over the body $\Omega_0 \backslash \Gamma_{\mathrm{I}0}$ described in Section 3.1. Besides, on the uncracked surfaces $\Gamma_{\mathrm{IU}0}$, the solution has to be continuous, i.e.

$$[\![\boldsymbol{u}^\mathrm{exact}]\!] = \mathbf{0}, [\![\mathbf{P}^\mathrm{exact}]\!] = \mathbf{0}, \left[\!\left[\tilde{Z}^\mathrm{exact}\right]\!\right] = 0, \left[\!\left[\mathbf{C}_\mathrm{l} \cdot \boldsymbol{\nabla}_0 \tilde{Z}^\mathrm{exact}\right]\!\right] = \mathbf{0} \text{ on } \Gamma_\mathrm{IU}. \tag{3.83}$$

On the cracked surfaces $\Gamma_{\mathrm{IC}0}$, the relationships (3.71)-(3.72) govern the field evolution across the discontinuity. The traction forces are obtained via the cohesive band model described in Section 3.2. The switch from uncracked to cracked interfaces occurs wherever either the criterion (3.81) or (3.82) is fulfilled.

3.3.2 Weak form of the equations

The initial body Ω_0, presented in Sections 3.1 and 3.2, is now approximated by a collection of finite volume elements B^e with a boundary S^e such as $\cup_e B^e \simeq \Omega_0$. In the discontinuous Galerkin framework, the sought approximation for $(\boldsymbol{u}, \dot{\tilde{Z}})$ is element-wise continuous and discontinuous across them, i.e. $(\boldsymbol{u}, \dot{\tilde{Z}}) \in \mathcal{H}^1(B^e)$ and $(\boldsymbol{u}, \dot{\tilde{Z}}) \in \mathcal{L}^2(\Omega_0)$.[3] The tests functions $(\boldsymbol{w_u}, w_{\tilde{Z}})$ share the same properties. The potential crack surface locations Γ_{I} are therefore no longer totally arbitrary but have to follow internal element boundaries, i.e. $\Gamma_{\mathrm{I}} = \cup_e S^e \backslash \Gamma_0$. An interface element S^s is inserted on the common boundary surface $S^s = S^{e+} \cap S^{e-}$ between each pair of elements (arbitrary called B^{e+} and B^{e-}).

Proceeding as to obtain 2.71 leads to finding $(\boldsymbol{u}, \dot{\tilde{Z}})$ such that

$$\begin{aligned}
&\int_{\Omega_0} \rho_0 \boldsymbol{w_u} \cdot \ddot{\boldsymbol{u}} dV_0 + \int_{\Omega_0} \mathbf{P} : \boldsymbol{\nabla}_0 \boldsymbol{w_u} dV_0 + \int_{\Gamma_{\mathrm{IC}}} [\![\boldsymbol{w_u}]\!] \cdot \langle \mathbf{P}_{\mathrm{b}} \rangle \cdot \boldsymbol{N}_{\mathrm{I}}^- dS_0 \\
&\quad + \int_{\Gamma_{\mathrm{IU}}} [\![\boldsymbol{w_u}]\!] \cdot \langle \mathbf{P} \rangle \cdot \boldsymbol{N}_{\mathrm{I}}^- dS_0 + \int_{\Gamma_{\mathrm{IU}}} [\![\boldsymbol{w_u}]\!] \otimes \boldsymbol{N}_{\mathrm{I}}^- : \left\langle \frac{\beta_{\mathrm{s}}}{h_{\mathrm{s}}} \boldsymbol{\mathcal{C}}^{\mathrm{e}} \right\rangle : [\![\boldsymbol{u}]\!] \otimes \boldsymbol{N}_{\mathrm{I}}^- dS_0 \\
&\quad + \int_{\Gamma_{\mathrm{IU}}} [\![\boldsymbol{u}]\!] \cdot \langle \boldsymbol{\mathcal{C}}^{\mathrm{e}} : \boldsymbol{\nabla}_0 \boldsymbol{w_u} \rangle \cdot \boldsymbol{N}_{\mathrm{I}}^- dS_0 = \int_{\Omega_0} \boldsymbol{w_u} \cdot \boldsymbol{b}_0 dV_0 + \int_{\Gamma_{\mathrm{N}0}} \bar{\boldsymbol{t}}_{\mathrm{N}0} \cdot \boldsymbol{w_u} dS_0 \,;
\end{aligned} \tag{3.84}$$

$$\begin{aligned}
&\int_{\Omega_0} \left(\dot{\tilde{Z}} w_{\tilde{Z}} + \boldsymbol{\nabla}_0 w_{\tilde{Z}} \cdot \mathbf{C}_{\mathrm{l}} \cdot \boldsymbol{\nabla}_0 \dot{\tilde{Z}} \right) dV_0 + \int_{\Gamma_{\mathrm{IU}}} [\![w_{\tilde{Z}}]\!] \left\langle \mathbf{C}_{\mathrm{l}} \cdot \boldsymbol{\nabla}_0 \dot{\tilde{Z}} \right\rangle \cdot \boldsymbol{N}_{\mathrm{I}}^- \, dS_0 \\
&+ \int_{\Gamma_{\mathrm{IU}}} [\![w_{\tilde{Z}}]\!] \, \boldsymbol{N}_{\mathrm{I}}^- \cdot \left\langle \frac{\beta_{\mathrm{s}}}{h_{\mathrm{s}}} \mathbf{C}_{\mathrm{l}} \right\rangle \cdot \boldsymbol{N}_{\mathrm{I}}^- \left[\!\!\left[\dot{\tilde{Z}} \right]\!\!\right] \, dS_0 + \int_{\Gamma_{\mathrm{IU}}} \left[\!\!\left[\dot{\tilde{Z}} \right]\!\!\right] \langle \mathbf{C}_{\mathrm{l}} \cdot \boldsymbol{\nabla}_0 w_{\tilde{Z}} \rangle \cdot \boldsymbol{N}_{\mathrm{I}}^- dS_0 \\
&\qquad = \int_{\Omega_0} \dot{Z} w_{\tilde{Z}} \, dV_0 \,,
\end{aligned} \tag{3.85}$$

for $\forall (\boldsymbol{w_u}, w_{\tilde{Z}})$ kinematically admissible. It introduces $\boldsymbol{\mathcal{C}}^{\mathrm{e}} = \frac{\partial \mathbf{P}}{\partial \mathbf{F}}\big|_{\mathbf{F}=\mathbf{I}}$ the constant elastic operator of the virgin material, $\beta_{\mathrm{s}} > 1$, a sufficiently high penalty parameter for solution stabilisation, and h_{s}, a characteristic mesh size parameter dependent on the element size and the involved polynomial approximation.

3.3.3 Finite element discretisation

The weak form (3.84)-(3.85) developed in the previous section is the starting point of the finite element discretisation. Inside each element, a nodal interpolation approximates the fields $(\boldsymbol{u}, \dot{\tilde{Z}})$ and their respective test functions $(\boldsymbol{w_u}, w_{\tilde{Z}})$. At each node a is associated one polynomial shape function $N^a(\boldsymbol{X})$, identical for each field and test function. The fields (and the test functions) are therefore estimated inside an element following:

$$\begin{aligned}
\boldsymbol{u}(\boldsymbol{X}) &= \sum_{a=1}^{N_{\mathrm{n}}} N^a(\boldsymbol{X}) \, \boldsymbol{u}^a, \qquad \Delta\tilde{Z}(\boldsymbol{X}) = \sum_{a=1}^{N_{\mathrm{n}}} N^a(\boldsymbol{X}) \, \Delta\tilde{Z}^a, \quad \text{and} \\
\boldsymbol{w_u}(\boldsymbol{X}) &= \sum_{a=1}^{N_{\mathrm{n}}} N^a(\boldsymbol{X}) \, \delta\boldsymbol{u}^a, \quad w_{\tilde{Z}}(\boldsymbol{X}) = \sum_{a=1}^{N_{\mathrm{n}}} N^a(\boldsymbol{X}) \, \delta\tilde{Z}^a,
\end{aligned} \tag{3.86}$$

[3] In the former, $\mathcal{H}^1$ corresponds to the Hilbert space and $\mathcal{L}^2$ to the square-integrable function space

from the N_{n} nodal values $(\boldsymbol{u}^a, \tilde{Z}^a)$ (and $(\delta\boldsymbol{u}^a, \delta\tilde{Z}^a)$) associated with each of the N_{n} nodes of the element. The degrees of freedom (DoF) are brought together in a nodal unknowns vector $\boldsymbol{q}^a = [(\boldsymbol{u}^a)^{\mathrm{T}}\, \Delta\tilde{Z}^a]^{\mathrm{T}}$ for a node a and in a global vector $\boldsymbol{q} = [\boldsymbol{u}^{\mathrm{T}}\, \Delta\tilde{\boldsymbol{Z}}^{\mathrm{T}}]^{\mathrm{T}}$ gathering all the DoF of the mesh. Applying to the weak form (3.84)-(3.85) the discrete approximation (3.86) of the different fields, the following set of differential equations is obtained by taking into account the inter-element discontinuities

$$\left\{\begin{array}{lcll} \mathbf{M}\ddot{\boldsymbol{u}} + \boldsymbol{f}_{\boldsymbol{u}\,\mathrm{int}}(\boldsymbol{q}) + \boldsymbol{f}_{\boldsymbol{u}\,\mathrm{I}}(\boldsymbol{q}) & = & \boldsymbol{f}_{\boldsymbol{u}\,\mathrm{ext}} & \\ \boldsymbol{f}_{\tilde{Z}\,\mathrm{int}}(\boldsymbol{q}) - \boldsymbol{f}_{Z\,\mathrm{int}}(\boldsymbol{q}) + \boldsymbol{f}_{\tilde{Z}\,\mathrm{I}}(\boldsymbol{q}) & = & \mathbf{0} & \end{array}\right. \quad \forall t > 0\,, \tag{3.87}$$

see Appendix B.4 for details and expressions. In the force equilibrium equations (3.87), $\boldsymbol{f}_{\boldsymbol{u}\,\mathrm{int}}$, $\boldsymbol{f}_{\boldsymbol{u}\,\mathrm{I}}$ and $\boldsymbol{f}_{\boldsymbol{u}\,\mathrm{ext}}$ respectively stand for the internal, interface and external force vectors related to the displacement field while $\mathbf{M}$ is the mass matrix. $\boldsymbol{f}_{\tilde{Z}\,\mathrm{int}}$, $\boldsymbol{f}_{Z\,\mathrm{int}}$ and $\boldsymbol{f}_{\tilde{Z}\,\mathrm{I}}$ are respectively the non-local internal, local internal and interface non-local force vectors.

3.3.4 Numerical time integration

The set of equations (3.87) obtained previously is integrated through time using the α-generalised method developed by Chung and Hulbert (1993) and presented in Section 2.3.2.2. The stiffness matrices involved in Eqs. (2.82) and (2.86) are developped in Appendix B.5.

3.3.5 Specific details of the algorithm

This section gathers some practical details of the numerical algorithm, contributing to the framework robustness.

- A crack surface is introduced at a whole interface element when the criterion is detected at least at one of its Gauss points. Void evolution is also blocked on the neighbouring volume elements (but not the plastic flow), in order to favor elastic unloading instead of further volume softening.
- In order to avoid inter-element penetration during crack opening, a (linear) penalty force is added. However, no friction relation is taken into account.
- At a crack insertion using the coupled model presented in Section 3.1.2.5, a small shift exits between the criterion (3.82) and the yield surface (3.38). To avoid stress discontinuity, an offset is therefore introduced in Eq. (3.38).

3.4 Numerical applications

The constitutive description of the ductile failure process and its numerical implementation is applied in this section to some numerical examples. At first, in order to verify the formulation, the problem analysed by Huespe et al. (2012), in which a crack is inserted at loss of ellipticity of a local model and in which the crack opening is governed by an adequate calibration of the Gurson model parameters, is reproduced with the developed framework. The effect of the band thickness and the non-dependence to the mesh size are analysed. Then, the more physical Thomason coalescence criterion is used as crack initiation criterion and the crack opening is governed by the Thomason coalescence model. It is shown that, in this case, although cracks are inserted during the strain softening stage of the process, because of the non-local formulation of the damage model, the solution is not mesh dependent. Furthermore, the model is able to reproduce the slant and cup-cone failure modes in plane-strain specimens and axisymmetric bars, either smooth or notched, respectively. Finally, the effect of the non-local characteristic length on the resulting material ductility is studied.

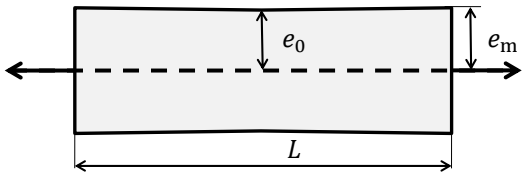

FIGURE 3.8: Geometry of the plane strain specimen.

3.4.1 Framework verification with a local Gurson model applied on a plane strain specimen

The current framework is first degenerated into a local Gurson model[4] to allow a comparison with the results discussed by Huespe et al. (2012). With the local version of the Gurson model, a crack is inserted when the loss of ellipticity is detected by the criterion (3.81) in order to preserve solution uniqueness. The failure process is governed by the same Gurson model in which coalescence is modelled by adequate parameters.

The plane strain specimen consists in a rectangular bar of thickness $2e_{\mathrm{m}} = 5$ [mm] and length $L = 3.5e_{\mathrm{m}}$ as drawn on Fig 3.8. Practically, the problem symmetry is exploited to model only one half of the specimen. To ensure localisation at the centre of the bar, a geometrical defect is introduced. For this purpose, the thickness linearly decreases with a minimum thickness $e_0 = 0.98e_{\mathrm{m}}$ in the middle of the bar. This smallest cross section is chosen as the reference surface area. The specimen is meshed using 6-node quadratic triangular elements with an aspect ratio between 4 and 5 in the necking zone to ensure a square mesh near failure. Three mesh sizes scaled by a refining factor of 1.5 are used: $l_{\mathrm{mesh}} = 75$ [μm] for the finest mesh, $l_{\mathrm{mesh}} = 110$ [μm] and $l_{\mathrm{mesh}} = 170$ [μm] for the coarsest (and an aspect ratio of 4) corresponding respectively to 65, 45 and 30 elements through the thickness, and including respectively 7180, 4224 and 2544 triangles in total. The stability parameter β_s is fixed to 50, a sufficiently high value to provide results independent of β_s. As dynamic effects are out of the scope of this work, the spectral radius ρ_∞ is set to 0 and the loading time is long enough for the results to become insensitive to it.

The material properties, gathered in Table 3.1, are similar to the one used by Huespe et al. (2012) and by Besson, Steglich, and Brocks (2003)[5]. The elastic properties are $E = 210$ [GPa] for the Young's modulus and $\nu = 0.3$ for the Poisson ratio. The density is equal to 7600 $\left[\mathrm{kg/m^3}\right]$. The hardening law consists in a Swift law in terms of the matrix plastic strain

$$\tau_{\mathrm{Y}}(p) = \tau_{\mathrm{Y0}}\left(1 + h_{\mathrm{y}} p\right)^{h_{\mathrm{exp}}} , \tag{3.88}$$

with $\tau_{\mathrm{Y0}} = 377$ [MPa] the initial yield stress, $h_{\mathrm{y}} = 555$ [$-$] the strain-hardening modulus, and $h_{\mathrm{exp}} = 0.12$ [$-$] the hardening exponent. The strain-controlled nucleation term is a Gaussian function (Chu and Needleman, 1980)

$$A_{\mathrm{nucl}} = \frac{f_{\mathrm{n}}}{s_{\mathrm{n}}\sqrt{2\pi}} \exp\left[-\frac{1}{2}\left(\frac{p - p_{\mathrm{n}}}{s_{\mathrm{n}}}\right)^2\right] , \tag{3.89}$$

where $f_{\mathrm{n}} = 4.0 \times 10^{-6}$, $p_{\mathrm{n}} = 0.1$ and $s_{\mathrm{n}} = 0.3$ are distribution parameters for the nucleated void part, identically to Huespe et al. (2012). The shear contribution from k_ω is also ignored. To recover a local model, a small non-local length is chosen, here equal to 5 [μm], i.e. one 15^{th}

[4] To recover a local model, the non-local framework is used with a small non-local length compared to the mesh size, here equal to 5 [μm], i.e. one 15^{th} of the finest element size. Moreover, the derivatives $\frac{\partial \mathbf{P}}{\partial \mathbf{F}}$ in the criterion (3.81) is substituted by $\frac{\partial \mathbf{P}}{\partial \mathbf{F}} + \frac{\partial \mathbf{P}}{\partial \hat{f}_{\mathrm{V}}} \frac{\partial f_{\mathrm{V}}}{\partial \mathbf{F}}$, since $\hat{f}_{\mathrm{V}} \simeq f_{\mathrm{V}}$ in this case.

[5] We refer to so-called "G-model" considered in this last reference

TABLE 3.1: Material properties for the local Gurson model, adapted from Huespe et al. (2012).

Elasto-plastic properties, Eqs. (3.21), (3.88):		
Density	ρ_0	7600 [kg/m^3]
Young's Modulus	E	210 [GPa]
Poisson ratio	ν	0.3
Initial yield stress	τ_{Y0}	377 [MPa]
Strain-hardening modulus	h_y	555
Strain-hardening exponent	h_{exp}	0.12
Porosity parameters, Eqs.(3.26), (3.89):		
Initial porosity	f_{V_0}	1.5×10^{-4}
Nucleation parameters	f_n	4.0×10^{-6}
	p_n	0.3
	s_n	0.1
Shear-induced parameter	k_ω	0
Gurson model parameters, Eq.(3.32):		
Gurson yield parameters	q_1, q_3	1.5
	q_2	1.15
Cohesive band model:		
Cohesive band thickness	h_b	12 [μm]

of the finest element size. A scatter of 1% is added to the initial porosity $f_{V_0} = 1.5 \times 10^{-4}$ in order to break the symmetry in the problem. The local Gurson model parameters are $q_1 = q_3 = 1.5$; q_2 is equal to 1.15 to simulate the coalescence similarly to Besson, Steglich, and Brocks (2003). The crack is introduced when the criterion (3.81), based on the loss of ellipticity, is satisfied. The band thickness is, in a first time, fixed to 12 [μm], slightly higher than Huespe et al. (2012) since these authors have considered an exponential smoothing of the porosity evolution contrarily to the present analysis.

The force evolution is represented in Fig. 3.9 as a function of the thickness reduction $\Delta e/e_0$ for the three mesh sizes. At first, on Fig. 3.9a, the results are shown for the local model without crack insertion. In this case, the results are mesh-dependent as expected. However, on Fig. 3.9b, solutions involving the insertion of the cohesive band model (continuous lines) at loss of ellipticity are mesh independent during the entire deformation process. Except for the coarsest mesh, characterised by too large elements to correctly model the problem, only small disparities are observed during crack propagation, essentially due to different crack paths that are constrained along the interface elements. Moreover, the results are globally in agreement with the ones obtained by Huespe et al. (2012).

The corresponding plastic strain and the porosity distributions (on a logarithmic scale) of the previous results are presented in Figs. 3.10 and 3.11 after the first crack insertion, during crack propagation, and at complete failure for the finest mesh. Two shear bands oriented at around 45°, noticeable by a higher plastic strain or a higher porosity value, intersect at the centre of the specimen. The crack initiates at the centre and spreads toward the surface, following one of those shear bands. While the coarsest mesh is again not refined enough to correctly model the problem, resulting in a crack orientation more vertical than expected, the crack orientation is around 45° for the other two meshes. We however note that the crack eventually bifurcates towards the secondary shear band direction as both localisation directions are possible. This behaviour was prevented in the work of Huespe et al. (2012) by systematically favouring one direction. We will further show that when considering a non-local model coupled with the Thomason coalescence criterion this is naturally avoided.

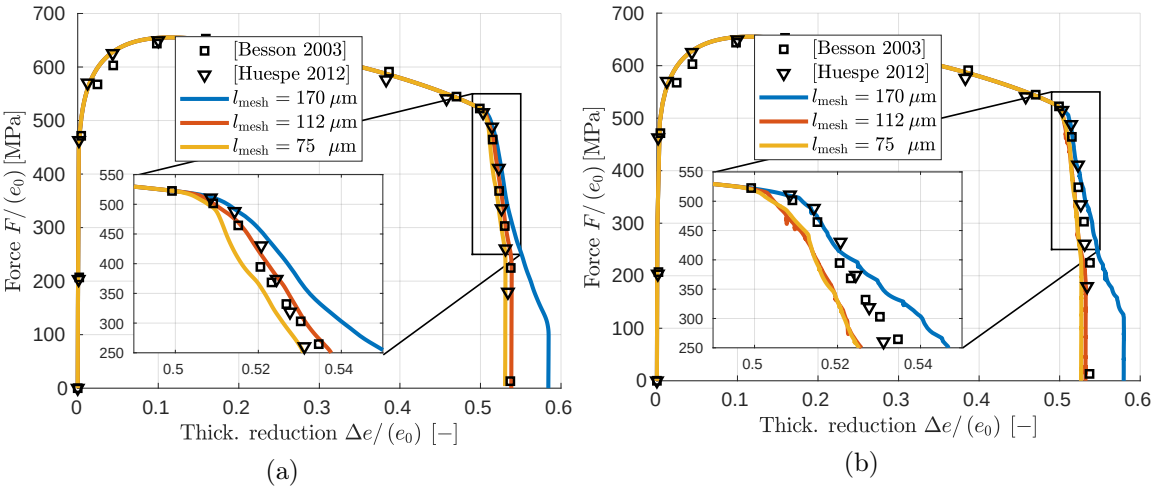

FIGURE 3.9: Variation of the applied load as a function of minimum cross-section thickness reduction of the plane strain specimen (a) for the local Gurson model without crack insertion, and (b) for the local Gurson model coupled with the CBM for the three mesh sizes, and comparison with the results of Besson, Steglich, and Brocks (2003) and Huespe et al. (2012) (square and triangle makers).

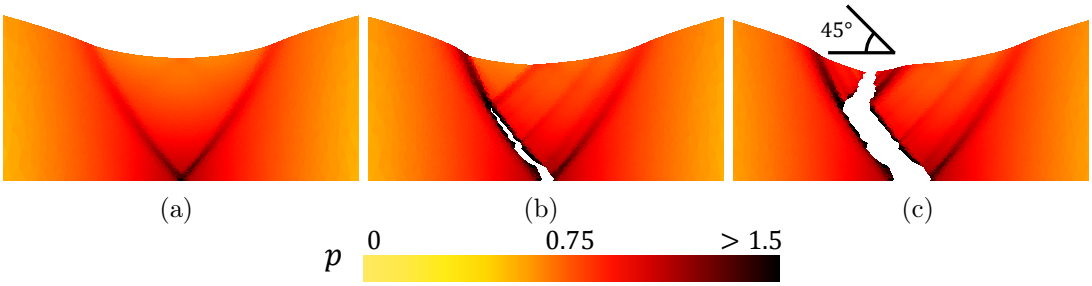

FIGURE 3.10: Matrix plastic strain distribution of the plane strain specimen model by introducing a crack at the loss of ellipticity occurring when the criterion in Eq. (3.81) is satisfied: (a) at failure initiation, (b) during crack propagation and (c) at total failure for the fine mesh.

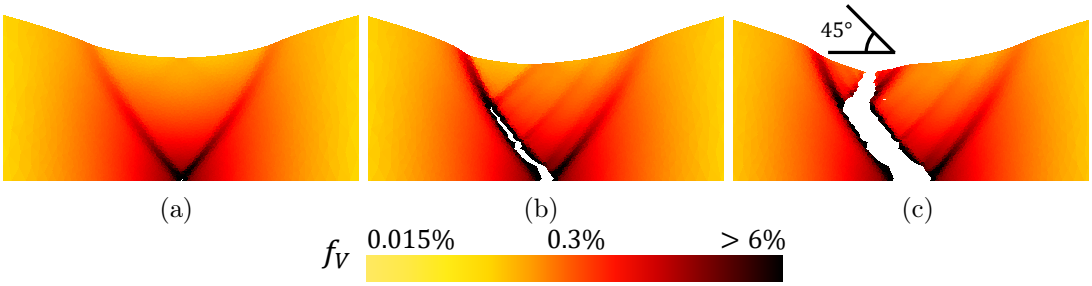

FIGURE 3.11: Porosity distribution inside the plane strain specimen model by introducing a crack at the loss of ellipticity occurring when the criterion in Eq. (3.81) is satisfied: (a) at failure initiation, (b) during crack propagation and (c) at total failure for the fine mesh.

The response in terms of the band thickness is now examined in Fig. 3.12 using the medium mesh (110 [μm]). If no clear trend is observed on the whole curve, the band thickness clearly

influences the response right after the onset of cracking as seen in the zoom: the behaviour is more ductile with a thicker band. However, quickly after the onset of cracking, crack paths slightly differ from one another, resulting in no comparable curves. A proper comparison could be performed by enforcing a pre-defined path. It is worth mentioning that a vanishing value of h_b, closer to a brittle fracture expected behaviour, results in a straight crack path. Indeed, the plastic strain distribution is compared on Fig. 3.13 for two values of h_b. In this case, increasing h_b does not change the crack orientation while decreasing it results in a straight crack. Surface energy dissipation, although small compared to the diffuse plastic dissipation, is therefore required to avoid this inconsistency with respect to physical evidences.

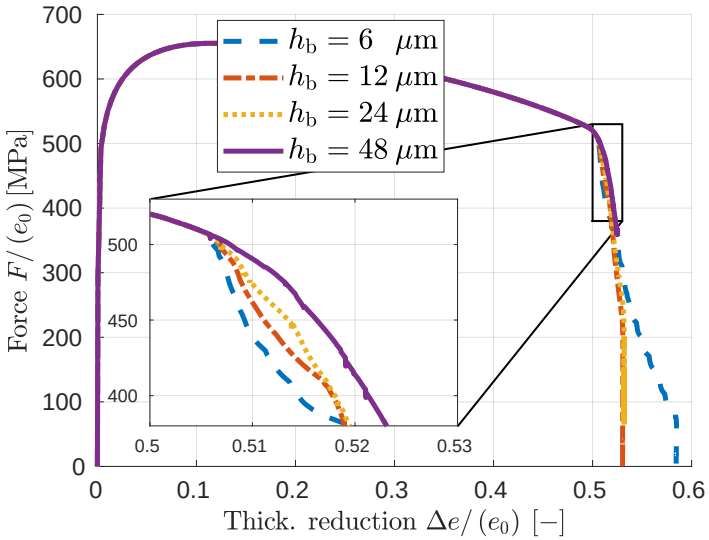

FIGURE 3.12: Variation of the applied force as a function of the minimum cross-section thickness reduction of the plane strain specimen for the local Gurson model coupled with the CBM and for different values of the band thickness. A zoom is provided for the response just at and after cracking initiation.

3.4.2 Non-local model and crack insertion based on Thomason coalescence model

The insertion criterion (3.81) is now replaced by the coalescence criterion (3.82) inspired from the Thomason coalescence model. This last one has the advantage to rely more on the void geometry evolution. As we will illustrate later, this condition is generally fulfilled beyond the softening point, hence the necessity of using the non-local model. After crack insertion, another coalescence model is used to govern the failure process: the coupled Gurson-Thomason model presented in Section 3.1.2.4. Since the model is different, in this section, the material properties of the Gurson-Thomason combined model are first identified in order to recover the results reported by Besson, Steglich, and Brocks (2003).

3.4.2.1 Parameters calibration

The elasto-plastic material parameters of Section 3.4.1 are used again, see Table 3.1. The other materials parameters are gathered in Table 3.2. The Gurson parameters are now $q_1 = q_3 = 1.5$ and $q_2 = 1.$, which are more micromechanically sound (see Faleskog, Gao, and Fong Shih (1998)) than the values used in Section 3.4.1. Two non-local lengths are investigated: 50 and 75 [μm], which are reasonable values with respect to literature but which are of course microstructure dependent, and will vary from one material to another (e.g. Zhang, Lorentz,

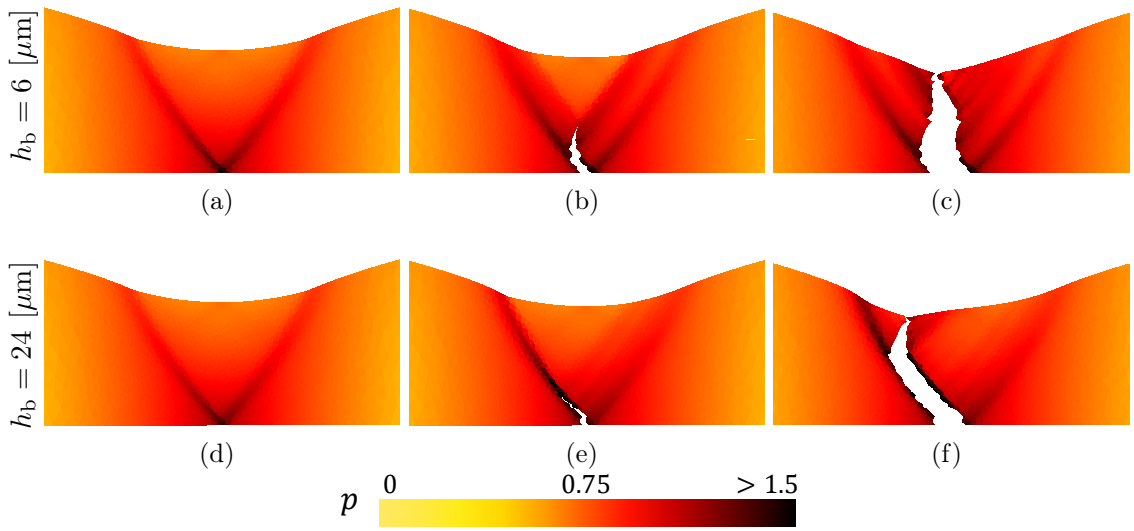

FIGURE 3.13: Plastic strain distribution within the plane strain specimen model by introducing a crack at the loss of ellipticity occurring when the criterion in Eq. (3.81) is satisfied for two values of h_b: (left) at failure initiation, (center) during crack propagation and (right) at total failure for the medium refined mesh.

and Besson (2018)). The band thickness is still equal to $h_b = 12$ [μm]. The ligament ratio χ is computed using $\lambda_0 = 0.5$ and $\kappa = 0.4$, see Eq. (3.31). In addition, the interpolation exponent n of the yield surface ϕ_T is equal to 10.

The nucleation term A_n and the shear contribution k_ω are then calibrated in terms of the non-local length $l_c = 50$ [μm] (resp. $l_c = 75$ [μm]) to predict the fracture strain value of the smooth round bar and of the plane strain specimen reported by Besson, Steglich, and Brocks (2003). As k_ω has no effect on failure initiation on the axisymmetric tests, as it will be shown, a significant nucleation term with $f_n = 2.0 \times 10^{-3}$ (resp. 3.5×10^{-3}), $p_n = 0.1$ and $s_n = 0.3$ is added to capture the correct initiation point of this test. Then, an approximate shear contribution, $k_\omega = 1$ (resp. $k_\omega = 0.5$) in agreement with literature (Xue et al., 2010, e.g.), is chosen to fit the fracture initiation of the plane strain specimen.

Unless otherwise stated, the simulations are performed with $l_c = 50$ [μm] and $k_\omega = 1$.

3.4.2.2 Slant fracture in a plane strain specimen

The framework is first applied to the plane strain specimen, previously presented in Section 3.4.1 with $l_c = 50$ [μm]. Figure 3.14a shows the force evolution predicted with the three meshes used earlier. Since the elements are quadratic, the distance $l_c = 50$ [μm] actually covers several integration points for the finest meshes. As observed previously, the simulations with the coarsest mesh do not represent correctly the failure process. Regarding other meshes, the expected necking process is recovered. Moreover, no mesh-dependency is observed in the force-thickness reduction curves.

The plastic strain distribution is represented in Fig. 3.15 for the medium refined mesh. Before crack insertion, two shear bands are developing at around 45° with respect to the loading direction at future crack propagation sites. Cracks are then introduced by following one of these localisation bands until total failure. We note that we do not have introduced a direction criterion to select the band direction. This insertion occurs in this case beyond the onset of softening shown by the coloured elements on Fig. 3.16. The process zone spreads

TABLE 3.2: Material properties for the non-local Gurson-Thomason model.

		$l_c = 50$ [μm]	$l_c = 75$ [μm]
Porosity param., Eqs.(3.26), (3.89):			
Initial porosity	f_{V_0}	1.5×10^{-4}	
Nucleation parameters	f_n	2.0×10^{-3}	3.5×10^{-3}
	p_n	0.3	
	s_n	0.1	
Shear-induced parameter	k_ω	1.0	0.5
Gurson model param., Eq.(3.32):			
Gurson yield parameters	q_1, q_3	1.5	
	q_2	1	
Thomason model param., Eqs. (3.38), (3.31), (3.39):			
Cell parameters	λ_0	0.5	
	κ	0.4	
Thomason yield surface parameters	α	0.196	
	β	1.24	
Cohesive band model:			
Cohesive band thickness	h_b	12 [μm]	

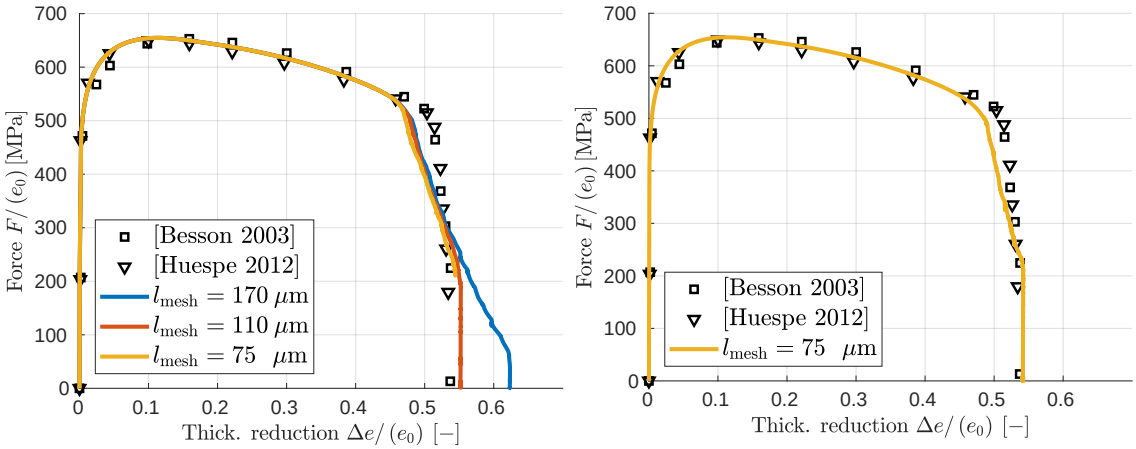

(a) $l_c = 50$ [μm] (b) $l_c = 75$ [μm]

FIGURE 3.14: Variation of the applied force as a function of the minimum cross-section thickness reduction of the plane strain specimen for the non-local Gurson-Thomason model coupled with the CBM (continuous lines) for two values of l_c, and comparison with the results of Besson, Steglich, and Brocks (2003) and Huespe et al. (2012) (respectively square and triangle markers).

over several elements and precedes the crack tip. While the process zone is almost symmetric at failure initiation, it is afterwards inclined at 45°.

3.4.2.3 Cup-cone fracture in round bar specimens

The framework is now applied to a different stress state by considering axisymmetric smooth and notched round bars, represented respectively in Figs. 3.17a and 3.17b. The round specimens have a radius $R_e = 5$ [mm] and a length $L = 3.5R_e$. The considered notch radius of the notched bars is equal to $R_n = 4$ [mm] with an external radius $R_e = 9$ [mm]. For the smooth

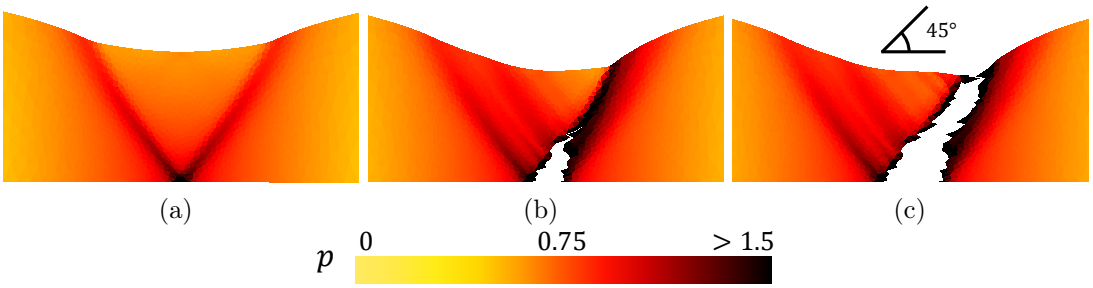

FIGURE 3.15: Matrix plastic strain distribution of the plane strain specimen using the non-local model with $l_c = 50$ [μm] and introducing a crack following Thomason coalescence criterion and for the medium refined mesh: (a) at failure initiation, (b) during crack propagation and (c) at total failure.

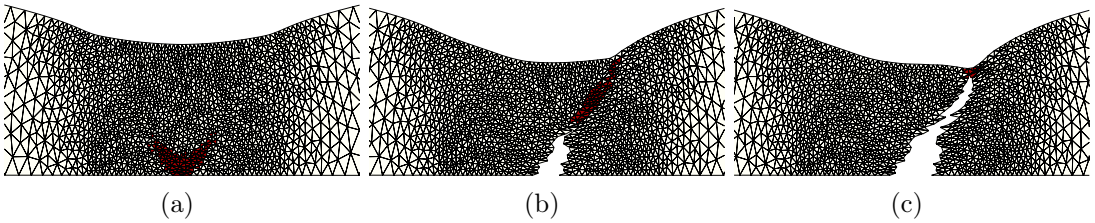

FIGURE 3.16: Mapping of the elements which entered strain softening stage in the plane strain specimen using the non-local model with $l_c = 50$ [μm] and the introduction of a crack following Thomason coalescence criterion (medium refined mesh) (a) at the failure initiation, (b) at a point during the failure process and (c) near the total failure.

round bar (i.e. $R_n = \infty$), a geometrical imperfection is introduced. It consists in a diameter reduction around the central section as applied by Huespe et al. (2012). The reduction follows a circular profile, extending on one seventh of the bar length from both sides of the maximum reduction $R_0 = 0.98R_e$ section. The minimum cross-section is used as reference surface S_0. The meshes for the different notch radii $R_n = \infty$ and 4 [mm] consist respectively in 16598 and 16116 6-node triangular elements of 75 [μm] size with an aspect ratio around to 7 and 5. Moreover, the DG-stability parameter is increased (here the value $\beta_s = 175$ is considered) because of the use of different elements (axisymmetric and not 2D ones). Besides, the term $\frac{1}{2}\frac{\partial[\![\boldsymbol{u}]\!]}{\partial \boldsymbol{X}}$ in Eq. (3.75) has been neglected. The material model and parameters are identical, as defined in the Section 3.4.2.1 and $l_c = 50$ [μm] is considered.

The variation of the tensile force applied on the smooth round bar is represented in Fig. 3.18 in terms of the radius reduction for $l_c = 50$ [μm]. A good correlation is obtained with both results presented by both Besson, Steglich, and Brocks (2001) and Huespe et al. (2012). Besides, the force evolution is also shown in Fig. 3.18 for different values of k_ω. As announced in Section 3.4.2.1, one can notice that k_ω has no influence on the crack initiation as the Lode term is vanishing near the bar center. However, once the crack is propagating, the stress state changes and the k_ω effect becomes noticeable. The force evolutions for the two notch radii are compared in Fig. 3.19a. A good correlation is obtained between the fracture strain measured by Besson, Steglich, and Brocks (2001) despite the fact that the numerical results slightly overestimate the real fracture strain.

Figs. 3.20a to 3.20c represent the deformed state of the smooth round bar at different points of the process as the plastic strain distribution for $k_\omega = 1$. At a necking factor of 0.5, a tensile crack initiates at the center. It radially propagates while shear bands are starting to

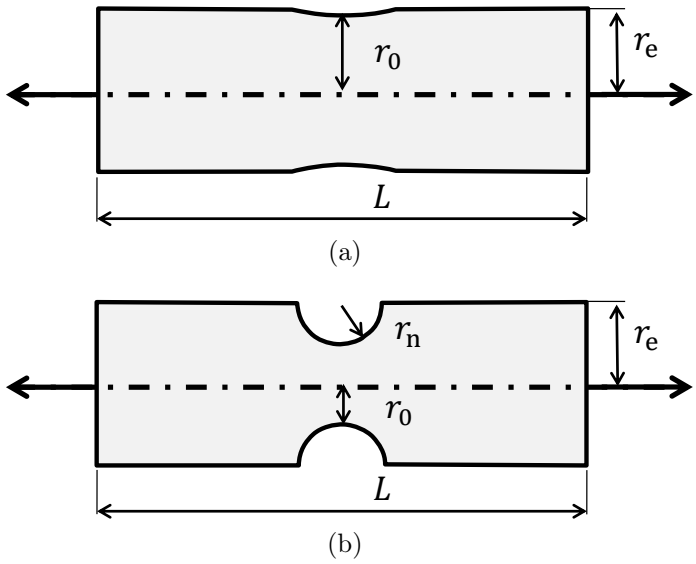

FIGURE 3.17: Geometries (a) of the round bar and (b) of the notched bar.

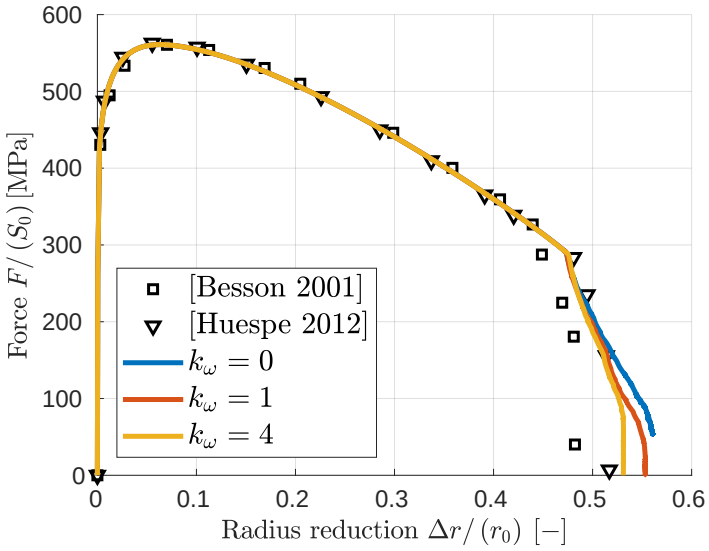

FIGURE 3.18: Variation of the applied force as a function of the central radius reduction of the smooth round bar for the non-local Gurson-Thomason model with $l_c = 50$ [μm] and the CBM, and comparison with the results of Besson, Steglich, and Brocks (2001) and Huespe et al. (2012) (respectively square and triangle markers).

develop aside of the crack (see Fig. 3.20b). At some point, the crack changes its direction, following those shear bands until it reaches the surface. A cup-cone failure is thus obtained as experimentally observed by Besson, Steglich, and Brocks (2001).

The plastic strain distributions in the deformed state of the notched bar are presented in Figs. 3.20d to 3.20f. The crack also starts from the center of the specimen but at a different plastic strain value. Indeed, the increase of the stress triaxiality, caused by a smaller notch radius, leads to an earlier failure initiation. At some point, the crack also bifurcates by following a shear band, resulting in a cup-cone failure mode as observed experimentally by Besson, Steglich, and Brocks (2001).

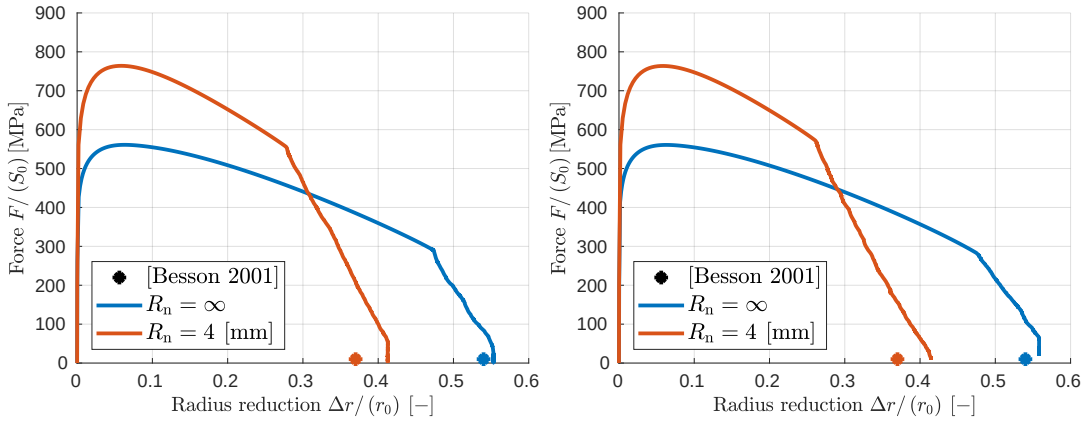

(a) $l_c = 50$ [μm] (b) $l_c = 75$ [μm]

FIGURE 3.19: Variation of the applied force as a function of the minimum cross-section radius reduction of the smooth and notched round bars for the non-local Gurson-Thomason model with the CBM for two values of l_c, and comparison with the experimental fracture strain given by Besson, Steglich, and Brocks (2001) (star markers).

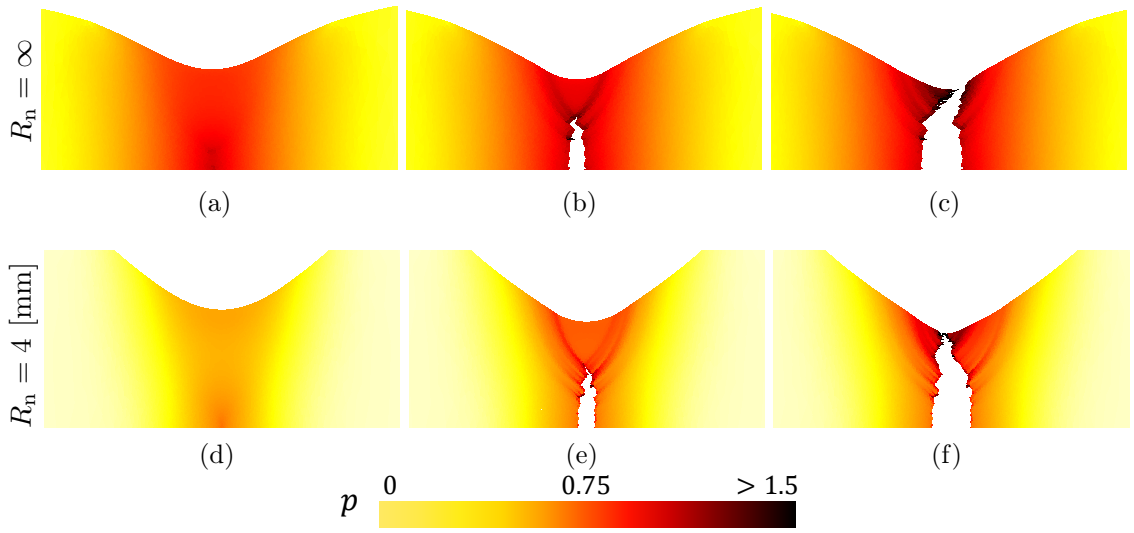

FIGURE 3.20: Matrix plastic strain distribution of the smooth ($R_n = \infty$) and the notched ($R_n = 4$ [mm]) round bar specimen using the non-local model with $l_c = 50$ [μm] and introducing a crack following Thomason coalescence criterion: (a) at failure initiation, (b) before crack tilting, and (c) at total failure.

3.4.2.4 Influence of the non-local length

Results presented in Sections 3.4.2.2 and 3.4.2.3 are now compared with the results obtained with the second set of material parameters calibrated in Section 3.4.2.1 for $l_c = 75$ [μm]. Similar results are obtained, either in terms of force evolution or fracture surface. As an illustration, the force evolution in terms of, respectively, the thickness and the diameter reductions are compared in Figs. 3.14b and 3.19b, showing that the model can still predict the correct trends and similar conclusions can be drawn about the results. The model is effectively rich enough to represent the slant and cup-cone fracture, characteristic of the ductile failure process. However, the simple procedure based on the information available to calibrate the model is

unable to determine a unique set of material parameters. As several parameters combinations can reproduce the expected behaviour, a more complete strategy needs to be adopted, based on physical arguments involving for instance the determination of the tearing resistance and fracture energy in problems with stable crack propagation. This task will be addressed in the Chapter 4.

3.5 Conclusions

We have developed a damage to crack transition numerical framework in order to predict the failure of porous ductile materials. This framework couples an implicit non-local damage model, which captures the initial diffuse damage stage, with a cohesive band model, which captures the void coalescence and crack extension opening stage. The cohesive band model allows considering complex 3D stress state effects during the final failure process. The transition has been numerically implemented within a discontinuous Galerkin formulation.

The Gurson-Tvergaard-Needleman (GTN) model was selected to simulate the void growth before the coalescence phase. First, in order to compare our results with the literature, a local model was considered and the cracks were inserted in a local model at the loss of ellipticity. Then, in order to illustrate the versatility of the non-local framework, we have considered the Thomason coalescence criterion as crack initiation indicator, and the Thomason coalescence model as crack opening governing law. In particular, it was shown that the Thomason coalescence criterion can be met during the strain softening stage, motivating the use of a non-local damage formulation.

The framework was then applied to reproduce the slant and cup-cone failure modes of plane-strain and axisymmetric specimens, respectively. In particular, it was shown that the numerical predictions converge with the mesh refinement, and that the cohesive band thickness governs the fracture energy released during the coalescence stage, and possibly the failure mode when vanishing values are considered.

The material model could be enhanced with more complex coalescence models: in this work, slant and cup-cone failures are captured because of the creation of the free surface. Nguyen, Pardoen, and Noels (2020) have recently introduced a non-local multi-surface approach accounting for void growth, internal necking and shearing mechanisms capturing these patterns without introducing a discontinuity. This non-local porous plasticity model will improve the quality of the predictions at low stress triaxiality.

Another step should focus on the material parameters calibration. A proper procedure should be developed, followed by a suitable experimental campaign. This step is addressed in the next chapter.

Chapter 4

Calibration of the material parameters for high-strength steels[1]

In this chapter, the CDM/CBM (continuous damage model / cohesive band model) transition framework developed in the previous chapters is calibrated for a high-strength steel alloy. In particular, we mainly focus on the micromechanical model suited to ductile failure in the context of finite strains, the Gurson-Thomason (GT) model, which was developed in Chapter 3. For this purpose, a thorough experimental campaign is involved to assess the material parameters values. Moreover, the mechanical tests are completed with micromechanical observations, cell numerical experiments and the development of a nucleation model allowing to reproduce the porosity evolution experimentally observed in an alloy exhibiting failure anisotropy.

Indeed, the micromechanical-based model developed in Chapter 3 entails numerous parameters to calibrate. Comparatively, the number of mechanical tests usually available is more limited. Therefore, this is possible to find a parameters combination by pure parametric optimisation which is close to the available experimental curves. However, due to this material parameters profusion, nothing would prevent overfitting and nothing would ensure this solution to be unique or the optimal one. In other words, even if we observe a good agreement between the available experimental results and the numerical ones, nothing would guarantee that the chosen combination of numerical parameters correctly predicts other loading cases. This would result in case-dependent parameters, which has to be prevented as previously stated in Chapter 1.

Therefore, to avoid any case-dependent parameters, a different strategy is chosen here. In parallel to mechanical tests, we benefit from the micromechanical-based model developed previously by linking as much as possible the parameters values to their physical interpretation. Hence, we mainly establish the calibration procedure as much as possible on micromechanics observations and arguments. In this way, the propensity to overfitting would be reduced.

To do so, we include an extensive microstructure analysis based on SEM (Scanning Electron Microscope) pictures. Those images have been taken before and after the mechanical tests at different locations as along the loading axis or on the failure surface. Those images provide precious insights on the mechanisms in play. In particular, this helps us to identify the failure sequence and its origin. Moreover, after image processing, the inclusions properties, their size, shape, spatial distribution and composition can be extracted.

We also use elementary cell computations. Such a computation consists in a finite element (FE) simulation of a Representative Volume Element (RVE) of the actual microstructure. Adequate boundary conditions are enforced with the elasto-plastic matrix behaviour identified from the mechanical tests. Since the early work of Needleman (1972), this method has been

[1] This calibration procedure is aimed to be published in two parts. This work is supported by different collaborations. Indeed, the mechanical tests, performed by Marie-Stéphane Colla and Matthieu Marteleur from UCLouvain, are completed by several micromechanical data's also provided by them. They have studied the microstructure properties and its evolution during the failure process using SEM pictures which they have taken. Furthermore, we apply the hardening law calibrated in collaboration with Van-Dung Nguyen. We also include the results of the elementary cell computations performed by Van-Dung Nguyen to assess a part of the void growth and coalescence parameters.

used with various levels of complexity in terms of loadings conditions, microstructure, matrix behaviour,... see the review by Pineau, Benzerga, and Pardoen (2016). In this work, we investigate the cell model considered by Pardoen and Hutchinson (2000).

This strategy is applied in this chapter on forged tubular blanks of a high-strength steel alloy. Due to its forming and manufacturing process, an anisotropy is expected in the mechanical properties because of the anisotropy arising in its microstructure. The campaign of experimental mechanical tests is designed in consequence. It involves various specimens to cover a large span of the stress state space with a focus on tensile behaviour since a significant dependency of the ductility on the stress conditions has been observed by Bai, Teng, and Wierzbicki (2009), Bai and Wierzbicki (2008), Brünig, Brenner, and Gerke (2015), Brünig, Gerke, and Schmidt (2018), Danas and Ponte Castañeda (2012), Driemeier et al. (2010), Dunand and Mohr (2011), Liu, Kang, and Ge (2019), Liu, Wong, and Guo (2016), and Nahshon and Hutchinson (2008) among others. However, in the design process of such tests, geometrical constraints from the available material have to be considered. Moreover, the extreme strength of the material also limits the size (i.e. the section) of the specimen. Furthermore, due to the expected anisotropy, some mechanical tests have to be reproduced in different material orientations.

As a summary, from the mechanical tests, the elasto-plastic parameters are first calibrated by considering a virgin material. In other words, we neglect the disparities created by the damage parameters between the microscopic matrix hardening properties and the apparent macroscopic ones. This assumption is usually applied for most metallic alloys since, providing a relatively low initial porosity, the damage parameters have generally a low influence on the apparent hardening properties. Also, we assume that the elasto-plastic behaviour does not exhibit anisotropy, the latter being limited to the porosity evolution and coalescence stage. The resulting plastic behaviour is then compared and validated with the experimental results. Besides, the stress conditions are evaluated at expected failure initiation points to analyse the stress state space covered by the mechanical tests.

Afterwards, we exploit the inclusions properties from the microstructure analyses to characterise the damage-related parameters. Indeed, those values serve as inputs to cell simulations which allow in return calibrating the Gurson growth and coalescence parameters. Moreover, we establish the calibration of characteristic lengths on the microstructure ones. Furthermore, the nucleation model is entirely based on the conclusions drawn from the microstructure observations performed post-mortem along the specimen loading axis. It consists in an extended version of the model of Beremin (1981) to anisotropic cases. This model, even though not all its capabilities are exploited in this work, allows reproducing the failure anisotropy observed during the mechanical campaign. Its predictions are validated by comparing the fracture strain as well as the porosity distributions to their experimental counterparts.

Finally, the effect of the shear induced growth parameter, see Eq. (3.27), is studied, and the damage-to-crack transition framework is applied ro reproduce the failure mode experimentally observed on round bars and groove specimens. The numerical results are then discussed. Guidelines to improve either the calibration or the materiel model are examined. Namely, we discuss how to use unexploited mechanical tests, such as the Compact Tension Specimen (CTS) or the Double-Edge Notched Tensile Specimen (DENT).

Consequently, this chapter is outlined as follows. At first, we present the results of the experimental campaign in Section 4.1. Namely, preliminary microstructure analyses are presented in Section 4.1.1 before the actual mechanical tests in Section 4.1.2. We also present the void fraction analysis in Section 4.1.3. Those experimental tests have been realised by Marie-Stéphane Colla and Matthieu Marteleur from UCLouvain. We then address the elasto-plastic law in Section 4.2 as a first estimation of the material behaviour. Afterwards, the damage related parameters for the non-local micromechanical-based model are determined in Section 4.3. Assumptions are first discussed in Section 4.3.1. Growth and coalescence related parameters are deduced from the material microstructure and from the cell experiments performed by

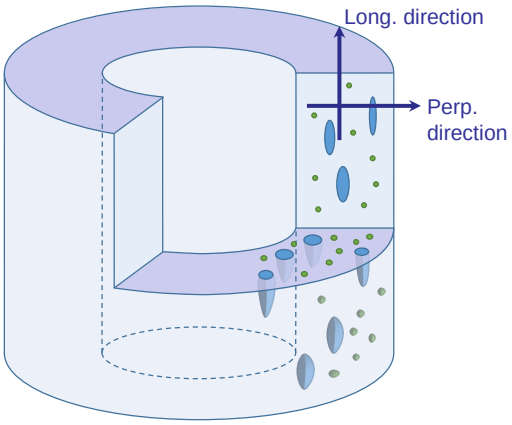

FIGURE 4.1: Schematic representation of the inclusion populations observed inside the studied material.

Van-Dung Nguyen in Section 4.3.2. The model characteristic lengths are evaluated in Section 4.3.3. Section 4.3.4 is devoted to the development of the nucleation model, its calibration and its validation. Then, the shear-induced growth parameter effect is the topic of Section 4.3.5. Finally, Section 4.4 is devoted to the damage to crack transition. In particular, the predicted crack patterns are compared to the experimental failure paths.

4.1 Experimental campaign

In this section, we detail the experimental campaign on which the calibration is based. Experimental tests and result analyses performed by Marie-Stéphane Colla and Matthieu Marteleur from UCLouvain are presented. At first, their preliminary microstructure analysis, performed on the raw material is described Section 4.1.1. In particular, a thorough analysis of the inclusions properties was carried. Next, Section 4.1.2 gather the results of their mechanical tests. SEM images of some failure surfaces are presented and discussed. Additional tests involved in this campaign, but which are not yet exploited in the following work, are not presented for conciseness. Finally, Section 4.1.3 gathers the microstructure porosity analysis performed on specimen post-mortem, i.e. after the mechanical failure.

The specimens are extracted from a forged tube, see Fig. 4.1. From now on, due to the tube anisotropy from which the specimens are extracted, we designate by the longitudinal direction (abbreviated by "long.") all properties links to the direction along the tube axis. Conversely, the perpendicular direction ("perp.") apply on properties related to any direction perpendicular to the blank axis, i.e along the tube thickness or circumference.

4.1.1 Preliminary analysis

In preparation to the mechanical tests, different analyses were performed a priori on the raw material by the UCLouvain in order to assess the chemical, mechanical and micromechanical properties of the studied high-strength steel. An anisotropic behaviour is expected. It would result from the manufacturing process of the studied material which is under the shape of tubular blanks obtained by forging. The main relevant results of this analysis performed by Marie-Stéphane Colla and Matthieu Marteleur are gathered here below.

At first, an optical emission spectrometry (ICP-OES) has been performed to determine the chemical composition. Therewith, the crystalline properties of the material were analysed by x-ray diffraction in order to determine the nature of the phase in the material. Coupled

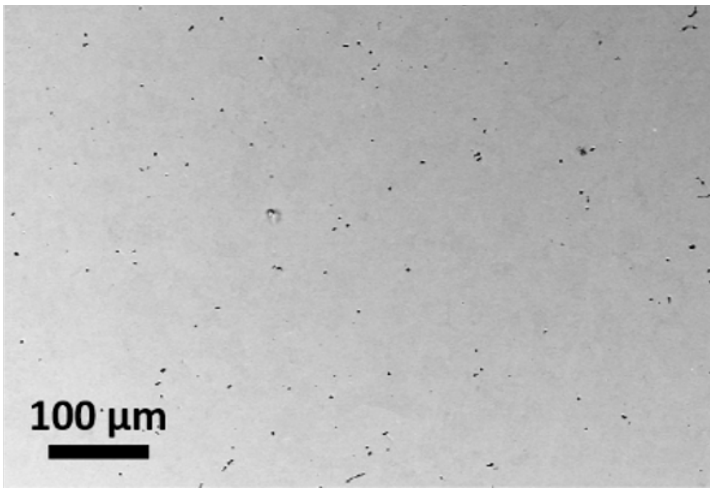

(a)

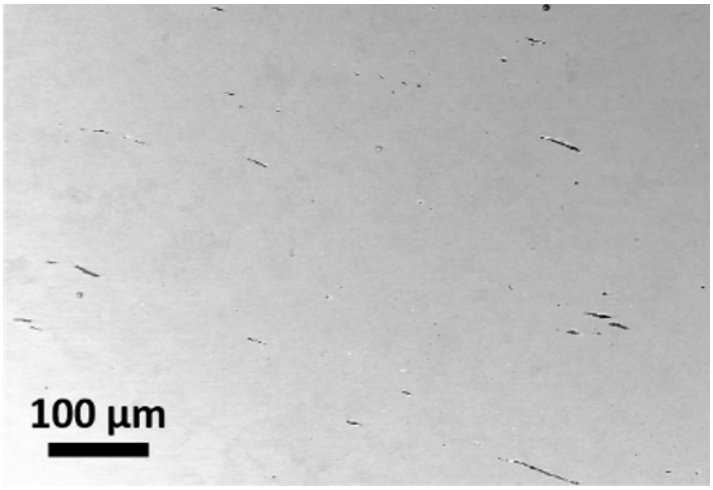

(b)

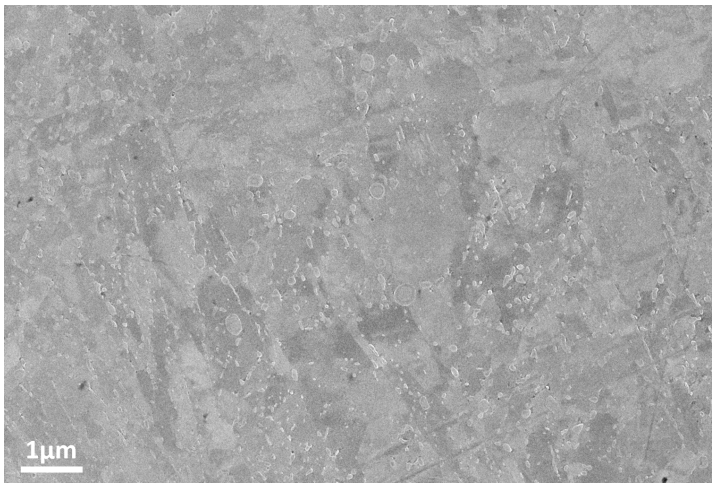

(c)

FIGURE 4.2: Inclusions populations observed under SEM: MnS inclusions in a direction (a) parallel to the blank axis, and (b) perpendicular to it; (c) carbides inclusions.

with a scanning electron microscope (SEM) analysis, a martensite phase is identified. Besides, diffraction results do not show preferential direction in the crystal texture. Therefore, plastic flow anisotropy is unlikely. This assumption will be verified in Section 4.1.2.1 and 4.2.2.

Furthermore, microstructural analyses were performed using a scanning electron microscope (SEM). This microscope is equipped with a detector suited for energy dispersive X-ray spectrometry. After image post-processing, they allow identifying the nature of the inclusions on pictures like on Fig. 4.2. Other geometrical properties are obtained by reproducing the methodology developed by Hannard et al. (2016). Moroever, this operation is repeated in two different directions to assess the material anisotropy.

This analysis highlights two populations of inclusions in the microstructure as schematised on Fig. 4.1. On the one hand, the largest population (in size) consists in highly-elongated MnS precipitates, around 20 [μm] in length, aligned along the blank axis. Indeed, they are visible as small disks on Fig. 4.2a taken parallel to the axis, and under small rods in a perpendicular direction on Fig. 4.2b. On the other hand, the second family is made of small spherical carbide particles of 0.06 [μm] in diameter (Fig. 4.2c).

More precisely, MnS inclusions are under the shape of prolate spheroids[2]. Resulting from the forging process, they are oriented along the forging direction as depicted on Fig. 4.1. Depending on the direction, one will observe circular inclusions in the tube axis (Fig. 4.2a) or rods in other perpendicular directions (Fig. 4.2b). The aspect ratio (width on length ratio) is estimated to be at around 16. However, it is probably higher as a small misalignment with the inclusion axis leads to a large underestimation of the real aspect ratio. The volumic fraction is equal to 2×10^{-3} and is extracted from the surface fraction in either directions. The voids are randomly distributed inside the metallic matrix as on Figs. 4.2a and 4.2b. Their mean inter-distance is almost isotropic and around 100 [μm]: the voids are separated by an average inter-distance of 120 [μm] in the long. direction and by 80 [μm] in the perp. direction. However, locally, inclusions are much closer and are regrouped into clusters. Those have an harmful effect on the material ductility as they are privileged sites of coalescence onset (Pineau, Benzerga, and Pardoen, 2016).

Besides, between those large MnS inclusions are spread smaller carbide particles inside the matrix as observed on Fig. 4.2c. Their size is around 60 ± 20 [nm] in diameter (i.e. at least 100 times smaller than MnS particles) with an aspect ratio close to 1. However, these small spheres account for 7.5% of volume fraction, which is 10 times higher than MnS inclusions.

Some expectations on the failure process can already be drawn from this microstructure analysis but they need to be completed with post-mortem analyses in Sections 4.1.2 and 4.1.3. Based on the microstructure, it is likely that MnS inclusions, as the largest population in size, will drive the failure process. Their highly-elongated shape will induce a failure anisotropy which needs to be assessed by the mechanical campaign tests.

4.1.2 Mechanical tests campaign

In this section, the mechanical test campaign is presented as well as the experimental results. In particular, each test configuration, its geometry and its purpose are detailed. The failure surface is also described. Most of those tests consist of applying a uniaxial tensile load on a steel sample with a particular geometry and observing the applied force evolution in terms of the elongation or striction respectively measured with an extensometer or a strictometer. All results are scaled using the initial yield stress τ_{Y0} and eventually, a reference cross-section.

In the literature, many authors (see the review by Pineau, Benzerga, and Pardoen (2016)) have demonstrated the predominant impact of the stress state on the experimental ductilities.

[2]Similarly to a rugby ball, a prolate spheroid is an ellipsoid of revolution, for which the larger demi-axis is perpendicular to the symmetry plane (in which both other demi-axes are equal), by opposition to an oblate spheroid.

The stress state, $\boldsymbol{\sigma}$ is defined (in absence of anisotropy) through its three principal stress values σ_{I}, σ_{II} and σ_{III} (such as $\sigma_{\mathrm{I}} > \sigma_{\mathrm{II}} > \sigma_{\mathrm{III}}$), which basically correspond to the eigenvalues of the tensor $\boldsymbol{\sigma}$. Equivalently, $\boldsymbol{\sigma}$ can be characterised through a combination of its three invariants:

- the hydrostatic pressure p_σ

$$p_\sigma = \frac{1}{3}\mathrm{tr}\left(\boldsymbol{\sigma}\right) = \frac{1}{3}\left(\sigma_{\mathrm{I}} + \sigma_{\mathrm{II}} + \sigma_{\mathrm{III}}\right) , \tag{4.1}$$

  which is equal to $\frac{1}{3}I_1$, the first invariant of the stress tensor;

- the von Mises equivalent stress σ^{eq}

$$\sigma^{\mathrm{eq}} = \sqrt{\frac{3}{2}\boldsymbol{\sigma}^{\mathrm{dev}} : \boldsymbol{\sigma}^{\mathrm{dev}}} = \sqrt{\frac{1}{2}\left(\sigma_{\mathrm{I}} - \sigma_{\mathrm{II}}\right)^2 + \left(\sigma_{\mathrm{II}} - \sigma_{\mathrm{III}}\right)^2 + \left(\sigma_{\mathrm{III}} - \sigma_{\mathrm{I}}\right)^2} , \tag{4.2}$$

  introducing $\boldsymbol{\sigma}^{\mathrm{dev}}$, the deviatoric part of $\boldsymbol{\sigma}$, which is related to the J_{σ_2}, the second invariant of the deviatoric stress tensor following $\sigma^{\mathrm{eq}} = \sqrt{3J_{\sigma_2}}$;

- the third invariant of the deviatoric stress tensor J_{σ_3}

$$J_{\sigma_3} = \det \boldsymbol{\sigma}^{\mathrm{dev}} = \left(\sigma_{\mathrm{I}} - p_\sigma\right)\left(\sigma_{\mathrm{II}} - p_\sigma\right)\left(\sigma_{\mathrm{III}} - p_\sigma\right) . \tag{4.3}$$

In general, it is more convenient to work with the equivalent stress σ^{eq} and the dimensionless parameters T and ζ. The stress triaxiality T corresponds to the dimensionless pressure $T = \dfrac{p_\sigma}{\sigma^{\mathrm{eq}}}$. The normalised third invariant ζ (Bai, Teng, and Wierzbicki, 2009; Dunand and Mohr, 2011) is the normalised version of J_{σ_3}:

$$\zeta = \frac{27 \det \boldsymbol{\sigma}^{\mathrm{dev}}}{2{\sigma^{\mathrm{eq}}}^3} \text{ with } -1 \leqslant \zeta \leqslant 1 , \tag{4.4}$$

so-called in the following the Lode variable. Besides, alternative definitions exist. The Lode angle θ_{L}, defined as

$$\zeta = \cos\left(3\theta_{\mathrm{L}}\right) \text{ with } 0 \leqslant \theta_{\mathrm{L}} \leqslant \frac{\pi}{3} , \tag{4.5}$$

has the advantage to entail a geometric interpretation in the Haigh–Westergaard stress space. A normalised version of the Lode angle, $\bar{\theta}_{\mathrm{L}}$, related to the previous definitions by

$$\bar{\theta}_{\mathrm{L}} = 1 - \frac{6\theta_{\mathrm{L}}}{\pi} \text{ with } -1 \leqslant \bar{\theta}_{\mathrm{L}} \leqslant 1 , \tag{4.6}$$

is also sometimes used (Bai, Teng, and Wierzbicki, 2009).

Depending on the specimen geometry, different ranges of stress state, defined in terms of stress triaxiality and Lode variable, can be covered. Spanning a large spectrum of stress states therefore requires several test geometries. The expected stress state is granted, in some cases, by analytical expressions. However, most of the time, finite element simulations are needed to determine its evolution during the process (see Section 4.2.2). Besides, when it is possible, a ductility measure specific to each specimen is defined either in terms of stress, strain or specific energy.

In order to evaluate the failure anisotropy suspected from the manufacturing process and observed in Section 4.1.3, some tests are reproduced using specimens sampled along different directions. The specimen orientation is respectively qualified of longitudinal ("long.") or perpendicular ("perp.") depending whether the loading axis is aligned or perpendicular to the tube axis.

The mechanical tests are grouped according to the stress conditions or their geometries. One can distinguish in this work the following traction tests: the round bars under axisymmetric conditions (see Section 4.1.2.1); the grooved plates under plane strain conditions (see Section 4.1.2.2); and the flat bars under plane stress condition, (see Section 4.1.2.3). Most of them differ from one to another by the presence or not of a notch. The notch consists in a geometrical defect (circular, v-shaped,...) which locally modifies the stress conditions (usually, by increasing the stress triaxiality, see the work by Kiran and Khandelwal (2014) for instance). Therewith, the ductility between those tests is compared through a strain measure: the mean true strain at failure, $\bar{\epsilon}_{\mathrm{f}}$ which is, from the equivalent plastic strain measure definition, equal to

$$\bar{\epsilon}_{\mathrm{f}} = \sqrt{\frac{2}{3}\left(\epsilon_{\mathrm{pf}_1}^2 + \epsilon_{\mathrm{pf}_2}^2 + \epsilon_{\mathrm{pf}_3}^2\right)}, \tag{4.7}$$

where ϵ_{pf_i} are the principal components of the plastic strain tensor at fracture. These components are approximated using the geometrical change between the initial reference geometry and the corresponding final one, customary measured post-mortem. The exact expression of Eq. (4.7) is adapted to each case. This measure has the main advantage to be gauge-length independent, compared to the drop point on the force-displacement curve, or compared to an extension measure for example.

In addition to those tensile tests, others mechanical tests, for which results are available (or partially) but not yet exploited, have been performed, and can be used to enhance the calibration procedure. Namely, Arcan specimens (Fagerholt et al., 2010) can reproduce various tensile or shear conditions depending on the loading direction. Besides, the Compact Tension specimen (CTS), a pre-cracked specimen involving a stable crack propagation allows assessing the failure energy as well as the crack advance through partial unloading during the experiments (this geometry has been previously involved in Section 2.4.3). The CTS was extracted with different sampling orientations to assess the anisotropy. Moreover, Double-Edge Notched Tensile (DENT) specimens with different ligament sizes were involved in the campaign to assess the essential work of failure (Pardoen, Marchal, and Delannay, 2002). Furthermore, strain-rate dependency was explored using Hopkinson bars.

4.1.2.1 Smooth and notched round bars

These mechanical tests consist in subjecting axisymmetric bars to a uniaxial tensile force. They are performed on specimens sampled in the two different directions, "long." and "perp.". The specimen geometries are represented on Figs. 4.3. Due to stricter geometrical constraints for specimen sampled in the "perp." direction than in the long. one, a smaller version, schematised on Figs. 4.3c and 4.3d with a reference radius $R_0 = 2$ [mm] are involved, compared to the geometry on Figs. 4.3a and 4.3b with $R_0 = 3$ [mm]. For the sake of completeness, samples with a reference radius of 2 [mm] are also extracted in the "long." direction.

The samples on Figs. 4.3a and 4.3c are usually nicknamed "dog-bone" due to their shape, which consists in a central part surrounded by thicker loading grips where the displacement is applied. The traction tests are performed on specimens sampled in the longitudinal direction for three different loading speeds in order to evaluate the strain-rate dependence. Each test is reproduced on three samples to assess the material and experimental variability.

Previous geometries can be modified by adding a circular notch in the central part. The resulting geometries are shown in Figs. 4.3b and 4.3d. The addition of the notch locally increases the stress triaxiality inside the minimum cross-section. Different notch sizes are considered in order to modulate this increase: the smaller the notch radius R_{n} is, the higher is the stress triaxiality.

For these tests, the triaxiality state conditions can be roughly estimated (for design purpose) using the analytical expressions initially developed by Bridgman (1952) or the corrected

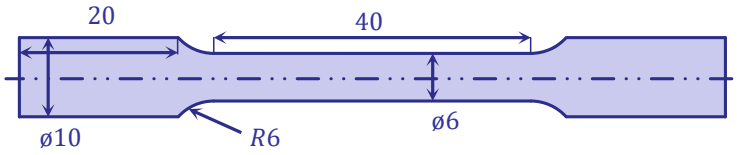

(a) Smooth round bars - $R_0 = 3$ [mm].

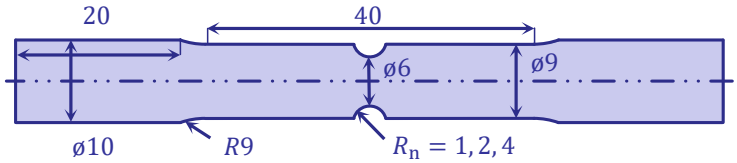

(b) Notched round bars - $R_0 = 3$ [mm].

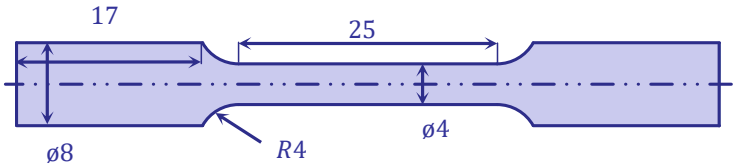

(c) Smooth round bars - $R_0 = 2$ [mm].

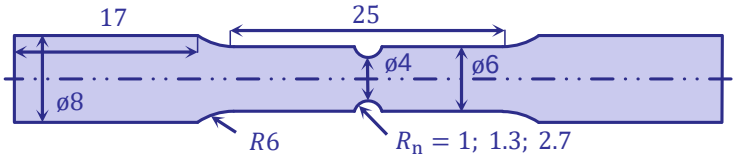

(d) Notched round bars - $R_0 = 2$ [mm].

FIGURE 4.3: Specimen geometries of (a,c) the smooth round bars and (b,d) the notched ones. Dimensions are all in [mm].

version of Bai, Teng, and Wierzbicki (2009). A uniform plastic flow along the radius and non-hardening material are assumed. The formula depends on the ratio R_0/R_n, where R_0 is the minimal cross-section radius and R_n is the notch radius. From Bridgman (1952), the stress triaxiality is estimated by

$$T = \frac{1}{3} + \ln\left(1 + \frac{R_0}{2R_n}\right). \tag{4.8}$$

One can notice that we recover the expected value of 1/3 for the uniaxial tension condition encountered in a smooth round bar, corresponding to an infinite notch radius. The (large) notched specimens correspond to a theoretical triaxiality value T of 0.65, 0.90 and 1.25 respectively for $R_n = 4$, 2 and 1 [mm]. The smaller versions match the same values excepted the smaller notch radius which is not exactly scaled, i.e. one has $T = 0.65$, 0.90 and 1.02 respectively for $R_n = 2.6$, 1.3 and 1 [mm]. Besides, the Lode variable ζ remains unchanged. It stays equal to 1 due to the tensile axisymmetric loading.

The results obtained on round bars are now shown on Figs. 4.4 and 4.5 for a loading speed equal to 1 [mm/min]. Experimental tests performed at higher speeds (10 and 100 [mm/min]) are similar. As we are not focusing on the strain rate effects and as the results do not exhibit significant strain rate effects, they are therefore omitted for conciseness although the implemented Gurson formalism allows considering them. On Fig. 4.4, the evolution of the tensile force is shown in terms of the elongation of the central part on the smooth round bars, and in terms of the diameter reduction for the notched ones. An extensometer with a length $L_0 = 30$ [mm] (resp. 20 [mm]) measures the central part elongation of the smooth specimen with $R_0 = 3$ [mm] (resp. 2 [mm]). The reference section S_0 corresponds to the minimal

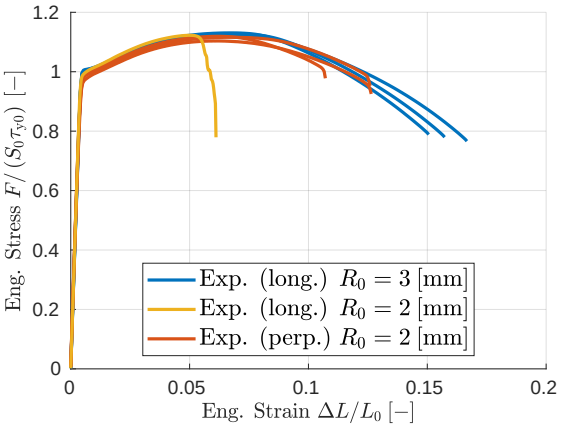

(a) Smooth round bars.

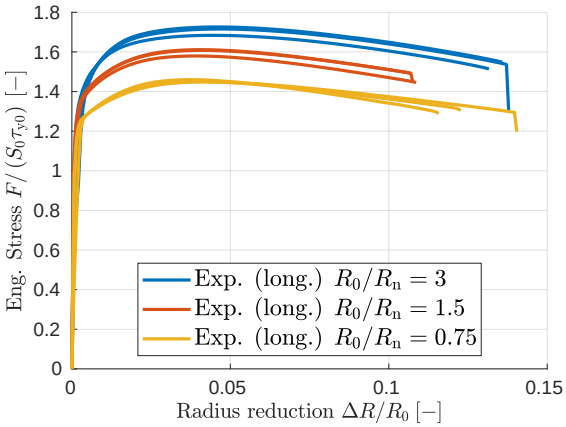

(b) Notched bars - $R_0 = 3$ [mm].

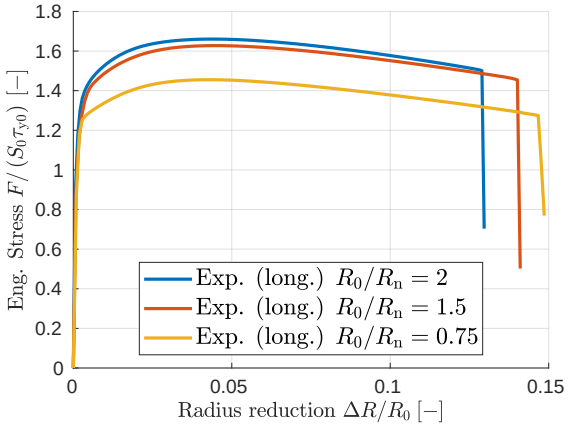

(c) "Long." notched bars with $R_0 = 2$ [mm].

FIGURE 4.4: Experimental measurements of the applied force F in terms of (a) the elongation ΔL for the smooth round bars, and (b-c) of the radius reduction ΔR for the notched bars.

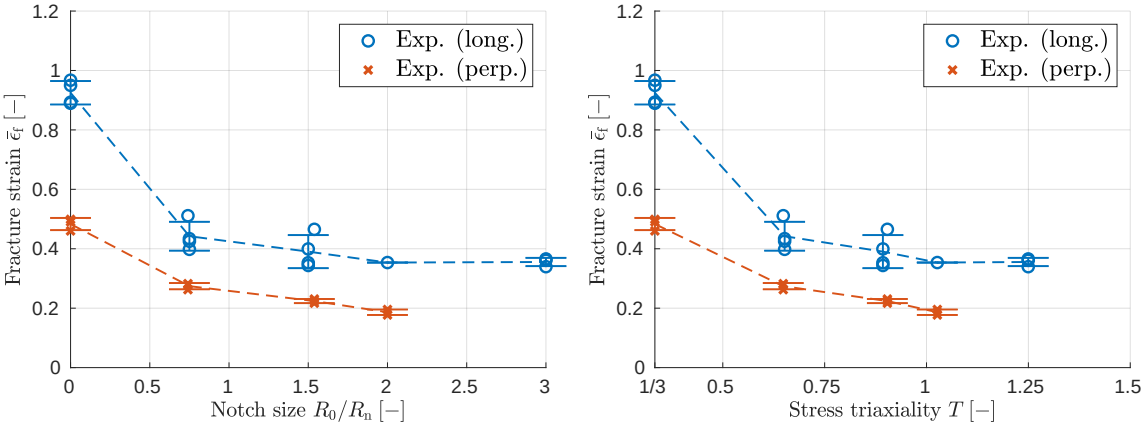

(a) (b)

FIGURE 4.5: Experimental measurements of the fracture strain on the round bars in terms of (a) the notch size and (b) the expected stress triaxiality from Eq. (4.8) in both directions.

cross section πR_0^2. As speculated in Section 4.1.1, no plastic flow anisotropy is visible between the "long." and "perp." direction. Besides, a good correspondence is observed between the smooth specimens with different sizes and directions on Fig. 4.4a. However, we note that one curve ("long. $R_0 = 2$ [mm]") seems to behave differently. This discrepancy is due to the necking zone which was decentered regarding the extensometer bounds. It then results in an underestimation of the elongation after the necking onset. On Figs. 4.4b and 4.4c related to the notched bars, higher levels of stress are obtained with smaller notch radii. This is due to the higher stress triaxiality state obtained when the notch radius is decreased.

Furthermore, the ductility of the material is assessed using the mean true strain at failure $\bar{\epsilon}_\mathrm{f}$ using Eq. (4.7). Given the axisymmetric conditions ($\epsilon_{\mathrm{pf}_2} = \epsilon_{\mathrm{pf}_3}$) and the plastic incompressibility ($\epsilon_{\mathrm{pf}_1} + \epsilon_{\mathrm{pf}_2} + \epsilon_{\mathrm{pf}_3} = 0$), it is evaluated from the diameter reduction measured after the specimen failure as

$$\bar{\epsilon}_\mathrm{f} = 2 \ln \left(\frac{R_0}{R_\mathrm{f}} \right), \tag{4.9}$$

where R_f is the post-mortem minimal cross-section radius. The results obtained for the round bars in both directions are shown on Fig. 4.5 either in terms of the notch size or of the expected stress triaxiality. One can observe that, for a fixed specimen size or direction, a smaller notch radius, or conversely, a higher stress triaxiality, results in a decrease of the ductility. Furthermore, the failure anisotropy suspected in Section 4.1.1 is clearly visible here: the "perp." specimens are globally less ductile than their "long." counterpart with an equivalent triaxiality state. However, this difference decreases when the stress triaxiality increases due to a smaller notch radius.

In addition, the failure surface is analysed on Figs. 4.6, 4.7 and 4.8. In the long. direction, the well-known cup-cone profile is obtained on the smooth round bars as shown on Fig. 4.6a: it consists of a central flat fracture surrounded by a slant crack near the surface. Cracks initiate at the specimen centre and propagate radially until the crack tilts around 45° as shearing takes over. This typical failure profile is even more clearly observed on Fig. 4.7 with the notched specimens.

Observed under a SEM, the central part is shown on Fig. 4.6b for the smooth bar and on Figs. 4.7d, 4.7e and 4.7f for the notched ones. This surface aspect is characteristic to failure by intervoid necking (Pineau, Benzerga, and Pardoen, 2016). Large micrometric dimples are the remnant of the voids formed around MnS particles which coalesce together by tensile internal necking during the last steps of the failure process. At the bottom of the dimples, a part of the inclusion is sometimes still visible (e.g. Fig. 4.7e). Smaller nanometric dimples are the results of voids created from carbides decohesion. However, it is yet not possible to determine at which moment they nucleate. A different surface aspect is obtained near the sample external surface on Fig. 4.6c where coalescence occurs under a higher shear contribution. Similar observations can be made concerning the other specimens.

Besides, the same analysis is performed in the perp. direction. A cup-cone profile is also obtained on Fig. 4.8a. However, the surface aspect is different: the central part seems fibrous. After zooming on Fig. 4.8b, the fibres originate from the prolate MnS inclusions loaded perpendicularly to their length and that have fused together, also by internal necking. Smaller voids formed around Carbides inclusions are also present.

4.1.2.2 Plane strain plates

This mechanical test corresponds to a traction test in plane strain condition. This test is only performed on specimens sampled in the longitudinal direction. The specimen consists in a thick plate with a groove excavated transversely to the loading direction. The corresponding geometry is shown on Fig. 4.9.

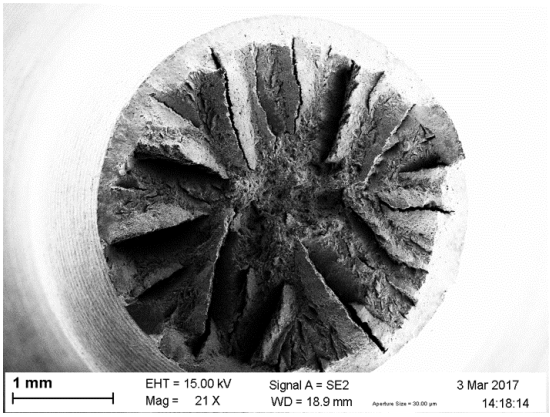

(a)

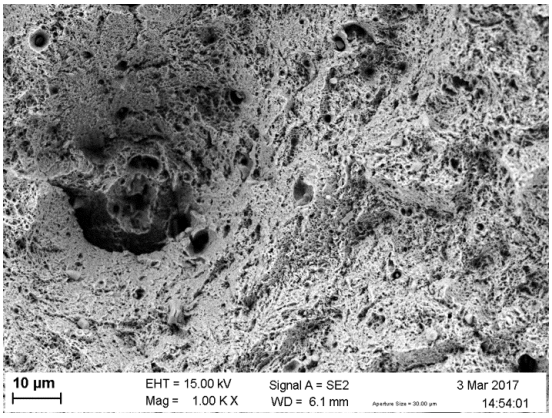

(b)

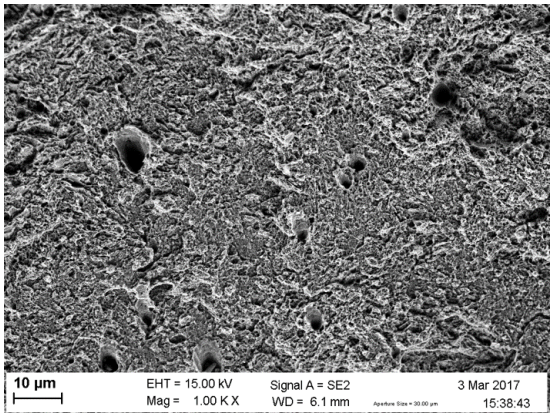

(c)

FIGURE 4.6: SEM pictures of the failure surface for a smooth round bar in the long. direction. (a) General view. (b) Zoom on the central part. (c) Zoom near the edge.

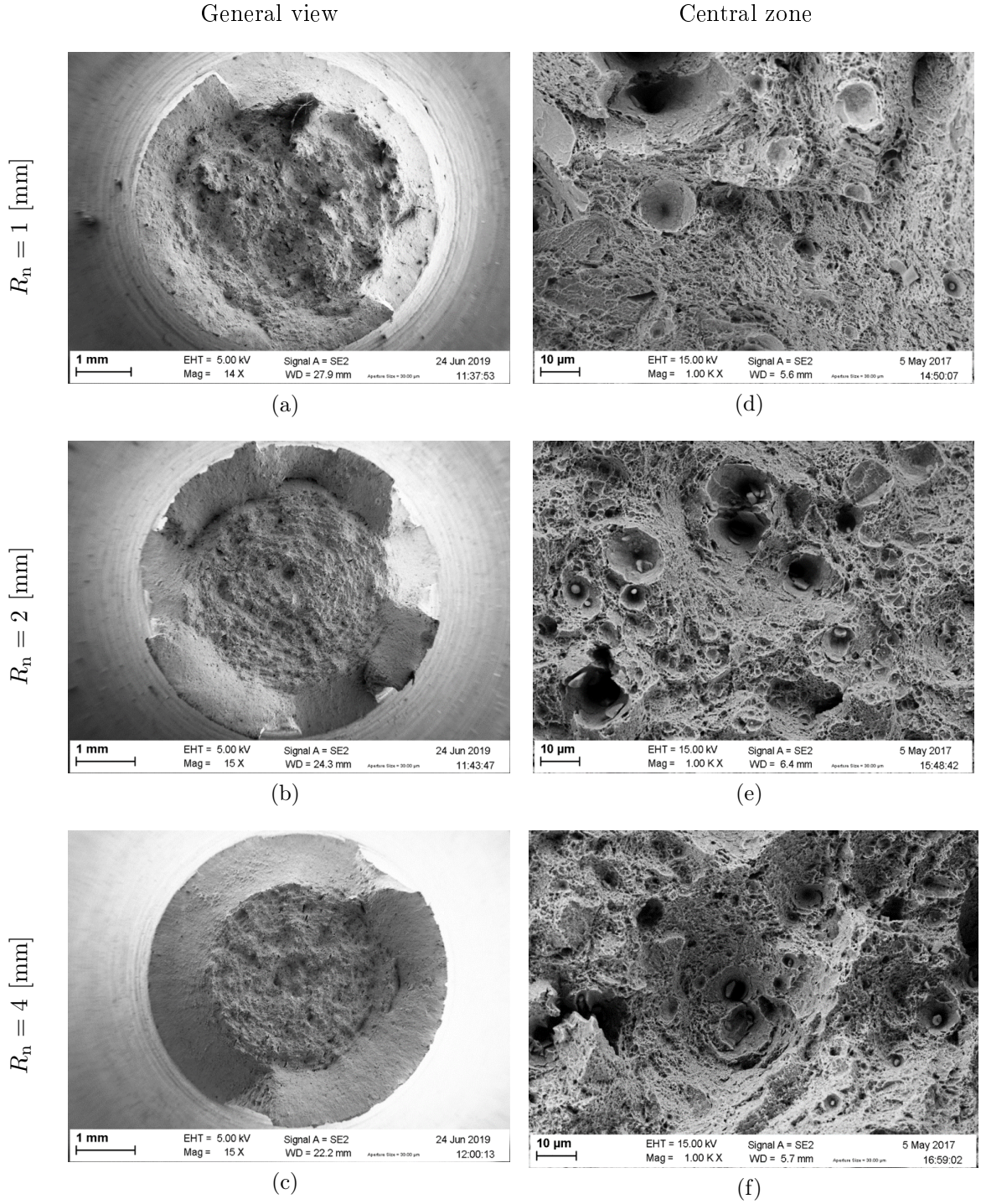

FIGURE 4.7: SEM pictures (a-c) of the failure surface for the notched round bars for the different notch radii in the long. direction. (d-f) Zoom on the central part.

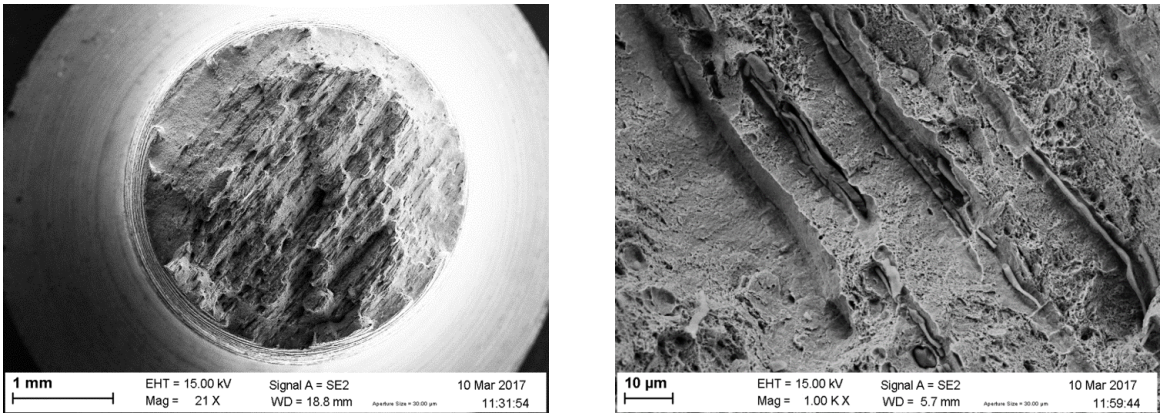

(a) (b)

FIGURE 4.8: SEM pictures of the failure surface for a smooth round bar in the perp. direction. (a) General view. (b) Zoom on the central part.

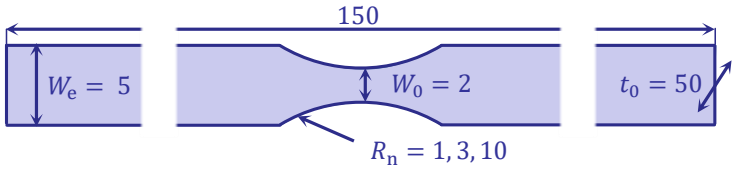

FIGURE 4.9: Specimen cross-section geometries of the grooved plates (in plane strain conditions). Dimensions are in [mm].

Similarly to the notched round bars (see Section 4.1.2.1), different groove radii R_n are considered to vary the stress triaxiality. It increases for smaller notch radii, which can be estimated using the analytical equations developed by Bai, Teng, and Wierzbicki (2009). Following this work, T is approximated by

$$T = \frac{\sqrt{3}}{3}\left[1 + 2\ln\left(1 + \frac{W_0}{4R_n}\right)\right], \tag{4.10}$$

where W_0 is the minimal in-plane thickness (see Fig. 4.9). Hence, one theoretically obtains $T = 1.05$, 0.76 and 0.63 respectively for $R_n = 1$, 3 and 10 [mm]. Meanwhile, the Lode variable ζ is equal to 0 due to the plane strain state.

The loading force evolution is represented on the Fig. 4.10 either in terms of the elongation of the central part measured with an extensometer, and in terms of the thickness reduction of the minimal cross-section measured with a strictometer. The extensometer has a length $L_0 = 18$ [mm]. The applied force is scaled using the reference surface $S_0 = W_0 t_0$ with $t_0 = 50$ [mm], the out-of-plane thickness and $W_0 = 2$ [mm], the in-plane thickness. Once again, reducing the notch radius induces a higher elastic stiffness and a higher level of measured stress due to a higher stress triaxiality in the centre of the specimen.

For this test family, the fracture strain $\bar{\epsilon}_f$ is estimated, given the plane strain state ($\epsilon_{pf_3} = 0$ and thus, $\epsilon_{pf_1} = -\epsilon_{pf_2}$), as

$$\bar{\epsilon}_f = \frac{2}{\sqrt{3}}\ln\left(\frac{W_0}{W_f}\right), \tag{4.11}$$

where W_f is the (in-plane) thickness measured at failure. The experimental measurements are gathered on Fig. 4.11 in terms of the notch size (Fig. 4.11a) and of the theoretical stress

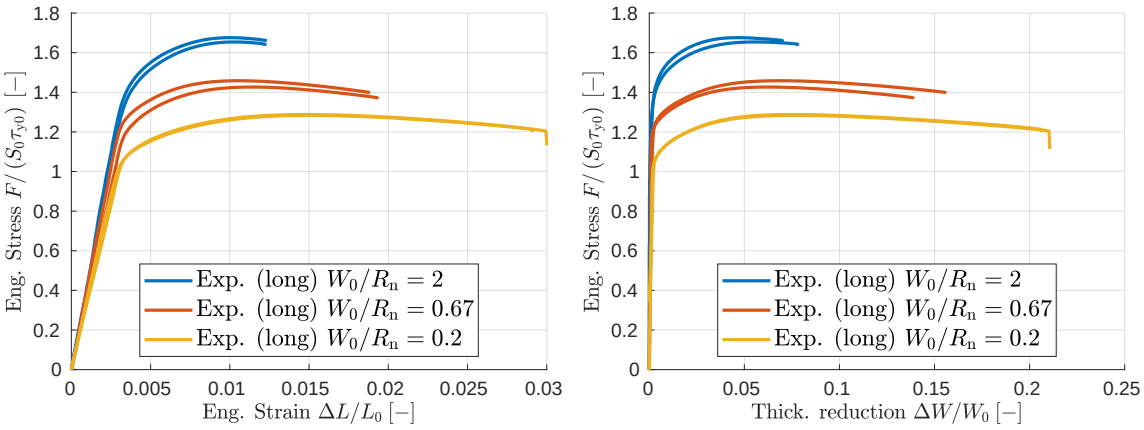

FIGURE 4.10: Experimental measurements of the applied force in terms of (a) the elongation ΔL and (b) of the thickness reduction ΔW for the grooved plates.

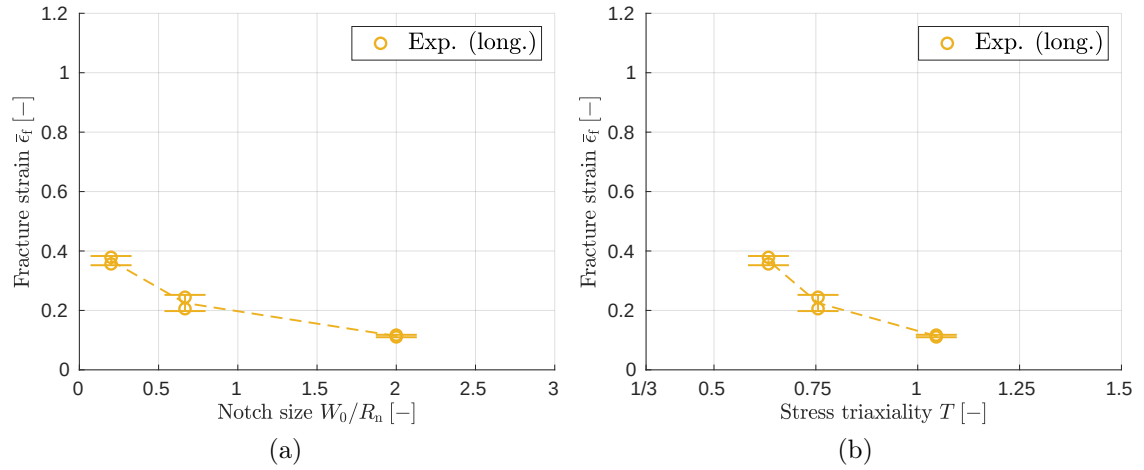

FIGURE 4.11: Experimental measurements of the fracture strain on the grooved specimens in terms of (a) the notch size, and (b) the expected triaxiality from Eq. (4.10).

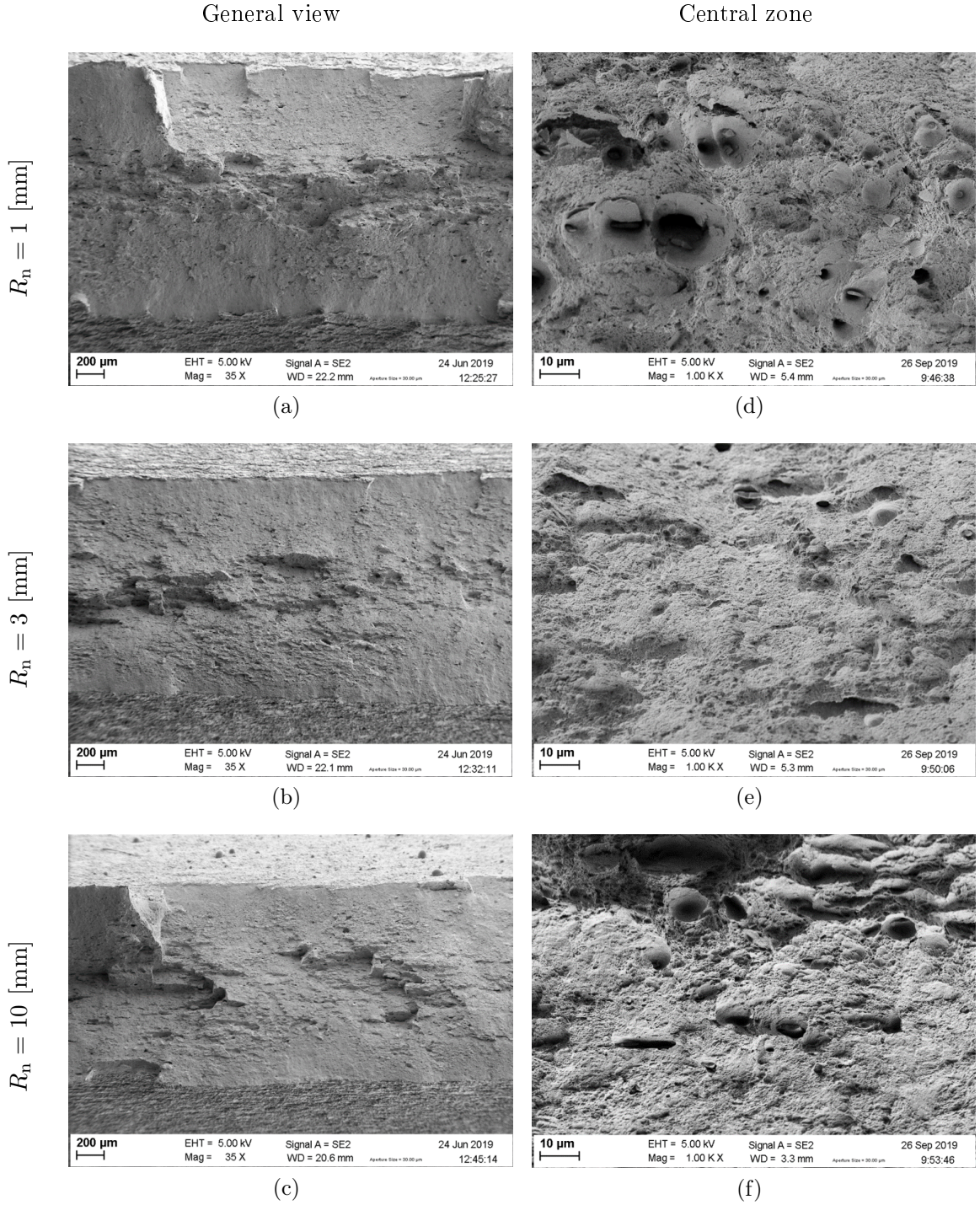

FIGURE 4.12: SEM pictures (a-c) of the failure surface for the grooved plates for the different notch radii in the long. direction. (d-f) Zoom on the central part.

triaxiality (Fig. 4.11b). One can note that the ductility is again decreasing with the notch size, or equivalently, the stress triaxiality. However, the encountered strain values are smaller compared to axisymmetric cases presented on Fig. 4.5b with comparable stress triaxiality. This difference can be explained by an additional shear-induced damage contribution dependent on ζ, which is active in plane strain states, but vacant in axisymmetric stress states.

In addition, Fig. 4.12 shows SEM pictures of the failure surface: a slant fracture is obtained for the three groove radii. The surface aspect includes characteristics of shear failure and intervoid necking. The latter is more visible on the specimen with $R_{\mathrm{n}} = 1$ [mm] where the stress triaxiality is the highest.

4.1.2.3 Plane stress flat bars

This family of mechanical tests involves dog-bone shaped flat specimens in plane stress conditions. This is achieved by using thin plates under uniaxial tension. The corresponding geometries are represented on Fig 4.13. Comparatively to the smooth specimens on Fig. 4.13a, a circular notch is introduced to modulate the stress triaxiality in the minimal cross-section of the specimens on Fig. 4.13b, similarly to the other specimen families.

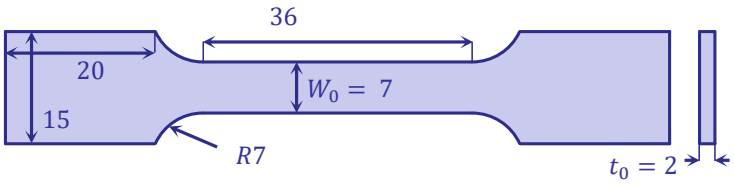

(a) Smooth flat bars.

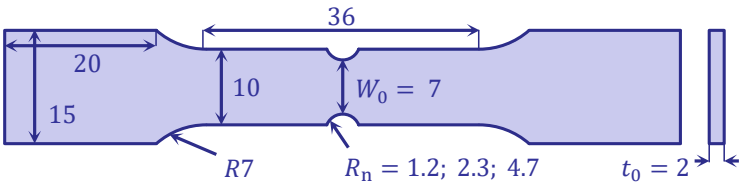

(b) Notched flat bars.

FIGURE 4.13: Specimen geometries of (a) the smooth flat bars and (b) the notched ones. Dimensions are in [mm].

Regarding the encountered stress conditions, the conditions are close to a uniaxial test: the stress triaxiality T is equal to $1/3$ for the smooth bars and slowly increases for smaller notch radius until $\sqrt{3}/3$ (which corresponds to a plane strain state). Besides, due to the plane stress conditions, the lode variable ζ is theoretically linked to the stress triaxiality (Bai and Wierzbicki, 2008; Brünig, Brenner, and Gerke, 2015) as

$$\zeta = -\frac{27}{2} T \left(T^2 - \frac{1}{3} \right) . \tag{4.12}$$

Therefore, its expected value is included between 1 for the uniaxial conditions of the smooth specimen and 0 for the (extreme) plane strain state.

Furthermore, the force evolutions either in terms of the elongation or of the thickness reduction are respectively given on Fig. 4.14a for the smooth flat bars and on Fig. 4.14b for the notched ones. The elongation is measured thanks to an extensometer of 30 [mm] and the reference surface to scale the loading force is equal to $S_0 = W_0 t_0$ with $t_0 = 2$ [mm], the out-of-plane thickness and $W_0 = 7$ [mm], the in-plane thickness.

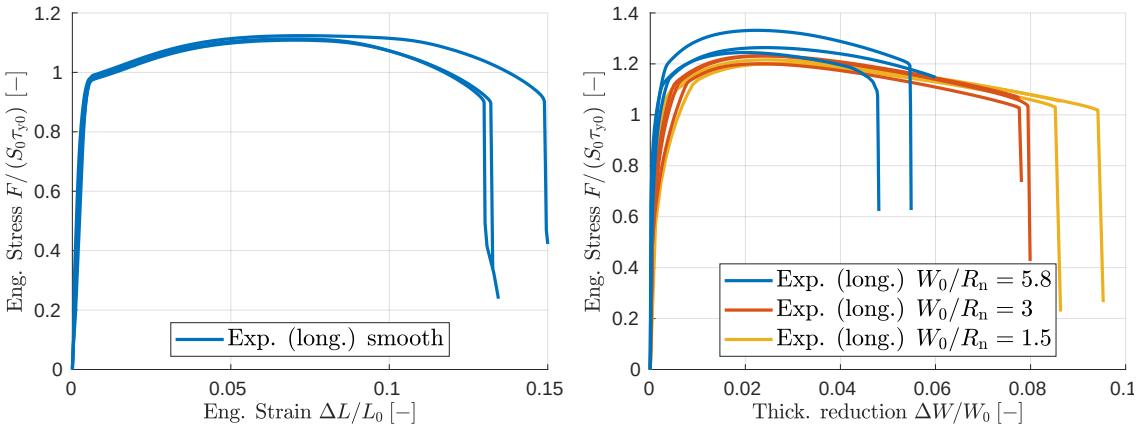

(a) Smooth flat bars. (b) Notched flat bars.

FIGURE 4.14: Experimental measurements of the applied force in terms of (a) the elongation ΔL and (b) the thickness reduction ΔR for the plane stress specimens.

Due to the similarities between the stress states, at least at the initiation, comparable stress values are involved for the smooth flat bars on Fig. 4.14a than for the smooth round bars (Fig. 4.4a). Moreover, reducing the notch radius results again in an increase of measured stress. However, the impact of the notch size is more limited on this specimen family as the range of reachable stress triaxiality value is more limited by the geometry.

Similarly to other tension specimens, the fracture strain is defined here in terms of the reduction of the reference cross-section measured post-mortem. It is obtained by measuring the in-plane thickness at failure W_f and the out-of-plane one t_f. Assuming that the section stays rectangular and applying Eq. (4.9), one has

$$\bar{\epsilon}_\mathrm{f} = \sqrt{\frac{2}{3}\left[\ln\left(\frac{W_0}{W_\mathrm{f}}\right)^2 + \ln\left(\frac{t_0}{t_\mathrm{f}}\right)^2 + \ln\left(\frac{W_0}{t_\mathrm{f}}\right)\ln\left(\frac{t_0}{t_\mathrm{f}}\right)\right]}. \tag{4.13}$$

However, as some experimental measurements are not available for all the samples, we assume in the following that the reduction ratios are equal in both directions. This should induce an underestimation of the real fracture strain. The results are shown on Fig. 4.15. In this case again, we observe a smaller fracture strain when the notch radius decreases.

4.1.3 Post-mortem microstructure analysis

After having performed the mechanical tests up to failure, the microstructure porosity distribution was studied by UCLouvain as follows. Small smooth round bar specimens (Fig. 4.3c) were cut following their axis. Pictures were then taken at different positions away from the crack surface with the electronic microscope (SEM). Some examples of the obtained pictures are shown on Figs. 4.16 and 4.17. Using image-processing, the surface fraction of the MnS inclusions and their associated surrounding cavity is computed. The porosity is then deduced by assuming that the surface fraction is equal to the volumic fraction.[3] The obtained values are then plotted in terms of the distance from the crack surface on Fig. 4.18 for both void populations.

The porosity of both populations is maximum near the crack surface and fades away of the crack. MnS inclusions nucleate very early in the process by particle cracking, on the one hand,

[3] which is the case for random distributed ellipsoidal voids.

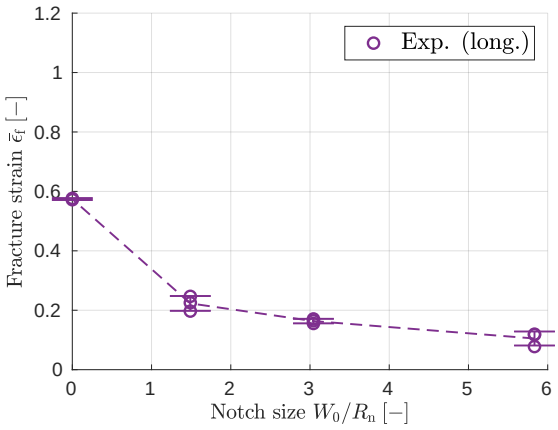

FIGURE 4.15: Experimental measurements of the fracture strain on the plane stress specimens in terms of the notch size.

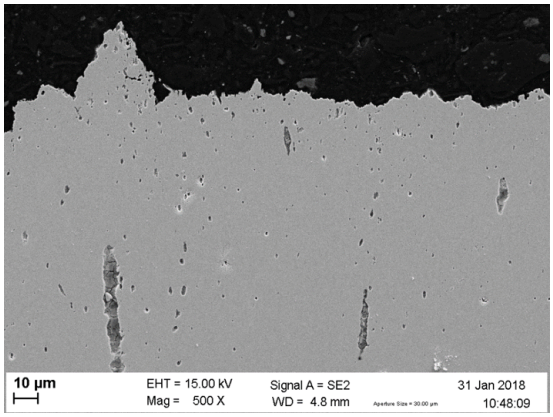

(a)

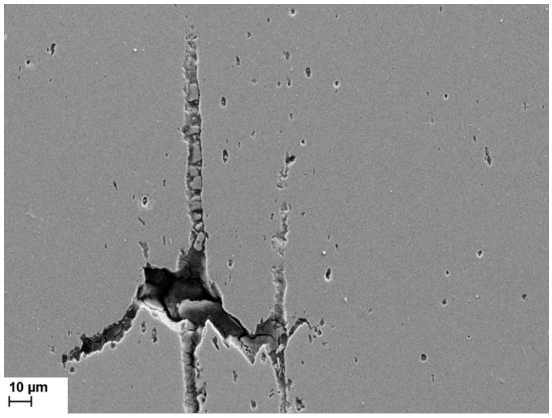

(b)

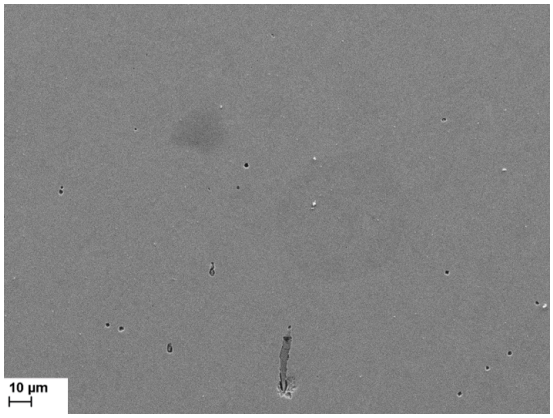

(c)

FIGURE 4.16: Example of SEM images obtained at different distances from the crack surface in the long. direction: (a) below the crack surface; (b) example of void coalescence below the crack surface; (c) far away, at yielding initiation

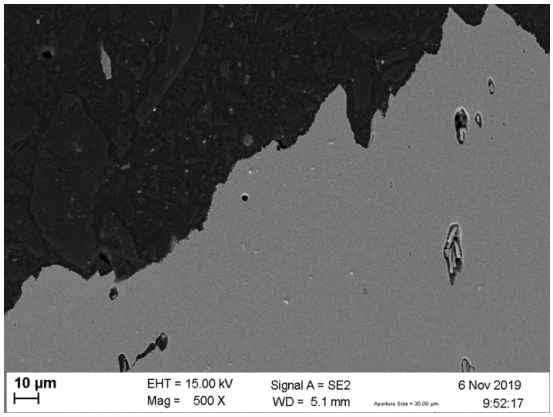

FIGURE 4.17: Example of a SEM image obtained below the crack surface in the perp. direction.

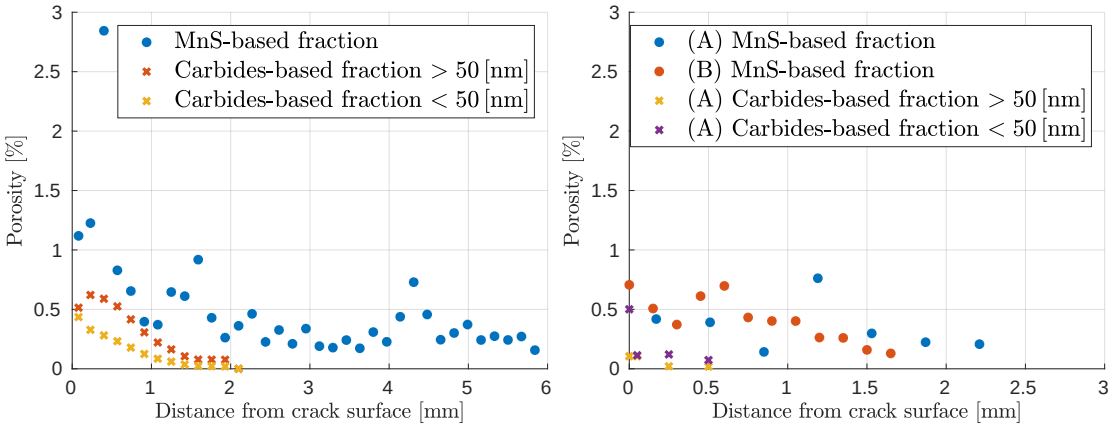

(a) Long. direction (b) Perp. direction

FIGURE 4.18: Experimental measurement of the different porosity populations (MnS and Carbides) in terms of the distance to the crack surface on (a) one specimen sampled in the long. direction and on (b) two specimens (A) and (B) sampled in the perp. direction.

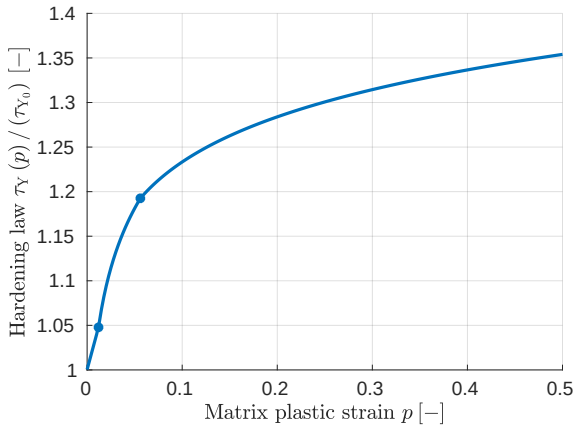

FIGURE 4.19: Evolution of the normalised hardening law function in term of the matrix plastic strain.

in the long. direction (Fig. 4.16c) or by matrix/particle decohesion in the perp. direction. On the other hand, Carbides nucleate later in the process by interface decohesion (see Figs. 4.16a).

The procedure to interpret those results is discussed in Section 4.3.1 once the elasto-plastic behaviour will have been modelled in Section 4.2.

4.2 Calibration and validation of the elasto-plastic behaviour

At first, the elasto-plastic behaviour is adressed. In particular, the calibration of the J2-hardening law is done in Section 4.2.1. Afterwards, each test is simulated in Section 4.2.2 using the freshly-calibrated law. The stress state involved in each specimen is analysed. It is sampled by averaging inside a small box near the point of interest to avoid sampling aliasing. A synthesis is performed in Section 4.2.3.

4.2.1 Calibration of the hardening law

The identification is performed by considering the smooth round bars in the long. direction (see Fig. 4.3a). More details are provided in Section 4.2.2.1 about the numerical simulations. At this point, we assume that the macroscopic plastic flow is equivalent to the microscopic or matrix one. This hypothesis is reasonable since the damage parameters have a low influence on the apparent hardening curve, at least on the curve beginning. We also suppose that this latter obeys to an isotropic J2 elasto-plastic law. Both assumptions will be verified in Section 4.2.2 by reproducing experimental tests under different stress states.

Therefore, the hardening curve has to be identified as a function which expresses the equivalent Kirchhoff stress in terms of the (natural) plastic strain. Prior to the necking, the material behaviour within the gauge length can be considered as uniform: the true stress and true strain measures during this stage can be used to identify the plastic hardening by curve fitting. The hardening curve is expressed by a linear relation followed by a power one until the peak stress, which corresponds to the necking initiation.

Once necking starts, these true stress-true strain curves are no longer valid since the deformation is no longer uniform. To ascertain the actual hardening behaviour during the necking stage, finite element computations of the smooth round bars with $R_0 = 3$ [mm] are performed. Those simulations have been performed by Van-Dung Nguyen. The parameters of post-necking hardening curves can be identified by matching the engineering stress-strain curves obtained

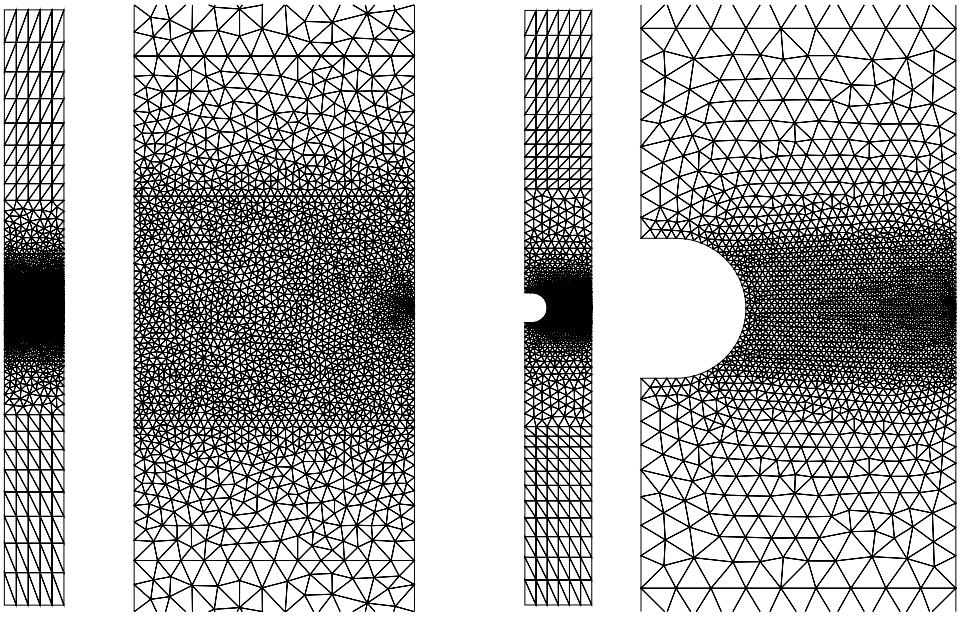

(a) Smooth round bar with $R_0 = 3$ [mm]; 5196 elements.

(b) Notched round bar with $R_0 = 3$ [mm], $R_n = 1$ [mm]; 4674 elements

FIGURE 4.20: Simulated mesh and zoom on its central part for two round bars: (a) a smooth round bar ($R_0 = 3$ [mm]) and (b) a notched round bar ($R_0 = 3$ [mm], $R_n = 1$ [mm]).

by the finite element and by experimental tests. During the necking stage, another power law is assumed.

As a result, the following hardening law $\tau_Y(p)$ is used:

$$\tau_Y(p) = \begin{cases} \tau_{Y0} + hp & \text{if } p \leq p_1\,, \\ \tau_{Y1}\left(\dfrac{p}{p_1}\right)^{n_1} & \text{if } p_1 < p \leq p_2\,, \\ \tau_{Y2}\left(\dfrac{p}{p_2}\right)^{n_2} & \text{if } p_2 \leq p\,. \end{cases} \tag{4.14}$$

which is graphically represented on Fig. 4.19.

4.2.2 Validation of the hardening law

In order to validate the hardening law of Eq. (4.14), experimental tests presented in Section 4.1.2 are reproduced. A J2-plastic flow is used under a large strain formulation. Time integration is performed using the dynamic scheme presented in Section 2.3.2.2. Parabolic elements are used within a continuous Galerkin framework. A mesh size sensitivity analysis has been systematically performed to ensure a sufficiently fine mesh to produce converged results within the studied range. Nevertheless, this analysis is omitted for conciseness.

4.2.2.1 Round bars

The round bar tests are reproduced using axisymmetric finite element computations. We illustrate on Fig. 4.20 the involved meshes for two round bars. Only the central part inside the extensometer region is modelled. Around 50 elements are used along the radius in the central zone or inside the notch, with a slightly finer zone near the failure initiation point. A

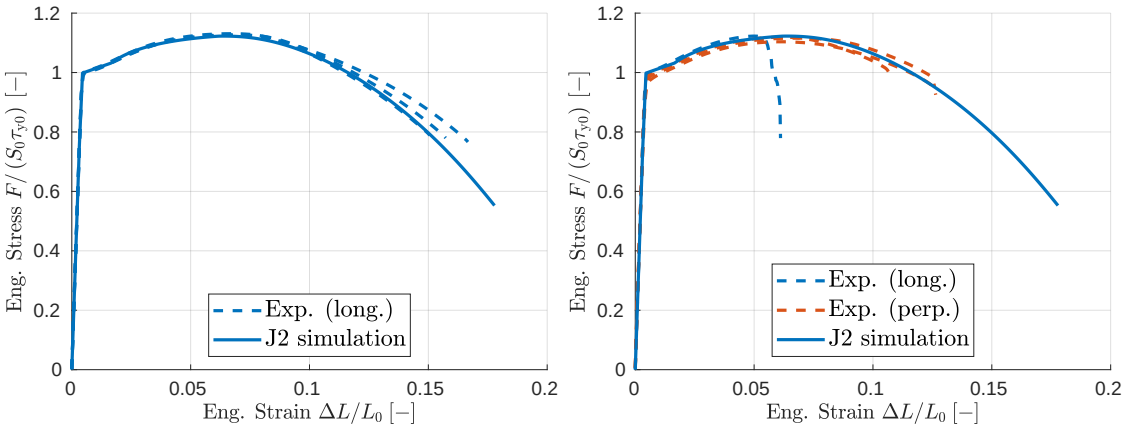

(a) $R_0 = 3$ [mm] (b) $R_0 = 2$ [mm]

FIGURE 4.21: Variation of the applied force as a function of the elongation ΔL for the smooth round bars simulated with the J2-plastic law (continuous lines) and comparison with the experimental measurements (discontinuous lines).

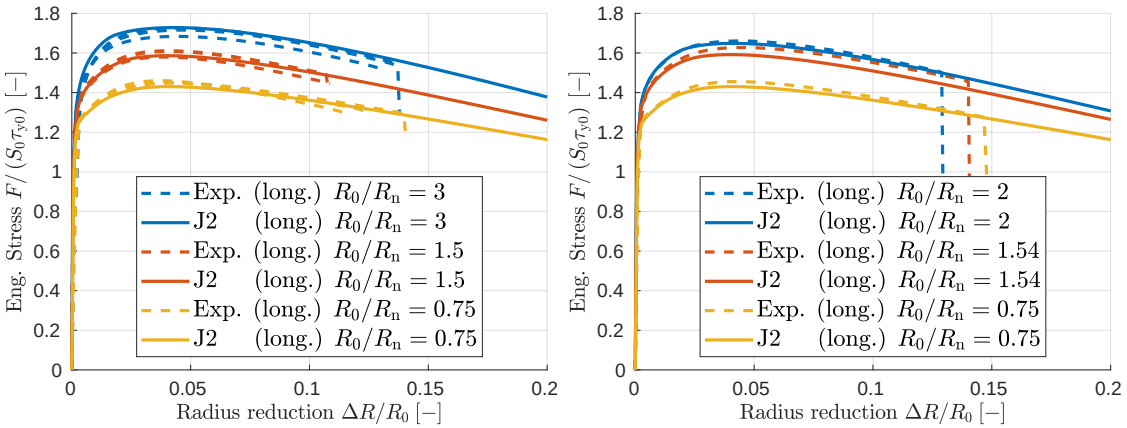

(a) $R_0 = 3$ [mm] (b) $R_0 = 2$ [mm]

FIGURE 4.22: Variation of the applied force as a function of the radius reduction ΔR for the notched round bars simulated with the J2-plastic law (continuous lines) and comparison with the experimental measurements (discontinuous lines).

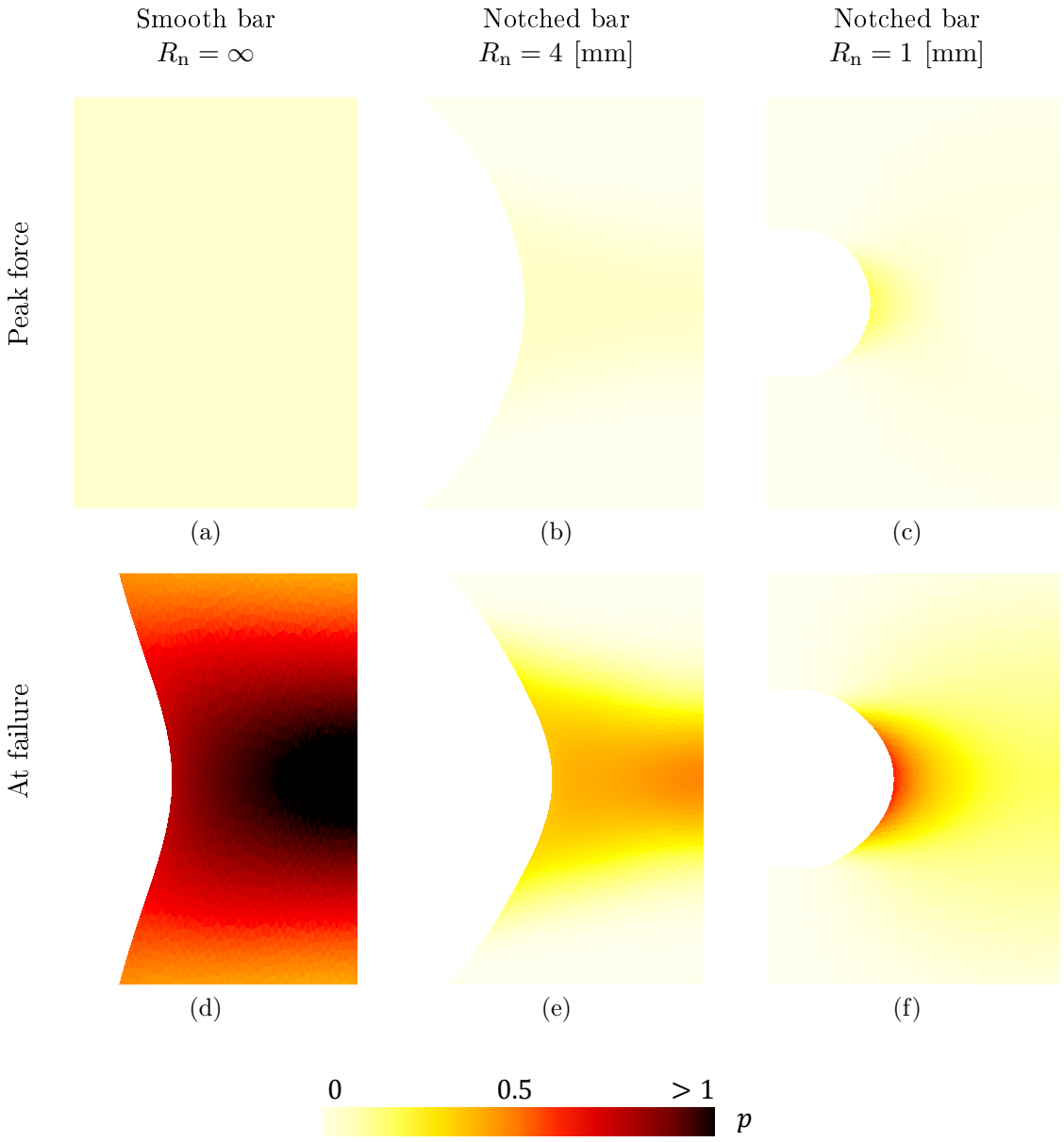

FIGURE 4.23: Distribution of the plastic strain p (a-c) when the peak stress is reached and (d-f) when the fracture strain is reached in the deformed configuration for (left) the smooth round bar, (centre) the notch round bar $R_n = 4$ [mm] and (right) the notch round bar $R_n = 1$ [mm], all with $R_0 = 3$ [mm].

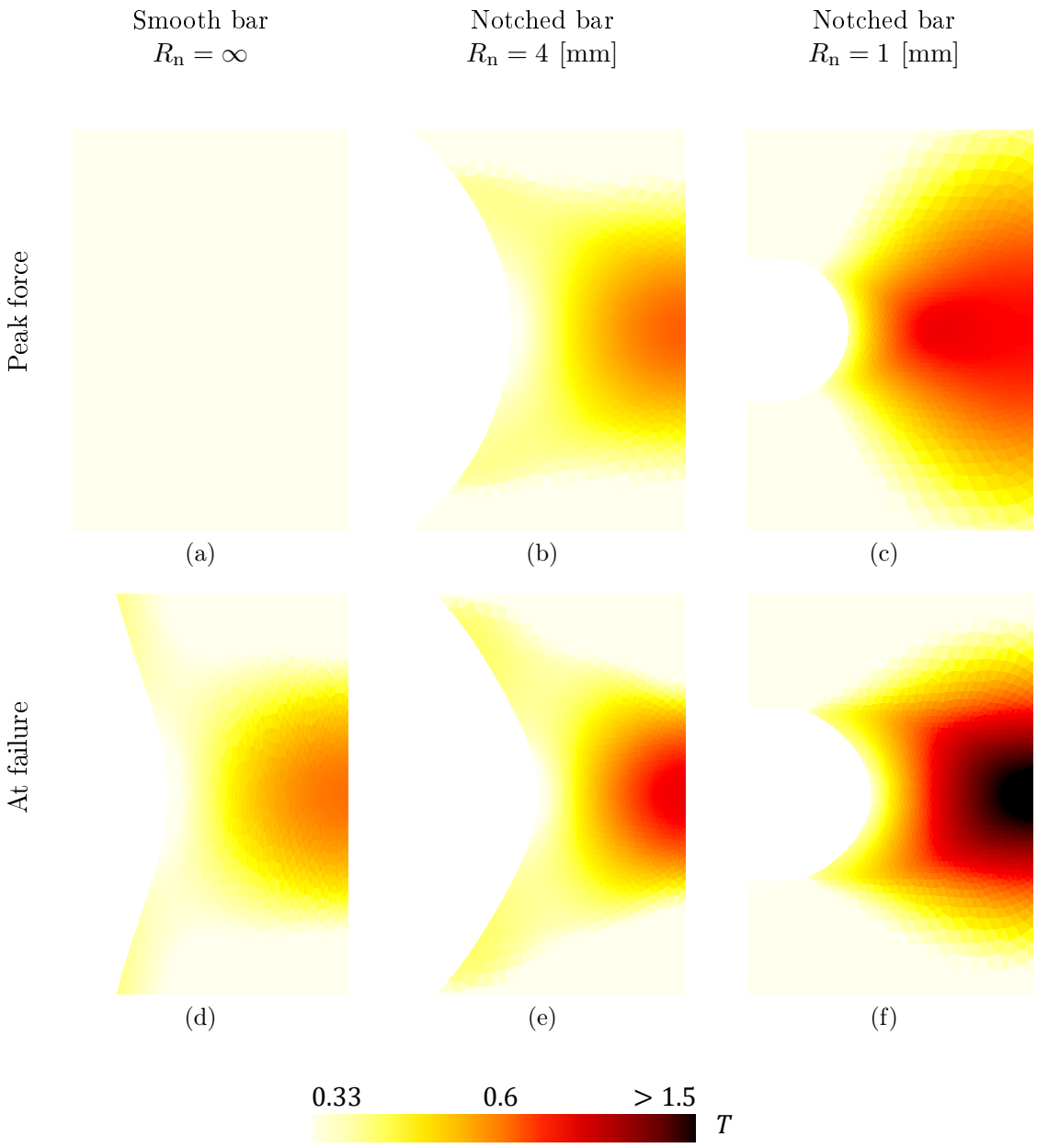

FIGURE 4.24: Distribution of the stress triaxiality T (a-c) when the peak stress is reached and (d-f) when the fracture strain is reached in the deformed configuration for (left) the smooth round bar, (centre) the notch round bar $R_n = 4$ [mm] and (right) the notch round bar $R_n = 1$ [mm], all with $R_0 = 3$ [mm].

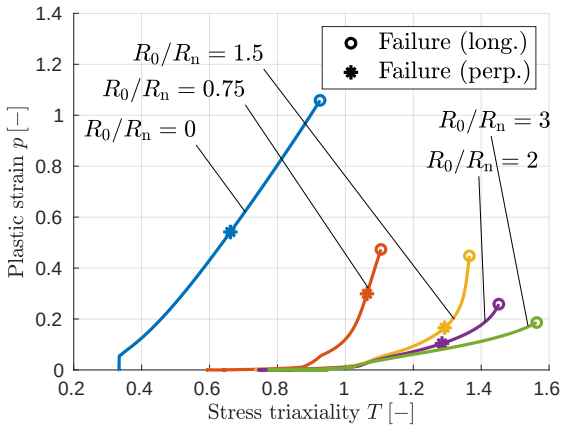

FIGURE 4.25: Variation of the triaxiality as a function of the plastic strain at the centre of the round bars simulated with the J2-plastic law.

coarser mesh is used elsewhere to spare elements. Inside the smooth bars, a small geometrical defect[4] at the centre is introduced to ensure that necking occurs where the mesh is refined.

On Fig. 4.21a, we see that the calibrated hardening law is able to reproduce the experimental curves on round bars with $R_0 = 3$ [mm]. The same observation is made on Fig. 4.21b for $R_0 = 2$ [mm]. The good agreement before material failure for both directions confirms the absence of plastic anisotropy.

However, the agreement with the notched bars seems to be less quantitative on Fig. 4.22. In fact, the strictometer measures the local value of the diameter reduction between its two pins. Therefore, it is very sensitive to misplacement or misalignment and tends to generally underestimate the real striction value. Nevertheless, the stress values, and namely the peak stress which is not affected by the strictometer misplacement, are correctly predicted by the simulations.

The distributions of the matrix plastic strain p and of the stress triaxiality T are shown in the deformed configuration on Figs. 4.23 and 4.24 when the force reaches its maximum and when the specimen reaches the (mean) experimental fracture strain for the smooth round bar and two notched bars in the long. direction. Plastic flow tends to be concentrated inside the notch region or in the necking zone once formed. The values reached at failure increases for larger notch radius due to their higher ductility. Besides, the stress triaxiality on Fig. 4.24 is higher for smaller notch radius as predicted by Eq. 4.8. These trends are confirmed on Fig. 4.25 where the stress triaxiality is sampled in terms of the plastic strain encountered at the specimen centre until the experimental fracture strain is reached. The triaxiality T globally increases with the plastic strain p as the plastic necking accentuates the potential pre-existing notch. At equivalent plastic strain values, T is higher for a smaller notch radius R_n. Besides, the approximation (4.8) looses in accuracy with the deformation increases as its assumptions are less and less valid. Indeed, as observable on Fig. 4.23, the plastic strains tend to concentrate near the specimen axis instead of a uniform flow along the radius. The evolution of the Lode variable is not shown as it is constant and equal to 1.

4.2.2.2 Grooved plates

The grooved thick plates are reproduced using 2D simulations in plane strain. The mesh is shown on Fig. 4.26 for the grooved plates with $R_n = 10$ [mm] and $R_n = 1$ [mm]. Once gain,

[4] Practically, the radius is minimal at the centre and equal R_0. It then linearly increases to reach R_0/d_g at the extremities with $d_g = 0.999$.

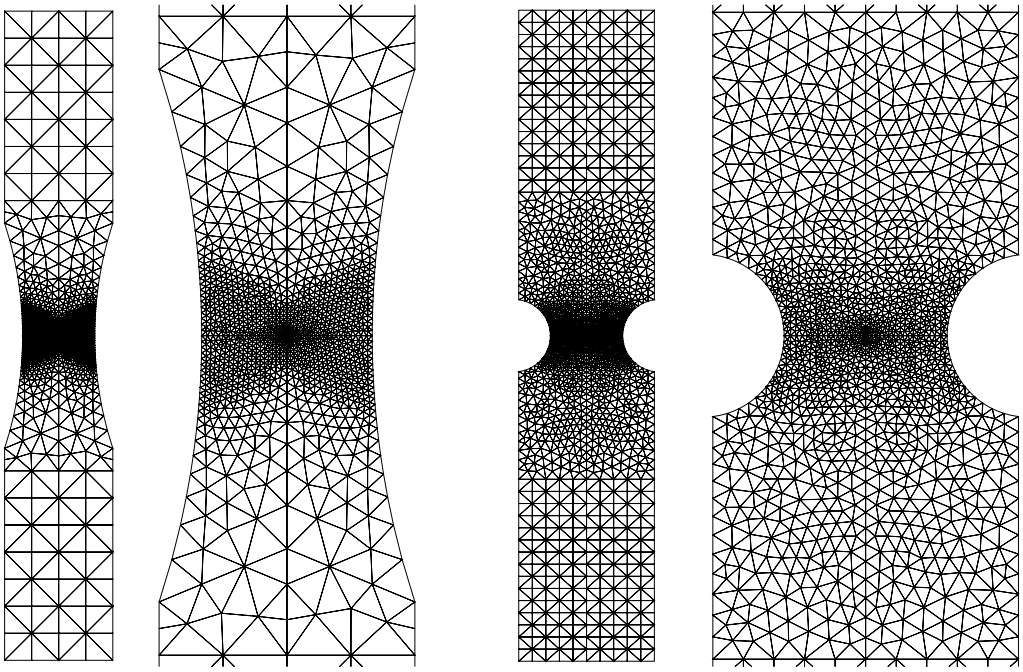

(a) Grooved plates with $R_{\mathrm{n}} = 10$ [mm]; 2589 elements.

(b) Grooved plates with $R_{\mathrm{n}} = 1$ [mm]; 3680 elements

FIGURE 4.26: Simulated mesh and zoom on its central part for two grooved plates: (a) $R_{\mathrm{n}} = 10$ [mm] and (b) $R_{\mathrm{n}} = 1$ [mm].

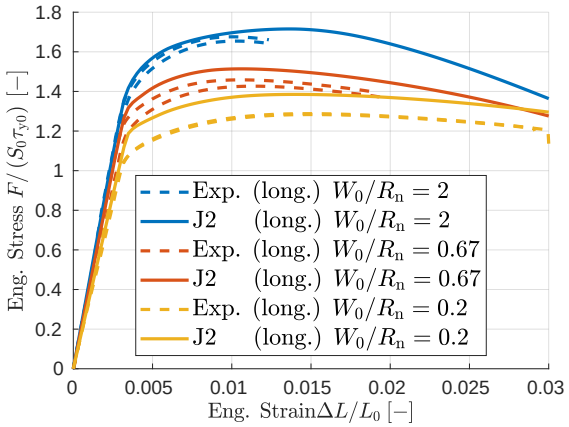

FIGURE 4.27: Variation of the applied force as a function of the elongation ΔL for the grooved plates simulated with the J2-plastic law (continuous lines) and comparison with the experimental measurements (discontinuous lines).

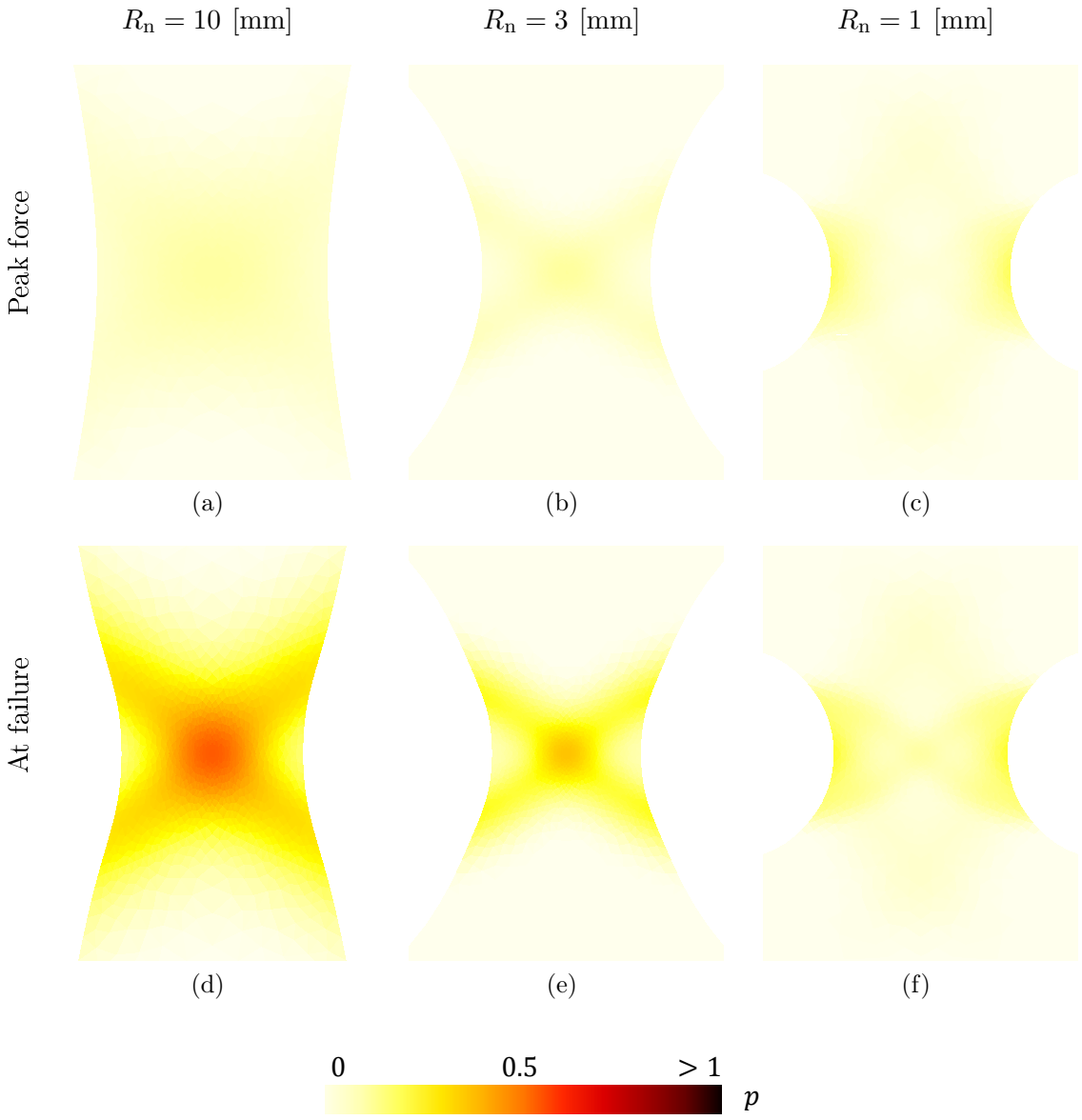

FIGURE 4.28: Distribution of the plastic strain p (a-c) when the peak stress is reached and (d-f) when the fracture strain is reached in the deformed configuration for the grooved plates with (left) $R_n = 10$ [mm], (centre) $R_n = 3$ [mm] and (right) $R_n = 1$ [mm].

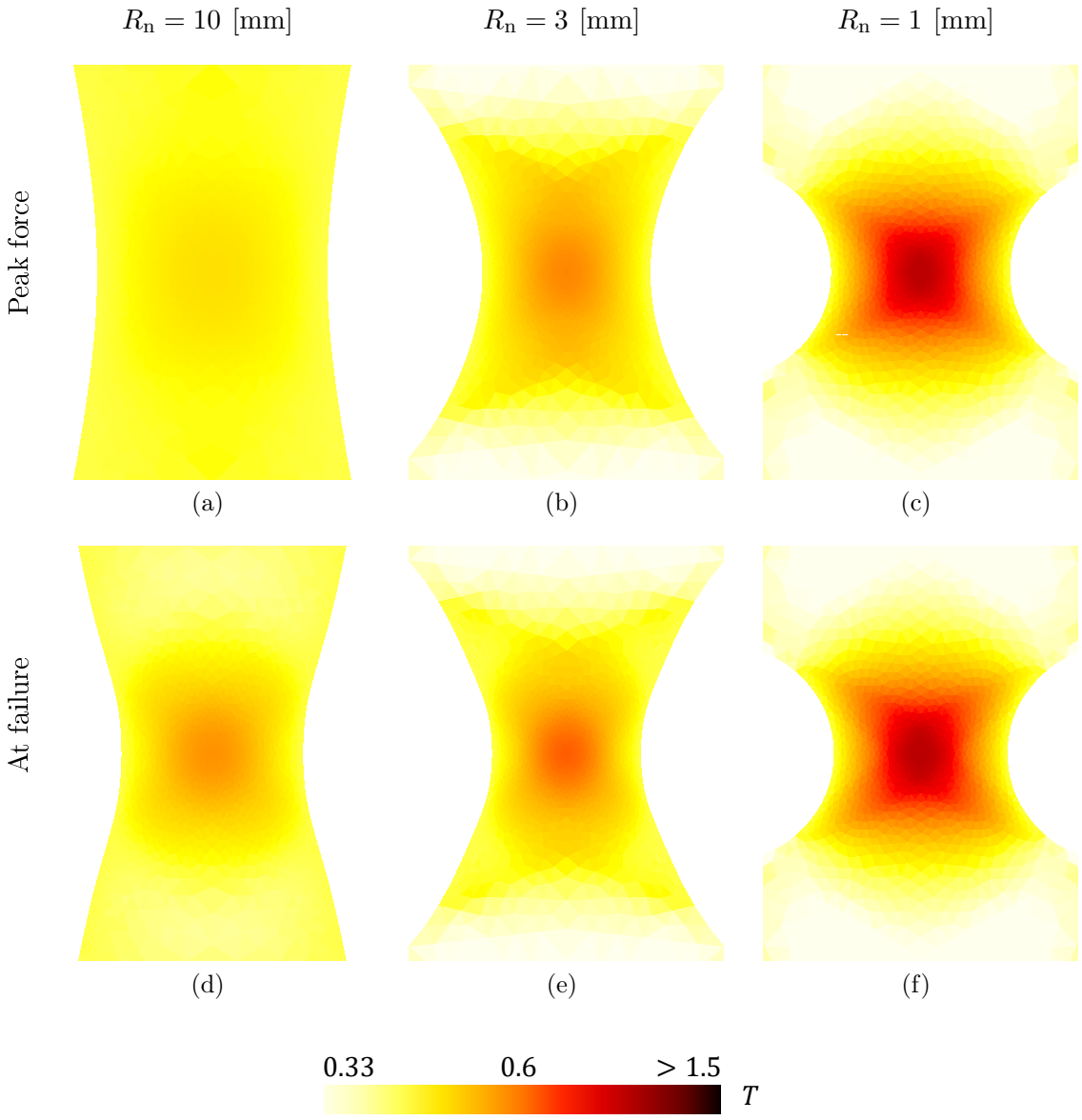

FIGURE 4.29: Distribution of the stress triaxiality T (a-c) when the peak stress is reached and (d-f) when the fracture strain is reached in the deformed configuration for the grooved plates with (left) $R_n = 10$ [mm], (centre) $R_n = 3$ [mm] and (right) $R_n = 1$ [mm].

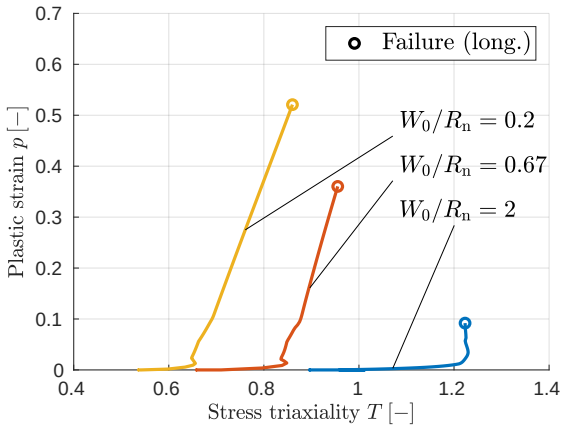

FIGURE 4.30: Variation of the triaxiality as a function of the plastic strain at the centre line of the grooved plates simulated with the J2-plastic law.

only the central part within the extensometer region is actually simulated. The finest zone is meshed with 35 [μm] long elements for a total of around 50 elements on thickness. However, because of tolerance issue during the tooling process, the thickness outside the grooves (i.e. W_e on Fig. 4.9) has been corrected to fit the elastic slope. The actually considered thicknesses are 3 [mm], 3.4 [mm] and 3.75 [mm] for respectively $R_n = 10$ [mm] , $R_n = 3$ [mm] and $R_n = 1$ [mm].

The simulated force evolutions are shown on Fig. 4.27 in terms of the specimen elongation. The agreement between the experimental curves and the numerical simulations is correct for at least two groove radii. The larger discrepancy on the $R_n = 10$ [mm] is larger (around 8% of the maximal force), although acceptable, than the error observed on others specimen. It could be either due to the plane strain approximation or due to another tooling issue. Another explanation could be a Lode-dependence of the plastic flow but this is unlikely as only this specimen seems impacted.

The distributions of the plastic strain p and the stress triaxiality T are respectively shown on Figs. 4.28 and 4.29 when the maximal loading force is applied and when the fracture strain is reached. Comparatively to the round bars on Fig. 4.23, the plastic strain p tends to form slanted shear bands. Those latter are more pronounced for the larger notch radius where the shear stress is more preponderant compared to the stress triaxiality. Besides, the evolution of the stress triaxiality at the specimen centre illustrated on Fig. 4.30 is coherent with the distributions displayed on Fig. 4.29. Once again, the stress triaxiality increases with the plastic strain and with smaller notch radius. Regarding the Lode variable, it stays constant at 0 due to the plane strain state.

4.2.2.3 Plane stress flat bars

The plane stress flat bars are simulated using 3D elements. The meshes are shown on Fig. 4.31, the different colours materialising the partitions of the mesh. The smooth bar is simulated with the loading grips while only the central section is modelled in the notched flat one. A symmetry along the specimen mid-plane is used consistently with the failure mode presented in Section 4.1.2.3. 100 [μm] are used in the most refined regions.

The applied force obtained numerically are compared to the experiments on Fig. 4.32 either in terms of the elongation for the smooth bar or of the thickness reduction for the notched ones. On Fig. 4.32a, a good concordance is observed between both results. Agreement is less good on Fig. 4.32b due to the measurement based on a strictometer, more sensitive to experimental errors. However, a good correlation is observed at least in terms of the encountered stress

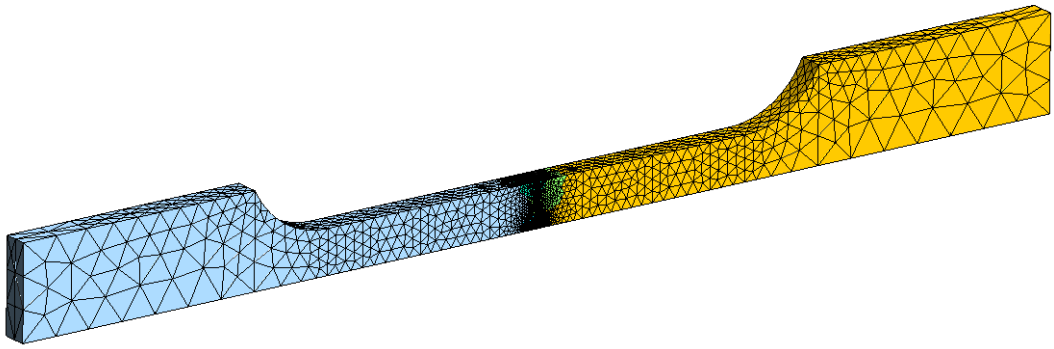

(a) Smooth flat specimen with 36732 elements and 6 partitions.

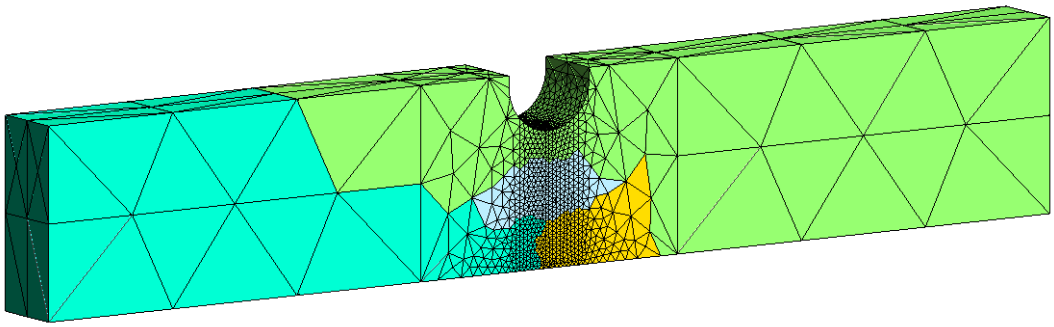

(b) Notched flat bar with $R_{\mathrm{n}} = 1.2$ [mm]; 36759 elements and 6 partitions.

FIGURE 4.31: 3D view of the partitioned mesh for (a) the smooth flat bar and (b) a notched flat bar ($R_{\mathrm{n}} = 1.2$ [mm]).

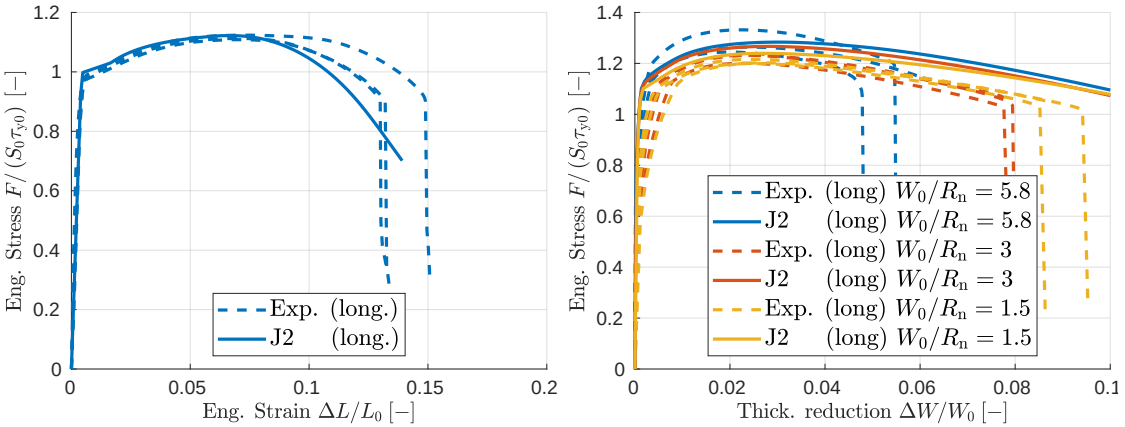

(a) (b)

FIGURE 4.32: Variation of the applied force as a function of (a) the elongation ΔL for the smooth plane stress plates and (b) the thickness reduction for the notched one simulated with the J2-plastic law (continuous lines) and comparison with the experimental measurements (discontinuous lines).

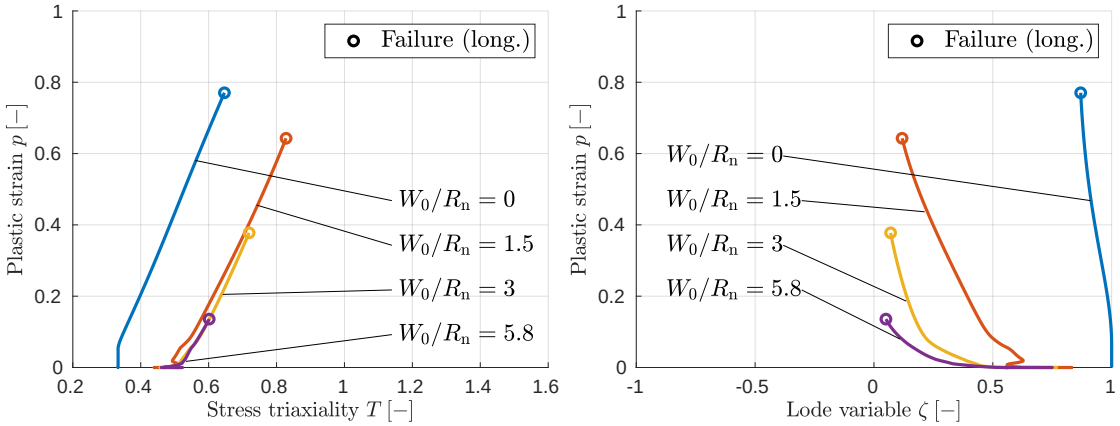

FIGURE 4.33: Variation of (a) the triaxiality and (b) the Lode variable as a function of the plastic strain at the centre of the mid-section of the plane stress plates simulated with the J2-plastic law.

values. The evolution of the stress state is shown on Fig. 4.33 in terms of the plastic strain p upon failure. The stress triaxiality globally increases with the plastic strain, however, unlike other mechanical tests, modifying the notch radius as a low impact on it but not on the resulting ductility. Besides, the Lode variable is not constant during the whole process: it slightly increases with the deformation. In particular, it tends towards 0 for the notched bars, evidence of a shear or a plane strain state occurring at the specimen center.

4.2.3 Fracture strain and stress conditions synthesis

In this section, the influence of the stress conditions on the fracture strain obtained with the different specimens presented in Section 4.1.2, is discussed. On Figs. 4.34, we regroup the evolution of the stress state for all the studied specimen for the sake of completeness. We then compare $\bar{\epsilon}_f$ in terms of the average value of the stress triaxiality and the Lode variable obtained during the J2 simulations presented in Section 4.2.2. Specimens at constant Lode value (i.e. the round bars and the grooved plates) experience a general decrease of their ductility with an increasing stress triaxiality value as already observed. Similarly, if we compare the round bars and the grooved plates which experience similar T-values but different ζ-values, the presence of shear stresses, when ζ drifts apart from $+1$ or -1, is harmful to the ductility. Besides, the stress conditions inside the plane stress specimens in terms of the notch radius are more complex. In this case, it seems that the fracture strain is controlled by the Lode variable which strongly varies from one specimen to another contrarily to the stress triaxiality.

4.3 Calibration and validation of the non-local porous law

In the previous section, we have calibrated and validated the elasto-plastic law as a first guess for the material behaviour. Now, the non-local porous law itself is identified. As already mentioned, parameters values should be as much as possible representative of the physical reality.

As already stated, this process, and the related micromechanical model includes different components: the nucleation, the growth and the coalescence part. Each part is separately addressed. At first, the different assumptions on the micromechanics model are presented in Section 4.3.1 from the interpretation of the experimental data presented in Section 4.1. Then,

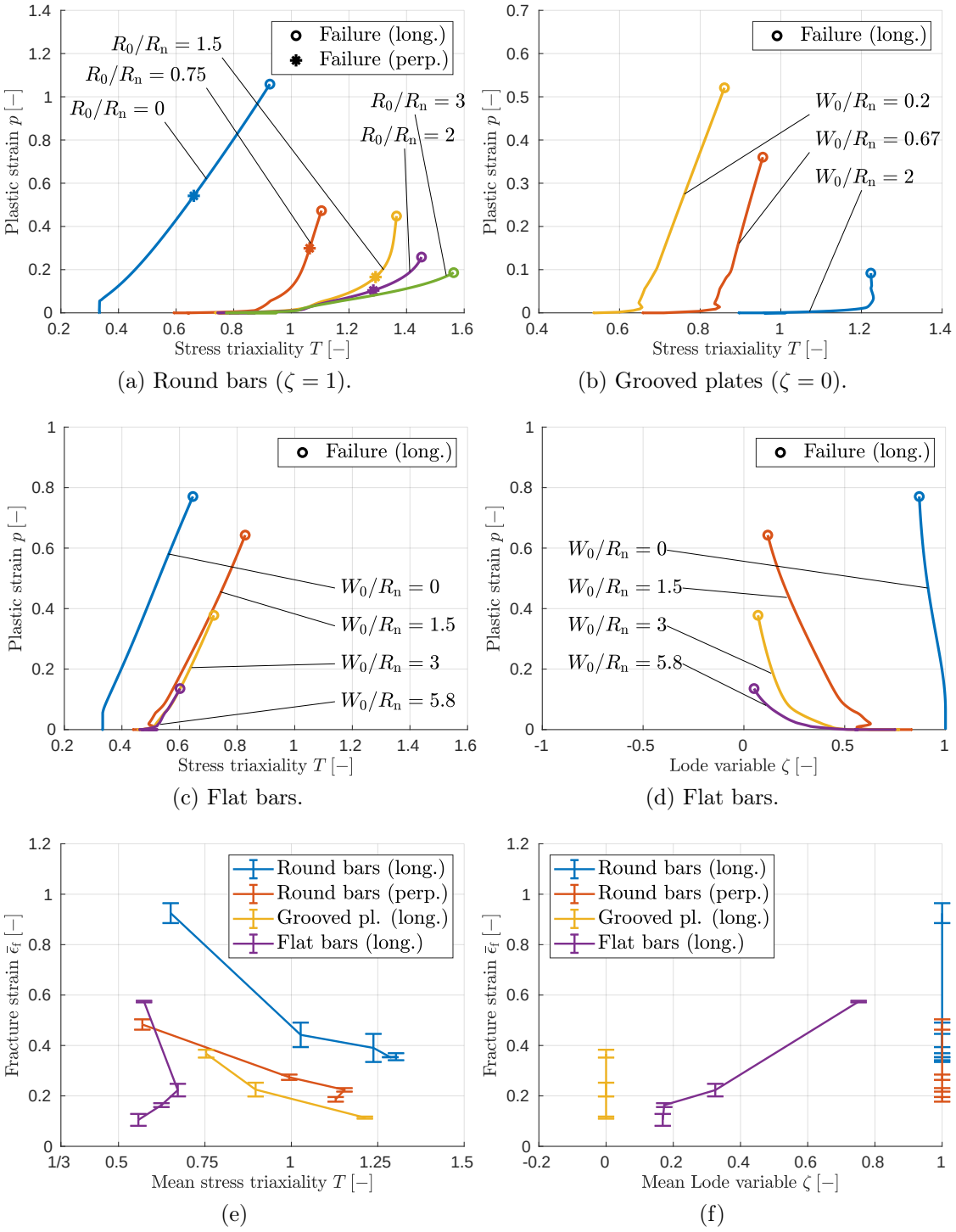

(a) Round bars ($\zeta = 1$). (b) Grooved plates ($\zeta = 0$).

(c) Flat bars. (d) Flat bars.

(e) (f)

FIGURE 4.34: Comparison of (a-d) the evolution of the stress triaxiality on the (a) round bars, (b) the grooved plates and (c) the flat bars, and the evolution of the Lode variable for the (d) flat bars at the centre of the reference cross-section of all the specimens simulated with the J2-plastic law; and (e-f) comparison of the fracture strain as a function of the corresponding mean value of (e) the triaxiality and (f) the Lode variable.

assuming a starting RVE geometry, the damage growth evolution parameters are evaluated in Section 4.3.2 using cell simulations and the hardening law from Section 4.2.1. The determination of the non-local length is investigated in Section 4.3.3. Afterwards, the nucleation parameters are estimated in order to tune the amount of initial damage emanating from the MnS inclusions. In particular, to include the directional effects, an anisotropic stress-triggered nucleation model is developed in Section 4.3.4. Finally, the impact of the shear stress is addressed in Section 4.3.5. Even if this part could be also estimated by RVE simulations, the only parameter k_ω is calibrated by parameter fitting since a relatively simple model is involved. This operation is performed using the plane strain grooved specimens. This choice is made as the plane strain conditions induces a Lode variable constantly equal to zero before coalescence.

4.3.1 Micromechanics-based failure process

Based on the micromechanical observations presented in Section 4.1, it appears that the failure process is mainly driven by the nucleation, growth and coalescence of voids originated from the MnS inclusions.

Indeed, those particles are well known to have low material integrity with respect to the matrix. As the largest and the less coherent inclusion population, they are the first nucleation sites to be activated at the yielding initiation[5] as shown on Fig. 4.16c. Depending on the considered direction, they break along their length or detach themselves from the matrix. The voids so created grow with the plastic flow (see Fig. 4.16a). At some point, plastic flow localises between voids, in particular where inclusions clustering is more important as shown on Fig. 4.16b. Voids finally merge by internal necking and create a crack. The resulting failure surface is the signature of this process. The largest dimples are the remaining of voids created around MnS inclusions. In some cases, the MnS inclusion itself is visible in the middle of the crater. The rest of the dimples, covering all the spectrum size, are partially the results of second inclusion population.

Moreover, the MnS inclusions are also responsible for the failure anisotropy through their shape: as proof, one can recall the radical of the failure surface between the long. (Fig. 4.6a) and the perp. direction (Fig. 4.8a) on the round bars. For loading along the perp. direction, void growth and coalescence are eased and result in a ductility drop.

Besides, the second void population, initiated from Carbide inclusions, has a different role on the failure process. Its effect is essentially summarised as a decrease of the ductility (Lassance et al., 2007) and an amplification of the primary-void shape effect. Therefore, we do not explicitly include thereafter the Carbides population. Moreover, new measurements need to be performed to improve the reliability of the data before its proper use. Indeed, the current ones have been performed away from the main MnS inclusions. However, Fabrègue and Pardoen (2008) have shown that the distribution of such second void population highly differs along the ligament between two voids. The voids of the second population nucleate more easily near larger voids where plastic flow is more intense and stress conditions higher. Consequently, we first focus on MnS inclusions in Section 4.3.4.2. However, the model presented further in Section 4.3.4 is suited for this application.

4.3.2 Calibration from elementary cells

In this section, we use elementary cell computations in order to assess the damage evolution parameters. In particular, we reproduce the analysis of Pardoen and Hutchinson (2000) mainly to determine the ligament growth parameter κ, see Eq. (3.31), in Section 4.3.2.5, consistently with the Thomason model presented in Section 3.1.2.4. At first, we present the RVE model

[5] potentially, nucleation can occur earlier but this hypothesis is difficult to verify due to the small elastic strains while having a low impact on the modelisation

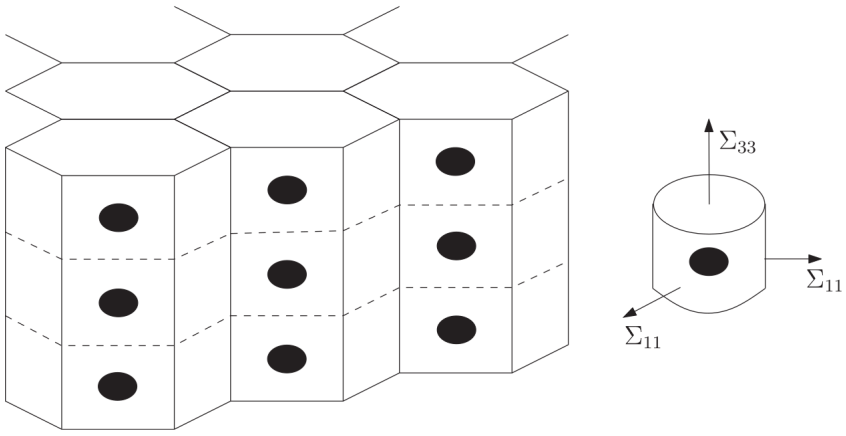

FIGURE 4.35: Assumed cell periodic arrangement. From Pineau, Benzerga, and Pardoen (2016).

in Section 4.3.2.1. The geometry is fixed by the microstructural data's gathered during the experimental campaign (Section 4.1) while the matrix behaviour was obtained in Section 4.2.1. Afterwards, results are discussed in Section 4.3.2.2. They are then used to calibrate the Gurson yield parameters (Section 4.3.2.3) while Section 4.3.2.4 is devoted to the identification of the coefficients of the Thomason concentration factors.

4.3.2.1 Elementary cell simulations

Cell simulations have been performed with various levels of complexity. In the present work, we restrain the applications to axisymmetric stress states for periodic voids, following the paper of Pardoen and Hutchinson (2000). According to them, the material continuum is here seen as a periodic hexagonal arrangement of unit cells with aligned void axis as shown on Fig. 4.35. The hexagonal cells are reasonably approximated by axisymmetric computations as shown by Worswick (1990).

The geometry and the boundary conditions of the simulated RVE are shown on Fig. 4.36a. The added subscript "0" refers to initial values. The RVE consists in an axisymmetric cell of axial and radial lengths L_z and L_r. An initially-ellipsoidal void of axial and radial semi-axes R_z and R_r results in a porosity of volumic fraction f_V. The initial geometry is determined by the numerical values of the porosity f_{V_0}, the initial cell aspect ratio λ_0 and the initial void aspect ratio W_0 following the geometrical relations:

$$f_{V_0} = \frac{2R_{r0}^2 R_{z0}}{3L_{r0}^2 L_{z0}}\,, \quad \lambda_0 = \frac{L_{z0}}{L_{r0}}\,, \quad W_0 = \frac{R_{z0}}{R_{r0}}\,. \tag{4.15}$$

Parallel distribution of the axisymmetric unit cell implies the deformation boundary of RVE to remain straight. A path-following method enforces the loading to be performed at fixed stress triaxiality T. The resulting principal stress at the mesoscopic scale in the axial direction Σ_z and in the radial one Σ_r are computed through the average force applied on the cell boundaries per current area. The mesoscopic equivalent stress Σ^{eq} and pressure Σ^h and stress triaxiality T are then given by

$$\Sigma^{eq} = |\Sigma_z - \Sigma_r| \;;\; \Sigma^h = \frac{1}{3}(\Sigma_z + 2\Sigma_r) \;;\; T = \Sigma^h/\Sigma^{eq}\,. \tag{4.16}$$

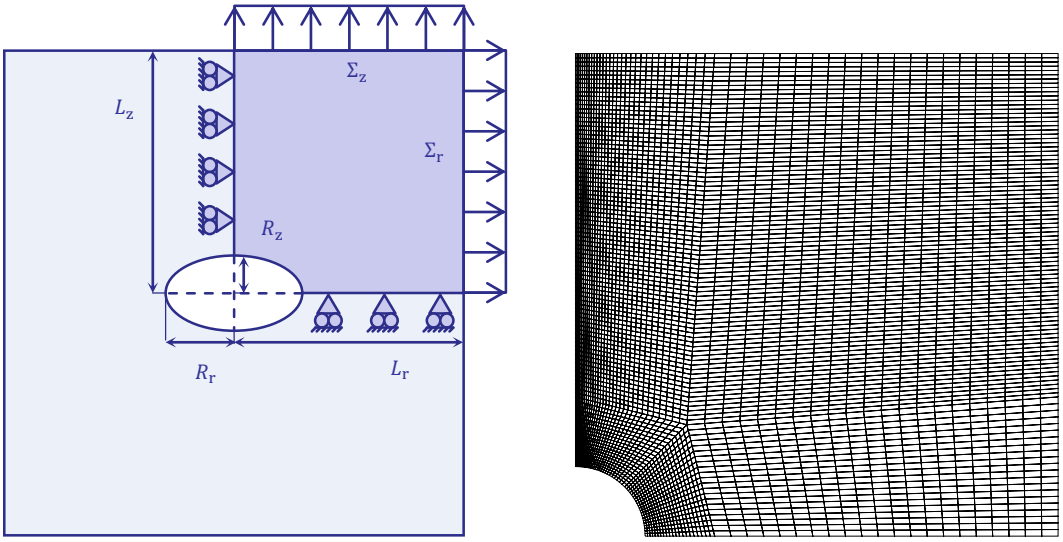

(a) (b)

FIGURE 4.36: Unit cell (a) geometry and boundary conditions and (b) the corresponding mesh for the initial parameters $f_{V_0} = 2 \times 10^{-3}$, $W_0 = 1$ and $\lambda_0 = 1$.

The corresponding strain measure are computed by

$$E_r = \ln \frac{L_r}{L_{r0}} \; ; \; E_z = \ln \frac{L_z}{L_{z0}} \; ; \; E^{eq} = \frac{2}{3} \left| E_z - E_r \right| , \tag{4.17}$$

from the current dimensions L_z and L_r of cell. In addition to E^{eq}, another plastic strain measure, p^{cell}, is implicitly defined following

$$(1 - f_{V_0}) \, \tau_Y \left(p^{cell} \right) \dot{p}^{cell} = \frac{1}{V_0} \int_{V_0} \tau_Y \left(p \right) \dot{p} dV_0 \, , \tag{4.18}$$

where V_0 is the matrix volume.

This definition allows then a comparison between the cell evolution and the porous model by analogy to Eq. (3.29). Others geometrical current values are computed as follows. The current porosity is computed by subtracting to the total cell volume the actual matrix volume, i.e.,

$$f_V = \frac{\pi L_r^2 L_z - \int_{V_0} J dV_0}{\pi L_r^2 L_z} \, , \tag{4.19}$$

where $J = \det \mathbf{F}$. The current void and cell aspect ratio are respectively defined by $W = R_z / R_r$ and $\lambda = L_z / L_r$. Simulations results are presented in the next Section 4.3.2.2.

4.3.2.2 Elementary cell results

The results obtained with the unit cell simulations presented in Section 4.3.2.1 are now discussed using the following set of initial values: $\left[f_{V_0} = 2.0 \times 10^{-3}, W_0 = 1 \, , \lambda_0 = 1 \right]$. Those values are based on the microstructure analysis performed in Section 4.1 expect concerning the aspect ratio because the cell simulations were performed before the obtention of all microstructure results. Besides, since the model will be used for samples extracted along the two directions, we here only consider the spherical asperity shape and will account for the effect of the aspect ratio in the nucleation law.

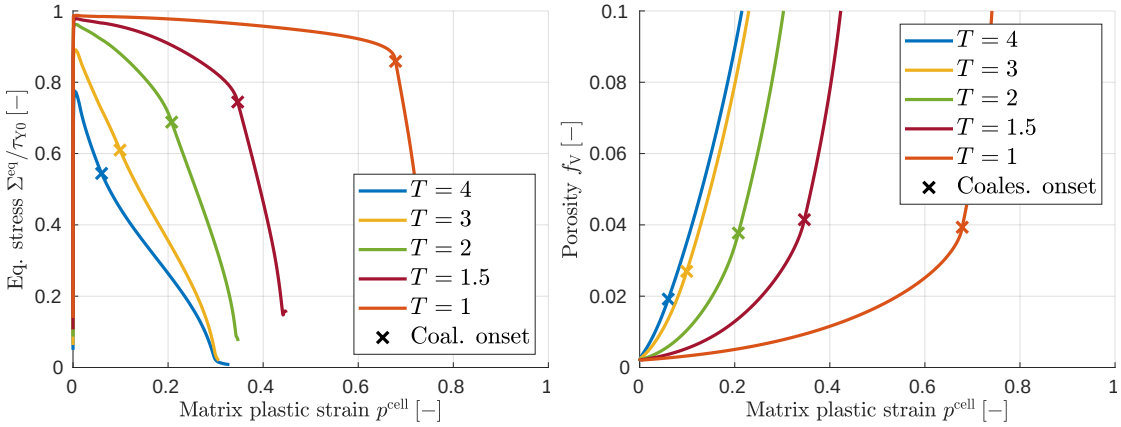

FIGURE 4.37: Comparison of the evolution of (a) the equivalent stress and (b) the porosity in terms of the matrix plastic strain for different prescribed stress triaxiality $T = \Sigma^{h}/\Sigma^{eq}$.

The evolution of the equivalent stress (4.16) and of the cell porosity (4.19) are compared respectively on Figs. 4.37a and 4.37b for different prescribed stress triaxiality values $T = \Sigma^{h}/\Sigma^{eq}$. The coalescence onset is also highlighted. In addition, the distribution of the plastic strain inside the matrix at different points of the simulations is illustrated on Fig. 4.38 for two stress triaxiality values: $T = 1.5$ and $T = 3$.

On Fig. 4.37, one can note that an increase of the stress triaxiality results in a faster void growth and a coalescence onset, marked by the change of curve slope, occurring earlier in terms of the plastic strain p^{cell}. These observations are coherent with the plastic strain distribution depicted on Fig. 4.38. Indeed,the resulting void volume fraction after undergoing an equivalent plastic strain p^{cell} of 5% is larger on Fig. 4.38d than on Fig. 4.38a obtained at a lower stress triaxiality. Besides, the decrease of ductility is visible at coalescence onset: the plastic strain inside the cell (beyond the immediate vicinity of the void) at this stage on Fig. 4.38e at $T = 3$ is lower than on Fig. 4.38b at $T = 1.5$. Ultimately, one can observe that, as expected for the investigated stress conditions, the failure occurs well through the void coalescence by internal necking.

The slope change on Fig. 4.37, indicating the transition between the growth and the coalescence stage, is sharper for lower triaxialities. Besides, one can observe that the porosity values at coalescence onset are not constant: this confirms that an approach similar to the GTN model (see Section 3.1.2.3) is not adequate for various stress conditions.

Those results will be used as reference in Sections 4.3.2.3 and 4.3.2.5 to calibrate the Gurson parameters q_1 and q_2, see Eq. (3.32) and the ligament growth parameter κ, see Eq. (3.31).

4.3.2.3 Calibration of the Gurson yield parameters

In this section, the porous-plastic model is compared to the results of the cell simulations in order to calibrate the Gurson parameters q_1 and q_2. These parameters are chosen such as minimising the difference in terms of the plastic work and the porosity evolution until coalescence between the cell simulations (see Fig. 4.37) and the Gurson model. Practically, an error is computed as the difference in the area under the curves $\sigma^{eq}(p)/\tau_{Y0}$ or $\Sigma^{eq}(p)/\tau_{Y0}$ and $f_V(p)$ from the initiation to the coalescence onset (defined in terms of the numerical value prediction p^{cell} observed on the cell simulations at coalescence onset), and so, for both the cells and Gurson simulations. This error is then minimised in the studied space $T \in [1;4] \times f_{V_0} \in \left[1 \times 10^{-3}; 2 \times 10^{-3}\right]$. The cumulated error is shown on Fig. 4.39 in terms of q_1

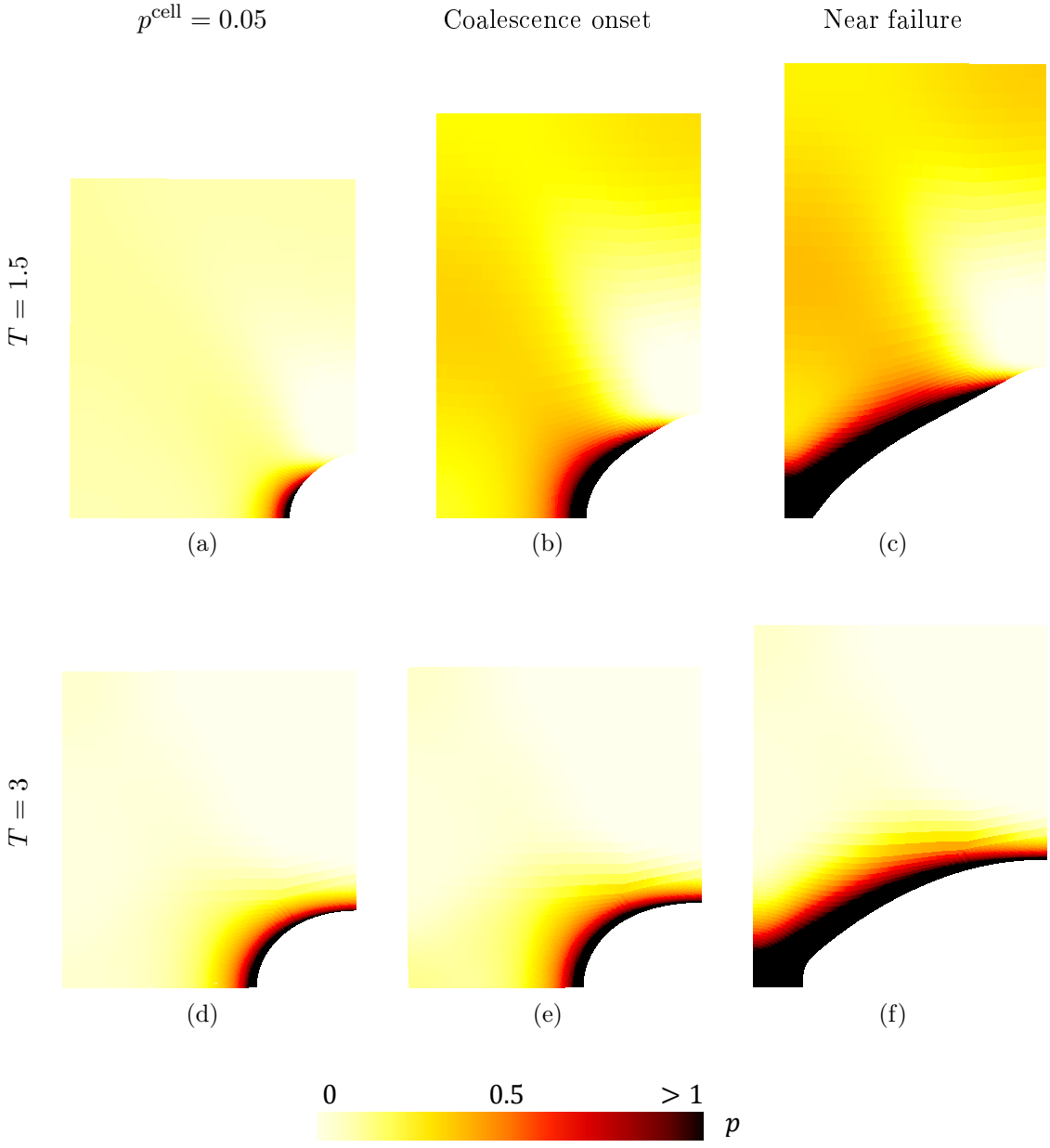

FIGURE 4.38: Distribution of the plastic strain p inside the unit cell (a-b) during the void growth phase (when the cell reaches $p^{\text{cell}} = 0.05$), (c-d) at the onset of coalescence and (e-f) near failure in the deformed configuration with (top) $T = 1.5$ and (bottom) $T = 3$.

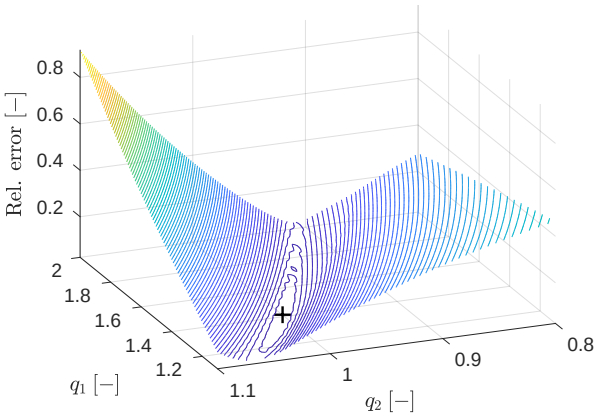

FIGURE 4.39: Relative error between the Gurson model and the cell simulations in terms of q_1 and q_2. The optimum point is marked with a black cross.

and q_2. The optimum is found for $q_1 = 1.414$ and $q_2 = 1.0$ which is quite close to the one used or computed in the literature (Faleskog, Gao, and Fong Shih, 1998). The resulting yield stress evolution and the porosity growth are shown on Figs. 4.40a and 4.40b with the Gurson model (dotted lines) using a direct resolution. A good correlation is obtained until coalescence onset. The behaviour after this point is addressed in the next Sections 4.3.2.4 and 4.3.2.5 with the calibration of the coalescence parameters.

4.3.2.4 Calibration of the concentration factor coefficients

The values of the coefficients appearing in the concentration factor $C_{\mathrm{T}}^{\phi}(\chi)$ presented in Eq. (3.39), α and β, are given by the relation provided by Pardoen and Hutchinson (2000). Even if the same result could be obtained from the cell computations, their results are still valid because of the hypotheses made here. Following Pardoen and Hutchinson (2000), one thus has

$$\alpha = 0.1 + 0.217 n_2 + 4.83 n_2^2 = 0.129 \quad \text{and } \beta = 1.24\,, \tag{4.20}$$

in terms of the strain-hardening exponent n_2, see Eq. (4.14) (which respects the condition $0 \leqslant n_2 \leqslant 0.3$).

4.3.2.5 Calibration of the ligament growth parameter

In this section, we estimate the ligament growth parameter κ governing the cell aspect ratio evolution rate through Eq. (3.31). For this purpose, the aspect ratio observed at coalescence onset, λ_{c}, is written in terms of κ as

$$\ln \frac{\lambda_{\mathrm{c}}}{\lambda_0} = \kappa p_{\mathrm{c}}\,, \tag{4.21}$$

where p_{c} is the matrix plastic strain at coalescence onset. One could directly use λ_{c} measured on the cell results. However, as this variable evolution is not accurately modelled in the GT approach, it is more reliable to deduce λ_{c} from the coalescence stress $\sigma_{\mathrm{c}}^{\mathrm{eq}} = \sigma^{\mathrm{eq}}(p_{\mathrm{c}})$ and the porosity $f_{\mathrm{V}\,\mathrm{c}} = f_{\mathrm{V}}(p_{\mathrm{c}})$ which have been observed from the cells simulations upon coalescence onset in Section 4.3.2.3. Therefore, in this context, λ_{c} is deduced from its definition (3.30):

$$\lambda_{\mathrm{c}} = \frac{2\chi_{\mathrm{c}}^3}{3 f_{\mathrm{V}\,\mathrm{c}}}\,. \tag{4.22}$$

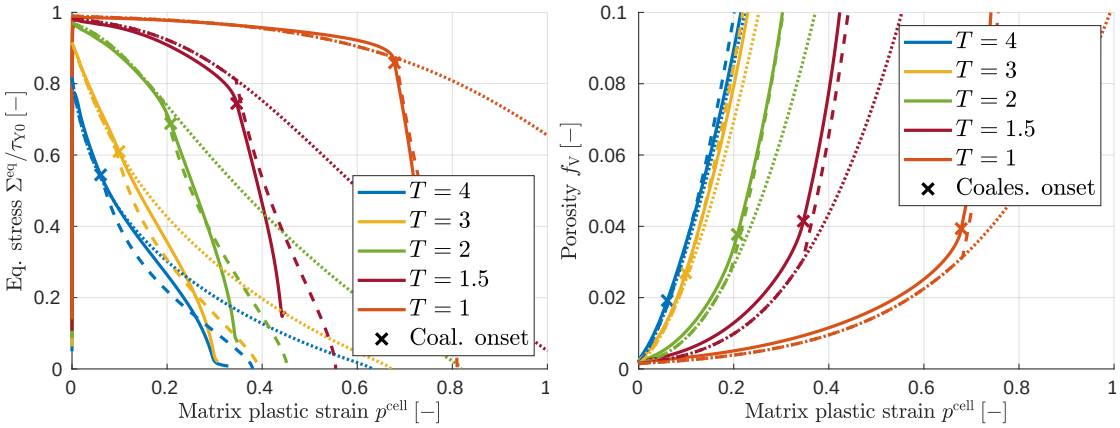

FIGURE 4.40: Comparison of the evolution of (a) the equivalent stress and (b) the porosity in terms of the matrix plastic strain for different prescribed stress triaxiality $T = \Sigma^h/\Sigma^{eq}$ using cell simulations (continuous lines), the Gurson model (dotted lines) or the Gurson-Thomason model (discontinuous lines).

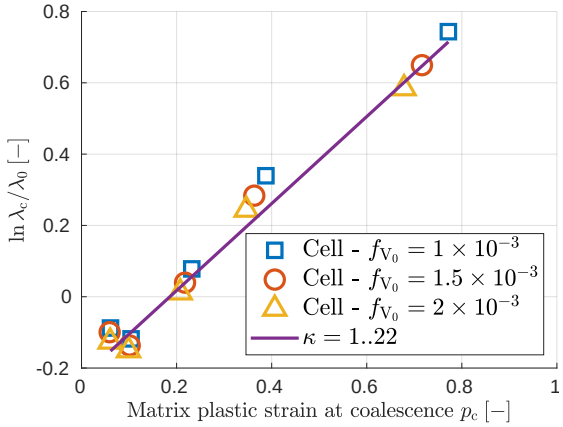

FIGURE 4.41: Cell aspect ratio at coalescence onset, λ_c, extracted from cell simulations and the Gurson model and fitting of the ligament growth parameter κ.

In this equation, only χ_c, the ligament ratio at coalescence onset, remains to be determined. Its value is implicitly obtained as the one which satisfies the Thomason yield surface at the corresponding stress state

$$\left(\frac{2}{3}+T\right) J\sigma_c^{eq}/\tau_Y\left(p_c\right) - C_T^{\phi}\left(\chi_c\right) = 0\,, \tag{4.23}$$

using the value α and β previously calibrated in Section 4.3.2.4.

As a result, the corresponding value λ_c at different triaxialities is shown on Fig. 4.41 for $f_{V_0} \in [0.001; 0.002]$. Using Eq. (4.21), the ligament growth parameter can be estimated as $\kappa = 1.22$ by curve-fitting. When coupled with the previous results of Sections 4.3.2.3 and 4.3.2.4, the evolutions of the equivalent stress and of the porosity with the Gurson-Thomason are compared on Figs. 4.40a and 4.40b to the cell simulations. This time, the agreement is improved as compared to the sole Gurson model and the validity zone is extended to the whole failure process.

4.3.3 Calibration of the non-local length

The (transition) model involves two characteristic lengths: the non-local length and the cohesive band thickness. Both control the dissipated energy but through different mechanisms. The first one is related to the porosity delocalisation through the non-local diffusion equation. The second one acts only once the transition occurs: it impacts the energy release rate during the crack propagation through the coalescence process. In the context of the Chapter 2, we have drawn a relationship between both lengths in order to ensure the energy consistency between the pure non-local case and the transition one (see Section 2.2) as we have assumed that the failure process is similar before and after the transition. In the present case, we no longer make this assumption. Instead, we consider two different processes with their own characteristic size.

Let us first consider the non-local length prior to the coalescence regime. In this case, the Gurson growth mechanism dominates. The related characteristic length should be a multiple of the relevant heterogeneities inter-distance (Geers et al., 1998), here the inter-void distance. As detailed in Section 4.1.1, this distance is around 100 [μm] which gives the first guess for l_c. Besides, an isotropic length is considered for the sake of simplicity and because there is no highly marked anisotropy in the void spatial distribution.

However, without transition, the dissipated energy related to the coalescence might be overestimated. Indeed, as observed on the SEM images, the characteristic size for coalescence is related to the voids thickness (i.e. the void size in the direction perpendicular to the coalescence plane). From the microstructural analysis, this void size is around $1-20$ [μm], i.e. around one or two orders of magnitude smaller than the intervoids distance. Besides, in the literature, the actual thickness of the process zone varies from a fraction of the void thickness (Scheyvaerts, Pardoen, and Onck, 2010) to several times the inter-voids distance (along the perpendicular direction to the coalescence plane) (Pineau, Benzerga, and Pardoen, 2016).

To avoid this dissipation overestimation, an alternative could be to use a smaller length once the coalescence has been detected, but a much smaller mesh size would be requested to resolve this length scale. Besides, the resulting error is quite small as the damage variable evolves much faster during the coalescence. This overestimation issue can be overcome if the transition scheme is used. Indeed, the cohesive band can be chosen around the size of the voids without numerical inconsistencies.

In short, the non-local length l_c is fixed at 100 [μm]. However, this first guess must be improved and calibrated in a future work using a pre-crack specimens as a CT or a DENT specimen. Moreover, the isotropy assumption must be confirmed using samples with initial cracks in different orientations.

4.3.4 Nucleation model derived from Beremin model

In Chapter 3, the nucleation law was assumed to be isotropic and strain-controlled. However, as seen in Section 4.1, the coalescence stage is highly anisotropic. In this work, we assume that the anisotropy results from the porosity nucleation triggered by the elongated MnS inclusion failure: when loaded in the long. direction, the MnS inclusions nucleate by particle cracking, whilst when loaded in the perp. direction, porosity arises from the matrix/particle decohesion. In both cases, the nucleation occurs very early in the process but the generated void possesses a different shape and volume fraction depending on the loading direction. These properties then impact the void growth and coalescence process previously studied in the Section 4.3.2. Assuming a monotonic loading, this effect is here included by generating an effective micromechanics-based nucleation fraction as suggested by the work of Lassance, Scheyvaerts, and Pardoen (2006). It is performed through an anisotropic stress-triggered nucleation law developed in Section 4.3.4.1. The question of the effective amount of nucleated porosity and the shape of the nucleation function are discussed in 4.3.4.2. This approach is then compared in Section 4.3.4.3 to the experimental results gathered in Section 4.1.

4.3.4.1 New anisotropic nucleation model

Henceforth, we consider now a stress-triggered approach: nucleation occurs, by particle cracking or interface decohesion, when the maximum tensile stress in a given particle σ_{n}, reaches a critical value, $\sigma_{\mathrm{n_c}}$, i.e. the nucleation term in Eq. (3.26) becomes

$$\dot{f}_{\mathrm{V\,nucl}} = \begin{cases} A_{\mathrm{n}}\left(p\right)\dot{p} & \text{if there exists } t' < t \text{ such that } \sigma_{\mathrm{n}}\left(t'\right) > \sigma_{\mathrm{n_c}}\,, \\ 0 & \text{otherwise}\,. \end{cases} \tag{4.24}$$

In the initial model of Beremin (1981) (following Pineau, Benzerga, and Pardoen (2016)), nucleation initiation is assumed to be triggered by a critical local stress applied on the brittle particles. This effective stress is the sum of two contributions: the far-field stress enhanced by a contribution from the strain inhomogeneities effect around the inclusions. This latter is computed using the theory of Eshelby (1957) for elastic inclusions and inhomogeneities extended to elasto-plastic behaviour by Berveiller and Zaoui (1978). Concretely, the model links the applied macroscopic Cauchy stress state $\boldsymbol{\sigma}$ to the maximal microscopic stress σ_{n} induced on inclusions using the following relation:

$$\sigma_{\mathrm{I}} + k(\sigma^{\mathrm{eq}} - \sigma_{\mathrm{Y}}) = \sigma_{\mathrm{n}}\,, \tag{4.25}$$

where σ_{I} is the largest eigen-value or the maximal principal stress of $\boldsymbol{\sigma}$, σ^{eq} is the macroscopic von Mises stress, σ_{Y} is the initial yield stress, and k is a function of the inclusions shape and loading direction. Finally, combining Eq. (4.24) and (4.25), the nucleation activation criterion simply becomes

$$\sigma_{\mathrm{I}} + k(\sigma^{\mathrm{eq}} - \sigma_{\mathrm{Y}}) > \sigma_{\mathrm{n_c}}\,. \tag{4.26}$$

The main advantage of the Beremin model is the possibility to include a triaxiality dependency. Moreover, the inclusions shape effect can be included. However, no anisotropy was directly considered in the model: Beremin (1981) has originally accounted for anisotropy by fitting the parameter value along the loading direction. To overcome this issue, this approach is extended by considering the involved quantities as directional. Practically, the material parameters involved in the model, k and $\sigma_{\mathrm{n_c}}$, are no longer represented by scalars. They are substituted by a tensor form $\mathbf{k}$ and $\boldsymbol{\sigma}_{\mathrm{n_c}}$. The problem becomes as finding the direction which maximises the criterion, i.e

$$\max_{\boldsymbol{n}} \left[\boldsymbol{n}\cdot\boldsymbol{\sigma}\cdot\boldsymbol{n} + \boldsymbol{n}\cdot\mathbf{k}\cdot\boldsymbol{n}(\sigma^{\mathrm{eq}} - \sigma_{\mathrm{Y}}) - \boldsymbol{n}\cdot\boldsymbol{\sigma}_{\mathrm{n_c}}\cdot\boldsymbol{n}\right] > 0 \text{ with } \boldsymbol{n}\cdot\boldsymbol{n} = 1\,. \tag{4.27}$$

One can demonstrate, see Appendix C.1, that the solution of the previous problem is equivalent to finding the largest eigen-value of the tensor $\boldsymbol{\sigma} + \mathbf{k}(\sigma^{\mathrm{eq}} - \sigma_{\mathrm{Y}}) - \boldsymbol{\sigma}_{\mathrm{n_c}}$, associated with its eigenvector $\boldsymbol{n}^*$. Hence, the criterion corresponds to

$$\max\left[\mathrm{eig}\left(\boldsymbol{\sigma} + \mathbf{k}(\sigma^{\mathrm{eq}} - \sigma_{\mathrm{Y}}) - \boldsymbol{\sigma}_{\mathrm{n_c}}\right)\right] > 0\,. \tag{4.28}$$

Although, $\mathbf{k}$ and $\boldsymbol{\sigma}_{\mathrm{n_c}}$ are written in the current configuration, by assuming that the plastic flow does not influence the coefficients, those tensors are obtained from their counterparts in the initial configuration by using the rotation tensor $\mathbf{R}^{\mathrm{e}}$ computed from the polar decomposition of the elastic part of the deformation gradient $\mathbf{F}^{\mathrm{e}}$, with

$$\mathbf{k} = \mathbf{R}^{\mathrm{e}} \cdot \mathbf{k}_0 \cdot \mathbf{R}^{\mathrm{eT}} \text{ and } \boldsymbol{\sigma}_{\mathrm{n_c}} = \mathbf{R}^{\mathrm{e}} \cdot \boldsymbol{\sigma}_{\mathrm{n_c}0} \cdot \mathbf{R}^{\mathrm{eT}}\,. \tag{4.29}$$

4.3.4.2 Calibration of the nucleation model

In this section, we discuss how to calibrate the model developed in Section 4.3.4. In particular, we address the choice of the nucleation function $A_{\mathrm{n}}\left(p - p_{\mathrm{n_c}}, \boldsymbol{n}^*\right)$, its shape and its intensity depending on the plastic strain value $p_{\mathrm{n_c}}$ at which the criterion (4.28) is satisfied and the corresponding direction $\boldsymbol{n}^*$. As a matter of fact, two main indications can be deduced from the microstructure observations in Sections 4.1 and 4.3.1 to direct this choice. On the one hand, the anisotropy results mainly from the initial void shape and its distribution of the MnS inclusions. On the other hand, the nucleation is entirely settled directly after the onset of yielding.

Consequently, a Gaussian distribution, similarly to Chapter 3, is chosen with a very low deviation as follows:

$$A_{\mathrm{n}}\left(p - p_{\mathrm{n_c}}, \boldsymbol{n}^*\right) = \frac{f_{\mathrm{n}}\left(\boldsymbol{n}^*\right)}{s_{\mathrm{n}}\sqrt{2\pi}} \exp\left[-\frac{1}{2}\left(\frac{p - p_{\mathrm{n_c}} - 3s_{\mathrm{n}}}{s_{\mathrm{n}}}\right)^2\right], \tag{4.30}$$

with $s_{\mathrm{n}} = 0.005$ in order to ensure the end of the nucleation in the first plastic strain percent and $f_{\mathrm{n}}\left(\boldsymbol{n}^*\right)$, the effective intensity. Consistently with the criterion (4.28), $f_{\mathrm{n}}\left(\boldsymbol{n}^*\right)$ is computed through a tensorial entity $\mathbf{f}_{\mathrm{n}}$ following

$$f_{\mathrm{n}}\left(\boldsymbol{n}^*\right) = \boldsymbol{n}^* \cdot \mathbf{f}_{\mathrm{n}} \cdot \boldsymbol{n}^*\,, \tag{4.31}$$

which should directly depends on the MnS inclusions fraction.

The determination of the nucleation intensity is inspired from the work of Lassance, Scheyvaerts, and Pardoen (2006) and Lassance et al. (2007) who studied the growth and coalescence of penny-shaped voids in metallic alloys. When a void nucleates from the cracking of an inclusion of volumic fraction f_{p} and initial aspect ratio W_0, it generates a penny-shaped void of fraction f_{n} with a very small aspect ratio $W_{\mathrm{n}} << 1$, according to geometrical rules, equal to

$$f_{\mathrm{n}} = W_{\mathrm{n}} \frac{f_{\mathrm{p}}}{W_0}\,, \tag{4.32}$$

which depends on the nucleated void aspect ratio W_{n}. In addition, Lassance, Scheyvaerts, and Pardoen (2006) demonstrated, either with cell simulations or with the Gologanou model associated with the Thomason model, that the ductility is not sensitive to W_{n}, providing $W_{\mathrm{n}} < 1$ and a sufficiently low particle fraction ($f_{\mathrm{p}} < 2\%$). Furthermore, they also demonstrated that using an effective porosity f_{n} such as

$$f_{\mathrm{n}} = \frac{f_{\mathrm{p}}}{W_0}\,, \tag{4.33}$$

is a reasonable approximation in the context of a Gurson model to predict the coalescence onset for voids such that $W_{\mathrm{n}} < 1$. In the case where the particle breaks into $n+1$ fragments, the Eq. (4.33) becomes

$$f_{\mathrm{n}} = n\frac{f_{\mathrm{p}}}{W_0}\,. \tag{4.34}$$

Applied to our case, on the one hand, the MnS inclusions are loaded along their length in the longitudinal direction. SEM pictures show that inclusions break into n_{long} small square fragments. The longer the particles, the higher the number of fragments. Therefore, assuming that the inclusion breaks into a number equal to $W_{0,\mathrm{long}}$, the aspect ratio in the long. direction as suggested by the observations, one has

$$f_{\mathrm{n,long}} = n_{\mathrm{long}}\frac{f_{\mathrm{p}}}{W_{0,\mathrm{long}}} = f_{\mathrm{p}} = 2\times 10^{-3}\,. \tag{4.35}$$

On the other hand, in the perpendicular direction, the MnS inclusions are loaded along one of the small axes. Nucleation occurs when the inclusions separate from the matrix, resulting in one void only. Applying the previous formula (4.34), one has

$$f_{\mathrm{n,perp}} = \frac{f_{\mathrm{p}}}{W_{0,\mathrm{perp}}}\,. \tag{4.36}$$

which depends on the aspect ratio $W_{0,\mathrm{perp}}$. This latter is computed from the ratio between the inclusions semi-axis R_i. For a given direction 1, the related aspect ratio W_1 is equal to (Lassance, Scheyvaerts, and Pardoen, 2006)

$$W_1 = \frac{R_1}{\sqrt{R_2R_3}}\,. \tag{4.37}$$

Therefore, for an oblate inclusions, one can obtain $W_{0,\mathrm{perp}} = W_{0,\mathrm{long}}^{-1/2}$. The preliminary microstructure analysis in Section 4.1.1 fixes the value of the inclusions aspect ratio around $W_{0,\mathrm{long}} = 16$. Here, in order to take into account neglected contributions to the observed anisotropic behaviour, such as the inclusion spacing, second incusions populations etc., which enhance the shape effects, a slightly higher value is chosen: $W_{0,\mathrm{long}} = 24$ and $W_{0,\mathrm{perp}} = 0.204$.

At the end of the day, if we assume that the "long." direction coincides with the z-direction, the tensor $\mathbf{f}_{\mathrm{n}}$ takes a diagonal form. Its components are computed using either Eq. (4.35) or (4.36): $f_{\mathrm{n_x}} = f_{\mathrm{n_y}} = f_{\mathrm{n,perp}}$ and $f_{\mathrm{n_z}} = f_{\mathrm{n,long}}$.

The remaining parameters to calibrate are the concentration factor $\mathbf{k}$ and the critical stress $\boldsymbol{\sigma}_{\mathrm{n_c}}$. Consistently with the previous orientation, the latter are chosen equal to $\sigma_{\mathrm{n_{cx}}} = \sigma_{\mathrm{n_{cy}}} = \sigma_{\mathrm{n_{cz}}} = \sigma_{\mathrm{Y0}}$ as MnS inclusions have a very low material integrity compared to the matrix, which induces nucleation immediately at the yielding onset as observed on SEM pictures. Therewith, the concentration factor $\mathbf{k}$ components are equal to $k_{\mathrm{x}} = k_{\mathrm{y}} = 5.35$ and $k_{\mathrm{z}} = 18.8$. Those values are computed using the inclusions geometry (analysed in Section 4.1.1) and thanks to the relation provided by Beremin (1981). In this work, the authors applied the extension of Eshelby (1957) by Berveiller and Zaoui (1978) to ellipsoidal inclusions assuming a monotonic loading and negligible elastic deformations. Even though they experimentally found out that the formulas tend to overestimate the real values, they still provide a reasonable and pragmatical guess in our context.

4.3.4.3 Validation of the nucleation model

The nucleation parameters computed in the previous Section 4.3.4.2 are now used with the nucleation model developed in Section 4.3.4.1. The numerical model is the same as the one

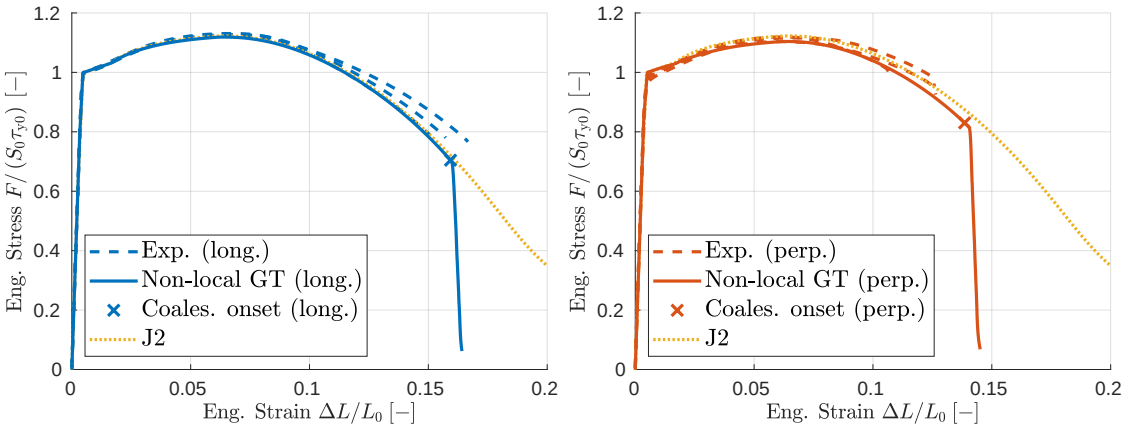

(a) Long. direction with $R_0 = 3$ [mm]

(b) Perp. direction with $R_0 = 2$ [mm]

FIGURE 4.42: Variation of the applied force as a function of the elongation ΔL for the smooth round bars simulated with the non-local Gurson-Thomason model (continuous lines) and comparison with the J2-elasto plastic law (dotted lines) and with the experimental measurements (discontinuous lines) in both directions.

described in Section 4.2.2, i.e. large strain continuous Galerkin finite element formulation with time integration performed using the dynamic scheme presented in Section 2.3.2.2 and with the mesh of parabolic elements presented in Fig 4.20a. However, this time, the full Gurson-Thomason model with the parameters identified in Sections 4.3.2, 4.3.3 and 4.3.4.2 is considered. The result obtained in terms of the ductility and in terms of the porosity distribution are then compared with experimental results. In particular, the measured porosity distribution is used to determine meaningful boundaries to the porosity evolution.

For this purpose, the simulation results of the Gurson-Thomason model for the round bars are analysed. At first, the force evolution for the smooth round bars are compared with the J2-plastic and the experimental results in both directions on Fig. 4.42. The introduction of the damage has a low impact on the results, only a slight reduction of the force amplitude is visible until the coalescence onset marked with a cross on the graph. After this point, the force abruptly drops (almost) vertically until nearly zero, signifying the specimen failure. One can note that this fall occurs later in the long. direction (Fig. 4.42a) than in the perp. one (Fig. 4.42b), which is a first sign of damage anisotropy.

Furthermore, the distribution of the representative internal variables of the model are compared for both directions on Figs. 4.43 at the coalescence onset which occurs each time at the specimen centre. Due to its higher ductility, the plastic strain values p are higher in the long. smooth round bars than in the perp. one. However, the non-local effective porosity values $\tilde{f}_V$, i.e. including the effects from the void shape, are higher in the perp. direction. Both previous observations countervail each other and lead to comparable values for the ligament ratio χ at the coalescence onset. Besides, beyond the coalescence initiation, the simulations produce a flat failure path in both directions as visible on Fig. 4.44. It consists in the darker line due to one layer of highly deformed elements surrounded by spurious non-local damage diffusion. This predicted failure path is not in agreement with experimental observations corresponding to a cup-cone because the Gurson-Thomason model does include shear coalescence mode (see the work of Nguyen, Pardoen, and Noels (2020)). Shearing will be capture with the transition model as shown in Section 4.4.

The previous analysis is also completed by the results obtained on the notched bars. As illustration, the force-striction curves obtained experimentally, with the GT model and with

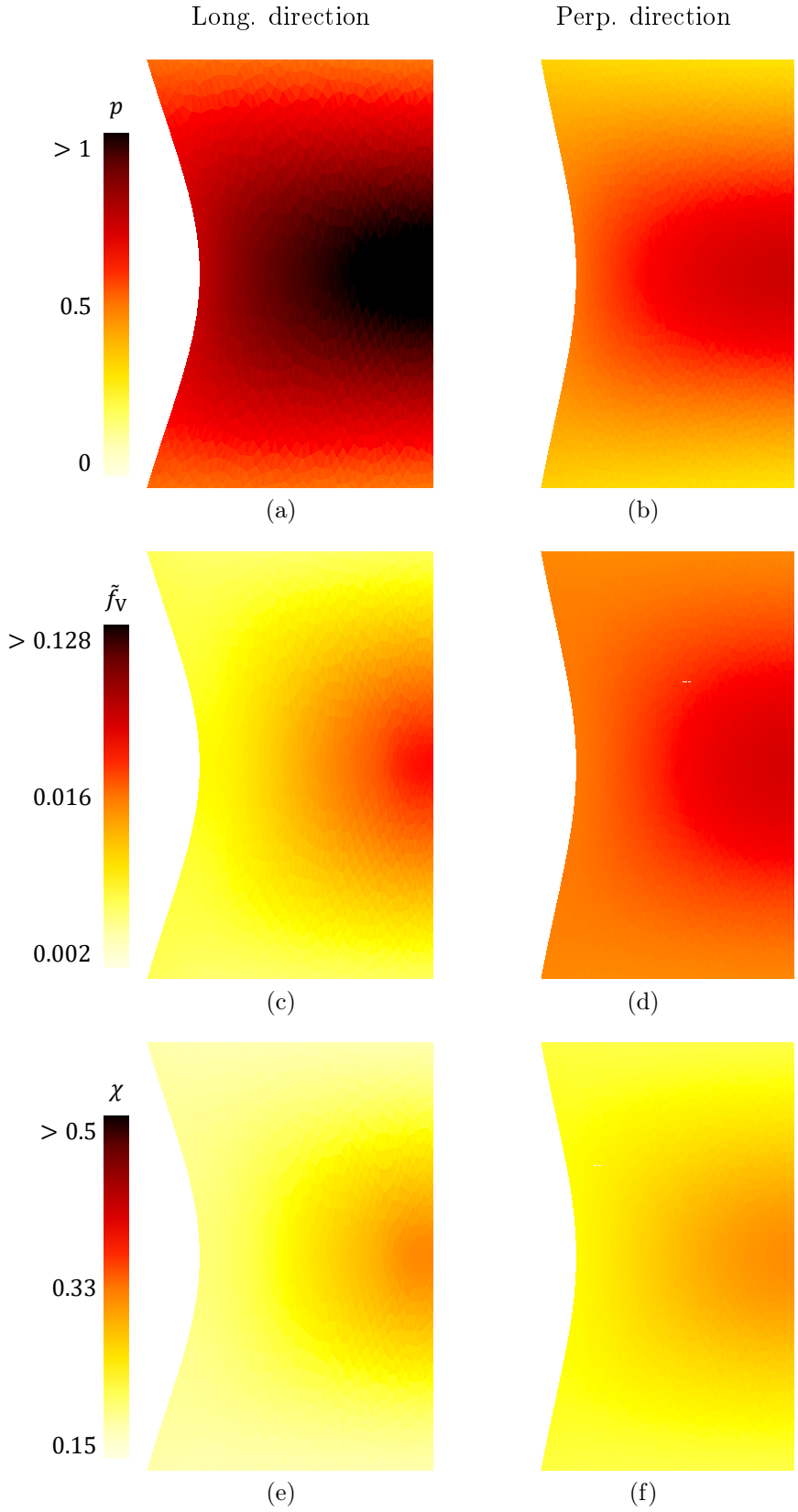

FIGURE 4.43: Distribution of (a-b) the matrix plastic strain p, (c-d) the non-local porosity $\tilde{f}_V$ and (e-f) the ligament ratio χ in the deformed configuration for the smooth round bars ($R_0 = 2$ [mm]) at the onset of coalescence (left) in the long. direction and (right) in the perp. direction.

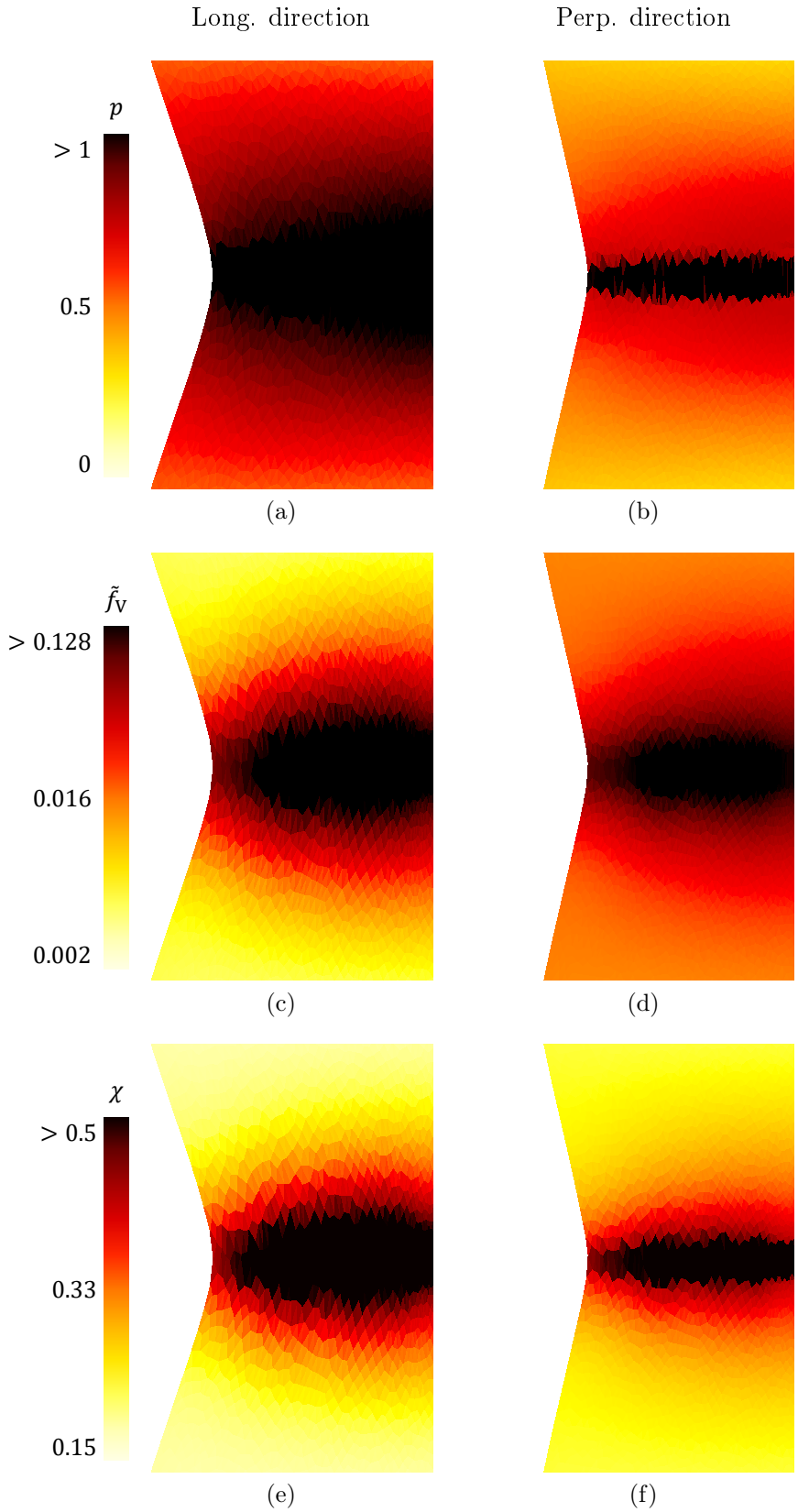

FIGURE 4.44: Distribution of (a-b) the matrix plastic strain p, (c-d) the non-local porosity $\tilde{f}_V$ and (e-f) the ligament ratio χ in the deformed configuration for the smooth round bars ($R_0 = 2$ [mm]) at final failure (left) in the long. direction and (right) in the perp. direction.

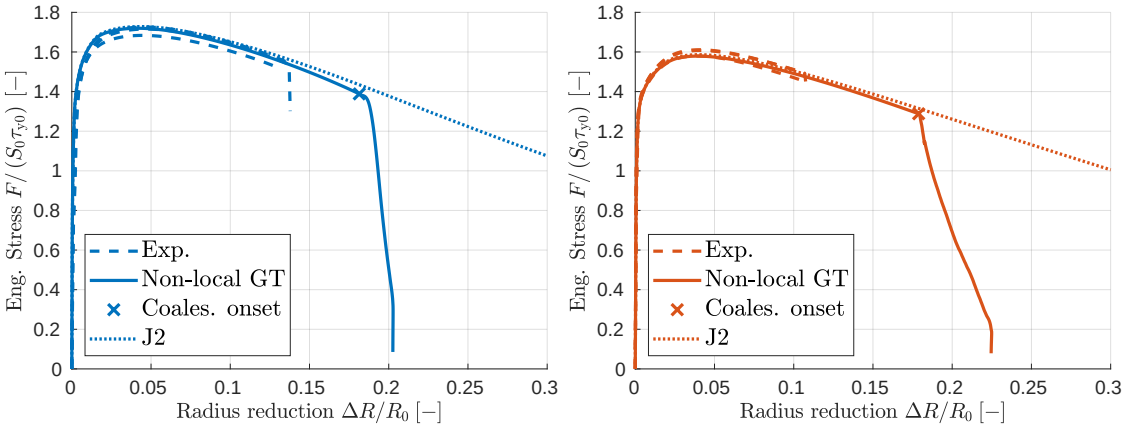

(a) $R_n = 1$ [mm] (b) $R_n = 2$ [mm]

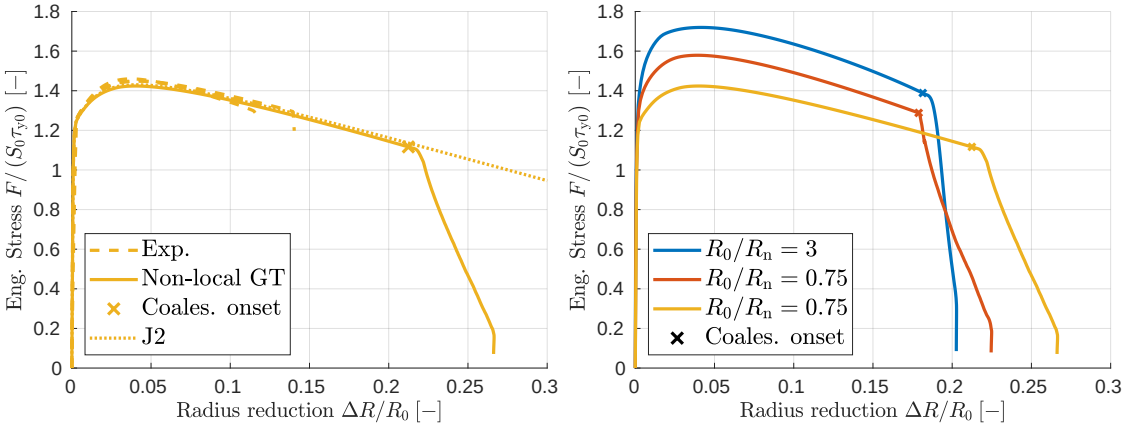

(c) $R_n = 4$ [mm] (d) $R_n = 1, 2, 4$ [mm]

FIGURE 4.45: Variation of the applied force as a function of the diameter reduction ΔR for the notched round bars simulated with the non-local Gurson-Thomason model (continuous lines) and comparison with the J2-elasto plastic law (dotted lines) and with the experimental measurements (discontinuous lines) with $R_0 = 3$ [mm].

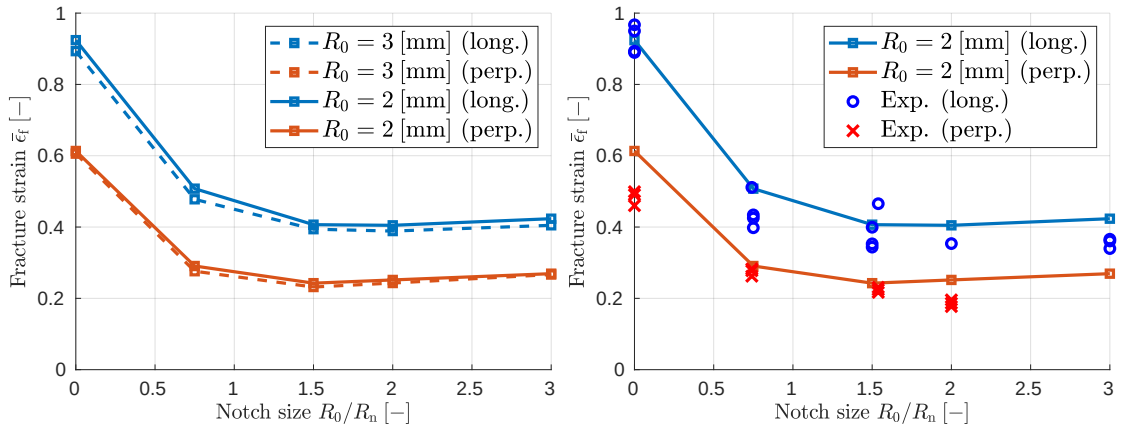

(a) (b)

FIGURE 4.46: Comparison of the fracture strain obtained by simulations of the round bars $R_0 = 3$ [mm] and $R_0 = 2$ [mm] for the two directions with all the available experimental measurements (i.e. with $R_0 = 3$ [mm] and $R_0 = 2$ [mm]).

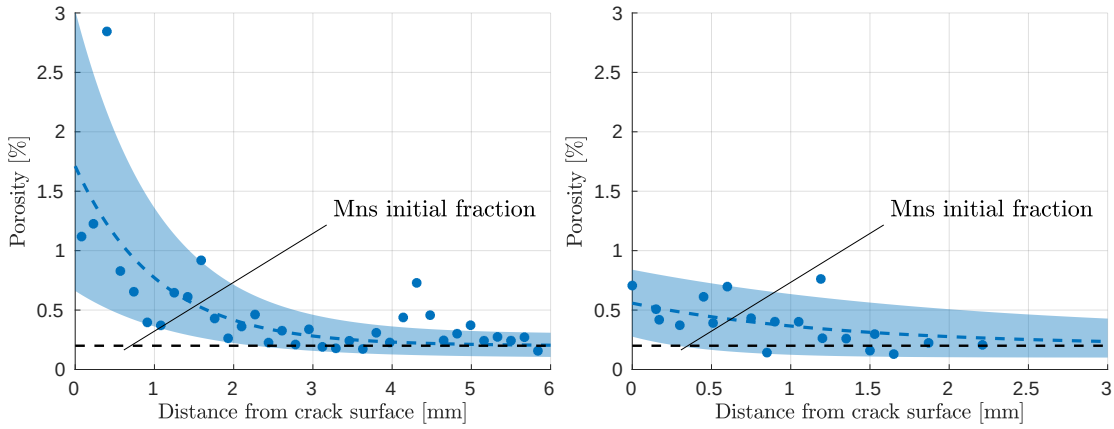

(a) Long. direction (b) Perp. direction

FIGURE 4.47: Experimental trend based on measurements of the MnS fractions in terms of the distance to the crack surface on (a) one specimen sampled in the long. direction and on (b) two specimens sampled in the perp. direction.

the J2-law are compared on Fig. 4.45 for the notched bars in the long. direction. The observations made previously on the smooth bars are still applicable in this case.

The ductilities obtained on the round bars are shown on Fig. 4.46 for both directions and both specimens sizes. The fracture strain is approximated by the value observed at the coalescence onset because, beyond this stage, the failure path is not correctly predicted. It will results in an overestimation of the real value. Thereby, on Fig. 4.46a, we compare the predicted fracture strain for $R_0 = 3$ [mm] and $R_0 = 2$ [mm] in both directions. At equivalent stress conditions, dictated by the notch size, the material response is slightly more ductile with smaller specimens. Indeed, since the dissipated energy is governed by the ratio between the non-local length compared to the specimen size, an increase of the latter results in a more ductile behaviour. In others words, decreasing the specimen size is equivalent to increasing the non-local length. Similar conclusions have been drawn previously in Section 2.2.4 in the elastic regime. However, as this effect is relatively small, only the numerical predictions obtained with $R_0 = 2$ [mm] are kept in the following. On Fig. 4.46b, the numerical results are compared to the experimental measurements. A good agreement compared to the experimental dispersion is obtained: only the fracture strain of the smooth round bar in the perpendicular direction is overestimated.

The current calibration is suitable to reproduce the frature strain of the round bars in both directions. Now, we need to challenge the current calibration towards the porosity measurements realised post-mortem. From MnS measurements presented on Fig. 4.18 in Section 4.1.3, an experimental trend is obtained for visualisation purpose on Fig. 4.47 by fitting the mean fraction value on a 0.5 mm bandwidth (the size of the uncertainty on the crack surface zero point) with an exponential function. Upper and lower bounds are similarly obtained by fitting the mean value +/- 2 times the standard deviation obtained on the same bandwidth. One can notice that the distribution tends toward the volumic fraction of MnS inclusions $f_\mathrm{p} = 2\times10^{-3}$, far away from the crack surface. On the previous distributions of Fig. 4.47, we added on Fig. 4.48 the apparent non-local porosity distributions obtained with the GT simulations. In these numerical predictions, the effects of the void shape was removed, i.e. while the GT considers the effective porosity $\tilde{f}_\mathrm{V}$ resulting from the nucleation law (4.30), the apparent porosity in the long. direction results from Eq. (4.35) and is equal to the effective one and the apparent porosity in the perp. direction results from Eq. (4.36) and is equal to $\tilde{f}_\mathrm{V}/W^{0.5}_{0,\mathrm{long}}$. Besides, the

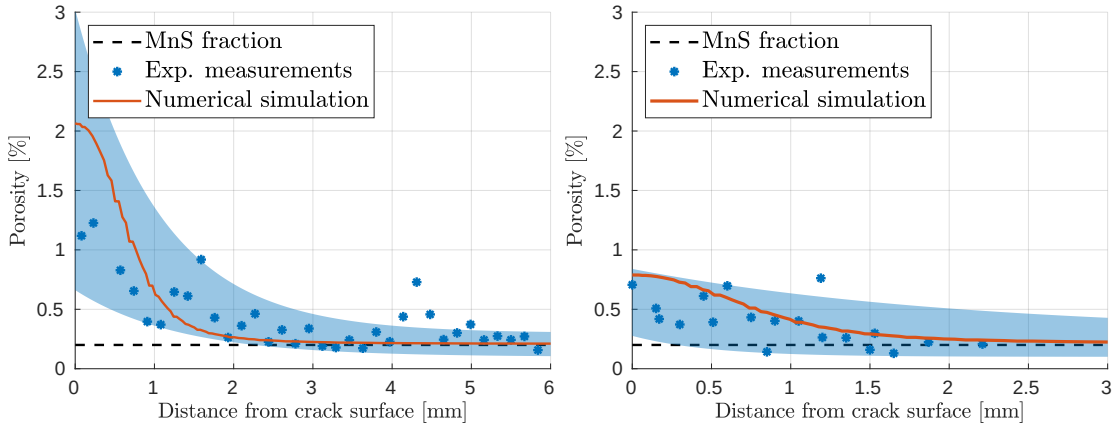

(a) Long. direction (b) Perp. direction

FIGURE 4.48: Comparison of the porosity distributions in terms of the distance to the crack surface obtained with the numerical simulations (in which case we consider the apparent and not effective porosity) of the smooth bar $R_0 = 2$ [mm] and the experimental measurements of the MnS fractions (a) in the long. direction and (b) in the perp. direction.

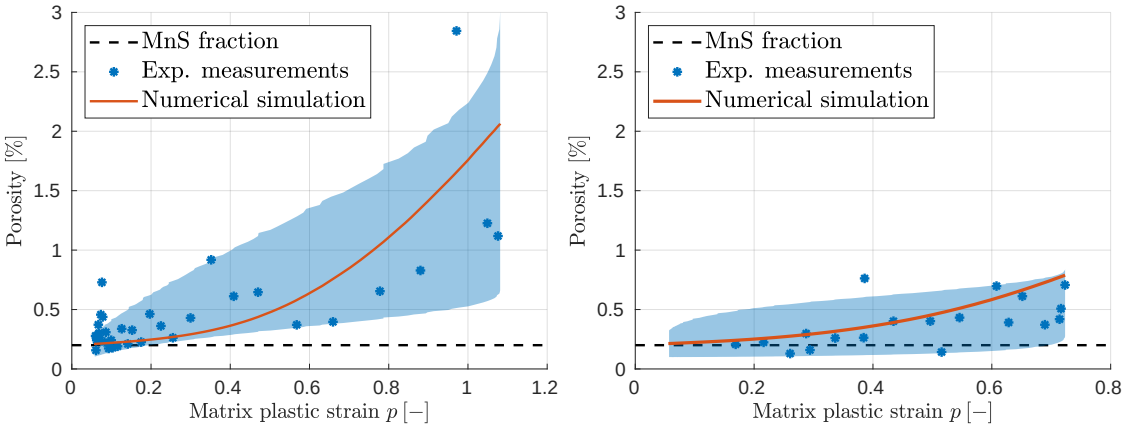

(a) Long. direction (b) Perp. direction

FIGURE 4.49: Comparison of the porosity distributions in terms of the distance to the crack surface obtained with the numerical simulations (in which case we consider the apparent and not effective porosity) of the smooth round bar $R_0 = 2$ [mm] and the experimental measurements of the MnS fractions (a) in the long. direction and (b) in the perp. direction.

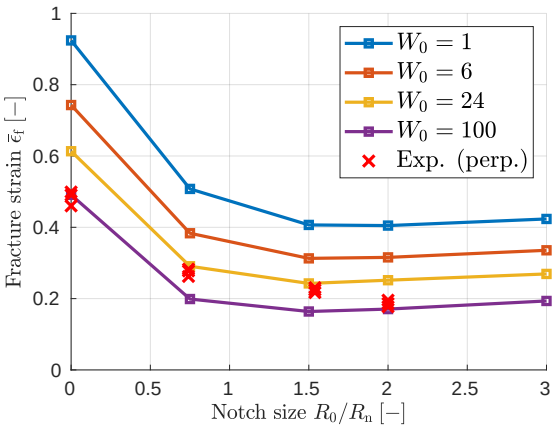

FIGURE 4.50: Comparison of the fracture strain obtained on the round bars $R_0 = 2$ [mm] for different values of the MnS inclusions aspect ratio W_0 and the experimental measurements.

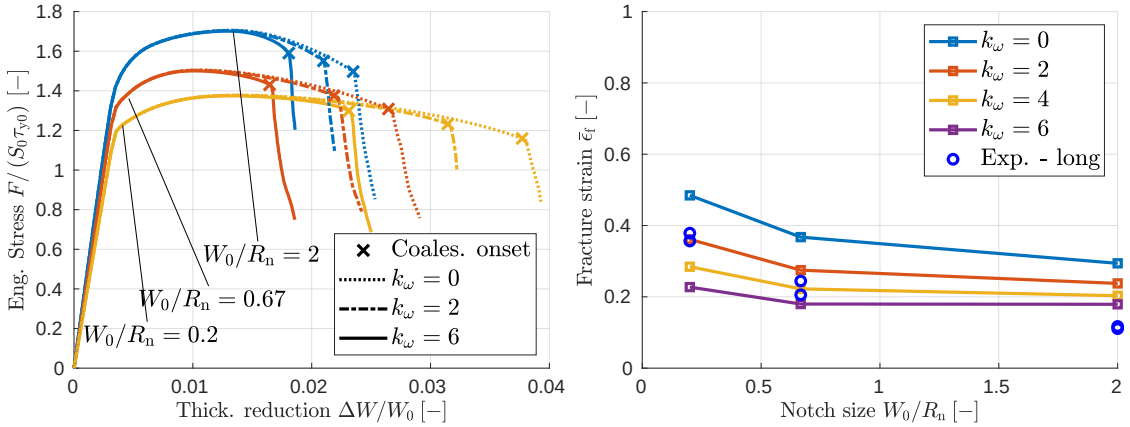

FIGURE 4.51: (a) Comparison of (a) the force evolution as a function of the specimen elongation on the grooved plates predicted for different values of k_ω and (b) of the corresponding fracture strain with the experimental measurements.

distributions are re-expressed in terms of the plastic strain on Fig. 4.49 although the resulting curve is not obtained at fixed triaxiality. One can observe that the numerical distributions are consistent and meaningful with the experiments in both directions despite the high data dispersion. However, this agreement will be not observed at the complete failure with the pure non-local model. Indeed, this model entails spurious damage diffusion visible on Fig. 4.44 which will pollute the results unless the transition is used, see Section 4.4.2.1.

In summary, the current calibration, while only using micromechanical-based arguments, is able so far to reproduce the failure anisotropy at different stress triaxiality values and consistently reproduces the observed microscopic porosity evolution. To complete this analysis, the effects of the inclusions aspect ratio, W_0, is represented on Fig. 4.50. As expected from Section 4.3.4.2, increasing W_0 results in an increase of nucleated quantity in the perpendicular direction, and therefore, a loss of ductility as observed on the graph. This motivates the use of $W_0 = 24$ although the expected value from the porosity geometries (see Section 4.1.1) $W_0 = 16$.

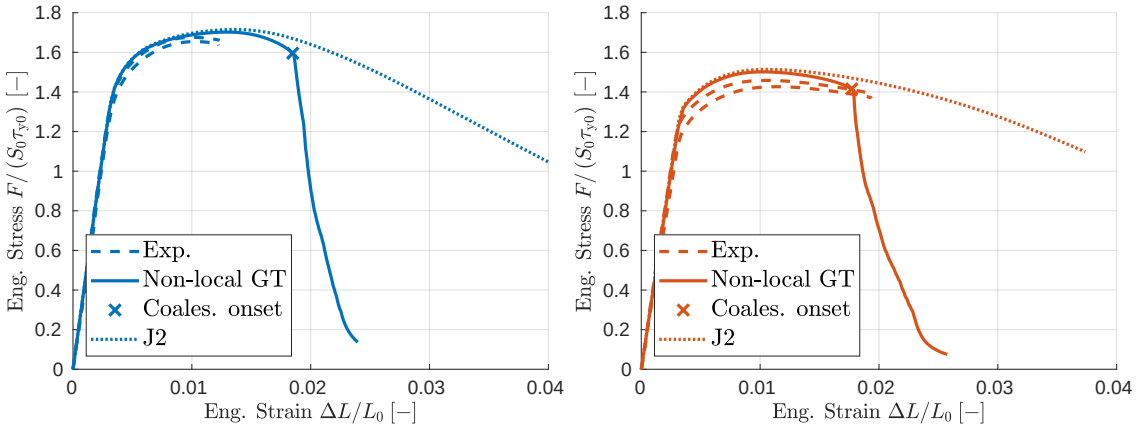

(a) $R_n = 1$ [mm] (b) $R_n = 3$ [mm]

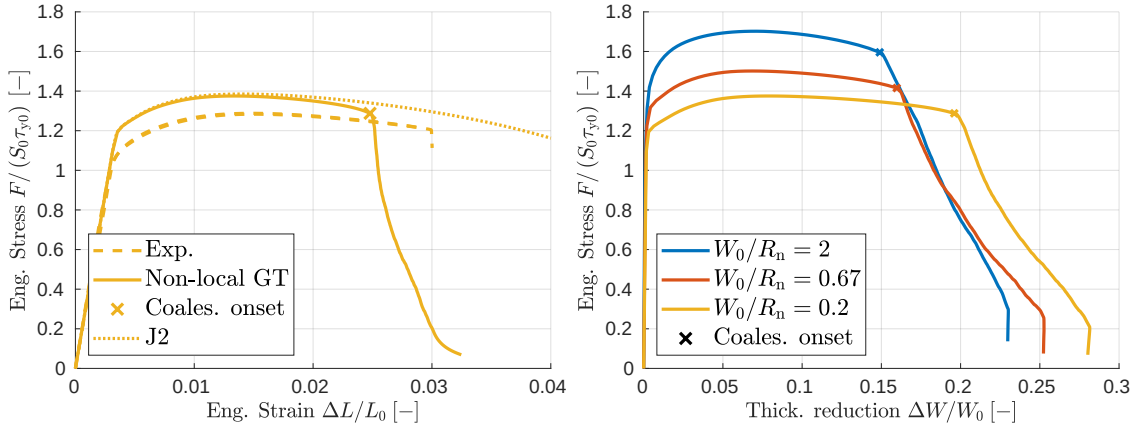

(c) $R_n = 10$ [mm] (d) $R_n = 1, 3, 10$ [mm]

FIGURE 4.52: Variation of the applied force as a function of the elongation ΔL or the thickness reduction ΔW for the grooved plates simulated with the non-local Gurson-Thomason model (continuous lines) and comparison with the J2-elasto plastic law (dotted lines) and with the experimental measurements (discontinuous lines).

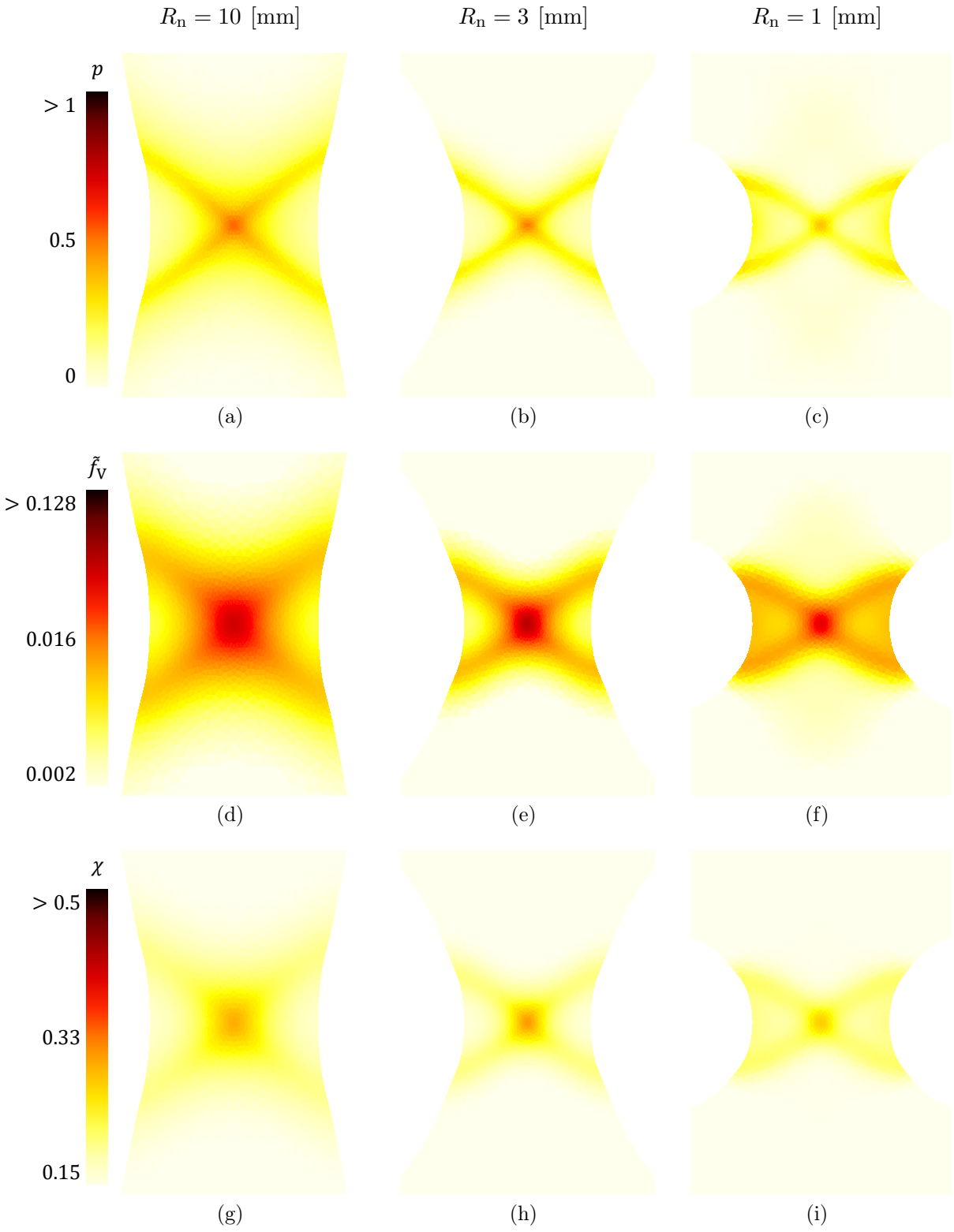

FIGURE 4.53: Distribution of (a-c) the matrix plastic strain p, (d-f) the non-local porosity $\tilde{f}_V$ and (g-i) the ligament ratio χ in the deformed configuration for the grooved plates at the onset of coalescence.

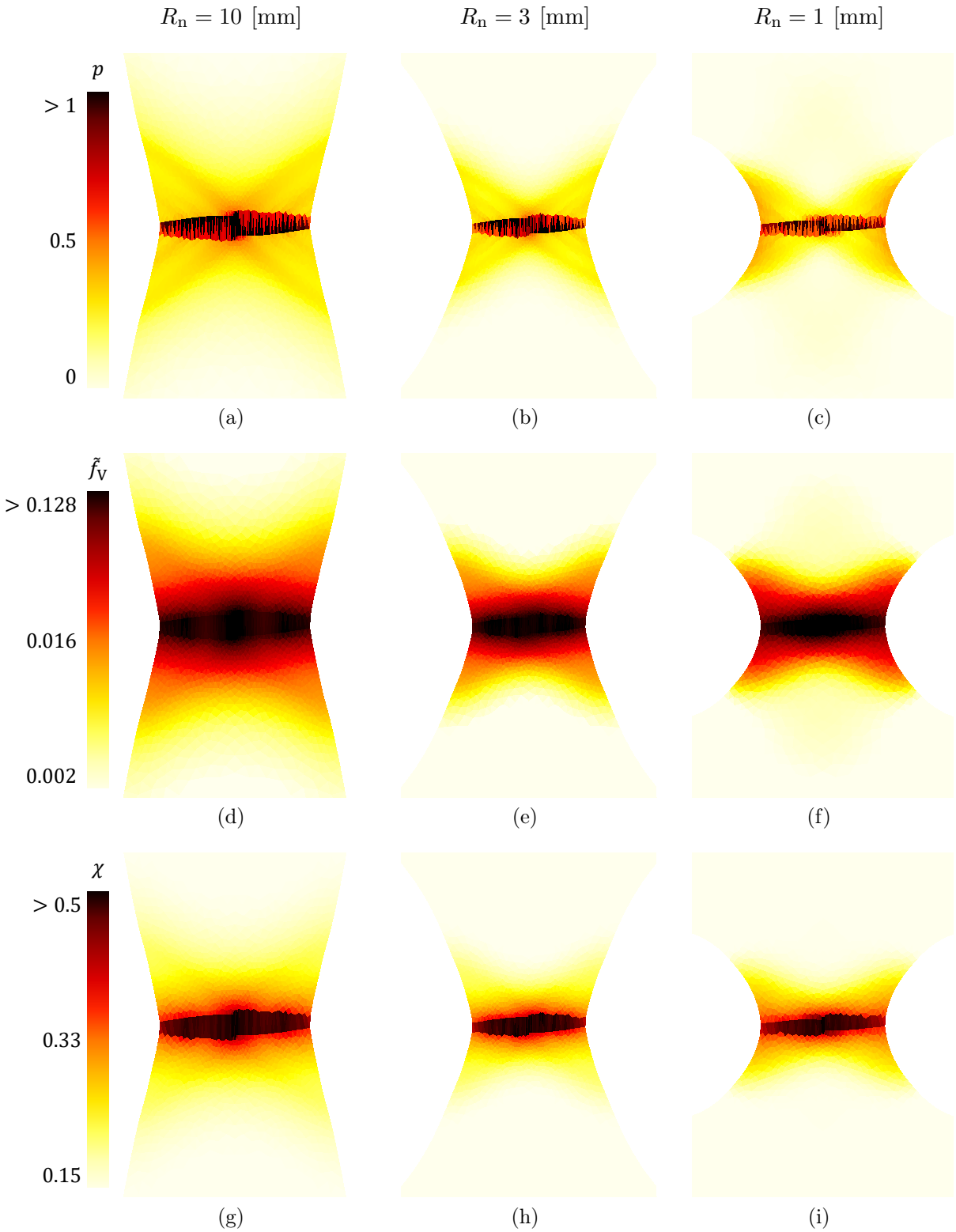

FIGURE 4.54: Distribution of (a-c) the matrix plastic strain p, (d-f) the non-local porosity $\tilde{f}_V$ and (g-i) the ligament ratio χ in the deformed configuration for the grooved plates near failure.

4.3.5 Calibration of the shear-induced growth

In this section, the last remaining parameter, the shear-induced growth coefficient k_ω, is calibrated. Nahshon and Hutchinson (2008) introduced this parameter in the porosity growth rate (3.26) to include a non-trivial porosity growth rate under shear conditions (by opposition to the classical Gurson model). We calibrate the value of k_ω in order to fit the experimental fracture strain observed on grooved specimens. Those latter are preferred to others specimens because of its stress condition state. Indeed, in plane strain, $\zeta = 0$ and, following Eq. (3.27), the parameter effect is maximised and constant along the whole test. Let us note that this does not have an effect on previous axisymmetric results because the shear term is negligible on the coalescence initiation occurring at $\zeta = \pm 1$.

The numerical model used here is the same as the one described in Section 4.2.2, i.e. large strain continuous Galerkin finite element formulation with time integration performed using the dynamic scheme presented in Section 2.3.2.2 and with the mesh of parabolic elements presented in Fig. 4.26. However, this time, the full Gurson-Thomason model with the parameters identified in Sections 4.3.2 and 4.3.3 and the nucleation law developed and identified in Section 4.3.4 is considered.

On Fig. 4.51, the effects of k_ω is studied for such grooved specimens. The force evolution is shown on Fig. 4.51a. On the latter, the coalescence onset, which is marked with a cross, is used as reference point for the fracture strain computation reported in Fig. 4.51b despite this choice will underestimate the real strain. We keep the same scale on Fig. 4.51b than on Fig. 4.46 to ease the comparison between specimen families. Increasing k_ω decreases the ductility. However, the effect weakens for a smaller notch size as the triaxiality is higher in those specimens. Choosing $k_\omega = 5.0$ allows obtaining a reasonable agreement with at least two specimens on three knowing that the current value are underestimated and an acceptable one on the third.

The loading force on the grooves specimen for the picked value of k_ω is represented on Fig. 4.52. In a similar fashion as the round bars, the non-local GT model stays close to the elasto-plastic results at the beginning of the curve. However, the gap gradually widens until the coalescence onset. After this point, the loading force drops in terms of both the elongation and of the striction. However, based and these curves, the amount of deformations after coalescence is not negligible and is likely overestimated.

In addition, the corresponding distribution of the damage-driving variables are depicted on Fig. 4.53 at the onset of the coalescence. The variables follow shear bands similar to the ones spotted previously on Fig. 4.28, but they are more noticeable here. Their counterparts near total failure are represented on Fig. 4.54. A flat crack path is obtained which is in opposition to the experiments displayed on Fig. 4.12. This inaccurate failure path arises because the Gurson-Thomason model does not include shear coalescence mode (see the work of Nguyen, Pardoen, and Noels (2020)). Shearing will be capture with the transition model as shown in Section 4.4. Moreover, the post-failure spurious non-local diffusion is clearly visible on those specimens. Indeed, one can compare the porosity distribution at the coalescence onset and at material failure, e.g. for Fig. 4.53d with Fig. 4.54d. Because of the wrong crack path, the excessive strain artificially increases the ductility and the fracture strain, justifying why we have considered the coalescence onset as fracture strain.

4.3.6 Validation on the plane stress specimens

In this section, we apply the calibrated non-local framework to the plane stress flat bars, presented in Section 4.1.2.3 and already simulated in Section 4.2.2.3 with the elasto-plastic law. We focus here on the fracture strain prediction only because the post-coalescence behaviour requires important computation time. We use here the same numerical model as presented in Section 4.2.2.3, i.e. large strain continuous Galerkin finite element formulation with time

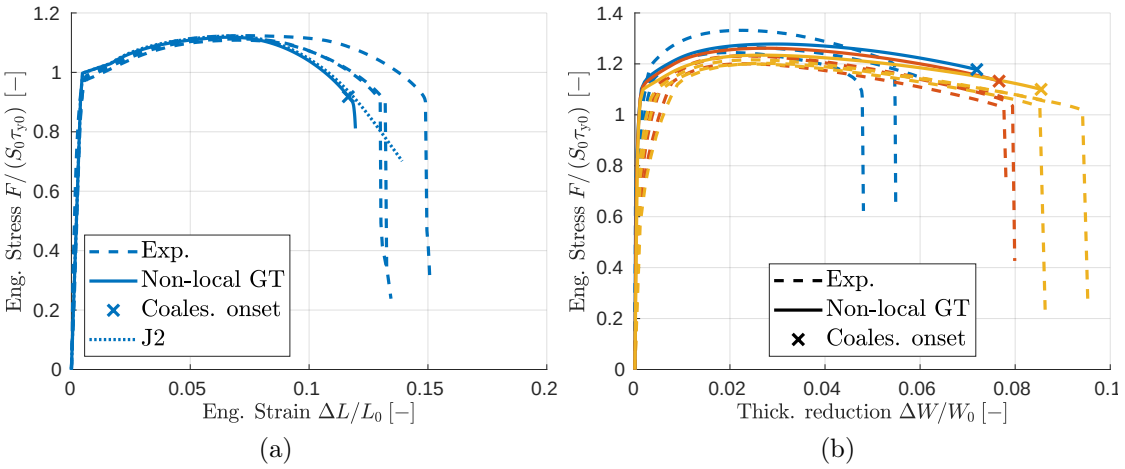

FIGURE 4.55: Comparison of the force evolution as a function (a) of the specimen elongation for the smooth flat bar and (b) of the thickness reduction for the notched flat bars.

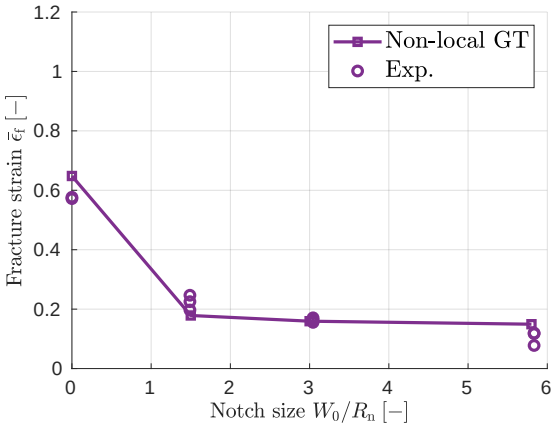

FIGURE 4.56: Comparison of the predicted fracture strain obtained on the flat specimens with the experimental measurements.

integration performed using the dynamic scheme presented in Section 2.3.2.2 and with the 3D mesh of second-order tetrahedra elements presented in Fig. 4.31.

On Fig. 4.55, the evolution of the applied force is compared with the experimental and the elasto-plastic results. Simulations are shown until the coalescence onset, highlighted with a cross, as we focus only on this part. Similarly to the previous specimens, either on Fig. 4.55a for the smooth flat bars or on Fig. 4.55b for the notched counterparts, the same qualitative correspondence is observed between the non-local porous model and the experimental results than it was observed on Fig. 4.32 in Section 4.2.2.3 with the elasto-plastic model. In addition, the fracture strain is shown on Fig. 4.56: the Gurson-Thomason model clearly reproduces the experimental results in terms of ductility.

4.3.7 Material parameters and fracture strain summary

In this section, we summarise all the material parameters identified during this calibration campaign for the non-local porous model in Tab. 4.1. We also gather the numerical predictions of the stress state and the fracture strain on each specimen on Fig. 4.57 and compare them to the experimental or the elasto-plastic analysis performed in Section 4.2.3. On Figs. 4.57a

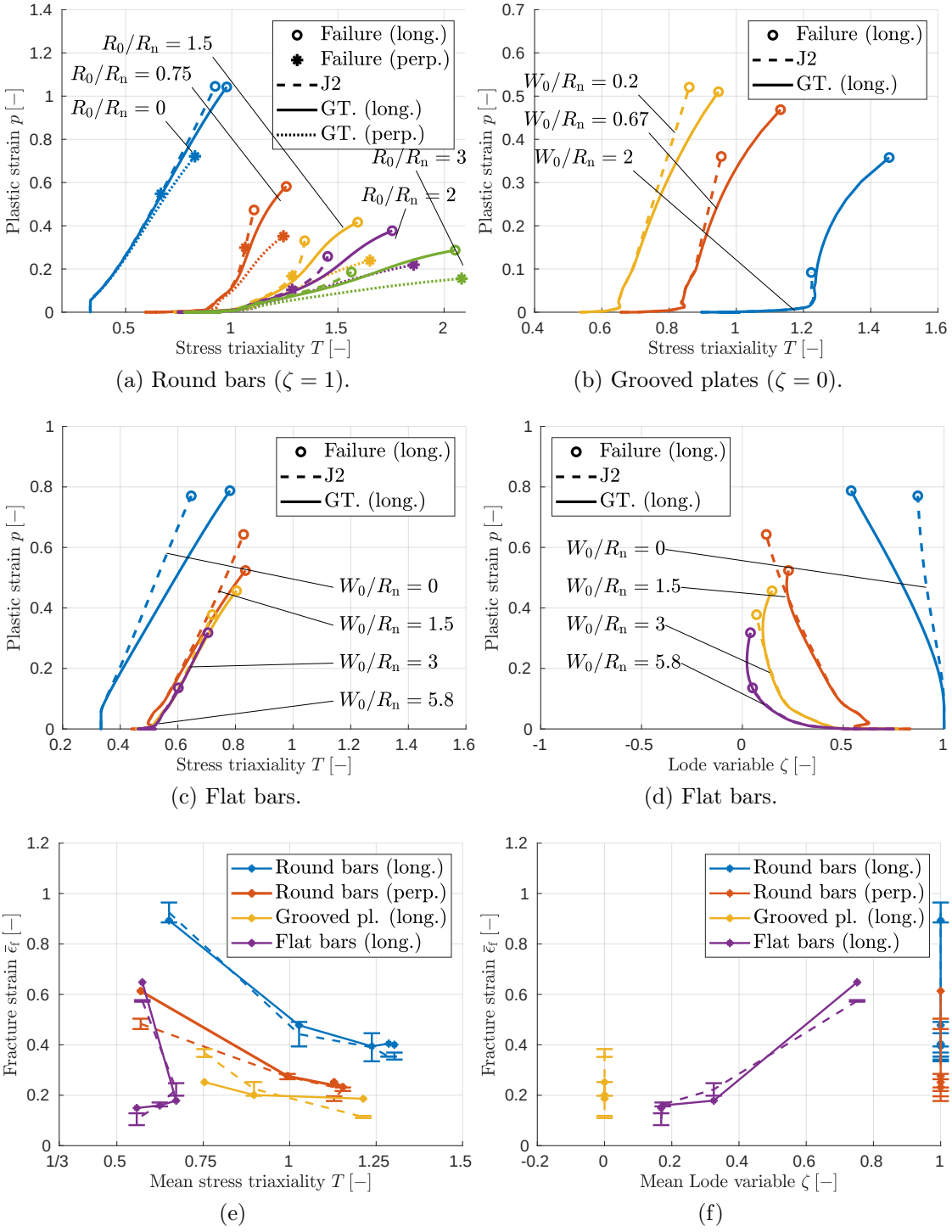

(a) Round bars ($\zeta = 1$). (b) Grooved plates ($\zeta = 0$).

(c) Flat bars. (d) Flat bars.

(e) (f)

FIGURE 4.57: Comparison of (a-d) the evolution of the stress triaxiality on (a) the round bars, (b) the grooved plates and (c) the flat bars, and the evolution of the Lode variable for (d) the flat bars at the centre of the reference cross-section of all the specimens simulated with the J2-plastic law (discontinuous lines) and with the Gurson-Thomason model in both directions (continuous lines for the long. direction and dotted lines for the perp. direction); and (e-f) comparison of fracture strain obtained numerically with the non-local porous model (continuous lines) and experimentally (discontinuous lines) as a function of the mean value of (e) the triaxiality and (f) the Lode variable at the centre of the reference cross-section of all the specimens simulated with the J2-plastic law.

TABLE 4.1: Calibrated material parameters.

E	Young modulus
ν	Poisson's ratio
$\tau_{\mathrm{Y}}(p)$	Isotropic stress hardening law
f_{V_0}	Initial porosity
s_{n}, p_{n}	Nucleation distribution parameters
$f_{\mathrm{n,long}}$, $f_{\mathrm{n,perp}}$	Nucleation intensity
k_{long}, k_{perp}	Nucleation stress concentration factors
$\sigma_{\mathrm{n_c\,long}}$, $\sigma_{\mathrm{n_c\,perp}}$	Critical nucleation stress parameters
λ_0 (or χ_0)	Initial spacing ratio (or initial ligament ratio)
q_1, q_2	Gurson yield surface coefficients
α, β	Thomason concentration load factors
κ	Void spacing growth factor
k_ω	Shear-induced growth factor
l_{c}	Non-local length

to 4.57f, the stress state evolutions inside each specimen are successively obtained with the elasto-plastic model (Section 4.2.2) and the calibrated non-local porous model. If both models undergo similar stress states at the yielding initiation, the difference increases with the plastic flow: the Gurson-Thomason results predict a higher stress triaxiality for a given plastic strain value, and the discrepancy is larger for higher stress triaxiality states. Besides, the predicted plastic strain at which fracture is observed differs significantly. This demonstrates that the effect of the porosity evolution on the stress state is not totally negligible.

One can observe on Figs. 4.57e and 4.57f a general agreement between the numerical predictions and the experimental observations[6]. Only the smooth round bars in the perp. direction and two of the grooved plates have a less good correspondence. Still, the trends described in Section 4.2.3 for the experimental specimens are also respected for the numerical simulations.

4.4 Calibration and validation of the damage to crack transition

Henceforth, we consider the complete non-local damage to crack transition developed in Chapter 3. For this, the Gurson-Thomason model with material parameters calibrated in Sections 4.2.1 and 4.3 is used, and the transition occurs once the criterion (3.82) is satisfied. The stability parameter for the Discontinuous Galerkin framework is fixed at $\beta_{\mathrm{s}} = 100$. At this point, only the cohesive band thickness needs to calibrated; Section 4.4.1 is dedicated to this task. Afterwards, the results obtained on the axisymmetric and the grooved specimens are presented and discussed in Section 4.4.2. In particular, the crack path is examined.

4.4.1 Calibration of the cohesive band thickness h_{b}

As already discussed in Section 4.3.3 about the non-local length, the cohesive band thickness should be representative of the mechanisms in play. Since the plastic flow during coalescence has collapsed inside the ligament between voids, it is meaningful to assume that the characteristic length linked to the coalescence is related to the void size. Therefore, the cohesive band thickness h_{b} is assumed to be equal to 8 [μm], the half of the void length.

[6] In the following, we keep the stress conditions extracted from the J2-simulations for the sake of simplicity.

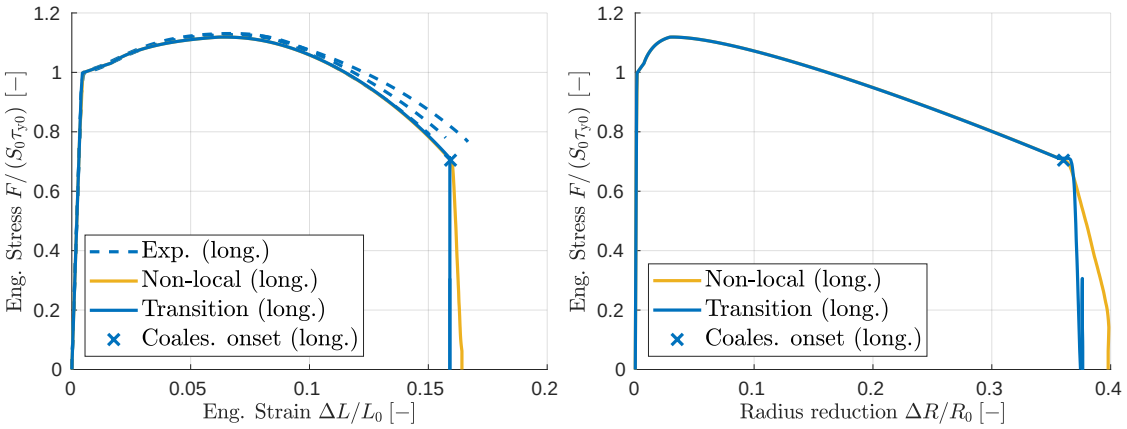

FIGURE 4.58: Variation of the applied force as a function of (a) the elongation ΔL and (b) the radius reduction ΔR for the smooth round bar ($R_0 = 3$ [mm]) simulated with the non-local Gurson-Thomason model within the transition framework and comparison with the non-local model in the long. direction.

However, this first value should be improved in a future work either by cell simulations or by mechanical tests performed on the CTS and DENT specimens. In the first case, one can obtain a more accurate guess for the coalescence characteristic size by evaluating the relative thickness inside which the plastic flow localises inside the RVE. In the second case, the fitting between the numerical and the experimental dissipated energy allows the h_b values to be estimated. Moreover, an anisotropy in this value is likely which can be estimated using samples in different orientations.

4.4.2 Validation of the transition framework

As the transition framework is now fully defined, it is applied on different specimens involved in the experimental campaign. The round bars are simulated in Section 4.4.2.1. Section 4.4.2.2 reproduces the grooved plates. Comparatively to the simulations of the previous sections, a scatter of 1% is applied on the nucleation intensity to promote crack kinking as it is often the case for fracture simulations involving CZM (Zhou and Molinari (2004)).

4.4.2.1 Round bars

The round bar specimens, presented in Section 4.1.2.1, are now simulated using the damage to crack transition. The results are shown on Figs. 4.58 and 4.59 for the smooth round bar in the long. direction. The force evolution is represented on Fig. 4.58 for the non-local model with and without crack insertion. Before crack insertion, no difference is noticeable. After it, both curves quickly fall. However, the drop is steeper with the transition: the fracture strain only increases of 0.05 after the onset compared to 0.13 for the non-local model. This fact highlights that the dissipation is lower with the crack transition. Another evidence is the force oscillations visible especially on Fig. 4.58b resulting from the dynamic integration. At the end of the day, the resulting fracture strain with the crack transition, equal to 0.95, is in agreement with the experimental values (relative error of 2%). Besides, it justifies the approximated link of the fracture strain to the values observed at the coalescence onset, as done in Section 4.3.4.3.

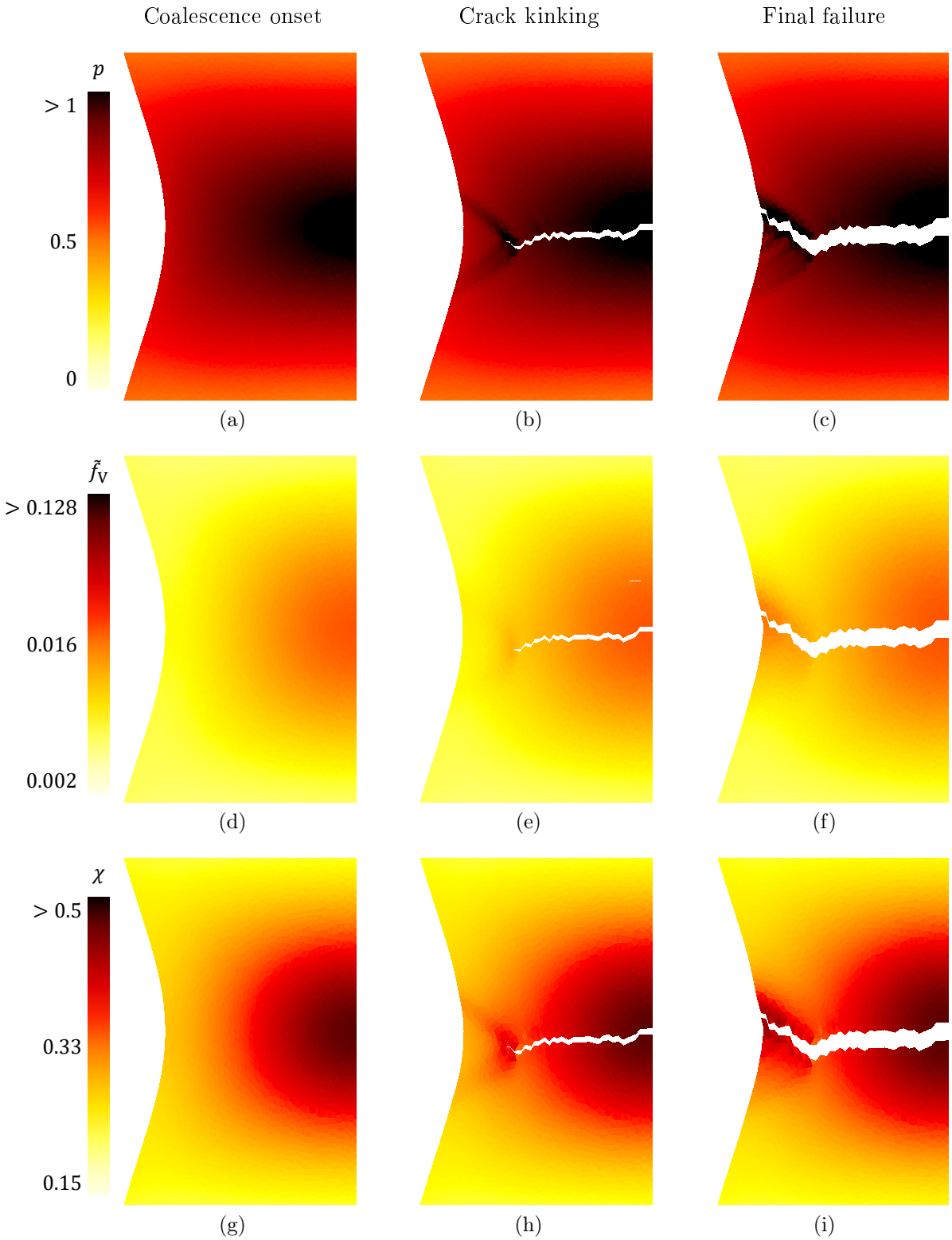

FIGURE 4.59: Distribution of (a-c) the matrix plastic strain p, (d-f) the non-local porosity $\tilde{f}_V$ and (g-i) the ligament ratio χ in the deformed configuration for the smooth round bar in the long. direction at different steps: (left) at coalescence onset, (centre) before crack kinking and (right) at final failure.

In addition, the distributions of the matrix plastic strain p, the non-local porosity $\tilde{f}_V$ and the ligament ratio χ are compared in the deformed configuration at different instants of the failure process: at the coalescence onset, before the slant bifurcation and at the total failure. Before crack insertion, the results are identical to the non-local model. A crack then initiates at the centre of the specimen and propagates radially, following the elements boundary. At some point, near the free surface, shear bands appear ahead the crack front and the crack tilts at around 45° to propagate until it reaches the surface. This results in a so-called cup-cone fracture, typically observed in literature (Pineau, Benzerga, and Pardoen, 2016, e.g.). It is also in accordance with the experimental fracture surface observed on Fig. 4.6.

However, it is worth mentioning that the robustness of the damage to crack transition, when capturing such a bifurcation, needs to be improved. Indeed, the current micromechanics-based model, succeeds well in predicting the failure onset and the crack orientation in tensile-dominated conditions through the internal necking coalescence. However, it is less the case in shear-dominated states. The cup-cone failure is captured because of the creation of free surfaces: their presence promotes the shear bands onset, the damage localisation inside these bands, followed by crack insertions. It also requires the use of a scatter in the material parameters. In fact, other localisation mechanisms and criteria come into play in those stress conditions and affect the failure process. In a future work, other coalescence modes (Nguyen, Pardoen, and Noels, 2020, e.g.), should enhance the actual micromechanical description in order to include these additional failure modes.

4.4.2.2 Grooved plates

The damage to crack transition is now applied in a different stress state on the grooved specimen with $R_n = 10$ [mm]. The evolution of the applied force is shown on Fig. 4.60. The results are qualitatively close to the ones of the previous section: the damage dissipation is more limited after the crack initiation. The distributions of the matrix plastic strain p, the non-local porosity $\tilde{f}_V$ and the ligament ratio χ in the deformed configuration are shown on Fig. 4.61. By opposition to the previous case, the plastic strain localises inside shear bands. The crack also initiates at the centre and then propagates towards the surface, forming a slanted crack. Comparatively to the smooth round bar, failure occurs at a lower level of plastic strain while the encountered porosity is higher. This observation is due to a higher triaxiality level compared to the smooth round bars, amplified by a contribution in shear. At the end of day, a slanted crack is observed on the numerical simulations, coherently to the experimental failure (Fig. 4.12c).

4.5 Conclusions

In this chapter, we have addressed the calibration of the micromechanical-based damage to crack transition framework developed in Chapter 3.

In particular, once the elasto-plastic behaviour has been identified from stress-strain loading curves, the Gurson-Thomason material parameters have been inferred from cell simulations. An anisotropic nucleation law has been developed in order to recover the difference of ductility observed for different loading directions. The parameters of this anisotropic nucleation law have been estimated from the morphology of the inclusions experimentally observed in the tested material. Finally the characteristic lengths involved in the model have been estimated from the inclusion morphology and distribution.

The different identification steps have been validated on different experimental samples, in terms of loading response but also in terms of porosity evolution. Although a pure Gurson-Thomason model cannot predict the observed slant and cup-cone failure modes of the grooved

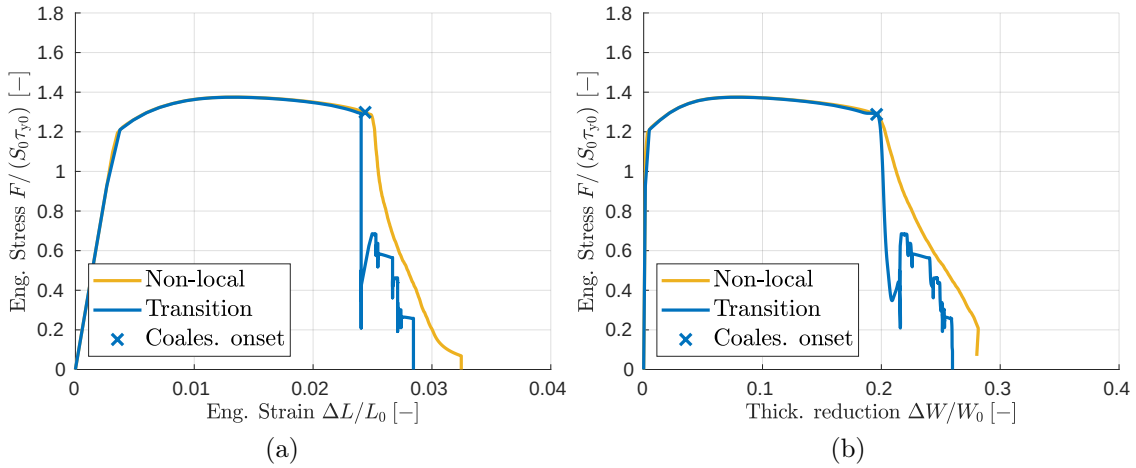

FIGURE 4.60: Variation of the applied force as a function of (a) the elongation ΔL and (b) the thickness reduction ΔW for the grooved plates ($R_n = 10$ [mm]) simulated with the non-local Gurson-Thomason model within the transition framework and comparison with the non-local model and the experimental measurements.

and axisymmetric specimens, because of the insertion of the free surfaces, the damage to crack transition framework is able to predict the crack kinking experimentally observed.

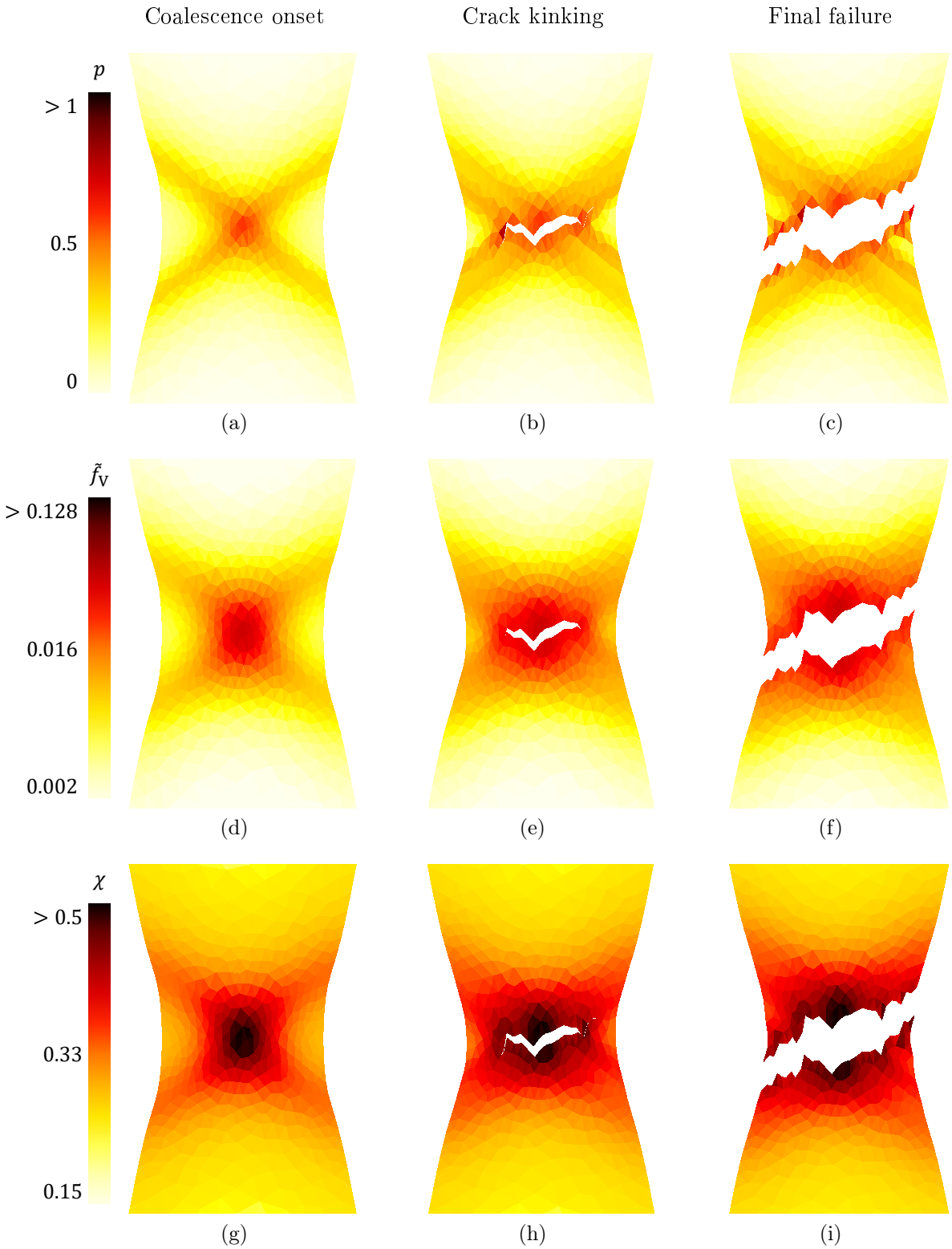

FIGURE 4.61: Distribution of (a-c) the matrix plastic strain p, (d-f) the non-local porosity $\tilde{f}_V$ and (g-i) the ligament ratio χ in the deformed configuration for the grooved plates (R_n = 10 [mm]) in the long. direction at different steps: (left) at the onset of coalescence, (centre) before crack kinking and (right) at final failure.

Chapter 5

General conclusions and perspectives

The main achievement of this work is the development of an original damage to crack transition framework suitable for modelling the ductile failure. Indeed, through the literature review in Chapter 1, most of the existing FE solutions are of limited reliability when the whole ductile failure process, see Fig. 1.1, has to be modelled. In particular, most of them suffer either from mesh-dependency or pathological case-dependency, from an inability to account for the stress-state effect, from energetic inconsistencies or again from the lack of scalability and 3D-applicability. This work focused on bringing a pragmatical and complete solution to such issues.

For this purpose, we considered as a starting point the DG-based transition framework including a non-local continuum-damage-mechanics model coupled with an extrinsic cohesive zone model developed in the work of Wu, Becker, and Noels (2014). Practically, the initial diffuse damage stage is modelled by a non-local implicit approach. However, large distortions appear inside the most damaged elements, which induce spurious damage spreading and numerical problems. To overcome this issue, a discontinuity is inserted through a CZM to simulate the last failure stage. This combination has the advantage to be mesh-independent thanks to the non-local method and the extrinsic nature of the CZM. Moreover, the scheme inherits from the numerical properties of the DG-method (including convergence, stability, scalability, and easiness of parallel and crack insertion implementation). However, the CZM is unable to account for the stress state effect on the energy release rate.

The originality lies here in the substitution of the CZM by a cohesive band model. It consists in a cohesive model with a fictitious finite thickness along which the displacement field discontinuity is assumed to be smeared. A strain tensor in this band is reconstructed by enhancing the neighbouring bulk strain by the cohesive jump. From this, the bulk material damage constitutive law is used in its local way to compute a stress tensor and then, the corresponding traction forces. Hence, the cohesive band model accounts for the triaxiality state during the crack opening, which was missing so far for any accurate ductile failure simulations.

In Chapter 2, we focused on the framework development in the context of small displacements for a damage-enhanced linear elasticity in order to demonstrate the proof of concept. In particular, we analysed the framework behaviour. Energetic equivalence and consistency were studied trough the influence of both involved material characteristic lengths: the non-local length and, the only one additional parameter introduced by our new model, the cohesive band thickness. This latter was determined from the former based on energetic considerations. The framework capabilities and its expected numerical properties are demonstrated through several examples in 2D and 3D. Besides, the superiority of our CBM over prevalent CZMs is shown by comparing simulations in different stress conditions. According to these results, one has to consider the triaxiality state in the failure process if the cohesive energy is not negligible. And it was shown that one efficient way to do so is to include the CBM which allows complex 3D stress state effects to be accounted for during the crack opening.

Afterwards, in Chapter 3, we extended the new framework to elasto-plastic material behaviours in large deformations; a more realistic context regarding the ductile failure. Huespe et al. (2012) have proposed to coupled a CBM with a Gurson model. In this approach the Gurson model represents the coalescence stage through a phenomenological porosity acceleration model (Tvergaard and Needleman, 1984). The loss of ellipticity is used as a criterion to introduce the crack band, so that no non-local formalism is required. However this approach suffers from a lack of micro-mechanics justification. Physically, it is more meaningful to introduce the crack at coalescence onset, which can occur beyond strain softening. Also the method should be general enough to consider different coalescence models. Towards this end, we developed an original suited material model. It consists in a non-local formulation of a porous plasticity model and its closed form iterative resolution algorithm. This formulation combines different micromechanics-based models in order to simulate the whole ductile failure process by void nucleation, growth and coalescence. It involves a Gurson model to simulate the void growth stage and a Thomason model to represent the coalescence phase. A shear-induced void growth term is also added to cover the damage evolution at low stress-triaxiality regime. We then coupled the damage to crack transition with this porous elasto-plastic model. Crack transition was managed using either the loss of ellipticity or using an original crack insertion criterion with the cohesive evolution law based on the coalescence part of the micro-mechanics model. This combination allows reproducing the well-known slant and cup-cone failure modes of plane-strain and axisymmetric specimens, respectively. In particular, it was shown that the numerical predictions converge with the mesh refinement, and that the cohesive band thickness governs the fracture energy released during the coalescence stage, and possibly the failure mode when vanishing values are considered. Moreover, it was shown that the Thomason coalescence criterion can be met during the strain softening stage, justifying the use of a non-local damage formulation.

In the Chapter 4, the numerical framework developed during the previous chapters was calibrated for a high-strength steel. Usually, the calibration lies on a reduced amount of macro-scale stress-strain curves (Liu, Kang, and Ge, 2019, e.g.), although some model parameters are evaluated from unit-cell simulations only (Faleskog, Gao, and Fong Shih, 1998, e.g). So the problem is to have a calibration that represents as many loading cases as possible. We took benefit from the micromechanical-based model developed previously by linking as much as possible the parameters values to their physical interpretation, including the characteristic lengths. Hence, in complement to the mechanical campaign results, the novelty is to establish the calibration procedure mainly on micromechanics observations and arguments by using unit cell simulations, inclusions morphology and their post-mortem distribution. This way, the propensity to material parameters overfitting is reduced compared to a pure classical parametric optimisation. We note that this approach would have been impossible or more complex with any other phenomenology-based damage model, or with a phase-field method for instance.

Besides, the considered high-strength steel has the particularity to exhibit failure anisotropy due to its microstructural morphology. In order to include those effects, we took as starting point the nucleation criterion suggested by Beremin (1981). In this work, they created a criterion to take into account the void inclusions but which is isotropic. On this basis, we created a new anisotropic void nucleation model allowing representing the failure anisotropy. As previously, its design and its calibration rests on micromechanical arguments. At the end of the day, the non-local model was shown to be able to predict the failure initiation for several stress conditions while taking into account the failure anisotropy. In addition, the transition allows reproducing the slant and cup-cone failure modes of plane-strain and axisymmetric specimens while the pure non-local model failed at it.

Nonetheless, this work should be brought further. Indeed, the current micromechanics-based model, coupled to the transition framework succeeds well in predicting the failure onset

and its orientation in tensile-dominated conditions through the internal necking coalescence. However, its predictions still lack of robustness in shear-dominated states. Slant and cup-cone failures are captured because of the creation of free surface. Their presence, as well the use of scatter in the material parameters, promotes the shear bands onset, the damage localisation inside these bands, followed by crack insertions. In fact, others localisation mechanisms and criteria come into play in those stress conditions and affect the failure process. In a future work, others coalescence modes, in particular shear dominated ones, (Nguyen, Pardoen, and Noels, 2020, e.g.), should enhance the actual micromechanical description in order to include these additional failure modes.

The micromechanics-based nucleation model could be also enhanced by incorporating the effects of the second inclusions population to improve the reliability of the simulations. Non-monotonic loading can be considered by extending the anisotropy from the nucleation model to the void growth and coalescence.

Regarding the material calibration itself, unused mechanical tests should be involved in the calibration procedure. In particular, the compact tension test and the double edge notched specimen would help to ascertain the characteristic lengths beyond the current first guess. Other tests as the Arcan and the Hopkinson results will extend the validity zone. Besides, some parts of the stress state spectrum are still be missing: compression tests would help to fill this lack.

Anyway, at the end of the day, the developed non-local CDM/CBM framework, combined to the micromechanical model and the micromechanics-based calibration, provides the basis of a comprehensive and operational method exploitable for industrial applications. Its use will allow reliable ductile failure predictions by discarding the numerical inconsistencies and the case-dependencies which are affecting most of actual numerical methods. Consequently, the access to those predictions for industrial applications will afford precious insights in the physical process with a reduced cost. Experimental campaign could be minimised while improving the structural design.

Moreover, the framework versatility renders it easily applicable to other material behaviours. Furthermore, its implementation requires only few modifications (comparatively to other crack insertion framework). This will ease the CDM/CBM integration into standard FE industrial codes (we note that user elements are already developed to introduce DG in commercial codes (Charles, 2014)). Besides, despite the DG-method advantages, the formalism can be combined with any other crack insertion techniques, as for instance, a node-splitting method or the xFEM for which the last improvements (Vigueras et al., 2015) in this framework makes it more attractive to industrial applications.

Appendix A

Appendix related to Chapter 2

A.1 Linearisation of the elastic damage model

One has from Eq. (2.39):

$$\delta\sigma_{ij} = \frac{\partial \sigma_{ij}}{\partial \epsilon_{kl}} \delta\epsilon_{kl} + \frac{\partial \sigma_{ij}}{\partial \tilde{e}} \delta\tilde{e}. \tag{A.1}$$

Depending if the applied damage model is local or non-local, the derivatives $\frac{\partial \boldsymbol{\sigma}}{\partial \boldsymbol{\epsilon}}$ and $\frac{\partial \boldsymbol{\sigma}}{\partial \tilde{e}}$ have different expressions. For the implicit non-local damage model, one has

$$\delta\sigma_{ij} = \underbrace{\left[(1-D)\,\mathcal{H}_{ijkl}\right]}_{\boldsymbol{\mathcal{C}_{uu}}} \delta\epsilon_{kl} + \underbrace{\left[-\mathcal{H}_{ijkl}\epsilon_{kl}\frac{\partial D}{\partial \tilde{e}}\right]}_{\mathbf{C}_{\boldsymbol{u}\tilde{e}}} \delta\tilde{e}, \tag{A.2}$$

while for the local damage model, applied in the cohesive band

$$\delta\sigma_{ij} = \underbrace{\left[(1-D)\,\mathcal{H}_{ijkl} - \mathcal{H}_{ijmn}\epsilon_{mn}\frac{\partial D}{\partial \epsilon_{kl}}\right]}_{\boldsymbol{\mathcal{C}}^{\mathrm{loc}}_{\boldsymbol{uu}}} \delta\epsilon_{kl} \tag{A.3}$$

Concerning the local value e, the linearisation of Eq. (2.41) gives

$$\delta e = \frac{\partial e}{\partial \epsilon_{ij}} \delta\epsilon_{ij} = \underbrace{\left[\sum_{k^+} \epsilon_k \frac{v_i^k v_j^k}{e}\right]}_{\mathbf{C}_{e\boldsymbol{u}}} \delta\epsilon_{ij}, \tag{A.4}$$

where ϵ_k is a eigenvalue of $\boldsymbol{\epsilon}$, $\boldsymbol{v}^k$ is the associated eigenvector, and where the sum $\sum_{k^+}$ carries only on positive eigenvalues.

A.2 Computation and linearisation of the cohesive band model stress tensor

The band deformation gradient is computed by applying the Eq. (2.31) on the corresponding side of the interface, using the corresponding deformation gradient F_{iJ}, the jump displacement $[\![u_i]\!]$ and the gradient of the jump displacement $\nabla_J [\![u_i]\!]$. The deformation gradient F_{iJ} and the jump displacement $[\![u_i]\!]$ are computed with the shape functions of the volume elements while the computation of $\nabla_J [\![u_i]\!]$ involves the shape functions of the interface elements only (because a node outside the interface does not have to influence this value in order to satisfy the condition (2.28)). As jump values and their gradients are not equal to zero before crack insertion due to the DG formalism, initial jump values (and their gradients) at crack insertion are deducted from the effective values used in (2.31).

The derivatives of the band deformation gradient $\mathbf{F}_\mathrm{b}$ (2.31) with respect to the bulk deformation gradient $\mathbf{F}$ read

$$\frac{\partial F_{\mathrm{b}iJ}}{\partial F_{kL}} = \frac{\partial}{\partial F_{kL}}\left[F_{iJ} - F_{iM}N_{\mathrm{I}M}N_{\mathrm{I}J}\right] = I_{ik}I_{JL} - I_{ik}N_{\mathrm{I}J}N_{\mathrm{I}L}, \tag{A.5}$$

and, with respect to the jump displacement at the interface read

$$\begin{aligned}\frac{\partial F_{\mathrm{b}iJ}}{\partial \left[\!\left[u_k\right]\!\right]} &= n_{\mathrm{I}i}n_{\mathrm{I}m}\left[F_{\mathrm{c}mL} - I_{mL}\right]N_{\mathrm{I}L}N_{\mathrm{I}J}\frac{n_{\mathrm{I}k}}{\delta_\mathrm{n}^{\max}}\mathbf{1}_{(<\delta_\mathrm{n}^{\max})}\left(\delta_\mathrm{n}\right)\\ &+ s_{\mathrm{I}i}s_{\mathrm{I}m}\left[F_{\mathrm{c}mL} - I_{mL}\right]N_{\mathrm{I}L}N_{\mathrm{I}J}\frac{s_{\mathrm{I}k}}{\delta_\mathrm{t}^{\max}}\mathbf{1}_{(<\delta_\mathrm{t}^{\max})}\left(\delta_\mathrm{t}\right)\\ &+ s'_{\mathrm{I}i}s'_{\mathrm{I}m}\left[F_{\mathrm{c}mL} - I_{mL}\right]N_{\mathrm{I}L}N_{\mathrm{I}J}\frac{s'_{\mathrm{I}k}}{\delta_\mathrm{s}^{\max}}\mathbf{1}_{(<\delta_\mathrm{s}^{\max})}\left(\delta_\mathrm{s}\right)\\ &+ \frac{N_{\mathrm{I}J}}{h_\mathrm{b}}\delta_{ik},\end{aligned} \tag{A.6}$$

where the function $\mathbf{1}_y(x)$ is equal to 1 if the argument x satisfies the condition y, and to 0 otherwise. The derivative with respect to the gradient of the displacement jump at the interface reads

$$\frac{\partial F_{\mathrm{b}iJ}}{\partial \nabla_L \left[\!\left[u_k\right]\!\right]} = \frac{1}{2}I_{ik}I_{JL}. \tag{A.7}$$

Then, the stress tensor $\boldsymbol{\sigma}_\mathrm{b}$ is computed using Eq. (2.46) as damage law evolution, leading to

$$\left\langle \boldsymbol{\sigma}_\mathrm{b}\right\rangle = \frac{\boldsymbol{\sigma}_\mathrm{b}^+\left(\boldsymbol{\epsilon}_\mathrm{b}^+, \boldsymbol{Z}^+\right) + \boldsymbol{\sigma}_\mathrm{b}^-\left(\boldsymbol{\epsilon}_\mathrm{b}^-, \boldsymbol{Z}^-\right)}{2} \tag{A.8}$$

Finally, the material tangent tensor of the cohesive band model can be obtained by linearisation of the band stress tensor:

$$\begin{aligned}\delta\left\langle\sigma_{\mathrm{b}ij}\right\rangle &= \frac{\partial\left\langle\sigma_{\mathrm{b}ij}\right\rangle}{\partial F^+_{mN}}\delta F^+_{mN} + \frac{\partial\left\langle\sigma_{\mathrm{b}ij}\right\rangle}{\partial F^-_{mN}}\delta F^-_{mN} + \frac{\partial\left\langle\sigma_{\mathrm{b}ij}\right\rangle}{\partial \left[\!\left[u_m\right]\!\right]}\delta\left[\!\left[u_m\right]\!\right] + \frac{\partial\left\langle\sigma_{\mathrm{b}ij}\right\rangle}{\partial \nabla_n\left[\!\left[u_m\right]\!\right]}\delta\nabla_n\left[\!\left[u_m\right]\!\right]\\ &= \frac{1}{2}\frac{\partial\sigma^+_{\mathrm{b}ij}}{\partial F^+_{\mathrm{b}kL}}\frac{\partial F^+_{\mathrm{b}kL}}{\partial F^+_{mN}}\delta F^+_{mN} + \frac{1}{2}\frac{\partial\sigma^-_{\mathrm{b}ij}}{\partial F^-_{\mathrm{b}kL}}\frac{\partial F^-_{\mathrm{b}kL}}{\partial F^+_{mN}}\delta F^-_{mN}\\ &+ \frac{1}{2}\left(\frac{\partial\sigma^+_{\mathrm{b}ij}}{\partial F^+_{\mathrm{b}kL}}\frac{\partial F^+_{\mathrm{b}kL}}{\partial \left[\!\left[u_m\right]\!\right]} + \frac{\partial\sigma^-_{\mathrm{b}ij}}{\partial F^-_{\mathrm{b}kL}}\frac{\partial F^-_{\mathrm{b}kL}}{\partial \left[\!\left[u_m\right]\!\right]}\right)\delta\left[\!\left[u_m\right]\!\right]\\ &+ \frac{1}{2}\left(\frac{\partial\sigma^+_{\mathrm{b}ij}}{\partial F^+_{\mathrm{b}kL}}\frac{\partial F^+_{\mathrm{b}kL}}{\partial \nabla_n\left[\!\left[u_m\right]\!\right]} + \frac{\partial\sigma^-_{\mathrm{b}ij}}{\partial F^-_{\mathrm{b}kL}}\frac{\partial F^-_{\mathrm{b}kL}}{\partial \nabla_n\left[\!\left[u_m\right]\!\right]}\right)\delta\nabla_n\left[\!\left[u_m\right]\!\right].\end{aligned} \tag{A.9}$$

By introducing

$$\begin{aligned}&\mathcal{C}^{\mathrm{b}\pm}_{\boldsymbol{u}\mathbf{F}ijmn} = \mathcal{C}^{\mathrm{loc}\pm}_{\boldsymbol{u}\boldsymbol{u}ijkl}\frac{\partial F^{\pm}_{\mathrm{b}kl}}{\partial F^{\pm}_{mn}}; \qquad \mathfrak{C}^{\mathrm{b}\pm}_{\boldsymbol{u}[\![\boldsymbol{u}]\!]ijm} = \mathcal{C}^{\mathrm{loc}\pm}_{\boldsymbol{u}\boldsymbol{u}ijkl}\frac{\partial F^{\pm}_{\mathrm{b}kl}}{\partial \left[\!\left[u_m\right]\!\right]}; \quad \text{and}\\ &\mathcal{C}^{\mathrm{b}\pm}_{\boldsymbol{u}\boldsymbol{\nabla}[\![\boldsymbol{u}]\!]ijmn} = \mathcal{C}^{\mathrm{loc}\pm}_{\boldsymbol{u}\boldsymbol{u}ijkl}\frac{\partial F^{\pm}_{\mathrm{b}kl}}{\partial \nabla_n\left[\!\left[u_m\right]\!\right]},\end{aligned} \tag{A.10}$$

with $\boldsymbol{\mathcal{C}}^{\mathrm{loc}}_{\boldsymbol{u}\boldsymbol{u}}$ as the material tangent in its local form, see Appendix A.1, the previous relation reads

$$\delta\left\langle\boldsymbol{\sigma}_\mathrm{b}\right\rangle = \frac{1}{2}\boldsymbol{\mathcal{C}}^{\mathrm{b}+}_{\boldsymbol{u}\mathbf{F}} : \delta\mathbf{F}^+ + \frac{1}{2}\boldsymbol{\mathcal{C}}^{\mathrm{b}-}_{\boldsymbol{u}\mathbf{F}} : \delta\mathbf{F}^- + \left\langle\boldsymbol{\mathfrak{C}}^{\mathrm{b}}_{\boldsymbol{u}[\![\boldsymbol{u}]\!]}\right\rangle\cdot\delta\left[\!\left[\boldsymbol{u}\right]\!\right] + \left\langle\boldsymbol{\mathcal{C}}^{\mathrm{b}}_{\boldsymbol{u}\boldsymbol{\nabla}[\![\boldsymbol{u}]\!]}\right\rangle : \delta\boldsymbol{\nabla}\left[\!\left[\boldsymbol{u}\right]\!\right] \tag{A.11}$$

A.3 Formulation of finite element forces

From the weak form (2.71), the nodal forces are derived by applying the discretisation (2.72). This leads to the following elementary nodal forces for the volume elements B^e and the interface elements S^s.

- Inertial forces $\mathbf{M}^{e,ab} \cdot \ddot{\boldsymbol{u}}^b$:

$$\delta \boldsymbol{u}^a \cdot \mathbf{M}^{e,ab} \cdot \ddot{\boldsymbol{u}}^b = \int_{B^e} \rho \boldsymbol{w}_{\boldsymbol{u}} \cdot \ddot{\boldsymbol{u}} dV = \delta \boldsymbol{u}^a \cdot \int_{B^e} N^a \rho N^b dV \ddot{\boldsymbol{u}}^b; \tag{A.12}$$

- Internal forces $\boldsymbol{f}^{e,a}_{\boldsymbol{u}\,\mathrm{int}}$:

$$\delta \boldsymbol{u}^a \cdot \boldsymbol{f}^{e,a}_{\boldsymbol{u}\,\mathrm{int}} = \int_{B^e} \boldsymbol{\nabla} \boldsymbol{w}_{\boldsymbol{u}} : \boldsymbol{\sigma} dV = \delta \boldsymbol{u}^a \cdot \int_{B^e} \boldsymbol{\sigma} \cdot \boldsymbol{\nabla} N^a dV; \tag{A.13}$$

- External forces $\boldsymbol{f}^{e,a}_{\mathrm{ext}}$:

$$\begin{aligned} \delta \boldsymbol{u}^a \cdot \boldsymbol{f}^{e,a}_{\mathrm{ext}} &= \int_{B^e} \rho \boldsymbol{w}_{\boldsymbol{u}} \cdot \boldsymbol{b} dV + \int_{S^s_{\mathrm{N}}} \boldsymbol{w}_{\boldsymbol{u}} \cdot \bar{\boldsymbol{t}}_{\mathrm{N}} dS \\ &= \delta \boldsymbol{u}^a \cdot \int_{B^e} \rho N^a \boldsymbol{b} dV + \delta \boldsymbol{u}^a \cdot \int_{S^s_{\mathrm{N}}} N^a \bar{\boldsymbol{t}}_{\mathrm{N}} dS; \end{aligned} \tag{A.14}$$

- Interface forces $\boldsymbol{f}^{s,a^\pm}_{\boldsymbol{u}\,\mathrm{I}}$

$$\begin{aligned} \delta \boldsymbol{u}^{a^\pm} \cdot \boldsymbol{f}^{s,a^\pm}_{\boldsymbol{u}\,\mathrm{I}} &= \int_{S^s_{\mathrm{IC}}} [\![\boldsymbol{w}_{\boldsymbol{u}}]\!] \cdot \langle \boldsymbol{\sigma}_{\mathrm{b}} \rangle \cdot \boldsymbol{n}_{\mathrm{I}} dS + \int_{S^s_{\mathrm{IU}}} [\![\boldsymbol{w}_{\boldsymbol{u}}]\!] \cdot \langle \boldsymbol{\sigma} \rangle \cdot \boldsymbol{n}_{\mathrm{I}} dS \\ &\quad + \int_{S^s_{\mathrm{IU}}} [\![\boldsymbol{w}_{\boldsymbol{u}}]\!] \otimes \boldsymbol{n}_{\mathrm{I}} : \left\langle \frac{\beta_{\mathrm{s}}}{h_{\mathrm{s}}} \boldsymbol{\mathcal{H}} \right\rangle : [\![\boldsymbol{u}]\!] \otimes \boldsymbol{n}_{\mathrm{I}} dS \\ &\quad + \int_{S^s_{\mathrm{IU}}} [\![\boldsymbol{u}]\!] \cdot \langle \boldsymbol{\mathcal{H}} : \boldsymbol{\nabla} \boldsymbol{w}_{\boldsymbol{u}} \rangle \cdot \boldsymbol{n}_{\mathrm{I}} dS \\ &= \delta \boldsymbol{u}^{a^\pm} \cdot \int_{S^s_{\mathrm{IC}}} \left(\pm N^{a^\pm} \right) \langle \boldsymbol{\sigma}_{\mathrm{b}} \rangle \cdot \boldsymbol{n}_{\mathrm{I}} dS \\ &\quad + \delta \boldsymbol{u}^{a^\pm} \cdot \int_{S^s_{\mathrm{IU}}} \left(\pm N^{a^\pm} \right) \langle \boldsymbol{\sigma} \rangle \cdot \boldsymbol{n}_{\mathrm{I}} dS \\ &\quad + \delta \boldsymbol{u}^{a^\pm} \cdot \int_{S^s_{\mathrm{IU}}} \left(\pm N^{a^\pm} \right) \boldsymbol{n}_{\mathrm{I}} \cdot \left[\left\langle \frac{\beta_{\mathrm{s}}}{h_{\mathrm{s}}} \boldsymbol{\mathcal{H}} \right\rangle : \left[\!\left[N^b \boldsymbol{u}^b \right]\!\right] \otimes \boldsymbol{n}_{\mathrm{I}} \right] dS \\ &\quad + \frac{1}{2} \delta \boldsymbol{u}^{a^\pm} \cdot \int_{S^s_{\mathrm{IU}}} \left[\!\left[N^b \boldsymbol{u}^b \right]\!\right] \cdot \left[\boldsymbol{\mathcal{H}}^\pm : \boldsymbol{\nabla} N^{a^\pm} \otimes \boldsymbol{n}_{\mathrm{I}} \right] dS; \end{aligned} \tag{A.15}$$

- Internal non-local forces $f^{e,a}_{\tilde{e}\,\mathrm{int}}$:

$$\begin{aligned} \delta \tilde{e}^a f^{e,a}_{\tilde{e}\,\mathrm{int}} &= \int_{B^e} \left(w_{\tilde{e}} \tilde{e} + l_{\mathrm{c}}^2 \boldsymbol{\nabla} w_{\tilde{e}} \cdot \boldsymbol{\nabla} \tilde{e} \right) dV \\ &= \delta \tilde{e}^a \int_{B^e} \left(N^a N^b \tilde{e}^b + l_{\mathrm{c}}^2 \boldsymbol{\nabla} N^a \cdot \boldsymbol{\nabla} N^b \tilde{e}^b \right) dV; \end{aligned} \tag{A.16}$$

- Internal local forces $f^{e,a}_{e\,\mathrm{int}}$:

$$\delta \tilde{e}^a f^{e,a}_{e\,\mathrm{int}} = \int_{B^e} w_{\tilde{e}} e dV = \delta \tilde{e}^a \int_{B^e} N^a e dV; \tag{A.17}$$

- Interface forces $f^{s,a^\pm}_{\tilde{e}\,\mathrm{I}}$:

$$\begin{aligned}
\delta\tilde{e}^{a^\pm} f^{s,a^\pm}_{\tilde{e}\,\mathrm{I}} &= \int_{S^s_{\mathrm{IU}}} [\![w_{\tilde{e}}]\!] \left\langle l_\mathrm{c}^2 \boldsymbol{\nabla}\tilde{e}\right\rangle \cdot \boldsymbol{n}_\mathrm{I} dS + \int_{S^s_{\mathrm{IU}}} [\![w_{\tilde{e}}]\!]\, \boldsymbol{n}_\mathrm{I} \left\langle \frac{\beta_\mathrm{s}}{h_\mathrm{s}} l_\mathrm{c}^2 \right\rangle \cdot \boldsymbol{n}_\mathrm{I}\, [\![\tilde{e}]\!]\, dS \\
&\quad + \int_{S^s_{\mathrm{IU}}} [\![\tilde{e}]\!] \left\langle l_\mathrm{c}^2 \boldsymbol{\nabla} w_{\tilde{e}}\right\rangle \cdot \boldsymbol{n}_\mathrm{I} dS \\
&= \delta\tilde{e}^{a^\pm} \int_{S^s_{\mathrm{IU}}} \left(\pm N^{a^\pm}\right) \left\langle l_\mathrm{c}^2 \boldsymbol{\nabla} N^b \tilde{e}^b \right\rangle \cdot \boldsymbol{n}_\mathrm{I} dS \\
&\quad + \delta\tilde{e}^{a^\pm} \int_{S^s_{\mathrm{IU}}} \left(\pm N^{a^\pm}\right) \left\langle \frac{\beta_\mathrm{s}}{h_\mathrm{s}} l_\mathrm{c}^2 \right\rangle [\![N^b \tilde{e}^b]\!]\, dS \\
&\quad + \frac{1}{2} \delta\tilde{e}^{a^\pm} \int_{S^s_{\mathrm{IU}}} [\![N^b \tilde{e}^b]\!]\, l_\mathrm{c}^{\pm 2} \boldsymbol{\nabla} N^{a^\pm} \cdot \boldsymbol{n}_\mathrm{I} dS.
\end{aligned} \tag{A.18}$$

In this section, the superscripts $a, b, ...$ refer to the corresponding node a of the considered element e. For interface elements s, the node is so-called a^+ or a^-, depending to which element between B^{e^+} or B^{e^-} the considered degree of freedom belongs to. The computation of the spatial gradient of the jump displacement field involves the shape functions associated with interface elements only in order to respect condition (2.28). So-called $N_s^{a^\pm}$, they are different from their volume counterparts noted $N^{a^\pm}$. Besides, the displacement field in the nodal forces are the ones associated to volume elements. Therefore, the symmetrisation term introduces a contribution of all nodes of both elements in the interface term. Integration on the volume is performed using reduced quadrature rules, while interface elements use full integration to avoid spurious penetration mode as shown by Noels and Radovitzky (2008). Notice the proposed implementation does not duplicate the nodes between shared interfaces, but directly the degrees of freedom by taking advantage of the flexible DoF manager of Gmsh.

A.4 Formulation of finite element stiffness matrices

The elementary stiffness matrices can be obtained by linearising the elementary forces of Eqs. (A.12) to (A.18). Those expressions involve material tangent matrices $\boldsymbol{\mathcal{C}}_{\boldsymbol{uu}}$, $\mathbf{C}_{\boldsymbol{u}\tilde{e}}$ and $\mathbf{C}_{e\boldsymbol{u}}$ and tangent matrices related to the cohesive band $\boldsymbol{\mathfrak{C}}^{\mathrm{b}}_{\boldsymbol{u}[\![\boldsymbol{u}]\!]}$, $\boldsymbol{\mathcal{C}}^{\mathrm{b}}_{\boldsymbol{u}\boldsymbol{\nabla}[\![\boldsymbol{u}]\!]}$ and $\boldsymbol{\mathcal{C}}^{\mathrm{b}}_{\boldsymbol{u}\mathbf{F}}$. They are respectively detailed in Appendix A.1 and A.2. Therefore, the different stiffness matrix contributions read

- Internal force stiffness matrices $K^{e,ab}_{\boldsymbol{uu}\,\mathrm{int}\,ij}$ and $K^{e,ab}_{\boldsymbol{u}\tilde{e}\,\mathrm{int}\,i}$:

$$K^{e,ab}_{\boldsymbol{uu}\,\mathrm{int}\,ik} = \frac{\partial f^{e,a}_{\boldsymbol{u}\,\mathrm{int}\,i}}{\partial u^b_k} = \int_{B^e} \nabla_j N^a \frac{\partial \sigma_{ij}}{\partial u^b_k} dV = \int_{B^e} \nabla_j N^a \mathcal{C}_{\boldsymbol{uu}ijkl} \nabla_l N^b dV, \tag{A.19}$$

$$K^{e,ab}_{\boldsymbol{u}\tilde{e}\,\mathrm{int}\,i} = \frac{\partial f^{e,a}_{\boldsymbol{u}\,\mathrm{int}\,i}}{\partial \tilde{e}^b} = \int_{B^e} \nabla_j N^a \frac{\partial \sigma_{ij}}{\partial \tilde{e}^b} dV = \int_{B^e} \nabla_j N^a C_{\boldsymbol{u}\tilde{e}ij} N^b dV; \tag{A.20}$$

- Interface force stiffness matrices $K^{s,a^\pm b^\pm}_{\boldsymbol{u}\boldsymbol{u}\,\mathrm{I}\quad ij}$ and $K^{s,a^\pm b^\pm}_{\boldsymbol{u}\tilde{e}\,\mathrm{I}\quad i}$:

$$
\begin{aligned}
K^{s,a^\pm b^\pm}_{\boldsymbol{u}\boldsymbol{u}\,\mathrm{I}\quad ik} &= \frac{\partial f^{s,a^\pm}_{\boldsymbol{u}\,\mathrm{I}\quad i}}{\partial u^{b^\pm}_k} && \text{(A.21)}\\
&= \int_{S^s_{\mathrm{IC}}} \left(\pm N^{a^\pm}\right) \left\langle \frac{\partial \sigma_{\mathrm{b}\,ij}}{\partial u^{b^\pm}_k} \right\rangle n_{\mathrm{I}j}\, dS + \int_{S^s_{\mathrm{IU}}} \left(\pm N^{a^\pm}\right) \left\langle \frac{\partial \sigma_{ij}}{\partial u^{b^\pm}_k} \right\rangle n_{\mathrm{I}j}\, dS\\
&\quad + \int_{S^s_{\mathrm{IU}}} \left(\pm N^{a^\pm}\right) n_{\mathrm{I}j} \left\langle \frac{\beta_{\mathrm{s}}}{h_{\mathrm{s}}} \mathcal{H}_{ijkl} \right\rangle \left(\pm N^{b^\pm}\right) n_{\mathrm{I}l}\, dS\\
&\quad + \frac{1}{2} \int_{S^s_{\mathrm{IU}}} \left(\pm N^{b^\pm}\right) \mathcal{H}^\pm_{ikjl} \nabla_j N^{a^\pm} n_{\mathrm{I}l}\, dS\\
&= \int_{S^s_{\mathrm{IC}}} \left(\pm N^{a^\pm}\right) \left(\left\langle \mathfrak{C}^{\mathrm{b}}_{\boldsymbol{u}[\![\boldsymbol{u}]\!]ijk} \right\rangle \left(\pm N^{b^\pm}_s\right) \right.\\
&\quad \left. + \left\langle \mathcal{C}^{\mathrm{b}}_{\boldsymbol{u}\boldsymbol{\nabla}[\![\boldsymbol{u}]\!]ijkl} \right\rangle \left(\pm \nabla_l N^{b^\pm}_s\right) \right) n_{\mathrm{I}j}\, dS\\
&\quad + \frac{1}{2} \int_{S^s_{\mathrm{IC}}} \left(\pm N^{a^\pm}\right) \mathcal{C}^{\mathrm{b}\pm}_{\boldsymbol{u}\mathbf{F}ijkl} \nabla_l N^{b^\pm} n_{\mathrm{I}j}\, dS\\
&\quad + \frac{1}{2} \int_{S^s_{\mathrm{IU}}} \left(\pm N^{a^\pm}\right) \mathcal{C}^{\pm}_{\boldsymbol{u}\boldsymbol{u}ijkl} \nabla_l N^{b^\pm} n_{\mathrm{I}j}\, dS\\
&\quad + \int_{S^s_{\mathrm{IU}}} \left(\pm N^{a^\pm}\right) n_{\mathrm{I}j} \left\langle \frac{\beta_{\mathrm{s}}}{h_{\mathrm{s}}} \mathcal{H}_{ijkl} \right\rangle \left(\pm N^{b^\pm}\right) n_{\mathrm{I}l}\, dS\\
&\quad + \frac{1}{2} \int_{S^s_{\mathrm{IU}}} \left(\pm N^{b^\pm}\right) \mathcal{H}^\pm_{ikjl} \nabla_j N^{a^\pm} n_{\mathrm{I}l}\, dS,\\
K^{s,a^\pm b^\pm}_{\boldsymbol{u}\tilde{e}\,\mathrm{I}\quad i} &= \frac{\partial f^{s,a^\pm}_{\boldsymbol{u}\,\mathrm{I}\quad i}}{\partial \tilde{e}^{b^\pm}} = \int_{S^s_{\mathrm{IU}}} \left(\pm N^{a^\pm}\right) \left\langle \frac{\partial \boldsymbol{\sigma}_{ij}}{\partial \tilde{e}^{b^\pm}} \right\rangle n_{\mathrm{I}j}\, dS && \text{(A.22)}\\
&= \frac{1}{2} \int_{S^s_{\mathrm{IU}}} \left(\pm N^{a^\pm}\right) \mathbf{C}_{\boldsymbol{u}\tilde{e}ij} N^{b^\pm} n_{\mathrm{I}j}\, dS;
\end{aligned}
$$

- Internal non-local force stiffness matrices $K^{s,ab}_{\tilde{e}\boldsymbol{u}\,\mathrm{int}\,k}$ and $K^{s,ab}_{\tilde{e}\tilde{e}\,\mathrm{int}}$:

$$
\begin{aligned}
K^{s,ab}_{\tilde{e}\boldsymbol{u}\,\mathrm{int}\,k} &= \frac{\partial f^{e,a}_{\tilde{e}\,\mathrm{int}}}{\partial u^b_k} = 0, && \text{(A.23)}\\
K^{s,ab}_{\tilde{e}\tilde{e}\,\mathrm{int}} &= \frac{\partial f^{e,a}_{\tilde{e}\,\mathrm{int}}}{\partial \tilde{e}^b} = \int_{B^e} \left(N^a N^b + l_{\mathrm{c}}^2 \nabla_i N^a \nabla_i N^b \right) dV; && \text{(A.24)}
\end{aligned}
$$

- Internal local force stiffness matrices $K^{e,ab}_{e\boldsymbol{u}\,\mathrm{int}\,k}$ and $K^{e,ab}_{e\tilde{e}\,\mathrm{int}}$:

$$
\begin{aligned}
K^{e,ab}_{e\boldsymbol{u}\,\mathrm{int}\,k} &= \frac{\partial f^{e,a}_{e\,\mathrm{int}}}{\partial u^b_k} = \int_{B^e} N^a \frac{\partial e}{\partial u^b_k} dV = \int_{B^e} N^a \mathbf{C}_{e\boldsymbol{u}ki} \nabla_i N^b dV, && \text{(A.25)}\\
K^{e,ab}_{e\tilde{e}\,\mathrm{int}} &= \frac{\partial f^{e,a}_{e\,\mathrm{int}}}{\partial \tilde{e}^b} = 0; && \text{(A.26)}
\end{aligned}
$$

- Interface non-local force stiffness matrices $K^{s,a^\pm b^\pm}_{\tilde{e}\boldsymbol{u}\,\mathrm{I}\quad k}$ and $K^{s,a^\pm b^\pm}_{\tilde{e}\tilde{e}\,\mathrm{I}}$:

$$K^{s,a^{\pm}b^{\pm}}_{\tilde{e}\boldsymbol{u}\,\mathrm{I}\quad k} = \frac{\partial f^{s,a^{\pm}}_{\tilde{e}\,\mathrm{I}}}{\partial u^{b^{\pm}}_{k}} = 0, \tag{A.27}$$

$$\begin{aligned} K^{s,a^{\pm}b^{\pm}}_{\tilde{e}\tilde{e}\,\mathrm{I}} &= \frac{\partial f^{s,a^{\pm}}_{\tilde{e}\,\mathrm{I}}}{\partial \tilde{e}^{b^{\pm}}} = \frac{1}{2}\int_{S^{s}_{\mathrm{IU}}} \left(\pm N^{a^{\pm}}\right) l_{\mathrm{c}}^{\pm 2} \nabla_i N^{b^{\pm}} n_{\mathrm{I}i} dS \\ &+ \int_{S^{s}_{\mathrm{IU}}} \left(\pm N^{a^{\pm}}\right) \left\langle \frac{\beta_{\mathrm{s}}}{h_{\mathrm{s}}} l_{\mathrm{c}}^{2} \right\rangle \left(\pm N^{b^{\pm}}\right) dS \\ &+ \frac{1}{2}\int_{S^{s}_{\mathrm{IU}}} \left(\pm N^{b^{\pm}}\right) l_{\mathrm{c}}^{\pm 2} \nabla_i N^{a^{\pm}} n_{\mathrm{I}i} dS. \end{aligned} \tag{A.28}$$

Appendix B

Appendix related to Chapter 3

B.1 Formulation of the plastic residual form

The details on the determination of the plastic corrector omitted in Section 3.1.3 are presented here.

B.1.1 Gurson residual form

When the Gurson model is used, the residues involve the yield surface (3.32) and its derivatives. The derivatives of ϕ_{G} are given by

$$N_{\mathrm{G}}^{\mathrm{d}} = 2\frac{\tau^{\mathrm{eq}}}{\tau_{\mathrm{Y}}^2} \quad \text{and} \quad N_{\mathrm{G}}^{\mathrm{q}} = \frac{3q_1q_2\hat{f}_{\mathrm{V}}}{\tau_{\mathrm{Y}}}\sinh\left(\frac{3q_2p_\tau}{2\tau_{\mathrm{Y}}}\right), \tag{B.1}$$

and

$$\frac{\partial\phi_{\mathrm{G}}}{\partial\tau_{\mathrm{Y}}} = -2\frac{\tau^{\mathrm{eq}2}}{\tau_{\mathrm{Y}}^3} - \frac{3q_1q_2p_\tau\hat{f}_{\mathrm{V}}}{\tau_{\mathrm{Y}}^2}\sinh\left(\frac{3q_2p_\tau}{2\tau_{\mathrm{Y}}}\right) \quad \text{and} \quad \frac{\partial\phi_{\mathrm{G}}}{\partial\chi} = 0\,, \tag{B.2}$$

while the derivatives of the normal are

$$\frac{\partial N_{\mathrm{G}}^{\mathrm{d}}}{\partial\tau^{\mathrm{eq}}} = \frac{2}{\tau_{\mathrm{Y}}^2} \quad \text{and} \quad \frac{\partial N_{\mathrm{G}}^{\mathrm{q}}}{\partial\tau^{\mathrm{eq}}} = 0\,, \tag{B.3}$$

$$\frac{\partial N_{\mathrm{G}}^{\mathrm{d}}}{\partial p_\tau} = 0 \quad \text{and} \quad \frac{\partial N_{\mathrm{G}}^{\mathrm{q}}}{\partial p_\tau} = \frac{9q_1q_2^2\hat{f}_{\mathrm{V}}}{2\tau_{\mathrm{Y}}^2}\cosh\left(\frac{3q_2p_\tau}{2\tau_{\mathrm{Y}}}\right), \tag{B.4}$$

and

$$\frac{\partial N_{\mathrm{G}}^{\mathrm{d}}}{\partial\tau_{\mathrm{Y}}} = -4\frac{\tau^{\mathrm{eq}}}{\tau_{\mathrm{Y}}^3} \quad \text{and} \quad \frac{\partial N_{\mathrm{G}}^{\mathrm{q}}}{\partial\tau_{\mathrm{Y}}} = -\frac{9q_1q_2^2\hat{f}_{\mathrm{V}}p_\tau}{2\tau_{\mathrm{Y}}^3}\cosh\left(\frac{3q_2p_\tau}{2\tau_{\mathrm{Y}}}\right) - \frac{3q_1q_2\hat{f}_{\mathrm{V}}}{\tau_{\mathrm{Y}}^2}\sinh\left(\frac{3q_2p_\tau}{2\tau_{\mathrm{Y}}}\right). \tag{B.5}$$

B.1.2 Thomason residual form

When Thomason model is used, the yield surface (3.38) steps in the residues $\boldsymbol{r}_{\mathrm{p}}(\boldsymbol{v})$. The derivatives of ϕ_{T} are

$$\frac{\partial\phi_{\mathrm{T}}}{\partial\tau_{\mathrm{Y}}} = -C_{\mathrm{T}}^{\phi} \quad \text{and} \quad \frac{\partial\phi_{\mathrm{T}}}{\partial\chi} = -\tau_{\mathrm{Y}}\frac{\partial C_{\mathrm{T}}^{\phi}}{\partial\chi}\,, \tag{B.6}$$

with

$$\begin{aligned}\frac{\partial C_{\mathrm{T}}^{\phi}}{\partial\chi} \;=\; & -(2\chi)\left[\alpha(1/\chi-1)^2+\beta\sqrt{1/\chi}\right] \\ & -\left(1-\chi^2\right)\left[2\alpha(1/\chi-1)(1/\chi^2)+\tfrac{1}{2}\beta\chi^{-3/2}\right],\end{aligned} \tag{B.7}$$

The normal components are

$$N_{\mathrm{T}}^{\mathrm{d}} = \frac{2}{3}\left({\tau_+}^n+{\tau_-}^n\right)^{\frac{1-n}{n}}\left({\tau_+}^{n-1}+{\tau_-}^{n-1}\right), \tag{B.8}$$

and

$$N_{\mathrm{T}}^{\mathrm{q}} = \left({\tau_+}^n + {\tau_-}^n\right)^{\frac{1-n}{n}} \left({\tau_+}^{n-1} - {\tau_-}^{n-1}\right) . \tag{B.9}$$

The derivatives of the normal components are

$$\begin{aligned}\frac{\partial N_{\mathrm{T}}^{\mathrm{d}}}{\partial \tau^{\mathrm{eq}}} = \frac{4}{9}(n-1)\Big[&\left({\tau_+}^n + {\tau_-}^n\right)^{\frac{1}{n}-1}\left({\tau_+}^{n-2} + {\tau_-}^{n-2}\right)\\ &-\left({\tau_+}^n + {\tau_-}^n\right)^{\frac{1}{n}-2}\left({\tau_+}^{n-1} + {\tau_-}^{n-1}\right)^2\Big] ,\end{aligned} \tag{B.10}$$

$$\begin{aligned}\frac{\partial N_{\mathrm{T}}^{\mathrm{q}}}{\partial \tau^{\mathrm{eq}}} = \frac{2}{3}(n-1)\Big[&\left({\tau_+}^n + {\tau_+}^n\right)^{\frac{1}{n}-1}\left({\tau_-}^{n-2} - {\tau_-}^{n-2}\right)\\ &-\left({\tau_+}^n + {\tau_-}^n\right)^{\frac{1}{n}-2}\left({\tau_+}^{2n-2} - {\tau_-}^{2n-2}\right)\Big] ,\end{aligned} \tag{B.11}$$

$$\begin{aligned}\frac{\partial N_{\mathrm{T}}^{\mathrm{d}}}{\partial p_\tau} = \frac{2}{3}(n-1)\Big[&\left({\tau_+}^n + {\tau_-}^n\right)^{\frac{1}{n}-1}\left({\tau_+}^{n-2} - {\tau_-}^{n-2}\right)\\ &-\left({\tau_+}^n + {\tau_-}^n\right)^{\frac{1}{n}-2}\left({\tau_+}^{2n-2} - {\tau_-}^{2n-2}\right)\Big] ,\end{aligned} \tag{B.12}$$

$$\begin{aligned}\frac{\partial N_{\mathrm{T}}^{\mathrm{q}}}{\partial p_\tau} = (n-1)\Big[&\left({\tau_+}^n + {\tau_-}^n\right)^{\frac{1}{n}-1}\left({\tau_+}^{n-2} + {\tau_-}^{n-2}\right)\\ &-\left({\tau_+}^n + {\tau_-}^n\right)^{\frac{1}{n}-2}\left({\tau_+}^{n-1} - {\tau_-}^{n-1}\right)^2\Big] ,\end{aligned} \tag{B.13}$$

$$\frac{\partial N^{\mathrm{d}}}{\partial \tau_{\mathrm{Y}}} = 0 \quad \text{and} \quad \frac{\partial N^{\mathrm{q}}}{\partial \tau_{\mathrm{Y}}} = 0 . \tag{B.14}$$

B.2 Formulation of the material operators

The material operator is obtained by linearising the output of the bulk constitutive law in terms of the input. Four terms are therefore required: $\frac{\partial \mathbf{P}}{\partial \mathbf{F}}$, $\frac{\partial f_{\mathrm{V}}}{\partial \mathbf{F}}$, $\frac{\partial \mathbf{P}}{\partial \tilde{f}_{\mathrm{V}}}$, $\frac{\partial f_{\mathrm{V}}}{\partial \tilde{f}_{\mathrm{V}}}$.

B.2.1 Stress tensor derivatives

From its definition (3.54), the derivative of the first Piola-Kirchhoff tensor reads

$$\begin{aligned}\frac{\partial \mathbf{P}}{\partial \mathbf{F}} &= \frac{\partial \mathbf{F}^{\mathrm{e}}}{\partial \mathbf{F}}^{2} \cdot (\boldsymbol{\tau} : \boldsymbol{\mathcal{L}}^{\mathrm{e}}) \cdot \mathbf{F}^{\mathrm{p}-T} + \mathbf{F}^{\mathrm{e}} \cdot^{3} \left(\frac{\partial \boldsymbol{\tau}}{\partial \mathbf{F}}^{1,2} : \boldsymbol{\mathcal{L}}^{\mathrm{e}}\right)^{4} \cdot \mathbf{F}^{\mathrm{p}-T}\\ &\quad + \mathbf{F}^{\mathrm{e}} \cdot \left(\boldsymbol{\tau} : \frac{\partial \boldsymbol{\mathcal{L}}^{\mathrm{e}}}{\partial \mathbf{F}}\right) \cdot \mathbf{F}^{\mathrm{p}-T} + \mathbf{F}^{\mathrm{e}} \cdot (\boldsymbol{\tau} : \boldsymbol{\mathcal{L}}^{\mathrm{e}}) \cdot \frac{\partial \mathbf{F}^{\mathrm{p}-T}}{\partial \mathbf{F}} ,\end{aligned} \tag{B.15}$$

$$\begin{aligned}\frac{\partial \mathbf{P}}{\partial \tilde{f}_{\mathrm{V}}} &= \frac{\partial \mathbf{F}^{\mathrm{e}}}{\partial \tilde{f}_{\mathrm{V}}} \cdot (\boldsymbol{\mathcal{L}}^{\mathrm{e}} : \boldsymbol{\tau}) \cdot \mathbf{F}^{\mathrm{p}-\mathrm{T}} + \mathbf{F}^{\mathrm{e}} \cdot \left(\frac{\partial \boldsymbol{\tau}}{\partial \tilde{f}_{\mathrm{V}}} : \boldsymbol{\mathcal{L}}^{\mathrm{e}}\right) \cdot \mathbf{F}^{\mathrm{p}-T}\\ &\quad + \mathbf{F}^{\mathrm{e}} \cdot \left(\boldsymbol{\tau} \frac{\partial \boldsymbol{\mathcal{L}}^{\mathrm{e}}}{\partial \tilde{f}_{\mathrm{V}}}\right) \cdot \mathbf{F}^{\mathrm{p}-T} + \mathbf{F}^{\mathrm{e}} \cdot (\boldsymbol{\tau} : \boldsymbol{\mathcal{L}}^{\mathrm{e}}) \cdot \frac{\partial \mathbf{F}^{\mathrm{p}-T}}{\partial \tilde{f}_{\mathrm{V}}} ,\end{aligned} \tag{B.16}$$

where $\left[\mathbf{A} \cdot^{3} \boldsymbol{\mathcal{B}}\right]_{ijkl} = A_{km}\mathcal{B}_{ijml}$.

In Eqs. (B.15) and (B.16), the derivative of each factor has still to be developed. For this purpose, one has for:

- The inverse of the plastic deformation mapping $\mathbf{F}^{\mathrm{p}-1}$:

$$\begin{cases} \frac{\partial F^{\mathrm{p}\,-1}_{IJ}}{\partial F_{kL}} & = -F^{\mathrm{p}\,-1}_{IM}\frac{\partial F^{\mathrm{p}}_{MN}}{\partial F_{kL}}F^{\mathrm{p}\,-1}_{NJ}\,, \\ \frac{\partial F^{\mathrm{p}\,-1}_{IJ}}{\partial \tilde{f}_{\mathrm{V}}} & = -F^{\mathrm{p}\,-1}_{IM}\frac{\partial F^{\mathrm{p}}_{MN}}{\partial \tilde{f}_{\mathrm{V}}}F^{\mathrm{p}\,-1}_{NJ}\,; \end{cases} \tag{B.17}$$

- The elastic deformation gradient $\mathbf{F}^{\mathrm{e}}$:

$$\begin{cases} \frac{\partial F^{\mathrm{e}}_{iJ}}{\partial F_{kL}} & = \delta_{ik}F^{\mathrm{p}\,-1}_{LJ} + F_{iM}\frac{\partial F^{\mathrm{p}\,-1}_{MJ}}{\partial F_{kL}}\,, \\ \frac{\partial F^{\mathrm{e}}_{iJ}}{\partial \tilde{f}_{\mathrm{V}}} & = F_{iM}\frac{\partial F^{\mathrm{p}\,-1}_{MJ}}{\partial \tilde{f}_{\mathrm{V}}}\,; \end{cases} \tag{B.18}$$

- The approximation of the strain measure derivatives $\boldsymbol{\mathcal{L}}^{\mathrm{e}}$:

$$\frac{\partial \boldsymbol{\mathcal{L}}^{\mathrm{e}}}{\partial \mathbf{F}} = \frac{\partial \boldsymbol{\mathcal{L}}^{\mathrm{e}}}{\partial \mathbf{C}^{\mathrm{e}}} : \frac{\partial \mathbf{C}^{\mathrm{e}}}{\partial \mathbf{F}^{\mathrm{e}}} : \frac{\partial \mathbf{F}^{\mathrm{e}}}{\partial \mathbf{F}} \quad \text{and} \quad \frac{\partial \boldsymbol{\mathcal{L}}^{\mathrm{e}}}{\partial \tilde{f}_{\mathrm{V}}} = \frac{\partial \boldsymbol{\mathcal{L}}^{\mathrm{e}}}{\partial \mathbf{C}^{\mathrm{e}}} : \frac{\partial \mathbf{C}^{\mathrm{e}}}{\partial \mathbf{F}^{\mathrm{e}}} : \frac{\partial \mathbf{F}^{\mathrm{e}}}{\partial \tilde{f}_{\mathrm{V}}}\,. \tag{B.19}$$

Combining Eqs. (B.17), (B.18) and (B.19), the derivatives (B.15) - (B.16) can be expressed in terms of the derivatives of $\mathbf{F}^{\mathrm{p}}$ and $\boldsymbol{\tau}$ only. The derivative in terms of $\mathbf{F}$ in the previous equations can be substituted by a derivative in terms of $\mathbf{E}^{\mathrm{e}}_{\mathrm{pr}}$ by using the chain rule and the following relation

$$\frac{\partial E^{\mathrm{e}}_{\mathrm{pr}\,IJ}}{\partial F_{kL}} = \frac{1}{2}\mathcal{L}^{\mathrm{e}}_{\mathrm{pr}\,IJMN}\left(F^{\mathrm{e}}_{\mathrm{pr}\,kN}F^{\mathrm{p}\,-1}_{\mathrm{pr}\,LM} + F^{\mathrm{e}}_{\mathrm{pr}\,kM}F^{\mathrm{p}\,-1}_{\mathrm{pr}\,LN}\right)\,, \tag{B.20}$$

obtained from the Eqs. (3.41), (3.42) and the definition of $\boldsymbol{\mathcal{L}}^{\mathrm{e}}_{\mathrm{pr}} = \frac{\partial \ln \mathbf{C}^{\mathrm{e}}_{\mathrm{pr}}}{\partial \mathbf{C}^{\mathrm{e}}_{\mathrm{pr}}}$.

In the case of an elastic step, no plastic flow occurs and it follows that the only non-trivial derivative is

$$\frac{\partial \boldsymbol{\tau}}{\partial \mathbf{E}^{\mathrm{e}}_{\mathrm{pr}}} = 2G\boldsymbol{\mathcal{I}}^{\mathrm{dev}} + K\mathbf{I}\otimes\mathbf{I}\,, \tag{B.21}$$

obtained from Eq. (3.21), with $\boldsymbol{\mathcal{I}}^{\mathrm{dev}} = \boldsymbol{\mathcal{I}} - \frac{1}{3}\mathbf{I}\otimes\mathbf{I}$ and $\boldsymbol{\mathcal{I}}$ the fourth-order symmetric unit tensor.

Otherwise, in case of plasticity, the derivatives of the plastic deformation mapping are obtained from its definition (3.44), leading to

$$\begin{array}{rcccl} \frac{\partial \mathbf{F}^{\mathrm{p}\,\mathrm{T}}}{\partial \mathbf{E}^{\mathrm{e}}_{\mathrm{pr}}} & = & \mathbf{F}^{\mathrm{p}\;\mathrm{T}}_{\mathrm{pr}}\cdot\frac{\partial \exp\left(\Delta\gamma\mathbf{N}^{\mathrm{p}}\right)}{\partial \mathbf{E}^{\mathrm{e}}_{\mathrm{pr}}} & = & \mathbf{F}^{\mathrm{p}\;\mathrm{T}}_{\mathrm{pr}}\cdot\boldsymbol{\mathcal{E}} : \frac{\partial(\Delta\gamma\mathbf{N}^{\mathrm{p}})}{\partial \mathbf{E}^{\mathrm{e}}_{\mathrm{pr}}}\,, \\ \frac{\partial \mathbf{F}^{\mathrm{p}\,\mathrm{T}}}{\partial \tilde{f}_{\mathrm{V}}} & = & \mathbf{F}^{\mathrm{p}\;\mathrm{T}}_{\mathrm{pr}}\cdot\frac{\partial \exp\left(\Delta\gamma\mathbf{N}^{\mathrm{p}}\right)}{\partial \tilde{f}_{\mathrm{V}}} & = & \mathbf{F}^{\mathrm{p}\;\mathrm{T}}_{\mathrm{pr}}\cdot\boldsymbol{\mathcal{E}} : \frac{\partial(\Delta\gamma\mathbf{N}^{\mathrm{p}})}{\partial \tilde{f}_{\mathrm{V}}}\,, \end{array} \tag{B.22}$$

where $\boldsymbol{\mathcal{E}} = \frac{\partial \exp(\Delta\gamma\mathbf{N}^{\mathrm{p}})}{\partial \Delta\gamma\mathbf{N}^{\mathrm{p}}}$ depends on the approximation used to compute the tensor exponential. The plastic corrections appearing here above, computed by Eq. (3.45) and (3.52), are also derived

$$\begin{array}{rcl} \frac{\partial \Delta\gamma\mathbf{N}^{\mathrm{p}}}{\partial \mathbf{E}^{\mathrm{e}}_{\mathrm{pr}}} & = & \frac{3(\boldsymbol{\tau}_{\mathrm{pr}})^{\mathrm{dev}}}{2\tau^{\mathrm{eq}}_{\mathrm{pr}}}\otimes\frac{\partial \Delta d}{\partial \mathbf{E}^{\mathrm{e}}_{\mathrm{pr}}} + \frac{3G\Delta d}{\tau^{\mathrm{eq}}_{\mathrm{pr}}}\left(\boldsymbol{\mathcal{I}}^{\mathrm{dev}} - \frac{3(\boldsymbol{\tau}_{\mathrm{pr}})^{\mathrm{dev}}\otimes(\boldsymbol{\tau}_{\mathrm{pr}})^{\mathrm{dev}}}{\tau^{\mathrm{eq}\,2}_{\mathrm{pr}}}\right) + \frac{1}{3}\mathbf{I}\otimes\frac{\partial \Delta q}{\partial \mathbf{E}^{\mathrm{e}}_{\mathrm{pr}}}\,, \\ \frac{\partial \Delta\gamma\mathbf{N}^{\mathrm{p}}}{\partial \tilde{f}_{\mathrm{V}}} & = & \frac{\partial \Delta d}{\partial \tilde{f}_{\mathrm{V}}}\frac{3(\boldsymbol{\tau}_{\mathrm{pr}})^{\mathrm{dev}}}{2\tau^{\mathrm{eq}}_{\mathrm{pr}}} + \frac{1}{3}\frac{\partial \Delta q}{\partial \tilde{f}_{\mathrm{V}}}\mathbf{I}\,. \end{array} \tag{B.23}$$

The Kirchhoff stress is also linearised from Eqs. (3.47)-(3.50) and one finally has

$$\begin{aligned}\frac{\partial \boldsymbol{\tau}}{\partial \mathbf{E}^{\mathrm{e}}_{\mathrm{pr}}} &= \left(1-\frac{3G\Delta d}{\tau^{\mathrm{eq}}_{\mathrm{pr}}}\right)2G\boldsymbol{\mathcal{I}}^{\mathrm{dev}} - \frac{3G}{\tau^{\mathrm{eq}}_{\mathrm{pr}}}\left(\boldsymbol{\tau}_{\mathrm{pr}}\right)^{\mathrm{dev}}\otimes\left[\frac{\partial\Delta d}{\partial\mathbf{E}^{\mathrm{e}}_{\mathrm{pr}}} - \frac{3G\Delta d(\boldsymbol{\tau}_{\mathrm{pr}})^{\mathrm{dev}}}{2\tau^{\mathrm{eq}2}_{\mathrm{pr}}}\right] \\ &\quad + K\mathbf{I}\otimes\left(\mathbf{I}-\frac{\partial\Delta q}{\partial\mathbf{E}^{\mathrm{e}}_{\mathrm{pr}}}\right), \\ \frac{\partial\boldsymbol{\tau}}{\partial\tilde{f}_{\mathrm{V}}} &= -\frac{3G}{\tau^{\mathrm{eq}}_{\mathrm{pr}}}\frac{\partial\Delta d}{\partial\tilde{f}_{\mathrm{V}}}\left(\boldsymbol{\tau}_{\mathrm{pr}}\right)^{\mathrm{dev}} - K\frac{\partial\Delta q}{\partial\tilde{f}_{\mathrm{V}}}\mathbf{I}.\end{aligned} \tag{B.24}$$

The last missing steps are the derivatives of the plastic increments, computing through Eq. (3.69) and results of Appendix B.2.3.

B.2.2 Porosity derivatives

The derivatives of the local porosity is obtained by derivation of Eq. (3.61)

$$\begin{aligned}\frac{\partial f_{\mathrm{V}}}{\partial\mathbf{E}^{\mathrm{e}}_{\mathrm{pr}}} &= \frac{\partial f_{\mathrm{V}}}{\partial B_{\mathrm{n}}}\frac{\partial B_{\mathrm{n}}}{\partial\mathbf{E}^{\mathrm{e}}_{\mathrm{pr}}} + \frac{\partial f_{\mathrm{V}}}{\partial\Delta d}\frac{\partial\Delta d}{\partial\mathbf{E}^{\mathrm{e}}_{\mathrm{pr}}} + \frac{\partial f_{\mathrm{V}}}{\partial\Delta q}\frac{\partial\Delta q}{\partial\mathbf{E}^{\mathrm{e}}_{\mathrm{pr}}} + \frac{\partial f_{\mathrm{V}}}{\partial\Delta p}\frac{\partial\Delta p}{\partial\mathbf{E}^{\mathrm{e}}_{\mathrm{pr}}}, \\ \frac{\partial f_{\mathrm{V}}}{\partial\tilde{f}_{\mathrm{V}}} &= \frac{\partial f_{\mathrm{V}}}{\partial\Delta d}\frac{\partial\Delta d}{\partial\tilde{f}_{\mathrm{V}}} + \frac{\partial f_{\mathrm{V}}}{\partial\Delta q}\frac{\partial\Delta q}{\partial\tilde{f}_{\mathrm{V}}} + \frac{\partial f_{\mathrm{V}}}{\partial\Delta p}\frac{\partial\Delta p}{\partial\tilde{f}_{\mathrm{V}}},\end{aligned} \tag{B.25}$$

combined with Eq. B.20 to obtain the derivatives in terms of the deformation gradient. In addition, one has

$$\frac{\partial B_{\mathrm{n}}}{\partial\mathbf{E}^{\mathrm{e}}_{\mathrm{pr}}} = -4Gk_{\omega}{\zeta_{\mathrm{pr}}}^{2}\left[\left(\boldsymbol{\tau}_{\mathrm{pr}}\right)^{\mathrm{dev}\,-\mathrm{T}} - \frac{9}{2}\frac{\left(\boldsymbol{\tau}_{\mathrm{pr}}\right)^{\mathrm{dev}}}{\tau^{\mathrm{eq}2}_{\mathrm{pr}}}\right] : \boldsymbol{\mathcal{I}}^{\mathrm{dev}}, \tag{B.26}$$

and

$$\begin{aligned}\frac{\partial f_{\mathrm{V}}}{\partial\Delta d} &= \frac{B_{\mathrm{n}}}{1+\Delta q - B_{\mathrm{n}}\Delta d}f_{\mathrm{V}}, \\ \frac{\partial f_{\mathrm{V}}}{\partial\Delta q} &= \frac{1}{1+\Delta q - B_{\mathrm{n}}\Delta d}\left(1-f_{\mathrm{V}}\right), \\ \frac{\partial f_{\mathrm{V}}}{\partial\Delta p} &= \frac{A_{\mathrm{n}} + \frac{\partial A_{\mathrm{n}}}{\partial p}\Delta p}{1+\Delta q - B_{\mathrm{n}}\Delta d}.\end{aligned} \tag{B.27}$$

B.2.3 Internal variables derivatives

In order to complete the tangent operator formulation, the derivatives of the plastic increment in terms of the predictor strain, appearing in Eq. (3.68), are obtained thanks to

$$\frac{\partial\boldsymbol{r}_{\mathrm{p}}}{\partial\mathbf{E}^{\mathrm{e}}_{\mathrm{pr}}} = \frac{\partial\boldsymbol{r}_{\mathrm{p}}}{\partial\tau^{\mathrm{eq}}_{\mathrm{pr}}}\otimes\frac{\partial\tau^{\mathrm{eq}}_{\mathrm{pr}}}{\partial\mathbf{E}^{\mathrm{e}}_{\mathrm{pr}}} + \frac{\partial\boldsymbol{r}_{\mathrm{p}}}{\partial p_{\tau_{\mathrm{pr}}}}\otimes\frac{\partial p_{\tau_{\mathrm{pr}}}}{\partial\mathbf{E}^{\mathrm{e}}_{\mathrm{pr}}} = \frac{\partial\boldsymbol{r}_{\mathrm{p}}}{\partial\tau^{\mathrm{eq}}_{\mathrm{pr}}}\otimes\frac{3G\left(\boldsymbol{\tau}_{\mathrm{pr}}\right)^{\mathrm{dev}}}{\tau^{\mathrm{eq}}_{\mathrm{pr}}} + \frac{\partial\boldsymbol{r}_{\mathrm{p}}}{\partial p_{\tau_{\mathrm{pr}}}}\otimes K\mathbf{I}, \tag{B.28}$$

with

$$\frac{\partial r_{\mathrm{p}1}}{\partial\tau^{\mathrm{eq}}_{\mathrm{pr}}} = N^{\mathrm{d}}, \quad \frac{\partial r_{\mathrm{p}2}}{\partial\tau^{\mathrm{eq}}_{\mathrm{pr}}} = \Delta d\frac{\partial N^{\mathrm{q}}}{\partial\tau^{\mathrm{eq}}} - \Delta q\frac{\partial N^{\mathrm{d}}}{\partial\tau^{\mathrm{eq}}}, \quad \frac{\partial r_{\mathrm{p}3}}{\partial\tau^{\mathrm{eq}}_{\mathrm{pr}}} = -\Delta d, \text{ and} \tag{B.29}$$

$$\frac{\partial r_{\mathrm{p}1}}{\partial p_{\tau_{\mathrm{pr}}}} = N^{\mathrm{q}}, \quad \frac{\partial r_{\mathrm{p}2}}{\partial p_{\tau_{\mathrm{pr}}}} = \Delta d\frac{\partial N^{\mathrm{q}}}{\partial p_{\tau}} - \Delta q\frac{\partial N^{\mathrm{d}}}{\partial p_{\tau}}, \quad \frac{\partial r_{\mathrm{p}3}}{\partial p_{\tau_{\mathrm{pr}}}} = -\Delta q. \tag{B.30}$$

The derivatives with respect to the non-local porosity are given by:

$$\frac{\partial r_{\mathrm{p}1}}{\partial\tilde{f}_{\mathrm{V}}} = \frac{\partial\phi}{\partial\hat{f}_{\mathrm{V}}}, \quad \frac{\partial r_{\mathrm{p}2}}{\partial\tilde{f}_{\mathrm{V}}} = \Delta d\frac{\partial N^{\mathrm{q}}}{\partial\hat{f}_{\mathrm{V}}} - \Delta q\frac{\partial N^{\mathrm{d}}}{\partial\hat{f}_{\mathrm{V}}} \quad \text{and} \quad \frac{\partial r_{\mathrm{p}3}}{\partial\tilde{f}_{\mathrm{V}}} = 0, \tag{B.31}$$

where the derivatives of ϕ and $\mathbf{N}^{\mathrm{p}}$ depends on the considered strain mechanisms.

B.2.3.1 Gurson model

If the Gurson model is used, the derivatives of the yield surface are, for the non-local model as well for the local one,

$$\frac{\partial \phi_{\mathrm{G}}}{\partial \hat{f}_{\mathrm{V}}} = 2q_1 \cosh\left(\frac{3q_2 p_\tau}{2\tau_{\mathrm{Y}}}\right) - 2q_3^2 \hat{f}_{\mathrm{V}}\,, \tag{B.32}$$

while those of the plastic normal read

$$\frac{\partial N^{\mathrm{d}}_{\mathrm{G}}}{\partial \hat{f}_{\mathrm{V}}} = 0 \quad \text{and} \quad \frac{\partial N^{\mathrm{q}}_{\mathrm{G}}}{\partial \hat{f}_{\mathrm{V}}} = \frac{3q_1 q_2}{\tau_{\mathrm{Y}}} \sinh\left(\frac{3q_2 p_\tau}{2\tau_{\mathrm{Y}}}\right). \tag{B.33}$$

B.2.3.2 Thomason model

The derivatives of ϕ and $\mathbf{N}^{\mathrm{p}}$ in terms of the effective porosity are, for the non-local model as well for the local one,

$$\frac{\partial \phi_{\mathrm{T}}}{\partial \hat{f}_{\mathrm{V}}} = -\tau_{\mathrm{Y}} \frac{\partial C^{\phi}_{\mathrm{T}}}{\partial \chi} \frac{\partial \chi}{\partial \hat{f}_{\mathrm{V}}}\,, \tag{B.34}$$

and

$$\frac{\partial N^{\mathrm{d}}_{\mathrm{G}}}{\partial \hat{f}_{\mathrm{V}}} = 0 \quad \text{and} \quad \frac{\partial N^{\mathrm{q}}_{\mathrm{G}}}{\partial \hat{f}_{\mathrm{V}}} = 0\,. \tag{B.35}$$

B.3 Formulation in the local form

This section presents the modifications required to bring to the constitutive law under its local form.

B.3.1 Local residual form

The local residual form (3.70) is computed in a similar way as the non-local one (3.53). However, the effective porosity is no longer fixed at the predictor state by the non-local increment and Eq. (3.61) is no longer aside but is coupled within the Newton-Raphson scheme. The Jacobian matrix (3.64) of the system is consequently modified:

$$\begin{aligned}
J_{v1,\Delta d} &= -3GN^{\mathrm{d}} + \left(\frac{\partial \phi}{\partial \hat{f}_{\mathrm{V}}} + \frac{\partial \phi}{\partial \chi}\frac{\partial \chi}{\partial \hat{f}_{\mathrm{V}}}\right)\frac{\partial f_{\mathrm{V}}}{\partial \Delta d}\,,\\
J_{v1,\Delta q} &= -KN^{\mathrm{q}} + \left(\frac{\partial \phi}{\partial \hat{f}_{\mathrm{V}}} + \frac{\partial \phi}{\partial \chi}\frac{\partial \chi}{\partial \hat{f}_{\mathrm{V}}}\right)\frac{\partial f_{\mathrm{V}}}{\partial \Delta q}\,,\\
J_{v1,\Delta p} &= \frac{\partial \phi}{\partial \tau_{\mathrm{Y}}} h + \left(\frac{\partial \phi}{\partial \hat{f}_{\mathrm{V}}} + \frac{\partial \phi}{\partial \chi}\frac{\partial \chi}{\partial \hat{f}_{\mathrm{V}}}\right)\frac{\partial f_{\mathrm{V}}}{\partial \Delta p} + \frac{\partial \phi}{\partial \chi}\frac{\partial \chi}{\partial \Delta p}\,,
\end{aligned} \tag{B.36}$$

$$\begin{aligned}
J_{v2,\Delta d} &= N^{\mathrm{q}} + \Delta d\left(\frac{\partial N^{\mathrm{q}}}{\partial \hat{f}_{\mathrm{V}}}\frac{\partial f_{\mathrm{V}}}{\partial \Delta d} - 3G\frac{\partial N^{\mathrm{q}}}{\partial \tau^{\mathrm{eq}}}\right) - \Delta q\left(\frac{\partial N^{\mathrm{d}}}{\partial \hat{f}_{\mathrm{V}}}\frac{\partial f_{\mathrm{V}}}{\partial \Delta d} - 3G\frac{\partial N^{\mathrm{d}}}{\partial \tau^{\mathrm{eq}}}\right)\,,\\
J_{v2,\Delta q} &= \Delta d\left(\frac{\partial N^{\mathrm{q}}}{\partial \hat{f}_{\mathrm{V}}}\frac{\partial f_{\mathrm{V}}}{\partial \Delta q} - K\frac{\partial N^{\mathrm{q}}}{\partial p_\tau}\right) - N^{\mathrm{d}} - \Delta q\left(\frac{\partial N^{\mathrm{d}}}{\partial \hat{f}_{\mathrm{V}}}\frac{\partial f_{\mathrm{V}}}{\partial \Delta q} - K\frac{\partial N^{\mathrm{d}}}{\partial p_\tau}\right)\,,\\
J_{v2,\Delta p} &= \Delta d\left(\frac{\partial N^{\mathrm{q}}}{\partial \hat{f}_{\mathrm{V}}}\frac{\partial f_{\mathrm{V}}}{\partial \Delta p} + \frac{\partial N^{\mathrm{q}}}{\partial \tau_{\mathrm{Y}}} h\right) - \Delta q\left(\frac{\partial N^{\mathrm{d}}}{\partial \hat{f}_{\mathrm{V}}}\frac{\partial f_{\mathrm{V}}}{\partial \Delta p} + \frac{\partial N^{\mathrm{d}}}{\partial \tau_{\mathrm{Y}}} h\right)\,,
\end{aligned} \tag{B.37}$$

and $J_{v3,\boldsymbol{v}}$ is left unchanged. The derivatives appearing in the previous expressions can be found in Appendices B.1 and B.2.

B.3.2 Formulation of the local material operators

The procedure is similar to the method explained in Section 3.1.3.3 and Appendix B.2. Equations (B.15) to (B.24) are still applicable to express $\frac{\partial \mathbf{P}}{\partial \mathbf{F}}$ in terms of the plastic increment $\boldsymbol{v}$. These derivatives are extracted using Eq. (3.69) and the corresponding modified version of Eq. (B.28) for the residues derivatives reads

$$\frac{\partial \boldsymbol{r}_{\mathrm{p}}}{\partial \mathbf{E}^{\mathrm{e}}_{\mathrm{pr}}} = \frac{\partial \boldsymbol{r}_{\mathrm{p}}}{\partial \tau^{\mathrm{eq}}_{\mathrm{pr}}} \otimes \frac{3G\left(\boldsymbol{\tau}_{\mathrm{pr}}\right)^{\mathrm{dev}}}{\tau^{\mathrm{eq}}_{\mathrm{pr}}} + \frac{\partial \boldsymbol{r}_{\mathrm{p}}}{\partial p_{\tau\,\mathrm{pr}}} \otimes K\mathbf{I} + \frac{\partial \boldsymbol{r}_{\mathrm{p}}}{\partial \hat{f}_{\mathrm{V}}} \otimes \frac{\partial f_{\mathrm{V}}}{\partial \mathbf{E}^{\mathrm{e}}_{\mathrm{pr}}}\,. \tag{B.38}$$

B.4 Formulation of the finite element forces

The expressions of the finite element forces appearing in Eq. (3.87) are presented here. The weak form (3.84)-(3.85) developed in Section 3.3.2 is the starting point of the finite element discretisation. By taking into account the discretisation (3.86) and the discontinuities between elements, one has the following elementary terms:

- Inertial forces $\mathbf{M}^{e\,ab} \cdot \ddot{\boldsymbol{u}}^{b}$ with:

$$M^{e\,ab}_{ij} = \int_{B^e} \rho_0 N^a N^b \delta_{ij}\, dV_0\,; \tag{B.39}$$

- Internal forces $\boldsymbol{f}^{e}_{\boldsymbol{u}\,\mathrm{int}}{}^{a}$:

$$f^{e}_{u\,\mathrm{int}\,i}{}^{a} = \int_{B^e} P_{iK} \left(\boldsymbol{\nabla}_0 N^a\right)_K \, dV_0\,; \tag{B.40}$$

- External forces $\boldsymbol{f}^{e}_{u\,\mathrm{ext}}{}^{a}$:

$$f^{e}_{u\,\mathrm{ext}\,i}{}^{a} = \int_{B^e} \rho_0 b_{0\,i} N^a \, dV_0 + \int_{S^s_{\mathrm{N}}} \bar{t}_{\mathrm{N}0\,i} N^a \, dS_0\,; \tag{B.41}$$

- Interface forces $\boldsymbol{f}^{s}_{u\,\mathrm{I}}{}^{a^{\pm}}$:

$$\begin{aligned} f^{s}_{u\,\mathrm{I}\,i}{}^{a^{\pm}} \;=\; & \int_{S^s_{\mathrm{IC}}} \left(\pm N^{a^{\pm}}\right) \langle P_{\mathrm{b}iK} \rangle \, N^{-}_{\mathrm{I}\;K} \, dS_0 + \int_{S^s_{\mathrm{IU}}} \left(\pm N^{a^{\pm}}\right) \langle P_{iK} \rangle \, N^{-}_{\mathrm{I}\;K} \, dS_0 \\ & + \int_{S^s_{\mathrm{IU}}} \left(\pm N^{a^{\pm}}\right) N^{-}_{\mathrm{I}K} \left\langle \frac{\beta_{\mathrm{s}}}{h_{\mathrm{s}}} \mathcal{C}^{\mathrm{e}}_{iKmN} \right\rangle [\![u_m]\!] \, N^{-}_{\mathrm{I}N} \, dS_0 \\ & + \frac{1}{2} \int_{S^s_{\mathrm{IU}}} [\![u_k]\!] \, \mathcal{C}^{\mathrm{e}\pm}_{kMiN} \left(\boldsymbol{\nabla}_0 N^{a^{\pm}}\right)_N N^{-}_{\mathrm{I}M} \, dS_0\,. \end{aligned} \tag{B.42}$$

- Internal non-local forces $f^{e}_{\tilde{Z}\,\mathrm{int}}{}^{a}$:

$$f^{e}_{\tilde{Z}\,\mathrm{int}}{}^{a} = \int_{B^e} \left(\Delta\tilde{Z} N^a + \left(\boldsymbol{\nabla}_0 N^a\right)_K C_{\mathrm{l}KL} \left(\boldsymbol{\nabla}_0 \Delta\tilde{Z}\right)_L\right) dV_0\,; \tag{B.43}$$

- Internal local forces $f^{e}_{Z\,\mathrm{int}}{}^{a}$:

$$f^{e}_{Z\,\mathrm{int}}{}^{a} = \int_{B^e} \Delta Z N^a \, dV_0\,; \tag{B.44}$$

- Interface non-local forces ${f^s_{\tilde{Z}\,\mathrm{I}}}^{a^\pm}$:

$$
\begin{aligned}
{f^s_{\tilde{Z}\,\mathrm{I}}}^{a^\pm} \;=\; & \int_{S^s_{\mathrm{IU}}} \left(\pm N^{a^\pm}\right) \langle C_{\mathrm{l}} \rangle_{KL} \left(\boldsymbol{\nabla}_0 \Delta\tilde{Z}\right)_L N_{\mathrm{I}\,K}^- \, dS_0 \\
& + \int_{S^s_{\mathrm{IU}}} \left(\pm N^{a^\pm}\right) N_{\mathrm{I}\,K}^- \left\langle \frac{\beta_{\mathrm{s}}}{h_{\mathrm{s}}} C_{\mathrm{l}\,KL} \right\rangle \left[\!\left[\Delta\tilde{Z}\right]\!\right] N_{\mathrm{I}\,L}^- \, dS_0 \\
& + \frac{1}{2} \int_{S^s_{\mathrm{IU}}} \left[\!\left[\Delta\tilde{Z}\right]\!\right] N_{\mathrm{I}\,K}^- C^\pm_{\mathrm{l}\,KL} \left(\boldsymbol{\nabla}_0 N^{a^\pm}\right)_L \, dS_0 \,.
\end{aligned}
\tag{B.45}
$$

In those expressions, the superscripts $a, b, \ldots$ stand for the node a which belongs to a volume element B^e or to a interface one S^s. The sign $+$ or $-$ in the case of interface elements differentiates if the node (i.e. a^+ or a^-) belongs to B^{e^+} or B^{e^-}. Practically, only the degrees of freedom are duplicated at the interfaces and not the node itself. The computation of the volume element force involves the shape functions of the volume elements. All nodes of both volume elements are therefore contributing in the interface term thanks to the symmetrisation term. Only the gradient of the jump displacement uses interface shape functions to naturally respect condition (3.76). The quadratic volume elements are integrated using a reduced integration while the surface element are fully-integrated to avoid spurious penetration modes.

B.5 Formulation of the finite element stiffness matrices

The expressions of the contribution ot finite element stiffness matrix $\mathbf{K}$ appearing in Eq. (2.86) are detailed here. The stiffness matrix regroups all the stiffness components resulting from the linearisation of the elementary forces in equations (B.39) to (B.45). One obtains

$$
\mathbf{K} = \begin{bmatrix}
\mathbf{K}_{\boldsymbol{uu}\,\mathrm{int}} + \mathbf{K}_{\boldsymbol{uu}\,\mathrm{I}} & \mathbf{K}_{\boldsymbol{u}\tilde{Z}\,\mathrm{int}} + \mathbf{K}_{\boldsymbol{u}\tilde{Z}\,\mathrm{I}} \\
\mathbf{K}_{\tilde{Z}\boldsymbol{u}\,\mathrm{int}} - \mathbf{K}_{Z\boldsymbol{u}\,\mathrm{int}} + \mathbf{K}_{\tilde{Z}\boldsymbol{u}\,\mathrm{I}} & \mathbf{K}_{\tilde{Z}\tilde{Z}\,\mathrm{int}} - \mathbf{K}_{Z\tilde{Z}\,\mathrm{int}} + \mathbf{K}_{\tilde{Z}\tilde{Z}\,\mathrm{I}}
\end{bmatrix} ,
\tag{B.46}
$$

with

- Internal force stiffness terms ${\mathbf{K}^e_{\boldsymbol{uu}\,\mathrm{int}}}^{ab}$ and ${\mathbf{K}^e_{\boldsymbol{u}\tilde{Z}\,\mathrm{int}}}^{ab}$:

$$
K^e_{\boldsymbol{uu}\,\mathrm{int}\,ij}{}^{ab} = \frac{\partial {f^e_{\boldsymbol{u}\,\mathrm{int}}}_i^a}{\partial u_j^b} = \int_{B^e} \mathcal{C}_{\boldsymbol{u}\mathbf{F}\,iKjL} \left(\boldsymbol{\nabla}_0 N^a\right)_K \left(\boldsymbol{\nabla}_0 N^b\right)_L \, dV_0 \,;
\tag{B.47}
$$

$$
K^e_{\boldsymbol{u}\tilde{Z}\,\mathrm{int}\,i}{}^{ab} = \frac{\partial {f^e_{\boldsymbol{u}\,\mathrm{int}}}_i^a}{\partial \tilde{Z}^b} = \int_{B^e} C_{\boldsymbol{u}\tilde{Z}\,iK} \left(\boldsymbol{\nabla}_0 N^a\right)_K N^b \, dV_0 \,;
\tag{B.48}
$$

- Interface force stiffness terms ${\mathbf{K}^s_{\boldsymbol{uu}\,\mathrm{I}}}^{a^\pm b^\pm}$ and ${\mathbf{K}^s_{\boldsymbol{u}\tilde{Z}\,\mathrm{I}}}^{a^\pm b^\pm}$:

$$
\begin{aligned}
K^{s}_{\boldsymbol{u}\boldsymbol{u}\,\mathrm{I}ij}{}^{a^{\pm}b^{\pm}} = \frac{\partial f^{s}_{\boldsymbol{u}\,\mathrm{I}i}{}^{a^{\pm}}}{\partial u^{b^{\pm}}_{j}} \;=\; & +\frac{1}{2}\int_{S^{s}_{\mathrm{IC}}} \left(\pm N^{a^{\pm}}\right) \mathcal{C}^{\mathrm{b}\,\pm}_{\boldsymbol{u}\mathbf{F}\,iKjL} \left(\boldsymbol{\nabla}_0 N^{b^{\pm}}\right)_L N^{-}_{\mathrm{I}\;K}\, dS_0 \\
& + \int_{S^{s}_{\mathrm{IC}}} \left(\pm N^{a^{\pm}}\right) \left\langle \mathfrak{C}^{\mathrm{b}}_{\boldsymbol{u}[\![\boldsymbol{u}]\!]\,iKj} \right\rangle \left(\pm N^{b^{\pm}}\right) N^{-}_{\mathrm{I}\;K}\, dS_0 \\
& + \int_{S^{s}_{\mathrm{IC}}} \left(\pm N^{a^{\pm}}\right) \left\langle \mathcal{C}^{\mathrm{b}}_{\boldsymbol{u}\boldsymbol{\nabla}[\![\boldsymbol{u}]\!]\,iKjL} \right\rangle \left(\pm \boldsymbol{\nabla}_0 N^{b^{\pm}}\right)_L N^{-}_{\mathrm{I}\;K}\, dS_0 \\
& + \frac{1}{2}\int_{S^{s}_{\mathrm{IU}}} \left(\pm N^{a^{\pm}}\right) \mathcal{C}^{\pm}_{\boldsymbol{u}\mathbf{F}\,iKjL} \left(\boldsymbol{\nabla}_0 N^{b^{\pm}}\right)_L N^{-}_{\mathrm{I}\;K}\, dS_0 \\
& + \int_{S^{s}_{\mathrm{IU}}} \left(\pm N^{a^{\pm}}\right) N^{-}_{\mathrm{I}K} \left\langle \frac{\beta_{\mathrm{s}}}{h_{\mathrm{s}}} \mathcal{C}^{\mathrm{e}}_{iKjN} \right\rangle \left(\pm N^{b^{\pm}}\right) N^{-}_{\mathrm{I}N}\, dS_0 \\
& + \frac{1}{2}\int_{S^{s}_{\mathrm{IU}}} \left(\pm N^{b^{\pm}}\right) \mathcal{C}^{\mathrm{e}}_{jMiN}{}^{\pm} \left(\boldsymbol{\nabla}_0 N^{a^{\pm}}\right)_N N^{-}_{\mathrm{I}M}\, dS_0 \,.
\end{aligned}
\tag{B.49}
$$

$$
K^{s}_{\boldsymbol{u}\tilde{Z}\,\mathrm{I}ij}{}^{a^{\pm}b^{\pm}} = \frac{\partial f^{s}_{\boldsymbol{u}\,\mathrm{I}i}{}^{a^{\pm}}}{\partial \tilde{Z}^{b^{\pm}}} = \frac{1}{2}\int_{S^{s}_{\mathrm{IU}}} \left(\pm N^{a}\right) C^{\pm}_{\boldsymbol{u}\tilde{Z}\,iK} N^{b^{\pm}} N^{-}_{\mathrm{I}\;K}\,; \tag{B.50}
$$

- Internal non-local force stiffness terms $\boldsymbol{K}^{e}_{\tilde{Z}\boldsymbol{u}\,\mathrm{int}}{}^{ab}$ and $K^{e}_{\tilde{Z}\tilde{Z}\,\mathrm{int}}{}^{ab}$:

$$
K^{e}_{\tilde{Z}\boldsymbol{u}\,\mathrm{int}\,j}{}^{ab} = \frac{\partial f^{e}_{\tilde{Z}\,\mathrm{int}}{}^{a}}{\partial u^{b}_{j}} = 0\,; \tag{B.51}
$$

$$
K^{e}_{\tilde{Z}\tilde{Z}\,\mathrm{int}}{}^{ab} = \frac{\partial f^{e}_{\tilde{Z}\,\mathrm{int}}{}^{a}}{\partial \tilde{Z}^{b}} = \int_{B^e} \left[N^{a} N^{b} + \left(\boldsymbol{\nabla}_0 N^{a}\right)_K C_{\mathrm{l}KL} \left(\boldsymbol{\nabla}_0 N^{b}\right)_L \right] dV_0\,; \tag{B.52}
$$

- Internal local force stiffness terms $\boldsymbol{K}^{e}_{Z\boldsymbol{u}\,\mathrm{int}}{}^{ab}$ and $K^{e}_{Z\tilde{Z}\,\mathrm{int}}{}^{ab}$:

$$
K^{e}_{Z\boldsymbol{u}\,\mathrm{int}\,j}{}^{ab} = \frac{\partial f^{e}_{Z\,\mathrm{int}}{}^{a}}{\partial u^{b}_{j}} = \int_{B^e} C_{Z\mathbf{F}jK} N^{a} \left(\boldsymbol{\nabla}_0 N^{b}\right)_K dV_0\,; \tag{B.53}
$$

$$
K^{e}_{Z\tilde{Z}\,\mathrm{int}}{}^{ab} = \frac{\partial f^{e}_{Z\,\mathrm{int}}{}^{a}}{\partial \tilde{Z}^{b}} = \int_{B^e} C_{Z\tilde{Z}} N^{a} N^{b}\, dV_0\,; \tag{B.54}
$$

- Interface non-local forces $\boldsymbol{K}^{s}_{\tilde{Z}\boldsymbol{u}\,\mathrm{I}}{}^{a^{\pm}b^{\pm}}$ and $K^{s}_{\tilde{Z}\tilde{Z}\,\mathrm{I}}{}^{a^{\pm}b^{\pm}}$:

$$
K^{s}_{\tilde{Z}\boldsymbol{u}\,\mathrm{I}j}{}^{a^{\pm}b^{\pm}} = 0\,; \tag{B.55}
$$

$$
\begin{aligned}
K^{s}_{\tilde{Z}\tilde{Z}\,\mathrm{I}}{}^{a^{\pm}b^{\pm}} = \frac{\partial f^{s}_{\tilde{Z}\,\mathrm{I}}{}^{a^{\pm}}}{\partial \tilde{Z}^{b^{\pm}}} \;=\; & \frac{1}{2}\int_{S^{s}_{\mathrm{IU}}} \left(\pm N^{a^{\pm}}\right) C_{\mathrm{l}KL} \left(\boldsymbol{\nabla}_0 N^{b^{\pm}}\right)_L N^{-}_{\mathrm{I}\;K}\, dS_0 \\
& + \int_{S^{s}_{\mathrm{IU}}} \left(\pm N^{a^{\pm}}\right) N^{-}_{\mathrm{I}\;K} \left\langle \frac{\beta_{\mathrm{s}}}{h_{\mathrm{s}}} C_{\mathrm{l}KL} \right\rangle \left(\pm N^{b^{\pm}}\right) N^{-}_{\mathrm{I}\;L}\, dS_0 \\
& + \frac{1}{2}\int_{S^{s}_{\mathrm{IU}}} \left(\pm N^{b^{\pm}}\right) C^{\pm}_{\mathrm{l}KL} \left(\boldsymbol{\nabla}_0 N^{a^{\pm}}\right)_L N^{-}_{\mathrm{I}\;K}\, dS_0 \,.
\end{aligned}
\tag{B.56}
$$

The expressions above involve material tangent tensors computed in Appendix B.2. If the considered point is not located on a cohesive band, the relations are directly obtained

$$\boldsymbol{\mathcal{C}}_{\boldsymbol{u}\mathbf{F}} = \frac{\partial \mathbf{P}}{\partial \mathbf{F}} \;,\; \mathbf{C}_{\boldsymbol{u}\tilde{Z}} = \frac{\partial \mathbf{P}}{\partial \Delta \tilde{f}_{\mathrm{V}}} \;,\; \mathbf{C}_{Z\mathbf{F}} = \frac{\partial \Delta f_{\mathrm{V}}}{\partial \mathbf{F}} \;,\; \mathcal{C}_{Z\tilde{Z}} = \frac{\partial \Delta f_{\mathrm{V}}}{\partial \Delta \tilde{f}_{\mathrm{V}}} \,. \tag{B.57}$$

If the point is located on a cohesive band model, the derivatives of the band deformation gradient $\mathbf{F}_{\mathrm{b}}$ have to be included. They directly derived from the computation of $\mathbf{F}_{\mathrm{b}}$ (3.75)

$$\delta F_{\mathrm{b}\,iJ}^{\pm} = \delta F_{iJ}^{\pm} + \frac{N_{\mathrm{I}J}}{h_{\mathrm{b}}} \delta \left[\!\left[u_i \right]\!\right] + \frac{1}{2} \delta \left(\boldsymbol{\nabla}_0 \left[\!\left[u_i \right]\!\right] \right)_J \,. \tag{B.58}$$

From the previous equation, the tangent stiffness terms are thus:

$$\boldsymbol{\mathcal{C}}^{\mathrm{b}}_{\boldsymbol{u}\mathbf{F}} = \frac{\partial \mathbf{P}_{\mathrm{b}}}{\partial \mathbf{F}_{\mathrm{b}}} \,, \tag{B.59}$$

$$\boldsymbol{\mathfrak{C}}^{\mathrm{b}}_{\boldsymbol{u}[\![\boldsymbol{u}]\!]} = \frac{\partial \mathbf{P}_{\mathrm{b}}}{\partial \mathbf{F}_{\mathrm{b}}} \cdot \frac{\boldsymbol{N}_{\mathrm{I}}}{h_{\mathrm{b}}} \,, \tag{B.60}$$

$$\boldsymbol{\mathcal{C}}^{\mathrm{b}}_{\boldsymbol{u}\boldsymbol{\nabla}[\![\boldsymbol{u}]\!]} = \frac{1}{2} \frac{\partial \mathbf{P}_{\mathrm{b}}}{\partial \mathbf{F}_{\mathrm{b}}} \,, \tag{B.61}$$

and the derivatives of $\frac{\partial \mathbf{P}_{\mathrm{b}}}{\partial \mathbf{F}_{\mathrm{b}}}$ corresponds to the local version of the material tangent calculated in Appendix B.3.2.

Appendix C

Appendix related to Chapter 4

C.1 Demonstration of the anisotropic criterion

The problem presented by Eq. (4.27) can be rewritten as the optimisation problem under constraint

$$\max_{\boldsymbol{n}} \left[\boldsymbol{n}\cdot\boldsymbol{\sigma}\cdot\boldsymbol{n} + \boldsymbol{n}\cdot\mathbf{k}\cdot\boldsymbol{n}(\sigma^{\mathrm{eq}} - \sigma_{\mathrm{Y}}) - \boldsymbol{n}\cdot\boldsymbol{\sigma}_{\mathrm{n_c}}\cdot\boldsymbol{n}\right] > 0 \text{ with } \boldsymbol{n}\cdot\boldsymbol{n} = 1\,, \tag{C.1}$$

with $\boldsymbol{n}$ a normed direction vector (the tensors and vectors are defined in the current configuration). This problem is rewritten using a dual form L

$$L = \left[\boldsymbol{n}\cdot\boldsymbol{\sigma}\cdot\boldsymbol{n} + \boldsymbol{n}\cdot\mathbf{k}\cdot\boldsymbol{n}(\sigma^{\mathrm{eq}} - \sigma_{\mathrm{Y}}) - \boldsymbol{n}\cdot\boldsymbol{\sigma}_{\mathrm{n_c}}\cdot\boldsymbol{n}\right] - \lambda\left[\boldsymbol{n}\cdot\boldsymbol{n} - 1\right]\,, \tag{C.2}$$

with λ a Lagrange multiplier. Following the Lagrange theorem, the solution $\boldsymbol{n}^*$ of the problem is among the stationary point of L, satisfying:

$$\begin{aligned} \frac{\partial L}{\partial \boldsymbol{n}} &= 2\left(\boldsymbol{\sigma} + \mathbf{k}(\sigma^{\mathrm{eq}} - \sigma_{\mathrm{Y}}) - \boldsymbol{\sigma}_{\mathrm{n_c}}\right)\cdot\boldsymbol{n} - 2\lambda\boldsymbol{n} = \mathbf{0}\,, \\ \frac{\partial L}{\partial \lambda} &= \boldsymbol{n}\cdot\boldsymbol{n} - 1 = 0\,. \end{aligned} \tag{C.3}$$

These equations could be satisfied only if $\boldsymbol{n}^*$ is a unitary eigenvector of the tensor $\boldsymbol{\sigma} + \mathbf{k}(\sigma^{\mathrm{eq}} - \sigma_{\mathrm{Y}}) - \boldsymbol{\sigma}_{\mathrm{n_c}}$. Moreover, the solution corresponds to the eigenvector associated to the largest eigenvalue.

Bibliography

Aduloju, Sunday C. and Timothy J. Truster (2019). "A variational multiscale discontinuous Galerkin formulation for both implicit and explicit dynamic modeling of interfacial fracture". In: *Computer Methods in Applied Mechanics and Engineering* 343, pp. 602–630. ISSN: 00457825. DOI: 10.1016/j.cma.2018.08.025. URL: https://linkinghub.elsevier.com/retrieve/pii/S0045782518304201.

Agathos, Konstantinos et al. (2018). "Stable 3D XFEM/vector level sets for non-planar 3D crack propagation and comparison of enrichment schemes". In: *International Journal for Numerical Methods in Engineering* 113.2, pp. 252–276. ISSN: 00295981. DOI: 10.1002/nme.5611. URL: http://doi.wiley.com/10.1002/nme.5611.

Aldakheel, Fadi (2017). "Micromorphic approach for gradient-extended thermo-elastic–plastic solids in the logarithmic strain space". In: *Continuum Mechanics and Thermodynamics* 29.6, pp. 1207–1217. ISSN: 0935-1175. DOI: 10.1007/s00161-017-0571-0. URL: http://link.springer.com/10.1007/s00161-017-0571-0.

Aldakheel, Fadi, Peter Wriggers, and Christian Miehe (2018). "A modified Gurson-type plasticity model at finite strains: formulation, numerical analysis and phase-field coupling". In: *Computational Mechanics* 62.4, pp. 815–833. ISSN: 0178-7675. DOI: 10.1007/s00466-017-1530-0. URL: http://link.springer.com/10.1007/s00466-017-1530-0.

Anderson, T. L. (2017). *Fracture Mechanics Fundamentals And Applications 3rd Ed.* Ed. by CRC Press. 4th ed. ISBN: 9781498728133.

Bai, Yuanli, Xiaoqing Teng, and Tomasz Wierzbicki (2009). "On the Application of Stress Triaxiality Formula for Plane Strain Fracture Testing". In: *Journal of Engineering Materials and Technology* 131.2, pp. 0210021–02100210. ISSN: 0094-4289. DOI: 10.1115/1.3078390. URL: https://asmedigitalcollection.asme.org/materialstechnology/article/doi/10.1115/1.3078390/455188/On-the-Application-of-Stress-Triaxiality-Formula.

Bai, Yuanli and Tomasz Wierzbicki (2008). "A new model of metal plasticity and fracture with pressure and Lode dependence". In: *International Journal of Plasticity* 24.6, pp. 1071–1096. ISSN: 07496419. DOI: 10.1016/j.ijplas.2007.09.004. URL: http://www.sciencedirect.com/science/article/pii/S0749641907001246.

Barenblatt, G.I. (1962). "The Mathematical Theory of Equilibrium Cracks in Brittle Fracture". In: *Advances in Applied Mechanics*. Ed. by H L Dryden et al. Vol. 7. Advances in Applied Mechanics C. Elsevier, pp. 55–129. DOI: 10.1016/S0065-2156(08)70121-2. URL: http://www.sciencedirect.com/science/article/pii/S0065215608701212https://linkinghub.elsevier.com/retrieve/pii/S0065215608701212.

Bažant, Zdeněk P., Ted B. Belytschko, and Ta-Peng Chang (1984). "Continuum Theory for Strain-Softening". In: *Journal of Engineering Mechanics* 110.12, pp. 1666–1692. ISSN: 0733-9399. DOI: 10.1061/(ASCE)0733-9399(1984)110:12(1666). URL: http://ascelibrary.org/doi/10.1061/{\%}28ASCE{\%}290733-9399{\%}281984{\%}29110{\%}3A12{\%}281666{\%}29.

Benzerga, A. Amine (2002). "Micromechanics of coalescence in ductile fracture". In: *Journal of the Mechanics and Physics of Solids* 50.6, pp. 1331–1362. ISSN: 00225096. DOI: 10.1016/S0022-5096(01)00125-9. URL: https://linkinghub.elsevier.com/retrieve/pii/S0022509601001259.

Benzerga, A. Amine, J. Besson, and A. Pineau (2004). "Anisotropic ductile fracture". In: *Acta Materialia* 52.15, pp. 4639–4650. ISSN: 13596454. DOI: 10.1016/j.actamat.2004.06.019. URL: https://linkinghub.elsevier.com/retrieve/pii/S135964540400357X.

Benzerga, A. Amine and Jean-Baptiste Leblond (2010). "Ductile Fracture by Void Growth to Coalescence". In: *Advances in Applied Mechanics*. Ed. by Hassan Aref and Erik van der Giessen. Vol. 44. Advances in Applied Mechanics. Elsevier, pp. 169–305. DOI: 10.1016/S0065-2156(10)44003-X. URL: https://linkinghub.elsevier.com/retrieve/pii/S006521561044003X.

— (2014). "Effective Yield Criterion Accounting for Microvoid Coalescence". In: *Journal of Applied Mechanics* 81.3, p. 031009. ISSN: 0021-8936. DOI: 10.1115/1.4024908. URL: https://asmedigitalcollection.asme.org/appliedmechanics/article/doi/10.1115/1.4024908/370377/Effective-Yield-Criterion-Accounting-for-Microvoid.

Benzerga, A. Amine et al. (2016). "Ductile failure modeling". In: *International Journal of Fracture* 201.1, pp. 29–80. ISSN: 0376-9429. DOI: 10.1007/s10704-016-0142-6. URL: https://doi.org/10.1007/s10704-016-0142-6.

Beremin, F. M. (1981). "Cavity formation from inclusions in ductile fracture of A508 steel". In: *Metallurgical Transactions A* 12.5, pp. 723–731. ISSN: 0360-2133. DOI: 10.1007/BF02648336. URL: http://link.springer.com/10.1007/BF02648336.

Berveiller, M. and A. Zaoui (1978). "An extension of the self-consistent scheme to plastically-flowing polycrystals". In: *Journal of the Mechanics and Physics of Solids* 26.5-6, pp. 325–344. ISSN: 00225096. DOI: 10.1016/0022-5096(78)90003-0. URL: https://linkinghub.elsevier.com/retrieve/pii/0022509678900030.

Besson, J. (2009). "Damage of ductile materials deforming under multiple plastic or viscoplastic mechanisms". In: *International Journal of Plasticity* 25.11, pp. 2204–2221. ISSN: 07496419. DOI: 10.1016/j.ijplas.2009.03.001. URL: http://www.sciencedirect.com/science/article/pii/S0749641909000357.

— (2010). "Continuum Models of Ductile Fracture: A Review". In: *International Journal of Damage Mechanics* 19.1, pp. 3–52. ISSN: 1056-7895. DOI: 10.1177/1056789509103482. URL: https://doi.org/10.1177/1056789509103482.

Besson, J., D. Steglich, and W. Brocks (2001). "Modeling of crack growth in round bars and plane strain specimens". In: *International Journal of Solids and Structures* 38.46-47, pp. 8259–8284. ISSN: 00207683. DOI: 10.1016/S0020-7683(01)00167-6. URL: https://linkinghub.elsevier.com/retrieve/pii/S0020768301001676.

— (2003). "Modeling of plane strain ductile rupture". In: *International Journal of Plasticity* 19.10, pp. 1517–1541. ISSN: 07496419. DOI: 10.1016/S0749-6419(02)00022-0. URL: https://linkinghub.elsevier.com/retrieve/pii/S0749641902000220.

Bosco, E., V. G. Kouznetsova, and M. G. D. Geers (2015). "Multi-scale computational homogenization-localization for propagating discontinuities using X-FEM". In: *International Journal for Numerical Methods in Engineering* 102.3-4, pp. 496–527. ISSN: 00295981. DOI: 10.1002/nme.4838. URL: http://doi.wiley.com/10.1002/nme.4838.

Bridgman, Percy Williams (1952). *Studies in Large Plastic Flow and Fracture*. New-York: McGraw-Hill. URL: https://linkinghub.elsevier.com/retrieve/pii/0022509653900192.

Brocks, W., D.-Z. Sun, and A. Hönig (1995). "Verification of the transferability of micromechanical parameters by cell model calculations with visco-plastic materials". In: *International Journal of Plasticity* 11.8, pp. 971–989. ISSN: 07496419. DOI: 10.1016/S0749-6419(95)00039-9. URL: https://www.sciencedirect.com/science/article/abs/pii/S0749641995000399.

Brünig, Michael, Daniel Brenner, and Steffen Gerke (2015). "Stress state dependence of ductile damage and fracture behavior: Experiments and numerical simulations". In: *Engineering Fracture Mechanics* 141, pp. 152–169. ISSN: 00137944. DOI: 10.1016/j.engfracmech.2015.05.022. URL: https://linkinghub.elsevier.com/retrieve/pii/S0013794415002192.

Brünig, Michael, Steffen Gerke, and Marco Schmidt (2018). "Damage and failure at negative stress triaxialities: Experiments, modeling and numerical simulations". In: *International Journal of Plasticity* 102, pp. 70–82. ISSN: 07496419. DOI: 10.1016/j.ijplas.2017.12.003. URL: https://linkinghub.elsevier.com/retrieve/pii/S0749641917305764.

Camacho, G.T. and M. Ortiz (1996). "Computational modelling of impact damage in brittle materials". In: *International Journal of Solids and Structures* 33.20-22, pp. 2899–2938. ISSN: 00207683. DOI: 10.1016/0020-7683(95)00255-3. URL: https://linkinghub.elsevier.com/retrieve/pii/0020768395002553.

Cazes, Fabien et al. (2009). "A thermodynamic method for the construction of a cohesive law from a nonlocal damage model". In: *International Journal of Solids and Structures* 46.6, pp. 1476–1490. ISSN: 00207683. DOI: 10.1016/j.ijsolstr.2008.11.019. URL: http://www.sciencedirect.com/science/article/pii/S0020768308004903.

Cazes, Fabien et al. (2010). "A cohesive zone model which is energetically equivalent to a gradient-enhanced coupled damage-plasticity model". In: *European Journal of Mechanics - A/Solids* 29.6, pp. 976–989. ISSN: 09977538. DOI: 10.1016/j.euromechsol.2009.11.003. URL: http://www.sciencedirect.com/science/article/pii/S0997753809001338.

Chaboche, J. L. (1988). "Continuum Damage Mechanics: Part II—Damage Growth, Crack Initiation, and Crack Growth". In: *Journal of Applied Mechanics* 55.1, pp. 65–72. ISSN: 0021-8936. DOI: 10.1115/1.3173662. URL: https://asmedigitalcollection.asme.org/appliedmechanics/article/55/1/65/390103/Continuum-Damage-Mechanics-Part-IIDamage-Growth.

Charles, Y. (2014). "A finite element formulation to model extrinsic interfacial behavior". In: *Finite Elements in Analysis and Design* 88, pp. 55–66. ISSN: 0168874X. DOI: 10.1016/j.finel.2014.05.008. URL: https://linkinghub.elsevier.com/retrieve/pii/S0168874X14000912.

Chu, C. C. and A. Needleman (1980). "Void Nucleation Effects in Biaxially Stretched Sheets". In: *Journal of Engineering Materials and Technology* 102.3, pp. 249–256. ISSN: 0094-4289. DOI: 10.1115/1.3224807. URL: https://asmedigitalcollection.asme.org/materialstechnology/article/102/3/249/394607/Void-Nucleation-Effects-in-Biaxially-Stretched.

Chung, J. and G. M. Hulbert (1993). "A Time Integration Algorithm for Structural Dynamics With Improved Numerical Dissipation: The Generalized-α Method". In: *Journal of Applied Mechanics* 60.2, pp. 371–375. ISSN: 0021-8936. DOI: 10.1115/1.2900803. URL: https://asmedigitalcollection.asme.org/appliedmechanics/article/60/2/371/423023/A-Time-Integration-Algorithm-for-Structural.

Comi, Claudia, Stefano Mariani, and Umberto Perego (2007). "An extended FE strategy for transition from continuum damage to mode I cohesive crack propagation". In: *International Journal for Numerical and Analytical Methods in Geomechanics* 31.2, pp. 213–238. ISSN: 03639061. DOI: 10.1002/nag.537. URL: http://doi.wiley.com/10.1002/nag.537.

Cortese, Luca, Filippo Nalli, and Marco Rossi (2016). "A nonlinear model for ductile damage accumulation under multiaxial non-proportional loading conditions". In: *International Journal of Plasticity* 85, pp. 77–92. ISSN: 07496419. DOI: 10.1016/j.ijplas.2016.07.003. URL: https://linkinghub.elsevier.com/retrieve/pii/S0749641916301036.

Cuitino, A. and M. Ortiz (1992). "A material-independent method for extending stress update algorithms from small-strain plasticity to finite plasticity with multiplicative kinematics". In: *Engineering Computations* 9.4, pp. 437–451. ISSN: 0264-4401. DOI: 10.1108/eb023876. URL: http://www.emeraldinsight.com/doi/10.1108/eb023876.

Cuvilliez, Sam et al. (2012). "A finite element approach coupling a continuous gradient damage model and a cohesive zone model within the framework of quasi-brittle failure". In: *Computer Methods in Applied Mechanics and Engineering* 237-240, pp. 244–259. ISSN:

00457825. DOI: 10.1016/j.cma.2012.04.019. URL: https://linkinghub.elsevier.com/retrieve/pii/S0045782512001466.

Danas, K. and P. Ponte Castañeda (2012). "Influence of the Lode parameter and the stress triaxiality on the failure of elasto-plastic porous materials". In: *International Journal of Solids and Structures* 49.11-12, pp. 1325–1342. ISSN: 00207683. DOI: 10.1016/j.ijsolstr.2012.02.006. URL: https://linkinghub.elsevier.com/retrieve/pii/S0020768312000467.

De Borst, René and Clemens V. Verhoosel (2016). "Gradient damage vs phase-field approaches for fracture: Similarities and differences". In: *Computer Methods in Applied Mechanics and Engineering* 312, pp. 78–94. ISSN: 00457825. DOI: 10.1016/j.cma.2016.05.015. URL: http://www.sciencedirect.com/science/article/pii/S0045782516303796.

De Borst, René et al. (2012). *Non-Linear Finite Element Analysis of Solids and Structures*. Chichester, UK: John Wiley & Sons, Ltd. ISBN: 9781118375938. DOI: 10.1002/9781118375938. URL: http://doi.wiley.com/10.1002/9781118375938.

Driemeier, Larissa et al. (2010). "Experiments on stress-triaxiality dependence of material behavior of aluminum alloys". In: *Mechanics of Materials* 42.2, pp. 207–217. ISSN: 01676636. DOI: 10.1016/j.mechmat.2009.11.012. URL: https://linkinghub.elsevier.com/retrieve/pii/S0167663609001999.

Dufour, Frederic et al. (2008). "Extraction of a crack opening from a continuous approach using regularized damage models". In: *Computers and Concrete* 5.4, pp. 375–388. ISSN: 1598-8198. DOI: 10.12989/cac.2008.5.4.375. URL: http://koreascience.or.kr/journal/view.jsp?kj=KJKHDQ{\&}py=2008{\&}vnc=v5n4{\&}sp=375.

Dugdale, D.S. (1960). "Yielding of steel sheets containing slits". In: *Journal of the Mechanics and Physics of Solids* 8.2, pp. 100–104. ISSN: 00225096. DOI: 10.1016/0022-5096(60)90013-2. URL: https://linkinghub.elsevier.com/retrieve/pii/0022509660900132.

Dunand, Matthieu and Dirk Mohr (2011). "Optimized butterfly specimen for the fracture testing of sheet materials under combined normal and shear loading". In: *Engineering Fracture Mechanics* 78.17, pp. 2919–2934. ISSN: 00137944. DOI: 10.1016/j.engfracmech.2011.08.008. URL: https://linkinghub.elsevier.com/retrieve/pii/S0013794411003067.

El Ghezal, M.I. and I. Doghri (2018). "Porous plasticity: Predictive second moment homogenization models coupled with Gurson's single cavity stress-strain solution". In: *International Journal of Plasticity* 108, pp. 201–221. ISSN: 07496419. DOI: 10.1016/j.ijplas.2018.05.006. URL: https://linkinghub.elsevier.com/retrieve/pii/S0749641917305946.

Eshelby, John Douglas (1957). "The determination of the elastic field of an ellipsoidal inclusion, and related problems". In: *Proceedings of the Royal Society of London. Series A. Mathematical and Physical Sciences* 241.1226, pp. 376–396. ISSN: 0080-4630. DOI: 10.1098/rspa.1957.0133. URL: https://royalsocietypublishing.org/doi/10.1098/rspa.1957.0133.

Esmaeili, Ali, Ali Javili, and Paul Steinmann (2016a). "A thermo-mechanical cohesive zone model accounting for mechanically energetic Kapitza interfaces". In: *International Journal of Solids and Structures* 92-93, pp. 29–44. ISSN: 00207683. DOI: 10.1016/j.ijsolstr.2016.04.035. URL: https://linkinghub.elsevier.com/retrieve/pii/S0020768316300592.

— (2016b). "Coherent energetic interfaces accounting for in-plane degradation". In: *International Journal of Fracture* 202.2, pp. 135–165. ISSN: 0376-9429. DOI: 10.1007/s10704-016-0160-4. URL: http://link.springer.com/10.1007/s10704-016-0160-4.

Esmaeili, Ali, Paul Steinmann, and Ali Javili (2017). "Non-coherent energetic interfaces accounting for degradation". In: *Computational Mechanics* 59.3, pp. 361–383. ISSN: 0178-7675. DOI: 10.1007/s00466-016-1342-7. URL: http://link.springer.com/10.1007/s00466-016-1342-7.

Fabrègue, D. and T. Pardoen (2008). "A constitutive model for elastoplastic solids containing primary and secondary voids". In: *Journal of the Mechanics and Physics of Solids* 56.3,

pp. 719–741. ISSN: 00225096. DOI: 10.1016/j.jmps.2007.07.008. URL: https://linkinghub.elsevier.com/retrieve/pii/S0022509607001585.

Fagerholt, E. et al. (2010). "Experimental and numerical investigation of fracture in a cast aluminium alloy". In: *International Journal of Solids and Structures* 47.24, pp. 3352–3365. ISSN: 00207683. DOI: 10.1016/j.ijsolstr.2010.08.013. URL: https://linkinghub.elsevier.com/retrieve/pii/S0020768310002921.

Faleskog, Jonas and Imad Barsoum (2013). "Tension–torsion fracture experiments—Part I: Experiments and a procedure to evaluate the equivalent plastic strain". In: *International Journal of Solids and Structures* 50.25-26, pp. 4241–4257. ISSN: 00207683. DOI: 10.1016/j.ijsolstr.2013.08.029. URL: https://linkinghub.elsevier.com/retrieve/pii/S0020768313003454.

Faleskog, Jonas, Xiaosheng Gao, and C. Fong Shih (1998). "Cell model for nonlinear fracture analysis - I. Micromechanics calibration". In: *International Journal of Fracture* 89.4, pp. 355–373. DOI: https://doi.org/10.1023/A:1007421420901. URL: https://doi.org/10.1023/A:1007421420901.

Falk, M. L., A. Needleman, and J. R. Rice (2001). "A critical evaluation of cohesive zone models of dynamic fractur". In: *Le Journal de Physique IV* 11.PR5, Pr5–43–Pr5–50. ISSN: 1155-4339. DOI: 10.1051/jp4:2001506. URL: http://www.edpsciences.org/10.1051/jp4:2001506.

Forest, Samuel (2009). "Micromorphic Approach for Gradient Elasticity, Viscoplasticity, and Damage". In: *Journal of Engineering Mechanics* 135.3, pp. 117–131. ISSN: 0733-9399. DOI: 10.1061/(ASCE)0733-9399(2009)135:3(117). URL: http://ascelibrary.org/doi/10.1061/{\%}28ASCE{\%}290733-9399{\%}282009{\%}29135{\%}3A3{\%}28117{\%}29.

Geers, M.G.D. et al. (1998). "Strain-based transient-gradient damage model for failure analyses". In: *Computer Methods in Applied Mechanics and Engineering* 160.1-2, pp. 133–153. ISSN: 00457825. DOI: 10.1016/S0045-7825(98)80011-X. URL: https://linkinghub.elsevier.com/retrieve/pii/S004578259880011X.

Geers, Marc G D (1997). "Experimental analysis and computational modelling of damage and fracture". PhD thesis. Technische Universiteit Eindhoven. DOI: 10.6100/IR477352.

Geuzaine, Christophe and Jean-François Remacle (2009). "Gmsh: A 3-D finite element mesh generator with built-in pre- and post-processing facilities". In: *International Journal for Numerical Methods in Engineering* 79.11, pp. 1309–1331. ISSN: 00295981. DOI: 10.1002/nme.2579. URL: http://doi.wiley.com/10.1002/nme.2579.

Gologanu, Mihai, Jean-Baptiste Leblond, and Josette Devaux (1993). "Approximate models for ductile metals containing non-spherical voids—Case of axisymmetric prolate ellipsoidal cavities". In: *Journal of the Mechanics and Physics of Solids* 41.11, pp. 1723–1754. ISSN: 00225096. DOI: 10.1016/0022-5096(93)90029-F. URL: https://linkinghub.elsevier.com/retrieve/pii/002250969390029F.

— (1994). "Approximate Models for Ductile Metals Containing Nonspherical Voids—Case of Axisymmetric Oblate Ellipsoidal Cavities". In: *Journal of Engineering Materials and Technology* 116.3. Ed. by P Suquet, pp. 290–297. ISSN: 0094-4289. DOI: 10.1115/1.2904290. URL: https://asmedigitalcollection.asme.org/materialstechnology/article/116/3/290/402774/Approximate-Models-for-Ductile-Metals-Containing.

Gurson, A. L. (1977). "Continuum Theory of Ductile Rupture by Void Nucleation and Growth: Part I—Yield Criteria and Flow Rules for Porous Ductile Media". In: *Journal of Engineering Materials and Technology* 99.1, pp. 2–15. ISSN: 0094-4289. DOI: 10.1115/1.3443401. URL: https://asmedigitalcollection.asme.org/materialstechnology/article/99/1/2/403937/Continuum-Theory-of-Ductile-Rupture-by-Void.

Guzmán, Carlos Felipe et al. (2018). "Damage prediction in single point incremental forming using an extended Gurson model". In: *International Journal of Solids and Structures* 151,

pp. 45–56. ISSN: 00207683. DOI: 10.1016/j.ijsolstr.2017.04.013. URL: https://linkinghub.elsevier.com/retrieve/pii/S0020768317301646.

Hannard, F. et al. (2016). "Characterization and micromechanical modelling of microstructural heterogeneity effects on ductile fracture of 6xxx aluminium alloys". In: *Acta Materialia* 103, pp. 558–572. ISSN: 13596454. DOI: 10.1016/j.actamat.2015.10.008. URL: https://linkinghub.elsevier.com/retrieve/pii/S1359645415300094.

Hillerborg, A., M. Modéer, and P.-E. Petersson (1976). "Analysis of crack formation and crack growth in concrete by means of fracture mechanics and finite elements". In: *Cement and Concrete Research* 6.6, pp. 773–781. ISSN: 00088846. DOI: 10.1016/0008-8846(76)90007-7. URL: https://linkinghub.elsevier.com/retrieve/pii/0008884676900077.

Huespe, A.E. et al. (2009). "A finite thickness band method for ductile fracture analysis". In: *International Journal of Plasticity* 25.12, pp. 2349–2365. ISSN: 07496419. DOI: 10.1016/j.ijplas.2009.03.005. URL: https://linkinghub.elsevier.com/retrieve/pii/S0749641909000461.

— (2012). "A finite strain, finite band method for modeling ductile fracture". In: *International Journal of Plasticity* 28.1, pp. 53–69. ISSN: 07496419. DOI: 10.1016/j.ijplas.2011.05.010. URL: https://linkinghub.elsevier.com/retrieve/pii/S0749641911000866.

Hulbert, Gregory M. and Jintai Chung (1996). "Explicit time integration algorithms for structural dynamics with optimal numerical dissipation". In: *Computer Methods in Applied Mechanics and Engineering* 137.2, pp. 175–188. ISSN: 00457825. DOI: 10.1016/S0045-7825(96)01036-5. URL: https://linkinghub.elsevier.com/retrieve/pii/S0045782596010365.

Johnson, Gordon R. and William H. Cook (1985). "Fracture characteristics of three metals subjected to various strains, strain rates, temperatures and pressures". In: *Engineering Fracture Mechanics* 21.1, pp. 31–48. ISSN: 00137944. DOI: 10.1016/0013-7944(85)90052-9. URL: https://linkinghub.elsevier.com/retrieve/pii/0013794485900529.

Keralavarma, S.M. and S. Chockalingam (2016). "A criterion for void coalescence in anisotropic ductile materials". In: *International Journal of Plasticity* 82, pp. 159–176. ISSN: 07496419. DOI: 10.1016/j.ijplas.2016.03.003. URL: https://linkinghub.elsevier.com/retrieve/pii/S0749641916300274.

Keralavarma, Shyam M. (2017). "A multi-surface plasticity model for ductile fracture simulations". In: *Journal of the Mechanics and Physics of Solids* 103, pp. 100–120. ISSN: 00225096. DOI: 10.1016/j.jmps.2017.03.005. URL: https://linkinghub.elsevier.com/retrieve/pii/S0022509616307359.

Kiran, Ravi and Kapil Khandelwal (2014). "Experimental Studies and Models for Ductile Fracture in ASTM A992 Steels at High Triaxiality". In: *Journal of Structural Engineering* 140.2, p. 04013044. ISSN: 0733-9445. DOI: 10.1061/(ASCE)ST.1943-541X.0000828. URL: http://ascelibrary.org/doi/10.1061/{\%}28ASCE{\%}29ST.1943-541X.0000828.

Koplik, J. and A. Needleman (1988). "Void growth and coalescence in porous plastic solids". In: *International Journal of Solids and Structures* 24.8, pp. 835–853. ISSN: 00207683. DOI: 10.1016/0020-7683(88)90051-0. URL: https://linkinghub.elsevier.com/retrieve/pii/0020768388900510.

Lassance, D., F. Scheyvaerts, and T. Pardoen (2006). "Growth and coalescence of penny-shaped voids in metallic alloys". In: *Engineering Fracture Mechanics* 73.8, pp. 1009–1034. ISSN: 00137944. DOI: 10.1016/j.engfracmech.2005.12.004. URL: https://linkinghub.elsevier.com/retrieve/pii/S0013794405003048.

Lassance, D. et al. (2007). "Micromechanics of room and high temperature fracture in 6xxx Al alloys". In: *Progress in Materials Science* 52.1, pp. 62–129. ISSN: 00796425. DOI: 10.1016/j.pmatsci.2006.06.001. URL: https://linkinghub.elsevier.com/retrieve/pii/S0079642506000399.

Leblond, Jean-Baptiste and Gérard Mottet (2008). "A theoretical approach of strain localization within thin planar bands in porous ductile materials". In: *Comptes Rendus Mécanique*

336.1-2, pp. 176–189. ISSN: 16310721. DOI: 10.1016/j.crme.2007.11.008. URL: https://linkinghub.elsevier.com/retrieve/pii/S1631072107002215.

Leclerc, Julien et al. (2018). "A damage to crack transition model accounting for stress triaxiality formulated in a hybrid nonlocal implicit discontinuous Galerkin-cohesive band model framework". In: *International Journal for Numerical Methods in Engineering* 113.3, pp. 374–410. ISSN: 00295981. DOI: 10.1002/nme.5618. URL: http://doi.wiley.com/10.1002/nme.5618.

Leclerc, Julien et al. (2020). "A micromechanics-based non-local damage to crack transition framework for porous elastoplastic solids". In: *International Journal of Plasticity* 127, p. 102631. ISSN: 07496419. DOI: 10.1016/j.ijplas.2019.11.010. URL: https://linkinghub.elsevier.com/retrieve/pii/S0749641919303821.

Lemaitre, Jean (1986). "Local approach of fracture". In: *Engineering Fracture Mechanics* 25.5-6, pp. 523–537. ISSN: 00137944. DOI: 10.1016/0013-7944(86)90021-4. URL: https://linkinghub.elsevier.com/retrieve/pii/0013794486900214.

Lemaitre, Jean et al. (2009). *Mécanique des matériaux solides-3eme édition*. Dunod.

Linder, C. and F. Armero (2007). "Finite elements with embedded strong discontinuities for the modeling of failure in solids". In: *International Journal for Numerical Methods in Engineering* 72.12, pp. 1391–1433. ISSN: 00295981. DOI: 10.1002/nme.2042. URL: http://doi.wiley.com/10.1002/nme.2042.

Liu, Yan, Lan Kang, and Hanbin Ge (2019). "Experimental and numerical study on ductile fracture of structural steels under different stress states". In: *Journal of Constructional Steel Research* 158, pp. 381–404. ISSN: 0143974X. DOI: 10.1016/j.jcsr.2019.04.001. URL: https://linkinghub.elsevier.com/retrieve/pii/S0143974X18313439.

Liu, Z.G., W.H. Wong, and T.F. Guo (2016). "Void behaviors from low to high triaxialities: Transition from void collapse to void coalescence". In: *International Journal of Plasticity* 84, pp. 183–202. ISSN: 07496419. DOI: 10.1016/j.ijplas.2016.05.008. URL: https://linkinghub.elsevier.com/retrieve/pii/S0749641916300821.

Mazars, Jacky and Gilles Pijaudier-Cabot (1996). "From damage to fracture mechanics and conversely: A combined approach". In: *International Journal of Solids and Structures* 33.20-22, pp. 3327–3342. ISSN: 00207683. DOI: 10.1016/0020-7683(96)00015-7. URL: https://linkinghub.elsevier.com/retrieve/pii/0020768396000157.

Mediavilla, J., R. H. J. Peerlings, and M. G. D. Geers (2006). "Discrete crack modelling of ductile fracture driven by non-local softening plasticity". In: *International Journal for Numerical Methods in Engineering* 66.4, pp. 661–688. ISSN: 0029-5981. DOI: 10.1002/nme.1572. URL: http://doi.wiley.com/10.1002/nme.1572.

Mergheim, J., E. Kuhl, and P. Steinmann (2004). "A hybrid discontinuous Galerkin/interface method for the computational modelling of failure". In: *Communications in Numerical Methods in Engineering* 20.7, pp. 511–519. ISSN: 10698299. DOI: 10.1002/cnm.689. URL: http://doi.wiley.com/10.1002/cnm.689.

Miehe, C., F. Welschinger, and M. Hofacker (2010). "Thermodynamically consistent phase-field models of fracture: Variational principles and multi-field FE implementations". In: *International Journal for Numerical Methods in Engineering* 83.10, pp. 1273–1311. ISSN: 00295981. DOI: 10.1002/nme.2861. URL: http://doi.wiley.com/10.1002/nme.2861.

Miehe, Christian, Martina Hofacker, and Fabian Welschinger (2010). "A phase field model for rate-independent crack propagation: Robust algorithmic implementation based on operator splits". In: *Computer Methods in Applied Mechanics and Engineering* 199.45-48, pp. 2765–2778. ISSN: 00457825. DOI: 10.1016/j.cma.2010.04.011. URL: https://linkinghub.elsevier.com/retrieve/pii/S0045782510001283.

Miehe, Christian et al. (2016). "Phase field modeling of fracture in porous plasticity: A variational gradient-extended Eulerian framework for the macroscopic analysis of ductile failure". In: *Computer Methods in Applied Mechanics and Engineering* 312, pp. 3–50. ISSN:

00457825. DOI: 10.1016/j.cma.2016.09.028. URL: https://linkinghub.elsevier.com/retrieve/pii/S0045782516305412.

Moës, Nicolas, John Dolbow, and Ted Belytschko (1999). "A finite element method for crack growth without remeshing". In: *International Journal for Numerical Methods in Engineering* 46.1, pp. 131–150. ISSN: 00295981. DOI: 10.1002/(SICI)1097-0207(19990910)46:1<131::AID-NME726>3.0.CO;2-J. URL: http://onlinelibrary.wiley.com/doi/10.1002/(SICI)1097-0207(19990910)46:1{\%}3C131::AID-NME726{\%}3E3.0.CO;2-J/abstract.

Molinari, J. F. et al. (2007). "The cohesive element approach to dynamic fragmentation: the question of energy convergence". In: *International Journal for Numerical Methods in Engineering* 69.3, pp. 484–503. ISSN: 00295981. DOI: 10.1002/nme.1777. URL: http://doi.wiley.com/10.1002/nme.1777.

Mota, Alejandro, Jaroslaw Knap, and Michael Ortiz (2008). "Fracture and fragmentation of simplicial finite element meshes using graphs". In: *International Journal for Numerical Methods in Engineering* 73.11, pp. 1547–1570. ISSN: 00295981. DOI: 10.1002/nme.2135. URL: http://doi.wiley.com/10.1002/nme.2135.

Nahshon, K. and J.W. Hutchinson (2008). "Modification of the Gurson Model for shear failure". In: *European Journal of Mechanics - A/Solids* 27.1, pp. 1–17. ISSN: 09977538. DOI: 10.1016/j.euromechsol.2007.08.002. URL: https://linkinghub.elsevier.com/retrieve/pii/S0997753807000721.

Needleman, A. (1972). "Void Growth in an Elastic-Plastic Medium". In: *Journal of Applied Mechanics* 39.4, pp. 964–970. ISSN: 0021-8936. DOI: 10.1115/1.3422899. URL: https://asmedigitalcollection.asme.org/appliedmechanics/article/39/4/964/423797/Void-Growth-in-an-ElasticPlastic-Medium.

— (1987). "A Continuum Model for Void Nucleation by Inclusion Debonding". In: *Journal of Applied Mechanics* 54.3, pp. 525–531. ISSN: 0021-8936. DOI: 10.1115/1.3173064. URL: https://asmedigitalcollection.asme.org/appliedmechanics/article/54/3/525/423262/A-Continuum-Model-for-Void-Nucleation-by-Inclusion.

Nguyen, Giang D., Alexander M. Korsunsky, and Jonathan P.H. Belnoue (2015). "A nonlocal coupled damage-plasticity model for the analysis of ductile failure". In: *International Journal of Plasticity* 64, pp. 56–75. ISSN: 07496419. DOI: 10.1016/j.ijplas.2014.08.001. URL: https://linkinghub.elsevier.com/retrieve/pii/S0749641914001491.

Nguyen, Van-Dung, Thomas Pardoen, and Ludovic Noels (2020). "A nonlocal approach of ductile failure incorporating void growth, internal necking, and shear dominated coalescence mechanisms". In: *Journal of the Mechanics and Physics of Solids* 137, p. 103891. ISSN: 00225096. DOI: 10.1016/j.jmps.2020.103891. URL: https://linkinghub.elsevier.com/retrieve/pii/S0022509619309275.

Nielsen, Kim Lau and Viggo Tvergaard (2010). "Ductile shear failure or plug failure of spot welds modelled by modified Gurson model". In: *Engineering Fracture Mechanics* 77.7, pp. 1031–1047. ISSN: 00137944. DOI: 10.1016/j.engfracmech.2010.02.031. URL: https://linkinghub.elsevier.com/retrieve/pii/S0013794410001128.

Noell, Philip J., Jay D. Carroll, and Brad L. Boyce (2018). "The mechanisms of ductile rupture". In: *Acta Materialia* 161, pp. 83–98. ISSN: 13596454. DOI: 10.1016/j.actamat.2018.09.006. URL: https://linkinghub.elsevier.com/retrieve/pii/S1359645418307006.

Noels, L. and R. Radovitzky (2006). "A general discontinuous Galerkin method for finite hyperelasticity. Formulation and numerical applications". In: *International Journal for Numerical Methods in Engineering* 68.1, pp. 64–97. ISSN: 0029-5981. DOI: 10.1002/nme.1699. URL: http://doi.wiley.com/10.1002/nme.1699.

— (2008). "An explicit discontinuous Galerkin method for non-linear solid dynamics: Formulation, parallel implementation and scalability properties". In: *International Journal for*

Numerical Methods in Engineering 74.9, pp. 1393–1420. ISSN: 00295981. DOI: 10.1002/nme.2213. URL: http://doi.wiley.com/10.1002/nme.2213.

Pandolfi, A. et al. (2000). "Three dimensional cohesive-element analysis and experiments of dynamic fracture in C300 steel". In: *International Journal of Solids and Structures* 37.27, pp. 3733–3760. ISSN: 00207683. DOI: 10.1016/S0020-7683(99)00155-9. URL: https://linkinghub.elsevier.com/retrieve/pii/S0020768399001559.

Pardoen, T. and J.W Hutchinson (2000). "An extended model for void growth and coalescence". In: *Journal of the Mechanics and Physics of Solids* 48.12, pp. 2467–2512. ISSN: 00225096. DOI: 10.1016/S0022-5096(00)00019-3. URL: https://linkinghub.elsevier.com/retrieve/pii/S0022509600000193.

Pardoen, T., Y. Marchal, and F. Delannay (2002). "Essential work of fracture compared to fracture mechanics—towards a thickness independent plane stress toughness". In: *Engineering Fracture Mechanics* 69.5, pp. 617–631. ISSN: 00137944. DOI: 10.1016/S0013-7944(01)00099-6. URL: https://linkinghub.elsevier.com/retrieve/pii/S0013794401000996.

Paulino, Glaucio H. et al. (2008). "A general topology-based framework for adaptive insertion of cohesive elements in finite element meshes". In: *Engineering with Computers* 24.1, pp. 59–78. ISSN: 0177-0667. DOI: 10.1007/s00366-007-0069-7. URL: http://link.springer.com/10.1007/s00366-007-0069-7.

Peerlings, R. H. J. et al. (1998). "Gradient-enhanced damage modelling of concrete fracture". In: *Mechanics of Cohesive-frictional Materials* 3.4, pp. 323–342. ISSN: 1082-5010. DOI: 10.1002/(SICI)1099-1484(1998100)3:4<323::AID-CFM51>3.0.CO;2-Z. URL: http://doi.wiley.com/10.1002/{\%}28SICI{\%}291099-1484{\%}281998100{\%}293{\%}3A4{\%}3C323{\%}3A{\%}3AAID-CFM51{\%}3E3.0.CO{\%}3B2-Z.

Peerlings, R. H.J. et al. (1996). "Gradient enhanced damage for quasi-brittle materials". In: *International Journal for Numerical Methods in Engineering* 39.19, pp. 3391–3403. ISSN: 00295981. DOI: 10.1002/(SICI)1097-0207(19961015)39:19<3391::AID-NME7>3.0.CO;2-D. URL: http://doi.wiley.com/10.1002/{\%}28SICI{\%}291097-0207{\%}2819961015{\%}2939{\%}3A19{\%}3C3391{\%}3A{\%}3AAID-NME7{\%}3E3.0.CO{\%}3B2-D.

Peerlings, R.H.J. et al. (2001). "A critical comparison of nonlocal and gradient-enhanced softening continua". In: *International Journal of Solids and Structures* 38.44-45, pp. 7723–7746. ISSN: 00207683. DOI: 10.1016/S0020-7683(01)00087-7. URL: https://linkinghub.elsevier.com/retrieve/pii/S0020768301000877.

Pijaudier-Cabot, Gilles and Zdeněk P. Bažant (1987). "Nonlocal Damage Theory". In: *Journal of Engineering Mechanics* 113.10, pp. 1512–1533. ISSN: 0733-9399. DOI: 10.1061/(ASCE)0733-9399(1987)113:10(1512). URL: http://ascelibrary.org/doi/10.1061/{\%}28ASCE{\%}290733-9399{\%}281987{\%}29113{\%}3A10{\%}281512{\%}29.

Pineau, A., A.A. Benzerga, and T. Pardoen (2016). "Failure of metals I: Brittle and ductile fracture". In: *Acta Materialia* 107, pp. 424–483. ISSN: 13596454. DOI: 10.1016/j.actamat.2015.12.034. URL: https://linkinghub.elsevier.com/retrieve/pii/S1359645415301403.

Poh, Leong Hien and Gang Sun (2017). "Localizing gradient damage model with decreasing interactions". In: *International Journal for Numerical Methods in Engineering* 110.6, pp. 503–522. ISSN: 00295981. DOI: 10.1002/nme.5364. URL: http://doi.wiley.com/10.1002/nme.5364.

Radovitzky, R. et al. (2011). "A scalable 3D fracture and fragmentation algorithm based on a hybrid, discontinuous Galerkin, cohesive element method". In: *Computer Methods in Applied Mechanics and Engineering* 200.1-4, pp. 326–344. ISSN: 00457825. DOI: 10.1016/j.cma.2010.08.014. URL: https://linkinghub.elsevier.com/retrieve/pii/S0045782510002471.

Reddi, D., V.K. Areej, and S.M. Keralavarma (2019). "Ductile failure simulations using a multi-surface coupled damage-plasticity model". In: *International Journal of Plasticity* 118, pp. 190–214. ISSN: 07496419. DOI: 10.1016/j.ijplas.2019.02.007. URL: https://linkinghub.elsevier.com/retrieve/pii/S0749641918307149.

Remmers, Joris J. C. et al. (2013). "The cohesive band model: a cohesive surface formulation with stress triaxiality". In: *International Journal of Fracture* 181.2, pp. 177–188. ISSN: 0376-9429. DOI: 10.1007/s10704-013-9834-3. URL: http://link.springer.com/10.1007/s10704-013-9834-3.

Reusch, Frederick, Bob Svendsen, and Dietmar Klingbeil (2003a). "A non-local extension of Gurson-based ductile damage modeling". In: *Computational Materials Science* 26.SUPPL. Pp. 219–229. ISSN: 09270256. DOI: 10.1016/S0927-0256(02)00402-0. URL: https://linkinghub.elsevier.com/retrieve/pii/S0927025602004020.

— (2003b). "Local and non-local Gurson-based ductile damage and failure modelling at large deformation". In: *European Journal of Mechanics - A/Solids* 22.6, pp. 779–792. ISSN: 09977538. DOI: 10.1016/S0997-7538(03)00070-6. URL: https://linkinghub.elsevier.com/retrieve/pii/S0997753803000706.

Rice, J.R. and D.M. Tracey (1969). "On the ductile enlargement of voids in triaxial stress fields". In: *Journal of the Mechanics and Physics of Solids* 17.3, pp. 201–217. ISSN: 00225096. DOI: 10.1016/0022-5096(69)90033-7. URL: https://linkinghub.elsevier.com/retrieve/pii/0022509669900337.

Riks, E. (1979). "An incremental approach to the solution of snapping and buckling problems". In: *International Journal of Solids and Structures* 15.7, pp. 529–551. ISSN: 00207683. DOI: 10.1016/0020-7683(79)90081-7. URL: https://linkinghub.elsevier.com/retrieve/pii/0020768379900817.

Roth, Christian C. et al. (2018). "Ductile damage mechanism under shear-dominated loading: In-situ tomography experiments on dual phase steel and localization analysis". In: *International Journal of Plasticity* 109, pp. 169–192. ISSN: 07496419. DOI: 10.1016/j.ijplas.2018.06.003. URL: https://linkinghub.elsevier.com/retrieve/pii/S0749641917306940.

Rousselier, G. (1987). "Ductile fracture models and their potential in local approach of fracture". In: *Nuclear Engineering and Design* 105.1, pp. 97–111. ISSN: 00295493. DOI: 10.1016/0029-5493(87)90234-2. URL: https://linkinghub.elsevier.com/retrieve/pii/0029549387902342.

Scheyvaerts, F., T. Pardoen, and P.R. Onck (2010). "A New Model for Void Coalescence by Internal Necking". In: *International Journal of Damage Mechanics* 19.1, pp. 95–126. ISSN: 1056-7895. DOI: 10.1177/1056789508101918. URL: http://journals.sagepub.com/doi/10.1177/1056789508101918.

Shen, Rilin, Haim Waisman, and Licheng Guo (2019). "Fracture of viscoelastic solids modeled with a modified phase field method". In: *Computer Methods in Applied Mechanics and Engineering* 346, pp. 862–890. ISSN: 00457825. DOI: 10.1016/j.cma.2018.09.018. URL: https://linkinghub.elsevier.com/retrieve/pii/S0045782518304699.

Siegmund, T. and W. Brocks (2000). "A numerical study on the correlation between the work of separation and the dissipation rate in ductile fracture". In: *Engineering Fracture Mechanics* 67.2, pp. 139–154. ISSN: 00137944. DOI: 10.1016/S0013-7944(00)00054-0. URL: https://linkinghub.elsevier.com/retrieve/pii/S0013794400000540.

Steinke, Christian, Imadeddin Zreid, and Michael Kaliske (2017). "On the relation between phase-field crack approximation and gradient damage modelling". In: *Computational Mechanics* 59.5, pp. 717–735. ISSN: 0178-7675. DOI: 10.1007/s00466-016-1369-9. URL: http://link.springer.com/10.1007/s00466-016-1369-9.

Tabiei, Ala and Wenlong Zhang (2017). "Cohesive element approach for dynamic crack propagation: Artificial compliance and mesh dependency". In: *Engineering Fracture Mechanics*

180, pp. 23–42. ISSN: 00137944. DOI: 10.1016/j.engfracmech.2017.05.009. URL: https://linkinghub.elsevier.com/retrieve/pii/S0013794416304519.

Tanguy, B. and J. Besson (2002). "An extension of the Rousselier model to viscoplastic temperature dependent materials". In: *International Journal of Fracture* 116.1, pp. 81–101. ISSN: 03769429. DOI: 10.1023/A:1020192527733. URL: https://doi.org/10.1023/A:1020192527733.

Tekoglu, C., J. W. Hutchinson, and T. Pardoen (2015). "On localization and void coalescence as a precursor to ductile fracture". In: *Philosophical Transactions of the Royal Society A: Mathematical, Physical and Engineering Sciences* 373.2038, p. 20140121. ISSN: 1364-503X. DOI: 10.1098/rsta.2014.0121. URL: https://royalsocietypublishing.org/doi/10.1098/rsta.2014.0121.

Tekoglu, C., J.-B. Leblond, and T. Pardoen (2012). "A criterion for the onset of void coalescence under combined tension and shear". In: *Journal of the Mechanics and Physics of Solids* 60.7, pp. 1363–1381. ISSN: 00225096. DOI: 10.1016/j.jmps.2012.02.006. URL: https://linkinghub.elsevier.com/retrieve/pii/S0022509612000373.

Thomason, P.F. (1985a). "A three-dimensional model for ductile fracture by the growth and coalescence of microvoids". In: *Acta Metallurgica* 33.6, pp. 1087–1095. ISSN: 00016160. DOI: 10.1016/0001-6160(85)90202-0. URL: https://linkinghub.elsevier.com/retrieve/pii/0001616085902020.

— (1985b). "Three-dimensional models for the plastic limit-loads at incipient failure of the intervoid matrix in ductile porous solids". In: *Acta Metallurgica* 33.6, pp. 1079–1085. ISSN: 00016160. DOI: 10.1016/0001-6160(85)90201-9. URL: https://linkinghub.elsevier.com/retrieve/pii/0001616085902019.

Torki, M.E. et al. (2017). "Theoretical and numerical analysis of void coalescence in porous ductile solids under arbitrary loadings". In: *International Journal of Plasticity* 91, pp. 160–181. ISSN: 07496419. DOI: 10.1016/j.ijplas.2017.02.011. URL: https://linkinghub.elsevier.com/retrieve/pii/S0749641916302595.

Torki, Mohammad E. (2019). "A unified criterion for void growth and coalescence under combined tension and shear". In: *International Journal of Plasticity* 119, pp. 57–84. ISSN: 07496419. DOI: 10.1016/j.ijplas.2019.02.002. URL: https://linkinghub.elsevier.com/retrieve/pii/S0749641918303152.

Tvergaard, V. and A. Needleman (1984). "Analysis of the cup-cone fracture in a round tensile bar". In: *Acta Metallurgica* 32.1, pp. 157–169. ISSN: 00016160. DOI: 10.1016/0001-6160(84)90213-X. URL: https://linkinghub.elsevier.com/retrieve/pii/000161608490213X.

Tvergaard, Viggo (1981). "Influence of voids on shear band instabilities under plane strain conditions". In: *International Journal of Fracture* 17.4, pp. 389–407. ISSN: 0376-9429. DOI: 10.1007/BF00036191. URL: http://link.springer.com/10.1007/BF00036191.

— (1990). "Effect of fibre debonding in a whisker-reinforced metal". In: *Materials Science and Engineering: A* 125.2, pp. 203–213. ISSN: 09215093. DOI: 10.1016/0921-5093(90)90170-8. URL: https://linkinghub.elsevier.com/retrieve/pii/0921509390901708.

— (2004). "Predictions of mixed mode interface crack growth using a cohesive zone model for ductile fracture". In: *Journal of the Mechanics and Physics of Solids* 52.4, pp. 925–940. ISSN: 00225096. DOI: 10.1016/S0022-5096(03)00115-7. URL: https://linkinghub.elsevier.com/retrieve/pii/S0022509603001157.

Tvergaard, Viggo and John W. Hutchinson (1992). "The relation between crack growth resistance and fracture process parameters in elastic-plastic solids". In: *Journal of the Mechanics and Physics of Solids* 40.6, pp. 1377–1397. ISSN: 00225096. DOI: 10.1016/0022-5096(92)90020-3. URL: https://linkinghub.elsevier.com/retrieve/pii/0022509692900203.

Vandoren, B. and A. Simone (2018). "Modeling and simulation of quasi-brittle failure with continuous anisotropic stress-based gradient-enhanced damage models". In: *Computer Methods in Applied Mechanics and Engineering* 332, pp. 644–685. ISSN: 00457825. DOI: 10.

1016/j.cma.2017.12.027. URL: https://linkinghub.elsevier.com/retrieve/pii/S0045782517307776.

Vigueras, Guillermo et al. (2015). "An XFEM/CZM implementation for massively parallel simulations of composites fracture". In: *Composite Structures* 125, pp. 542–557. ISSN: 02638223. DOI: 10.1016/j.compstruct.2015.01.053. URL: https://linkinghub.elsevier.com/retrieve/pii/S0263822315001063.

Wang, Yongxiang and Haim Waisman (2016). "From diffuse damage to sharp cohesive cracks: A coupled XFEM framework for failure analysis of quasi-brittle materials". In: *Computer Methods in Applied Mechanics and Engineering* 299, pp. 57–89. ISSN: 00457825. DOI: 10.1016/j.cma.2015.10.019. URL: https://linkinghub.elsevier.com/retrieve/pii/S0045782515003485.

— (2018). "An arc-length method for controlled cohesive crack propagation using high-order XFEM and Irwin's crack closure integral". In: *Engineering Fracture Mechanics* 199, pp. 235–256. ISSN: 00137944. DOI: 10.1016/j.engfracmech.2018.05.018. URL: https://linkinghub.elsevier.com/retrieve/pii/S0013794418301358.

Worswick, M (1990). "Void growth and constitutive softening in a periodically voided solid". In: *Journal of the Mechanics and Physics of Solids* 38.5, pp. 601–625. ISSN: 00225096. DOI: 10.1016/0022-5096(90)90025-Y. URL: https://linkinghub.elsevier.com/retrieve/pii/002250969090025Y.

Wu, C. T. et al. (2016). "A meshfree continuous–discontinuous approach for the ductile fracture modeling in explicit dynamics analysis". In: *Computational Mechanics* 58.3, pp. 391–409. ISSN: 0178-7675. DOI: 10.1007/s00466-016-1299-6. URL: http://link.springer.com/10.1007/s00466-016-1299-6.

Wu, L., G. Becker, and L. Noels (2014). "Elastic damage to crack transition in a coupled non-local implicit discontinuous Galerkin/extrinsic cohesive law framework". In: *Computer Methods in Applied Mechanics and Engineering* 279, pp. 379–409. ISSN: 00457825. DOI: 10.1016/j.cma.2014.06.031. URL: https://linkinghub.elsevier.com/retrieve/pii/S0045782514002175.

Wu, L. et al. (2013). "A micro–meso-model of intra-laminar fracture in fiber-reinforced composites based on a discontinuous Galerkin/cohesive zone method". In: *Engineering Fracture Mechanics* 104, pp. 162–183. ISSN: 00137944. DOI: 10.1016/j.engfracmech.2013.03.018. URL: https://linkinghub.elsevier.com/retrieve/pii/S0013794413001252.

Xu, Qiang and Zixing Lu (2013). "An elastic–plastic cohesive zone model for metal–ceramic interfaces at finite deformations". In: *International Journal of Plasticity* 41, pp. 147–164. ISSN: 07496419. DOI: 10.1016/j.ijplas.2012.09.008. URL: https://linkinghub.elsevier.com/retrieve/pii/S0749641912001386.

Xu, X.-P. and A. Needleman (1994). "Numerical simulations of fast crack growth in brittle solids". In: *Journal of the Mechanics and Physics of Solids* 42.9, pp. 1397–1434. ISSN: 00225096. DOI: 10.1016/0022-5096(94)90003-5. URL: https://linkinghub.elsevier.com/retrieve/pii/0022509694900035.

Xue, Z. et al. (2010). "Calibration procedures for a computational model of ductile fracture". In: *Engineering Fracture Mechanics* 77.3, pp. 492–509. ISSN: 00137944. DOI: 10.1016/j.engfracmech.2009.10.007. URL: https://linkinghub.elsevier.com/retrieve/pii/S0013794409003233.

Xue, Zhenyu, Jonas Faleskog, and John W. Hutchinson (2013). "Tension–torsion fracture experiments – Part II: Simulations with the extended Gurson model and a ductile fracture criterion based on plastic strain". In: *International Journal of Solids and Structures* 50.25-26, pp. 4258–4269. ISSN: 00207683. DOI: 10.1016/j.ijsolstr.2013.08.028. URL: https://linkinghub.elsevier.com/retrieve/pii/S0020768313003442.

Zehnder, Alan T (2012). *Fracture Mechanics*. Vol. 62. Lecture Notes in Applied and Computational Mechanics. Dordrecht: Springer Netherlands. ISBN: 978-94-007-2594-2. DOI: 10.

1007/978-94-007-2595-9. URL: http://link.springer.com/10.1007/978-94-007-2595-9.

Zhang, Yi, Eric Lorentz, and Jacques Besson (2018). "Ductile damage modelling with locking-free regularised GTN model". In: *International Journal for Numerical Methods in Engineering* 113.13, pp. 1871–1903. ISSN: 00295981. DOI: 10.1002/nme.5722. URL: http://doi.wiley.com/10.1002/nme.5722.

Zhang, Z.L, C. Thaulow, and J. Ødegård (2000). "A complete Gurson model approach for ductile fracture". In: *Engineering Fracture Mechanics* 67.2, pp. 155–168. ISSN: 00137944. DOI: 10.1016/S0013-7944(00)00055-2. URL: https://linkinghub.elsevier.com/retrieve/pii/S0013794400000552.

Zhou, Fenghua and Jean-Francois Molinari (2004). "Stochastic fracture of ceramics under dynamic tensile loading". In: *International Journal of Solids and Structures* 41.22-23, pp. 6573–6596. ISSN: 00207683. DOI: 10.1016/j.ijsolstr.2004.05.029. URL: https://linkinghub.elsevier.com/retrieve/pii/S0020768304002562.